Functionalization of Two-Dimensional Transition Metal Dichalcogenides

Trinity
College
Dublin
The University of Dublin

A thesis submitted for the degree of Doctor of Philosophy

By

Xin Chen

Supervisor: Prof. Aidan McDonald

School of Chemistry, CRANN/AMBER Nanoscience Institute

Trinity College Dublin, The University of Dublin

January 2018

Declaration

I, the author, declare that this thesis has not been submitted as an exercise for a degree at this or any other university and it is entirely my own work. I agree to deposit this thesis in the University's open access institutional repository or allow the library to do so on my behalf, subject to Irish Copyright Legislation and Trinity College Library conditions of use and acknowledgement.

Signature of author: ____

Xin Chen

January, 2018

Summary

Two-dimensional transition metal dichalcogenides (2D TMDs) have aroused enormous interest in recent years due to their intriguing properties and a wide array of potential applications. Further tailoring their colloidal and surface properties and fully harnessing their capabilities can be achieved through surface functionalization. In this thesis, two facile avenues to functionalize 2D TMDs with either organic thiols or inorganic complexes are demonstrated. A general route to functionalize exfoliated 2H-MoS_2 with organic thiols (e.g., L-cysteine and 1-octanethiol) was initially illustrated in Chapter 2. It was found that instead of adsorption of thiol monomers covalently or datively at sulfur vacancies, functionalization of 2D MoS_2 with organic thiols tends to produce the corresponding disulfide species physisorbed on the surface of nanosheets. The kinetic behaviors of 2H-MoS_2/1-octanethiol reaction under the inert atmosphere were illustrated in Chapter 3 in order to further elucidate the MoS_2 mediated thiol oxidation. The rate of 1-octanethiol oxidation (to dioctyl disulfide) was found to be directly related to the concentration of MoS_2 and 1-octanethiol, the thickness of MoS_2 nanosheets and the proton transfer process (KIE = 2). In the second approach, a stepwise functionalization strategy was developed (Chapter 4) to covalently bind $[Ru^{II}(bpy)_3]^{2+}$-based photosensitizer onto chemically exfoliated MoS_2 nanosheets (ce-1T-MoS_2). The photoelectrochemical (PEC) measurement of the $[Ru^{II}(bpy)_3]$-MoS_2 electrode in ascorbic acid displayed a significant improvement of photocurrent generation compared to the non-functionalized MoS_2, signifying the potential of the $[Ru^{II}(bpy)_3]$-MoS_2 covalent assembly in photo-hydrogen production. Efforts to further tune the PEC performance of such dye-sensitized MoS_2 system through the covalent incorporation of other photosensitizers were demonstrated in Chapter 5. The PEC performance of the whole dye-sensitized MoS_2 device was found to rely on both the surface coverage of photosensitizers and the catalytic activity of functionalized MoS_2.

Acknowledgments

I am grateful for a number of people who have helped me through the last few years and I would like to take this opportunity to offer my thanks to them.

First and foremost, I would like to sincerely thank my supervisor Prof. Aidan McDonald for all the guidance and support, both academically and personally, that he has given me over the past four years. He always inspires and encourages students to do their best to achieve exceptional goals and my appreciation to him will surely continue over the years.

I would also like to thank Dr. Claudia Backes, currently a group leader at the University of Heidelberg, for guiding me into the field of nanoscience by sharing her knowledge and experiences at the beginning of my Ph.D. I would like to extend my appreciation to Dr. Nina Berner and Dr. Cormac McGuinness for their assistance with the XPS measurements. I am also immensely grateful to Prof. Yurii Gun'ko and Prof. Valeria Nicolosi for facilitating my confirmation. I had many discussions with all of the aforementioned people, which were really helpful for my research. Many thanks to David McAteer, Dr. Zahra Gholamvand and Dr. Ian Godwin from Prof. Jonathan N. Coleman's group and Amy Lynes from Prof. Thorfinnur Gunnlaugsson's group for their valuable contributions to this research project. My gratitude to the AMBER platform, Science Foundation Ireland and Government of Ireland Scholarship for funding my research.

I would like to thank everyone in Bio-inspired Inorganic Chemistry group, in particular, Andrew Ure, Paolo Pirovano, Ciara McGlynn, Adriana Magherusan, Dr. Bertrand Gerey, Dr. Ankita Das, Giuseppe Spedalotto, Marta Lovisari, Dr. Duenpen Unjaroen and Daniel Nelis, for generously offering help and support along the way. A big thank you to Ciara McGlynn. I appreciate all the effort and time she spent in helping me to proofread the manuscripts and thesis. My acknowledgment to the technical staff in School of Chemistry and School of Physics, Dr. Gary Hessman, Dr. Manuel Ruether, Dr. Brendan Twamley, Dr. John O'Brien, Mr. Peter Brien, Ms. Peggy Brehon and Mr. David O'Mahony, for all the kind help and support.

Lastly, I would like to thank my family for all the love, encouragement and support throughout this adventure.

Xin
September, 2017

Contents

List of Abbreviations

2D	Two-dimensional
TMDs	Transition Metal Dichalcogenides
CVD	Chemical Vapor Deposition
HER	Hydrogen Evolution Reaction
SVs	Sulfur Vacancies
BN	Boron Nitride
HDS	Hydrodesulfurization Reaction
CB	Conduction Band
NMP	1-Methyl-2- pyrrolidone
HSP	Hansen solubility parameter
Tween 80	Polyoxyethylene sorbitan monooleate
PVP	Polyvinyl- pyrrolidone
PluronicP-123	Poly (ethyleneglycol)-*block*-poly (propyleneglycol)-*block*-poly (ethyl-ene glycol)
n-BuLi	n-Butyllithium
ce-1T-MoS$_2$	Chemically exfoliated MoS$_2$ nanosheets
XPS	X-ray photoelectron spectroscopy
ATR-FTIR	Solid-state attenuated total reflectance Fourier transform infrared
CP-MAS	Crosspolarization Magic-angle Spinning
TGA	Thermogravimetric Analysis
FETs	Field-Effect Transistors
PEG	Polyethyleneglycol

PMMA	Polymethylmethacrylate
STM	Scanning Tunneling Microscopy
DRIFT	Diffuse Reflectance Infrared Fourier Transform Spectroscopy
TEM	Transmission Electron Microscopy
OER	Oxygen Evolution Reaction
RGO	Reduced Graphene Oxide
MGF	Mesoporous Graphene Foams
CFP	Carbon Fiber Paper
DFT	Density functional theory
RHE	Reversible Hydrogen Electrode
SHE	Standard Hydrogen Electrode
DSC	Dye-sensitized Solar Cell
DSP	Dye-sensitized Photocatalysis
TOF	Turn-Over Frequency
IPA	Propan-2-ol
CHP	N-Cyclohexyl-2- pyrrolidone
KIE	Kinetic Isotope Effect
PEC	Photoelectrochemical
XRD	X-ray Powder Diffraction
SEM	Scanning Electron Microscopy
EDX	Energy-dispersive X-ray spectroscopy
LSV	Linear Sweep Voltammetry
CA	Chronoamperometry
ITO	Indium-tin Oxide

List of Figures

List of Tables

CHAPTER 1 Introduction

This chapter is partially based on the following manuscript:

X. Chen and A. R. McDonald*, *Adv. Mater.* **2016**, *28*, 5738-5746.

1.1 Overview

The rapid gains in graphene-based research and technology since 2004 has ignited increasing research enthusiasm in its close relatives and other two-dimensional (2D) materials such as layered nitrides, transition metal dichalcogenides, transition metal oxides. Among them, layered transition metal dichalcogenides (TMDs), in particular molybdenum disulfide (MoS_2) nanosheets, have attracted tremendous interest due to their natural abundance and intriguing electronic, physical, and chemical properties. [1-4]

One major focus of experimental research in recent years has concentrated on the development of experimental methods to produce high-quality and thin-layer TMD nanosheets. The commonly applied techniques include mechanical cleavage, solution-based exfoliation, chemical vapor deposition (CVD), and wet chemical synthesis.[5-9] All of these strategies for TMD nanosheets production allow for deeper investigation of their layer-dependent properties, and exploration of their potential applications. Among them, the solution-based exfoliation techniques such as liquid-phase exfoliation and chemical exfoliation hold particular promise in the scalable production of TMD nanosheets with low cost and convenient hybridization with other materials towards modified properties. Thus, in this work, TMD nanosheets were produced using solution-based exfoliation techniques.

Layered TMDs displayed a wealth of exceptional properties when the thickness is thinned down to few or single layer. The intense research on thin-layer MoS_2 in recent years was mainly inspired by two of its exotic properties. One is the sizeable bandgap (1.8-1.9 eV)[10] in monolayer MoS_2, which is of great interest for use in photochemical applications and optoelectronic devices. The other is its excellent catalytic activity for the hydrogen evolution reaction (HER).[11] In particular, incorporation of the MoS_2 catalyst into artificial photosynthesis devices for hydrogen production has emerged and has been gaining strength over the past 3 years, [12, 13] which would grant immense opportunities for solar energy storage and clean fuel production, positively impacting the environment and human health. The research gap in this area will be highlighted later in this chapter and a strategy to bridge the gap will be investigated as a preliminary study in the second part of this research.

Despite the significant progress that has been made in production and application of 2D TMDs, there remain many challenges associated with synthesis, processing, and fabrication of exfoliated TMDs into devices. To further optimize their processibility, modify their properties, fully harness their capabilities, and even broaden their applications, chemical functionalization of such layered TMD materials is an absolute necessity. One caveat to chemical functionalization of TMDs is the inert nature of the basal plane, wherein the surface chalcogen atoms are saturated, and thus are not highly reactive, while the metal sites are embedded beneath the chalcogen layers, all eliminating them from being useful for functionalization. This is apparent from the fact that, so far, successful covalent functionalization of the TMD slabs has only been reported on chemically exfoliated TMD nanosheets by reacting them with electrophiles (organoiodides and diazonium salts).[14, 15] In another strategy to circumvent this challenge, our group first demonstrated a metal coordination chemistry directed functionalization route, in which functionalization of liquid exfoliated 2H-MoS_2 using sulfur-specific metal acetate salts was achieved,[16] leading to the formation of metal-sulfur dative bonds at the metal acetates/MoS_2 basal plane interface. The third strategy tends to avoid the inert basal plane, and instead, has focused on the reactivity of defect sites of TMD lattices. These defect sites exist in the form of atom vacancies such as sulfur vacancies (SVs) on the surface and grain boundary of 2D MoS_2 and can potentially react with organic thiols.[17] To date functionalization of MoS_2 nanosheets using organic thiols has emerged as one of the most widely applied techniques to modify the structures and properties of TMDs, although the exact mechanism of MoS_2/thiol interaction remains unclear. In an effort to clarify this problem, a detailed study on MoS_2/thiol interaction will be demonstrated in the first part of this work.

In this chapter, the state-of-art studies of 2D TMDs nanosheets (focusing on MoS_2) will be reviewed with a particular attention on the exotic properties of 2D MoS_2, established strategies towards functionalization of MoS_2 and recent advances of MoS_2 based nanomaterials in electrocatalytic and photocatalytic hydrogen evolution. Based on the overview, the author will identify the challenges and opportunities in this burgeoning field, and set the basis for this research.

1.2 Two-dimensional materials

The field of two-dimensional (2D) materials was fueled by the successful isolation of graphene, a one-atom-thick *sp*^{2} hybridized carbon sheet, from bulk graphite using scotch tape by Novoselov and coworkers in 2004[18]. The exotic properties of graphene include high electrical and thermal conductivity, high mechanical strength, and high mobility, which has triggered enormous research projects since its discovery and continues to flourish with impressive advances. Noting that pristine graphene lacks an intrinsic bandgap and amenability for chemical modification, other 2D crystals such as transition metal chalcogenides (TMDs), oxides, layered nitrides, group-IV graphene-like 2D buckled nanosheets (e.g., silicene and germanene), phosphorene and layered transition metal carbides and carbonitrides (MXenes) have attracted increasing attention in recent years.[19-23](Fig. 1.1)

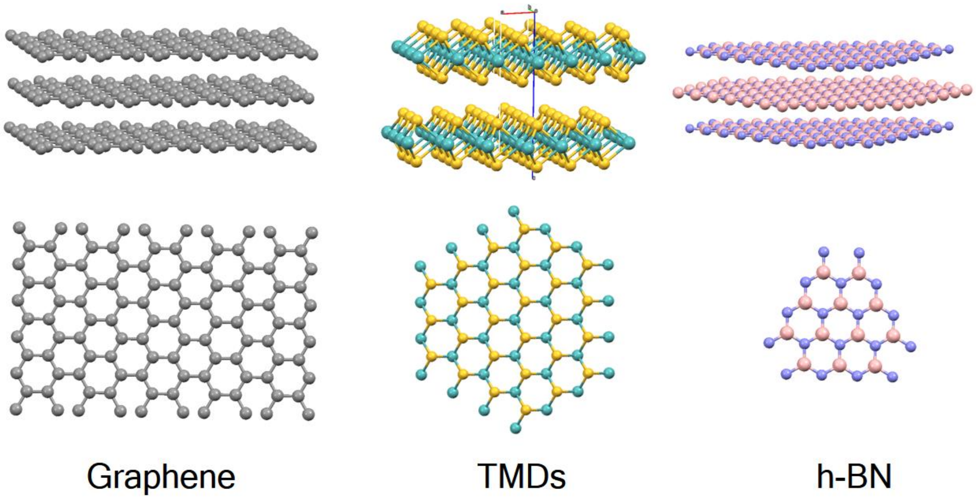

Figure 1.1 Crystal structures of representative two-dimensional materials. Top: side-on view of 3D crystal structures of graphite, TMDs and h-BN. Bottom: top-down view of 2D graphene, TMDs and h-BN.

The common feature of these layered materials is that bulk 3D crystalline solids are stacked structures, with strong covalent bonds within the plane and weak van der Waals interactions between adjacent sheets, which allows for easy delamination of 3D crystals into 2D nanosheets through exfoliation. When the thickness is reduced to few or single layer, a number of unusual physical phenomena will occur due to the quantum confinement effect and change of interlayer coupling as well as the lattice symmetry. As an example, bulk molybdenum disulfide (MoS_2) crystal is a semiconductor with an indirect bandgap about 1.3 eV[24], whereas the direct bandgap of ~1.8-1.9 eV[10] can be obtained when monolayer MoS_2 is achieved.

1.3 Two-dimensional Transition Metal Dichalcogenides

Layered TMDs are a class of materials with MX_2 stoichiometry, where M refers to a transition metal typically from Groups 4-7 (M = Ti, Nb, Ta, Mo, W) of the periodic table and X refers to a chalcogen such as S, Se or Te. To date, approximately 40 different layered TMDs have been identified.[19] Unlike graphene, single layer TMDs have a thickness of 6-7 Å[25]. Each individual layer of TMDs exists in a polymeric X-M-X form, with a plane of transition metal atoms sandwiched between two planes of chalcogen atoms.

Depending on the coordination environment of transition metal and the electronic configuration (*d*-electron count, thus metal and oxidation state determine electronic configuration), layered TMDs exhibit disparate electronic structures.[2] The coordination of metal atoms in layered TMDs can either be trigonal prismatic (2H polymorph) with D_{3h} point group symmetry or octahedral (1T polymorph) with D_{3d} point group symmetry. Which phase is thermodynamically preferred hinges primarily on the *d*-electron count of the transition metal. For example, the Group 6 TMDs (featuring d^2 transition metal center) such as MoS_2 and WS_2 primarily adopt the trigonal prismatic geometry, whereas Group 4 TMDs (d^0) are typically found in the octahedral structure.

For layered TMDs with metals in a trigonal prismatic geometry, the *d* orbitals are split into three sub-bands (d_{z^2} (a$_1$), $d_{x^2-y^2}$, d_{xy} (e), and $d_{xz,yz}$ (e′)) with a sizeable bandgap between the former two; whereas for layered TMDs with a octahedral coordination of metal, the *d* orbitals are split into two degenerated sub-bands (d_{z^2}, $d_{x^2-y^2}$ (e$_g$) and $d_{yz,xz,xy}$ (t$_{2g}$)). (Fig. 1.2) By varying the orbital occupation, diverse electronic properties of TMDs from metal to semiconductor and to topological insulators can be obtained. For example, 2H-$TaSe_2$ (d^1) is metallic due to the partially filled d_{z^2}, whereas 2H-WSe_2 (d^2) is a semiconductor due to the fully occupied d_{z^2}. On the other hand, for the materials containing the same MX_2 elemental formula, the different *d*-orbital splitting would lead to totally different electronic properties and thus distinct physical and chemical properties. For example, 2H-MoS_2 is semiconducting, whereas 1T-MoS_2 is metallic. [2, 26-28]

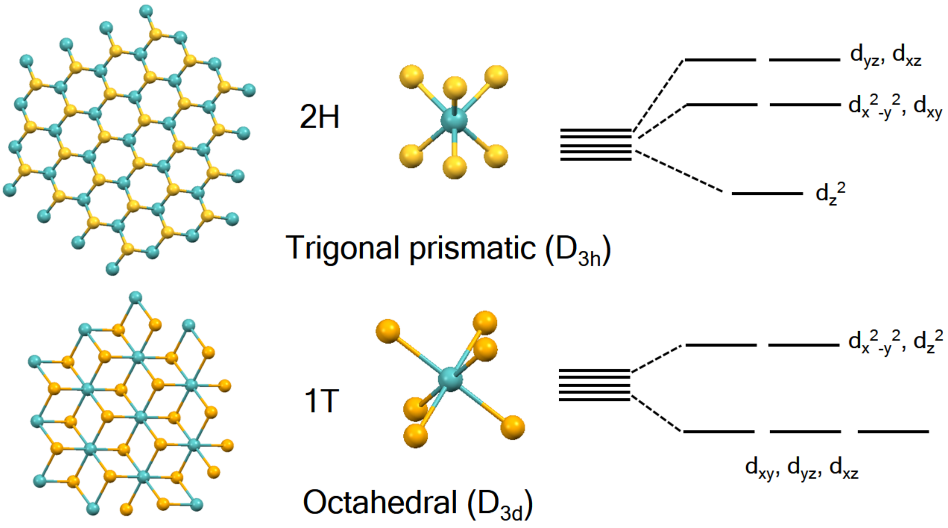

Figure 1.2 Left: top-down view of 2D TMDs with trigonal prismatic (2H-polymorph) and octahedral coordination (1T-polymorph). Atom color code: blue, transition metal; yellow, chalcogen. Right: *d*-orbital splitting diagrams of 2H-polymorph and 1T-polymorph, respectively.

1.4 Two-dimensional molybdenum disulfide (2D MoS_2)

As a prototypical TMD, 2D MoS_2 acts as an excellent model system to explore the chemistry of 2D TMDs. 2D MoS_2 (d^2) is often found in one of two polymorphs: trigonal prismatic 2H-polymorph and octahedral 1T-polymorph. In 2H-phase, the two *d* electrons fill the non-bonding band (a_1) in pairs, thus 2D 2H-MoS_2 is a semiconductor with a sizeable band gap. Whereas in 1T-polymorph, the two electrons partially fill the t_{2g} bands, yielding the metallic nature of 1T-MoS_2. 2H-MoS_2 is thermodynamically stable, whereas 1T-phase MoS_2 is metastable.[29] Therefore, natural MoS_2 predominantly exists in 2H-polymorph, unless the *d*-electron count is modified. It has been reported by several groups that lithium intercalation in semiconducting 2H-MoS_2 can lead to a phase transformation to metallic 1T-MoS_2. The modified *d*-electron filling by encapsulation of lithium into MoS_2 lattice and the free energy change of two phases likely account for this phase transformation, although the exact mechanism remains disputable.[19] On the other end, 1T-MoS_2 was found to undergo an irreversible exothermic transition to 2H-MoS_2 by annealing at 300 °C, this was confirmed by the re-emergence of bandgap photoluminescence[30]. In addition to the electronic structure, the presence of dangling bonds at the edges and defective sites of 2D MoS_2 can induce additional local chemical effects to the surface chemistry of MoS_2 nanoflakes. For example, sulfided Mo edges of MoS_2 are capable of binding with hydrogen via unsaturated sulfur atoms, thus exhibiting the catalytic activity for hydrogen evolution reaction.[31]

1.4.1 Properties and opportunities of 2D MoS_2

Optical and electronic properties

The attention on MoS_2 has been initially focused on its applications as a dry lubricant due to its chemical inertness and weak interlayer interactions. The rapid pace of progress in the methodology for nanosheets synthesis and isolation leads to more striking features of 2D MoS_2 being discovered. Of them, the direct bandgap (~1.9 eV) of monolayer 2H-MoS_2 is one of the most appealing properties. Inspired by this sizeable bandgap as well as latterly demonstrated high carrier mobility and high current on/off ratio[1, 32], soaring interest has been concentrated on the fabrication of 2H-MoS_2 based electronics and optoelectronics aiming to provide some alternative solutions to overcome the weakness of graphene (zero-bandgap). Moreover, the enlarged bandgap in monolayer 2H-MoS_2 enables an improved optical adsorption ability and a remarkably enhanced photoluminescence intensity and quantum yield compared to its bulk counterparts. 2H-MoS_2 is also found to have an excellent stability against photocorrosion due to the presence of an anti-bonding state on the top of the valence band.[33] All these features make thin layers of 2H-MoS_2 more advantageous over its bulk form and other traditional semiconductors such as cadmium sulfide (CdS) and titanium dioxide (TiO_2) in photochemical applications (e.g., optical sensors, solar cells, and photoelectrochemical cells). By contrast, 1T-MoS_2 is metallic and doesn’t display photoluminescence[30]. But it is hydrophilic, 10^7 times more conductive than 2H-MoS_2[30] and able to intercalate various cations[14]. These features make nanostructured 1T-MoS_2 an attractive material for using in a host of applications such as energy storage[14], and solar fuel generators[34], which remain to be explored.

Catalytic activity

MoS_2 (both bulk and delaminated) has been widely used as a catalyst for hydrodesulfurization (HDS) reaction in the petroleum industry to remove sulfur from refined petroleum oil and to reduce sulfur dioxide emissions. MoS_2 has also proven to be a good catalyst for electrochemical and photoelectrochemical hydrogen evolution reaction (HER). Both theoretical and experimental studies revealed that the edges of MoS_2 are catalytically active while the basal plane remains inert[31, 35] As such, delaminated MoS_2 possesses much higher catalytic activity due to its much higher specific surface area and exposure of active sites compared to its bulk counterpart. Moreover, 1T-MoS_2 obtained from lithium intercalation and exfoliation has shown dramatically improved activity over that of 2H-MoS_2, which was most likely attributed to the facile electrode kinetics, excellent conductivity as well as the proliferation of catalytic active sites in the basal plane, not only edges.[36, 37] Nevertheless, 1T-MoS_2 is thermodynamically metastable and it can undertake a phase reconversion to 2H-MoS_2 under moderate-temperature annealing.[36] So the origin of high catalytic activity of 1T-MoS_2 remains ambiguous unless the clear identification of the phase nature of catalysts during the electrochemical measurements is achieved.

By virtue of its extraordinary electronic, optical and catalytic properties, 2D MoS_2 has also been widely explored as a co-catalyst for photocatalytic HER. [38-42] Three of its merits are deemed to account for the boosted photocatalytic activity. Firstly, 2D MoS_2 has sizeable bandgap[10], thereby it can harvest a wide range of light from ultraviolet to infrared, improving the utilization efficiency of solar energy. As such, 2D MoS_2 can be used to sensitize the large bandgap semiconductors to make them useful[42]. Secondly, 2D MoS_2 displayed suitable band positions [43] such as a more negative conduction band (CB) edge than proton reduction potential (H^+/H_2), enabling the reduction of protons to H_2 by using the electrons in the CB of MoS_2. Thirdly, the layered structure of 2D MoS_2 allows for the formation of an intimate heterojunction with other semiconductors, [44, 45] facilitating the charge separation and inhibiting the photo-generated electron-hole recombination. Benefiting from the aforementioned merits, 2D MoS_2 is capable of acting as both light-absorber and catalyst for photocatalytic HER. However, the study on directly applying 2D MoS_2 as photocatalytic HER catalyst is rare due to the low throughput of 2D MoS_2, insufficient light adsorption, fast charge recombination as well as instability in aqueous solution. In an effort to bridge the gap in this area, a novel dye-sensitized MoS_2 photocatalytic system was constructed and evaluated for HER, and the outcomes will be presented in Chapter 4 and 5.

1.5 Synthesis of 2D TMDs

Many methods have been developed to prepare single- and multi-layer 2D TMDs, these methods can be classified into two categories: top-down methods and bottom-up methods. The examples of top-down methods include mechanical cleavage and solution-based exfoliation, which work to overcome the Van de Waals energy stored in the stacked/bulk TMD crystals by using external energy forces such as peeling and ultrasonication; whereas the bottom-up methods including chemical vapor deposition (CVD) and wet chemical synthesis are reliant on chemical reactions of metal and chalcogen sources to synthesis layered TMDs on substrates or in solution. [6-9, 46-48] Each method has its own advantages and disadvantages over specific applications.

1.5.1 Mechanical cleavage

Mechanical cleavage is the most traditional method to isolate 2D materials since it has been successfully used to isolate graphene from bulk graphite. The general process of mechanical cleavage involves peeling the atomically thin flakes from parent bulk crystals using adhesive scotch-tape[46]. (Fig. 1.3) It is regarded as a straightforward method to prepare high-quality 2D TMDs as it is less destructive and can create sheets with perfectly crystalline structures. Thus, TMD nanosheets prepared by mechanical cleavage are quite useful for exploration of high-performance electronic and photonic devices and condensed-matter phenomena. However, this method falls short of high throughput and controllable production of 2D TMDs.

1.5.2 Chemical vapor deposition (CVD)

Chemical vapor deposition (CVD) offers an effective way to prepare high-quality 2D TMDs with controllable size and thickness. Typically, mono- or few-layer TMDs nanosheets can be grown on substrates via the following pathways: a) chalcogen and metal precursors are vaporized followed by co-deposition onto a substrate; b) deposition of metal film onto a wafer heated with chalcogen source (Fig. 1.3); c) sulfurization of metal oxide to metal disulfide.[49, 50] Owing to its merits of high-quality and controllable production of TMD thin films, CVD technique has been widely explored in devices fabrication at lab-level. However, the rigid experiment conditions such as high temperature, high vacuum and specific substrates limit its applications at the industry level.

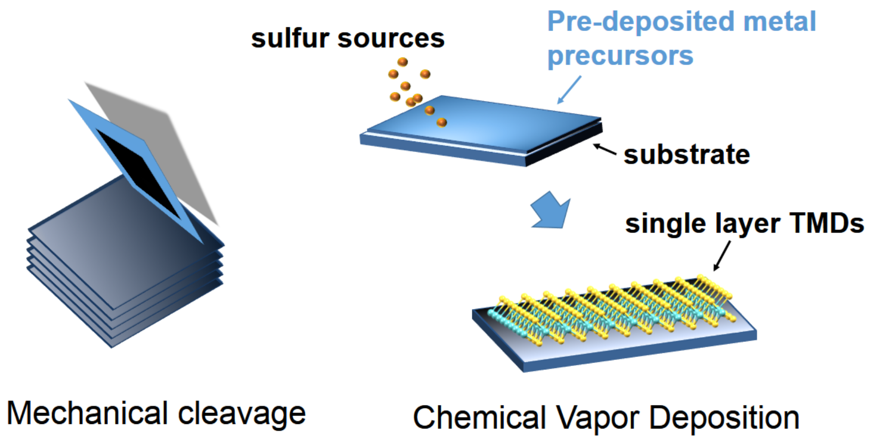

Figure 1.3 Schematic representation of mechanical cleavage and CVD methods for 2D TMDs preparation.

1.5.3 Wet chemical synthesis

The typical wet chemical synthesis based on hydrothermal and hot-injection methods is a traditional way to prepare nanomaterials with desired size and thickness.[51] In the hydrothermal process, the metal source such as ammonium molybdate ($(NH_4)_2MoS_4$) and chalcogen sources (e.g., sulfur powder or thiourea) are reacted in a sealed autoclave at elevated temperature and high pressure. Under this condition, the obtained TMDs tend to aggregate to form nanoflowers and nanotubes. Therefore, it is difficult to get well-dispersed monolayer TMD nanosheets by using the hydrothermal method. The alternate hot-injection method involves using high-boiling-point organic solvents to facilitate the nucleation and crystal growth, which are difficult to remove in the subsequent purification process, thus negatively impacting the purity and quality of the TMD films.

1.5.4 Solution-based exfoliation methods

Solvent-based exfoliation

Solution-based exfoliation involves sonication of bulk or stacked TMDs in various solvents or aqueous surfactant solutions, leading to the formation of a dispersion of few or monolayer TMD nanosheets. Sonication of bulk TMDs in various organic solvents is one of the most straightforward methods to prepare few-layered TMD nanosheets. (Fig. 1.4) The nature of solvent is key to determining the yield of exfoliation. A good solvent with a comparable surface tension to that of TMDs requires minimal energy for exfoliation.[52] Moreover, a good solvent should be capable of stabilizing the isolated nanosheets against re-stacking and aggregation.[53] The solvents screening by Coleman and coworkers has pointed out that the effective solvent should have a surface tension close to 40 mJ/m^2 and that 1-methyl-2-pyrrolidone (NMP) with the surface energy of ~70 mJ/m^2 was found to be the most effective solvent for exfoliation of MoS_2. The lateral size of the obtained MoS_2 flakes ranges from 50 to 1000 nm and the concentration is around 0.3 mg/mL.[54] In 2012, the same group found that the concentration of exfoliated MoS_2 in NMP showed a linear relationship with the initial MoS_2 mass and the maximum value achieved when the initial MoS_2 concentration was 100 mg/mL. The following sedimentation technique can selectively isolate the larger-size MoS_2 flakes with the mean length of approximately 2 μm and the concentration of exfoliated MoS_2 can reach 40 mg/mL upon sonication for 200 hrs.[55] A recent study on the mechanism of NMP facilitated MoS_2 exfoliation demonstrated that NMP had undergone an auto-oxidative decomposition in the presence of O_2 and H_2O, resulting in the formation of hydroperoxide, which oxidized the edges of MoS_2 nanosheets and aided the exfoliation.[56] Given the fact that NMP is toxic, unstable and hard to remove completely, it brings about some problems while purifying the exfoliated products for further applications. Therefore, development of other exfoliation methods using environment-friendly or volatile solvents is necessary.

The Hansen solubility parameter (HSP) theory[57], a semi-empirical description of dissolubility of solute in certain solvent based on the dispersive, polar and hydrogen-bonding interactions, shows that the smaller HSP distance Ra, the better solubility. Zhang and co-workers demonstrated that an ethanol-water co-solvent system was effective for exfoliation of MoS_2,[58] and the optimal volume ratio of ethanol/water is 45%, leading to the highest concentration of exfoliated MoS_2 nanosheets is approximately 0.018 ± 0.003 mg/mL. Later, Duan and co-workers developed a strategy for the rational design of co-solvent exfoliation of layered materials via directly probing the liquid-solid interfacial energy.[59] Their results showed that both co-solvent concentration and the molecular length of co-solvent played critical roles for the exfoliation.

Surfactant-assisted exfoliation

Alternatively, sonication of bulk TMDs in surfactant solution provides an effective way to prepare MoS_2 nanosheets in aqueous dispersion due to the high adsorption energy of surfactants to the surface of TMD nanosheets. (Fig. 1.4) For example, Coleman and co-workers have demonstrated that sonication of MoS_2 in sodium cholate aqueous solution (1.5 mg/mL) can lead to the formation of well exfoliated MoS_2 nanosheets that are stabilized by the surface coated sodium cholate.[6] Following the cascade centrifugation technique, a monolayer rich TMDs dispersion (MoS_2 and WS_2) can be obtained.[60, 61] Similarly, exfoliation of MoS_2 nanosheets by using non-ionic surfactants such as polyoxyethylene sorbitan monooleate (Tween 80), polyvinyl- pyrrolidone (PVP), and Pluronic P-123 was also explored, and the highest efficiency was obtained using P-123.[62] Although this surfactant-assisted exfoliation has enabled the scale-up production of mono-layered TMD nanosheets, the exact nature of the surfactant-TMDs interaction is still unclear. The presence of surfactant coating also presents some problems for producing clean TMD flakes, which is crucial for the electronic and optoelectronic device fabrication industry.

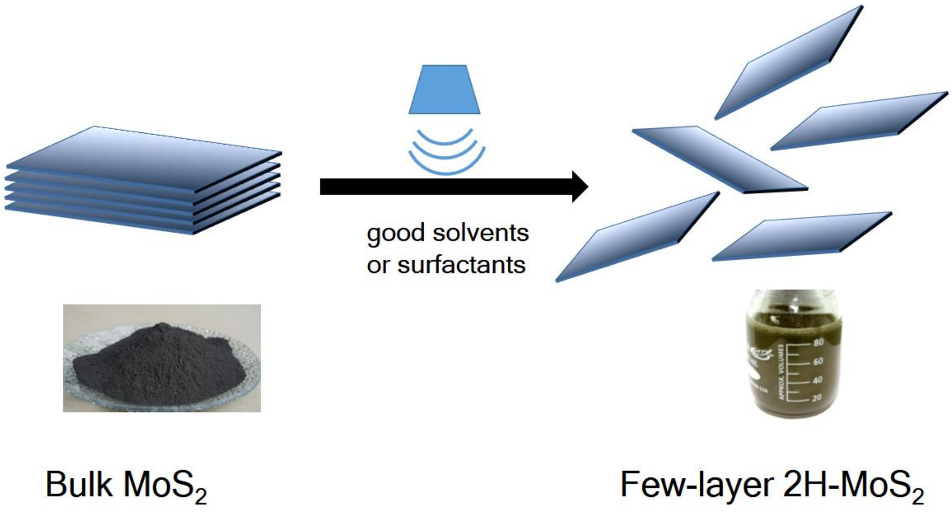

Figure 1.4 Schematic representation of solvent based and surfactant-assisted methods for exfoliation of 2H-MoS_2 nanosheets.

Ion intercalation and exfoliation (chemical exfoliation)

Ion-intercalation and exfoliation, which refers to “chemical exfoliation” in the following context, is another feasible route to prepare aqueous dispersions of few- to monolayer TMD nanosheets. The key step for chemical exfoliation is to synthesize the intercalated compounds, which can be achieved by either chemical or electrochemical means.[2, 13] Usually, alkali metal ions or Lewis base with small radii and suitable reducing ability are employed for intercalation.[63] The chemical intercalation of TMDs by lithium was first reported in 1970[64, 65]and then Morrison, Frindt, and co-workers demonstrated the intercalation-driven exfoliation[66]. The typical chemical exfoliation process (Fig. 1.5) involves a primary reaction of bulk TMD powder with lithium-containing agents such as n-butyllithium (n-BuLi) under an inert atmosphere to allow lithium ions to insert between TMD interlayers, which is accompanied by the expansion of the interlayer spacing, followed by sonication of the intercalated materials in water. The furious reaction between intercalated lithium and water generates substantial H_2 gas, which pushes the adjacent nanosheets further apart. With the agitation by sonication, a complete separation of TMD nanosheets can be achieved, leading to the formation of a well-dispersed TMD nanosheets in water.

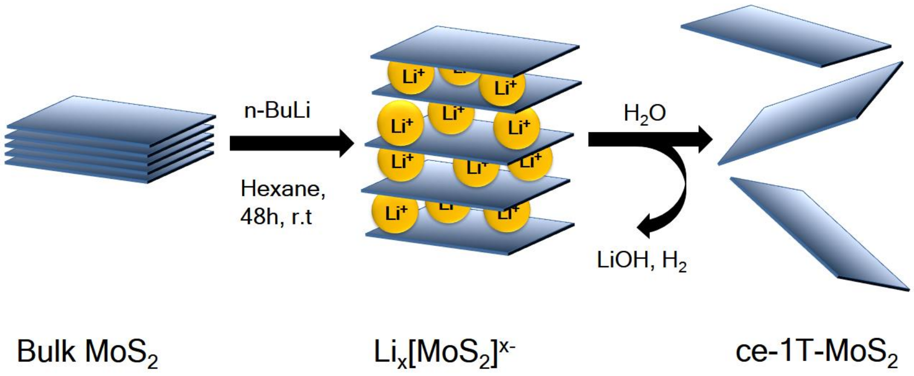

Figure 1.5 Schematic representation of preparation of ce-1T-MoS_2 nanosheets by lithium intercalation and exfoliation in H_2O.

One intriguing feature of chemical exfoliation is the local phase rearrangement which takes place during the course of lithium intercalation, therefore changing the surface property and electronic properties accordingly. In the case of chemical exfoliation of MoS_2, bulk 2H-MoS_2 is reductively intercalated with lithium ions to form an intercalated compound ($Li_x[MoS_2]^{x-}$), accompanied by the phase transformation from semiconducting 2H-polymorph to metallic 1T-polymorph, and this structural transformation is maintained in the final exfoliated product. Therefore, chemical exfoliation process yields the MoS_2 that contains predominantly the metallic 1T-polymorph, and thus we defined the product as ce-1T-MoS_2 in the following context. By using this chemical exfoliation technique, one can exfoliate bulk MoS_2 into monolayer nanosheets with a 1T-polymorph concentration of ~70% and obtain 100% monolayer MoS_2 nanosheets dispersed in water.[30]

Additionally, chemically exfoliated MoS_2 (ce-1T-MoS_2) retains some negative charges that are transferred from lithium during the intercalation process (Fig. 1.6). These charge residues in ce-1T-MoS_2 nanosheets are likely balanced by the water bilayer containing protons. And the presence of water bilayer also stabilizes the suspended nanosheets against re-stacking.[14, 67] However, the resultant ce-1T-MoS_2 suspension is unstable and tends to re-aggregate with time. This is possibly attributed to re-oxidation of the nanosheets in the presence of air. Such degradation processes can be effectively suppressed and prevented by storing ce-1T-MoS_2 dispersion in an inert atmosphere.[68]

$$MoS_2 \xrightarrow{Li^+,\ e^-} Li_x[MoS_2]^{x-} \xrightarrow{H_2O} [\ Li^+ \ + \ (MoS_2)^{x-} \ + \ (1-x)\ OH^-\ ]_{aq} \ + \ H_2$$

Figure 1.6 Mechanism of chemical exfoliation of MoS_2。

Given that the aforementioned chemical exfoliation involves the usage of highly pyrophoric organolithium reagents, and requires harsh reaction conditions over long reaction times, an alternative electrochemical lithiation-intercalation technique was developed by Zhang's group and Cui's group.[7, 69] The lithium intercalation was performed in a Li-ion battery set up with lithium foil as the anode and TMD materials as the cathode, lithiation takes place when galvanic discharge starts. The degree of lithiation and ratio of two structural phases can be monitored and tuned by controlling the discharge process. Then through the subsequent sonication in water, high-quality monolayer 1T-TMD nanosheets can be gained in 92% yield after purification. By employing the above lithium intercalation and exfoliation method, the semiconducting 2H-MoS_2 monolayer can be easily retrieved by annealing the monolayer 1T-MoS_2 on substrates above 300 °C for use in electronic devices. However, this process requires drying of monolayer 1T-MoS_2 at high temperature, which limits the further processibility. To overcome this limitation, Dravid and co-workers demonstrated a strategy to recover the semiconducting 2H-MoS_2 from 1T-MoS_2 directly in solution. This was achieved by functionalization of ce-1T-MoS_2 with (*Z*)-octadec-9-enylamine to change the hydrophilic nanosheets to hydrophobic followed by thermal-annealing of functionalized MoS_2 in high boiling point organic solvents such as octadec-1-ene (b.p. 315 °C) and *o*-dichlorobenzene (b.p. 180 °C). Yet, the downside of this strategy is the impurities and organic solvents residues may limit the practical use in devices fabrication.

Noting that electrochemical intercalation falls short of scalability in making monolayer TMDs, recently Loh and co-workers demonstrated a two-step expansion and intercalation strategy to produce high purity and large-sized TMD nanoflakes in high yield. This strategy involves pre-expansion of TMDs by reacting bulk crystal with hydrazine (N_2H_4) followed by intercalation of expanded TMDs with metal naphthalenide (metal: Li, Na and K). The 90% monolayer MoS_2 nanosheets with size up to 400 μm^2 can be achieved by using this technique.[70] This high efficiency approach opened a way to reach scale-up production of large-sized MoS_2 nanosheets, although the preparation process involving the usage of a self-igniting chemical is dangerous.

Despite the significant progress on the preparation of high quality and large scale 2D TMDs by using solution based exfoliation has been made in the past 10 years, there are still some challenges that need to be addressed. The production of high-yield, high-purity and large-sized TMDs (such as monolayer semiconducting 2H-MoS_2) in a facile way remains a bottle neck for practically applying exfoliated TMDs in device manufacturing industry. For the solvent and surfactant assisted exfoliation, the presence of solvents and surfactants residues as well as the byproducts formed during ultrasonication results in some problems for achieving pure TMD nanosheets. On the other hand, the randomly distributed defects in exfoliated TMDs are unfavorable for practical use in electronic and optoelectronic devices, thus employing other milder external forces to replace the high intensity ultrasonic tip and exploring new synthetic strategies to avoid defects formation are desperately required for high quality TMD nanosheets production. What’s more, the chemistry underlying the exfoliation techniques such as the TMDs/surfactants interactions and the sonochemistry involved in exfoliation process is still elusive, which makes the controllable preparation of defect-free TMDs with uniform size and thickness for practical applications even more challenging.

Compared to mechanical cleavage, CVD growth, and wet chemistry techniques, preparation of 2D TMDs using solution based exfoliation methods is more rewarding in terms of the low-cost and abundant bulk materials sources, scalability, simple size/thickness sorting process as well as easy derivatization and fabrication via wet chemistry. This Ph.D. work aims to address the issues associated with processing and fabrication of 2D TMDs through chemically modifying the TMD nanosheets. The solvent-assisted exfoliation method was employed to produce 2D 2H-MoS_2 and 2H-WS_2 nanosheets; while the chemical exfoliation was employed to produce 2D 1T-MoS_2 nanosheets.

1.6 Chemical functionalization of TMDs

To this date, 2D TMDs have proven inert to chemical functionalization due to the inert dangling-bond free surface. The most recent efforts towards functionalization of TMDs are particularly focused on MoS_2, the prototypical TMDs and both isolable polymorphs of MoS_2 (1T- and 2H-) have attracted equal attention.

1.6.1. Functionalization of 1T-MoS_2

Covalent functionalization of ce-1T-MoS_2 with organoiodides

As we described previously in section **1.5.4**, chemical exfoliation yields MoS_2 that contains predominantly the 1T-polymorph (2H-MoS_2 also present), and thus we define the product as ce-1T-MoS_2. Methods employing ce-1T-MoS_2 have provided the only routes to covalently functionalized TMDs (Fig. 1.7). The first example, by Chhowalla and co-workers[14], described the covalent functionalization of ce-1T-MoS_2, -WS_2, and -$MoSe_2$ nanosheets by reacting them with organoiodides (2-iodo-acetamide and iodomethane) or diazonium salts (also reported by Backes et al.)[71]. After preparing the ce-1T-TMDs in water, organoiodides were simply mixed into the aqueous dispersions and allowed to stir for 12 h. X-ray photoelectron spectroscopy (XPS) analysis of the resulting functionalized materials gave no indication of remnant iodine atoms, suggesting functionalization through nucleophilic attack by ce-1T-MoS_2, causing displacement of iodide, had occurred. XPS analysis also confirmed the presence of N- and C-atoms on the ce-1T-MoS_2

surface. Importantly, the S 2p region showed the presence of new S-atoms on the ce-1T-MoS_2 surface, indicating the formation of a new C–S bond. Solid-state attenuated total reflectance Fourier transform infrared (ATR-FTIR) and crosspolarization magic-angle spinning (CP-MAS) NMR studies provided further support of the presence of organic functionalities on the ce-1T-MoS_2 surface. By ATR-FTIR, a C–S vibration was observed at ν (C–S) = 700 cm $^{-1}$, demonstrating the formation of a C–S bond. Critically, the ^{13}C CP-MAS NMR showed dramatic shifts in the resonances attributed to the organic functionalities compared with their precursors, providing strong evidence of a covalent tethering to the ce-1T-MoS_2. The loading of organic functionalities was estimated to be ca. 30% through both thermogravimetric analysis (TGA) and XPS analyses. This result is important, as the high degree of loading suggests functionalization occurred on the basal plane, and not just on the more reactive edge-sites. The study was extended to WS_2 and $MoSe_2$, yielding the same functionalization outcomes.

Monolayers of ce-1T-MoS_2 are normally not photoluminescent, unlike monolayers of 2H- MoS_2 (ca. 1.9 eV); however, the covalently functionalized ce-1T-MoS_2 was photoluminescent with two characteristic bands at ca. 1.9 eV and ca. 1.6 eV. Another intriguing aspect of this work was that the functionalized ce-1T-MoS_2 could be converted to the semi-conducting polymorph, 2H-MoS_2 through annealing at 300 °C. A 100% yield of 2H-MoS_2 was obtained, according to XPS, and the organic functionalities appeared to be intact, although the extremes of temperature are not suitable for most organic functional groups. This discovery is very important because 2H-MoS_2 does not react with organic iodides or diazonium salts, thus functionalization routes to the more attractive semi-conducting 2H- MoS_2 are limited.

Covalent functionalization of ce-1T-MoS$_2$ with diazonium salts

Diazonium salts have been widely used to functionalize carbon-based nanomaterials including graphene and carbon nanotubes.[72] Backes and co-workers recently discovered that aryl-diazonium salts can be used for basal-plane functionalization of ce-1T-MoS$_2$.[15] ce-1T-MoS$_2$ was reacted with 4-methoxyphenyldiazonium tetrafluoroborate leading to an immediate flocculation of the nanosheets, indicating a change in the surface properties of the ce-1T-MoS$_2$. TGA of the functionalized ce-1T-MoS$_2$ showed a 7% weight loss in the temperature range 220-450 °C, suggesting the presence of organic guest molecules. TGA-coupled mass spectrometry (TGA-MS) verified that the weight loss during TGA heating originated from the organic functional groups (decay products of 4-methoxybenzene were detected). The degree of functionalization was considerably less than the 20% reported in the organoiodide Chemistry.[73] Backes et al prepared their ce-1T-MoS$_2$ in a slightly different fashion to Chhowalla, presumably leading to the lower degree of functionalization. Importantly, a S–C vibrational mode was observed at ν(S-C) = 695 cm^{-1} using FT-IR spectroscopy, indicating the formation of a C–S bond. Raman analysis showed that the intensity ratio of the A_{1g} mode (404 cm^{-1}) to the 2LA(M) mode (450 cm^{-1}) was significantly higher in the functionalized sample compared to non-functionalized ce-1T-MoS$_2$ and pristine 2H-MoS$_2$. Backes proposed that this intensity ratio could be used as an indicator for the functionalization of MoS$_2$. Finally, XPS analysis of the functionalized ce-1T-MoS$_2$ provided some interesting insights. Firstly, the S 2p XPS spectra suggested the appearance of unique, non-MoS$_2$ sulfur species on the surface, demonstrating that a C–S bond had likely been formed. Secondly, the functionalized ce-1T-MoS$_2$ displayed enhanced stability (*i.e.* the 1T-polymorph did not isomerize to the 2H-polymorph) over long periods of times. This is unusual for ce-1T-MoS$_2$, because it normally isomerizes over a period of 1 week. Finally, the methoxybenzene-functionalized ce-1T-MoS$_2$ was re-dispersible in anisole, unsurprisingly, given the molecular similarities between methoxybenzene and anisole. To estimate the electrical characteristics of functionalized 1T-MoS_2, ce-1T-MoS_2 and functionalized ce-1T-MoS_2 have been fabricated into field-effect transistors (FETs). The device fabricated by functionalized ce-1T-MoS_2 showed a clear improvement in on/off ratios (up to ca. 36) compared to that fabricated by solely ce-1T-MoS_2 (6.7), suggesting an improved semiconducting property after functionalization, which was possibly caused by the doping effect of functionalities. Additionally, the hole mobility decreased by 2.7×10^{-4} $cm^2/(Vs)$ after functionalization. The author speculated that the extra scattering centers from guest functional groups may account for this.

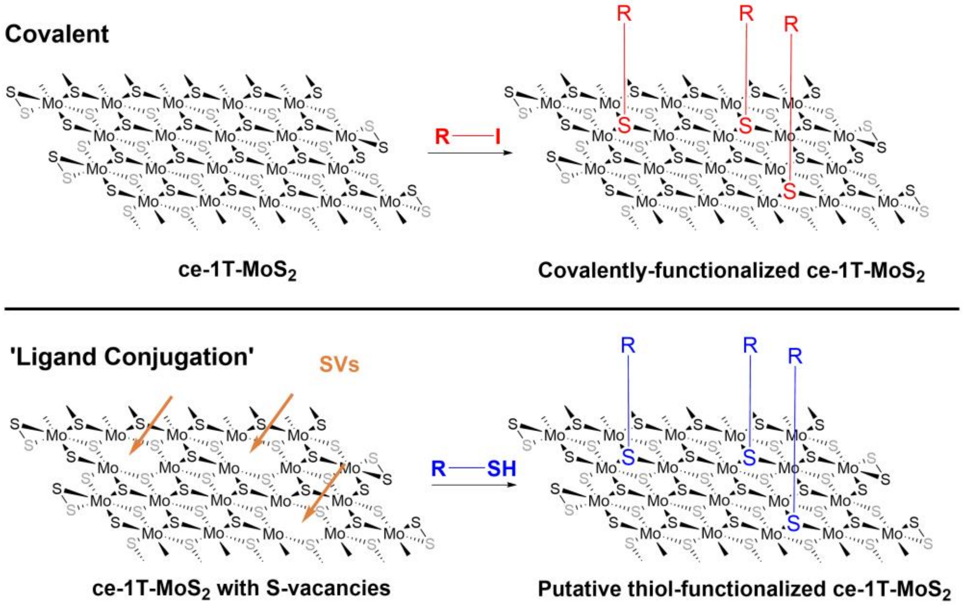

Figure 1.7 Graphical representations of various modes of ce-1T-MoS_2 functionalization with small molecules.[74]

‘Ligand Conjugation’ Functionalization of ce-1T-MoS_2

Dravid and co-workers reported the first example of an efficient functionalization of 2D TMDs (Fig. 1.7).[17] They reacted ce-1T-MoS_2 with bi-functional polyethylene glycol (PEG) molecules (one end of the polyether contained a thiol and the other end a hydroxyl, carboxylate, or ammonium functionality). Upon reaction between the ce-1T-MoS_2 and the organic thiol a marked change in the zeta-potential of the TMD nanosheets was observed, indicating a change in the ce-1T-MoS_2 surface properties. XPS analysis showed the presence of surface carbon and oxygen atoms, demonstrating the polyether functional groups were indeed bound to the surface of the ce-1T-MoS_2. Furthermore, FT-IR suggested that the thiol groups had reacted with the ce-1T-MoS_2, because the ν(S-H) at 2563 cm^{-1} disappeared upon functionalization. The disappearance of the thiol functionality would indicate it had reacted with the ce-1T-MoS_2. This observation was rather ambiguously described as the thiol being 'buried' within the ce-1T-MoS_2 surface.

The authors defined this functionalization technique as organic thiol 'ligand conjugation', although the exact nature of the thiol/MoS_2 interaction is unclear. It is possible that thiol ligands are coordinating to Mo-atoms in the ce-1T-MoS_2 at S-vacancies, yielding a 'ligand coordination' functionalization (Fig. 1.7). This is how the functionalization was defined pictographically, although little experimental support for this postulate exists (*i.e.* XPS or FT-IR support for new/altered C–S or Mo–S bonds on the surface). As addressed later, recent insights into the reaction between organic thiols and MoS_2 nanosheets appear to suggest the thiol functionality does not fill S-vacancies, but rather gets converted to a disulfide that is physisorbed on the MoS_2 surface.[75] Nonetheless, the 'ligand conjugated' ce-1T-MoS_2 functionalization method yielded ce-1T-MoS_2 nanosheets with interesting properties - the functionalized materials displayed extended colloidal stability compared to pristine ce-1T-MoS_2 (much like is observed when surfactants are used to exfoliate TMDs). Furthermore, the PEGylated ce-1T-MoS_2 was an efficient host/support for certain biomolecules, enabling selective complexation and inhibition of β-galactosidase (β-gal), a hydrolase enzyme. About 50% of β-gal activity was inhibited by 0.04 μg mL^{-1} of the PEGylated ce-1T-MoS_2.

Zhou and co-workers subsequently used a similar procedure to functionalize ce-1T-MoS_2 with smaller, simpler organic thiols (Fig. 1.8).[76] They coupled 1-mercaptopropionic acid, 1-thioglycerol, and L-cysteine to ce-1T-MoS_2 by reacting $Li_x[MoS_2]^{x-}$(formed from the reaction between n-butyl lithium and 2H-MoS_2) with the organic thiols dissolved in water. This method essentially mirrors Dravid's method,[17] where the $Li_x[MoS_2]^{x-}$ was oxidized and exfoliated prior to reaction with the organic thiol. Presumably, concomitant exfoliation and functionalization occurred using Zhou's method of reacting the $Li_x[MoS_2]^{x-}$ with aqueous thiols. TGA analysis showed 6-9% loading of the organic functionalities, which were desorbed from the material in a rather large temperature range of 150 - 700 °C. XPS analyses showed the presence of organic C-, O- and N- atoms on the MoS_2 surface indicating the organic functional groups were interacting with the surface. Raman analysis of the functionalized 1T-MoS_2 was used to confirm surface modification - broadening of the A_{1g} and E^1_{2g} resonances was determined to derive from the presence of surface organic molecules. Unfortunately, the FT-IR analysis of the functionalized materials provided limited insight into the functional groups and their interaction with the ce-1T-MoS_2. For example, no ν (C-S) was identified. One would expect this vibrational mode to shift dramatically if the organic thiol was coordinating to Mo-atoms at S-vacancies, and would thus provide definitive proof of ligand coordination to the nanomaterial surface. The exact nature of the ce-1T-MoS_2/organic thiol thus remains unclear.

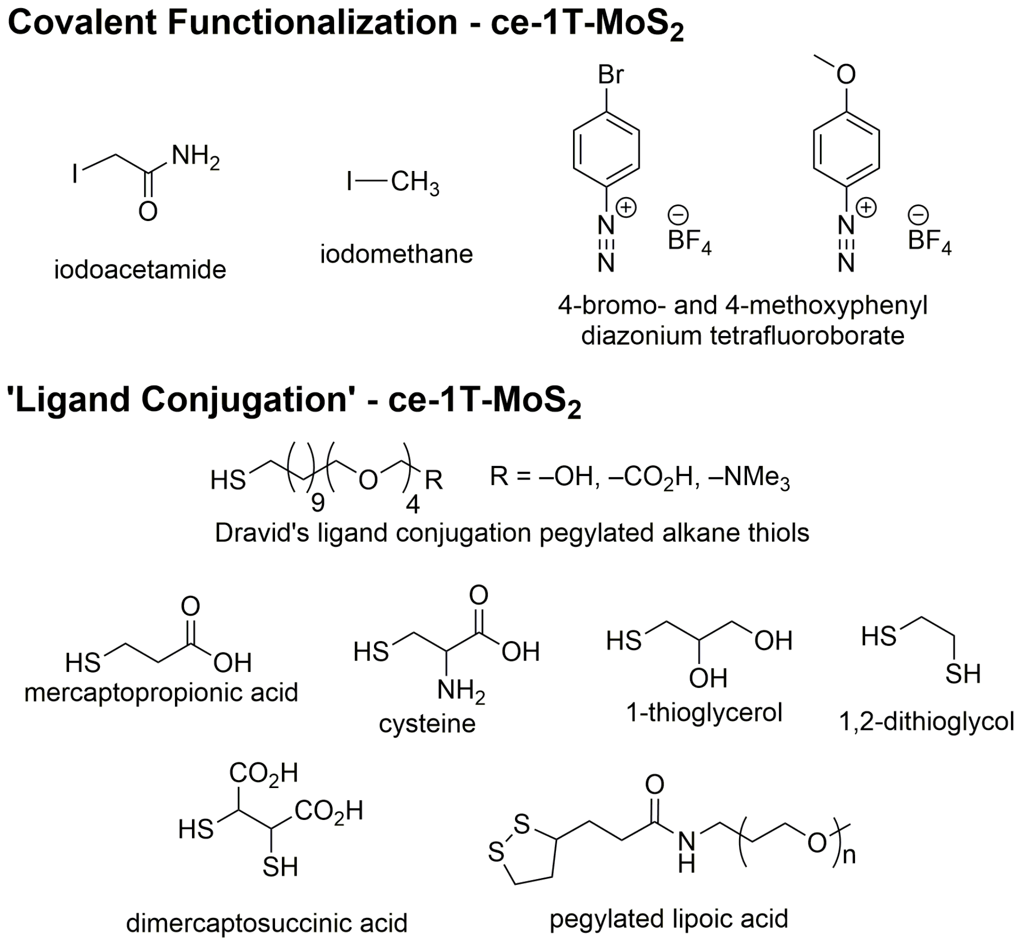

Figure 1.8 Functional compounds used for functionalization of ce-1T-MoS$_2$.

Zhou's functionalized materials displayed exciting possibilities for the coupling of both inorganic and organic polymeric entities to ce-1T-MoS$_2$ nanosheets. The carboxylate-functionalized material supported the formation of discrete and well-defined silver nanoparticles on the ce-1T-MoS$_2$ surface, whereas the un-functionalized material yielded highly aggregated surface silver nanoparticles. The carboxylate-functionalized materials were also reacted with a polymethylmethacrylate precursor (hydroxylethyl methacrylate), which yielded a ce-1T-MoS$_2$ functionalized with ethyl methacrylate esters. Polymerization of these precursors yielded polymethylmethacrylate (PMMA)-functionalized ce-1T-MoS$_2$. Along similar lines, the 1-thioglycerol-functionalized ce-1T-MoS$_2$ was reacted with caprolactone, yielding poly(caprolactone)-functionalized ce-1T-MoS_2. These examples represent some of the first examples of derivatization of functional groups on functionalized exfoliated ce-1T-MoS_2 and thus represent an important discovery. Thereafter, some modified organic thiols such as dithiogylcol.[77], meso-2,3-dimercaptosuccinic acid[78] and PEGylated lipoic acid[79] (Fig. 1.8) were widely utilized to functionalize ce-1T-MoS_2, affording the modified MoS_2 structures with interesting physical and chemical properties.

1.6.2. Functionalization of 2H-MoS_2

Functionalization of 2H-MoS_2 with thiophene

Besenbacher and co-workers produced a fascinating set of results on chemical vapor deposition (CVD) synthesized 2H-MoS_2 mono-layered nanoparticles.[80] They demonstrated the preparation of an array of MoS_2 clusters of varying size (from 3 Mo- and 7 S-atoms up to 36 Mo- and 102 S-atoms). These particles display varying degrees of S-atom vacancies as evidenced by scanning tunneling microscopy (STM) analysis. Amazingly, STM analysis showed that dibenzothiophene interacted with the MoS_2 nanoparticles, with the S-atom of the dibenzothiophene filling an S-atom vacancy (Fig. 1.9). This would suggest that the S-atom of dibenzothiophene coordinated (formed a dative bond) to the Mo-atom at an S-atom vacancy. The coordination site was quite open, at a corner site on a triangular particle, presumably providing sufficient space for the thioether ligand to access the Mo-atom in order to coordinate. Interestingly, no examples of the thioether ligand interacting with basal plane or edge sites were reported, suggesting the availability of corner sites is essential for S-atom containing molecules to interact with MoS_2 at S-atom vacancies.

Li and co-workers later took advantage of this functionalization technique by reacting thionine (3,7-diamino-5-phenothiazinium acetate), a molecular analogue of dibenzothiophene, with liquid exfoliated 2H-MoS_2 in the presence of an ionic liquid.[81] XPS analysis added critical weight to the observations of Besenbacher, because it provided conclusive proof that a new S 2p feature was present in the thionine-functionalized materials. Importantly, this new feature was distinctly different to S 2p features observed for pristine 2H-MoS_2 *and* thionine. This strongly indicates the formation of a S–Mo or S–S bond between thionine and MoS_2. Besenbacher's observations would suggest that this was a dative bond. The thionine-functionalized 2H-MoS_2 was used to detect DNA, displaying a decreased electrochemical response in the presence of DNA at very low concentrations, allowing for the efficient detection of DNA in highly dilute samples.

Functionalization of 2H-MoS_2 based on coordination chemistry

Our group reported one of the first examples of functionalization of 2H-MoS_2.[16] Coordination (formation of a dative bond) by basal plane S-atoms to metal salts yielded functionalized 2H-MoS_2 (Fig. 1.9). Liquid exfoliated 2H-MoS_2 dispersed in iso-propanol was reacted with metal-acetate salts ($M(OAc)_2$; M = Ni, Cu, Zn). X-ray photoelectron spectroscopy (XPS) analysis suggested that coordination of surface S-atoms to the $M(OAc)_2$ had occurred, as evidenced by the appearance of new S 2p features in the XPS core level spectra of the functionalized materials. Diffuse reflectance infrared Fourier transform (DRIFT) spectroscopy showed the presence of surface carboxylate vibrational modes that were shifted with respect to the $M(OAc)_2$ precursors, indicating coordination of surface S-atoms to the metal center. TGA showed the presence of organic functionalities that combusted at approximately 200 °C, while post-TGA DRIFT analysis showed the loss of the carboxylate stretching modes. Most interestingly, functionalization of the 2H-MoS_2

allowed for its dispersion/processing in more conventional lab solvents including acetone, rather than the highly toxic solvent N-methyl-2-pyrrolidone (NMP), which is normally used to disperse 2H-MoS_2. This coordination method is extremely facile and highly efficient, however it does not yield covalently or tightly-bound functionalized 2H-MoS_2, with the functionalities rather easily removed through multiple washings with NMP.

An analogous coordination chemistry-directed functionalization study was reported recently by Pulickel's group, wherein atomic layers of n-type InSe reacted with a typical Lewis acid $TiCl_4$ to form a planar p-type $[Ti^{4+}{}_n\ (InSe)].Cl^{-}{}_{4n}$ coordination complex[82]. Characterization of the functionalized product by XPS and Raman indicated the formation of Ti-Se bonds at interfaces. DFT calculation confirmed that the nature of Ti-Se bond was a coordinate covalent bond. Using this strategy, they fabricated planar p–n junctions (InSe-Ti/InSe) on 2D InSe with improved rectification and photovoltaic properties, without requiring heterostructure growth procedure and device fabrication processes. Most importantly, this strategy can be extended to other 2D materials such as MoS_2 and $MoSe_2$ by using various Lewis acids such as B^{3+}, Al^{3+} and Sn^{4+}.

Functionalization of 2H-MoS_2 with polymer

Leite and co-workers took an alternative approach to functionalizing 2H-MoS_2 in what they describe as a covalent manner.[83] Liquid exfoliated 2H-MoS_2 (NMP as exfoliating solvent) was mixed with polybutadiene in toluene/NMP over a period of six days. The resulting functionalized 2H-MoS_2 displayed greatly enhanced dispersibility in pure toluene, providing a strong indication of a change in the surface properties of the 2H-MoS_2. Transmission electron microscopy (TEM) provided evidence that the organic polymer was bound to the 2H-MoS_2 surface with an organic layer thickness of ~30 nm. The authors suggested that the TEM indicated the presence of a C–S bond at the interface between the polymer and 2H-MoS_2, however, the resolution is such that this postulate cannot be confirmed. XPS analysis of the polybutadiene functionalized 2H-MoS_2 showed the Mo- and S-atoms remained in the same chemical state as before functionalization, indicating that the PB/MoS_2 interaction was not covalent. FT-IR analysis showed the presence of a putative C–S vibrational mode (at a very low 630 cm^{-1}), providing support for their postulate that the functionalization was covalent. Interestingly, the functionalization appears to have occurred only at the disulfide-rich edge sites on the 2H-MoS_2 (according to TEM). This would suggest that the disulfide edge groups have attacked the polybutadiene alkene. Further investigations into the nature of the polybutadiene/2H-MoS_2 interaction are warranted, as this would represent the only example of covalent functionalization of 2H-MoS_2. Although the functionalization occurs at edge sites, and not the basal plane, it represents an important breakthrough.

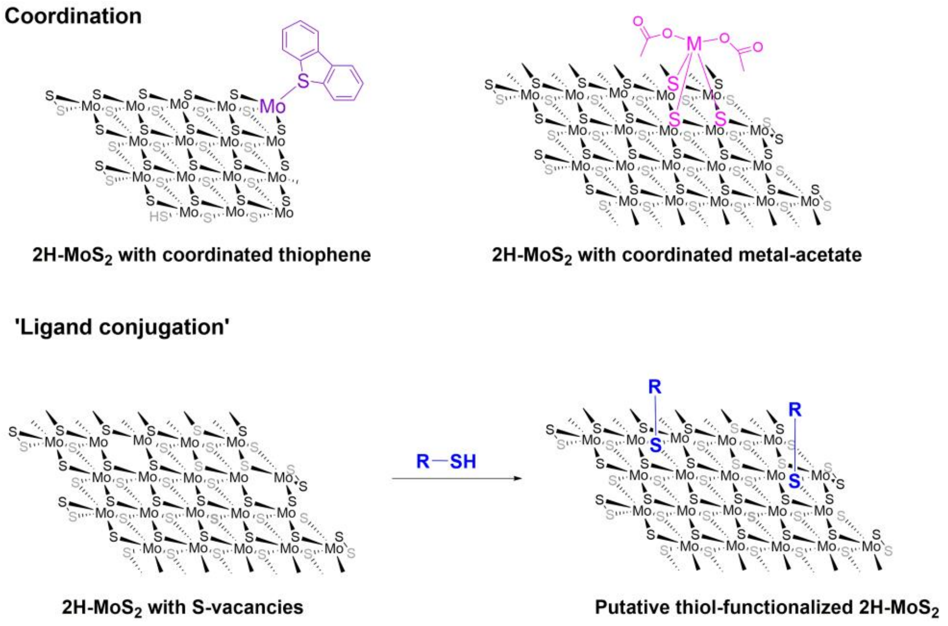

Figure 1.9 Graphical representations of various modes of 2H-MoS_2 functionalization.

Functionalization of 2H-MoS$_2$ with organic thiols

In an interesting, alternative, application of the thiol 'ligand conjugation' studies, two groups have used organic thiols as S-atom donors. S-atoms from these thiols were used to fill S-atom vacancies in 2H-MoS$_2$ monolayers, with the elimination of the remaining organic fragment. Makarova and Okawa reported that dodecanethiol or (3-mercaptopropyl)-trimethoxysilane molecules (Fig. 1.10) could coat a 2H-MoS$_2$ surface as evidenced by STM analysis.[84] Furthermore, they found that the STM tip could induce S-atom vacancy repairs in the presence of the dodecanethiol. In a similar (later) report Yu and Pan showed that by coating 2H-MoS$_2$ with (3-mercaptopropyl)-trimethoxysilane and then annealing (350 °C) the resulting material in the presence of H$_2$, S-atom vacancies in the 2H-MoS$_2$ monolayers were repaired .[85] The exact nature of the S-atom donation is not clear - it would require an unusual C–S bond scission step and the formation of organic by-products. Yu and Pan propose that initial coordination of the thiol ligand at S-atom vacancies precedes C–S bond scission. Unfortunately, the STM and high-resolution TEM images displayed in these reports cannot confirm this postulate. The extremes of condition (the STM tip or annealing at 350 °C in the presence of H$_2$) could facilitate the C–S bond breakage, however how the S-atom occupies S-atom vacancies prior to this is difficult to predict. Overall, however, these reports demonstrate a simple approach to developing pristine monolayers of 2H-MoS$_2$ from defect-rich materials.

Daenecke recently reported the functionalization of 2H-MoS$_2$ through reaction with organic thiols (4-mercaptophenol, thiophenol, 1-propanethiol, 1-nonanethiol, and 1-dodecanethiol, Fig. 1.10) in a fashion similar to Dravid's 'ligand conjugation' method.[86] As in the 'ligand conjugation' Chemistry, Daenecke noted the disappearance of thiol S-H (ν(S-H) ~ 2500 cm^{-1}) vibrational modes in the

ATR-FT-IR spectra of the functionalized materials. Interestingly, a comparison of the ATR-FT-IR spectra of the free thiols and the functionalized materials indicates minor chemical changes to the properties of the thiol groups tethered to the 2H-MoS_2. The photoluminescence spectra of the functionalized 2H-MoS_2 displayed slightly red-shifted emissions compared to pristine 2H-MoS_2, putatively as a result of the functionalities on the surface tuning the emission. Unfortunately, very little insight into the nature of the organic thiol/2H-MoS_2 interaction was provided (*i.e.* XPS, Raman, CP-MAS NMR), and thus there is insufficient support for the postulate that this is a covalent tethering.

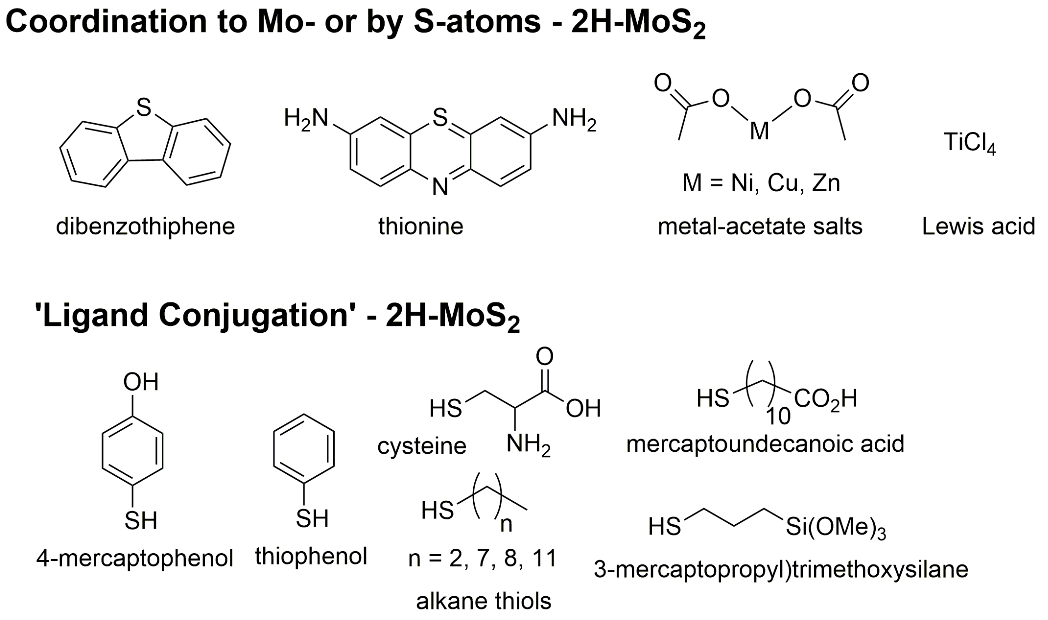

Figure 1.10 Functional compounds used for functionalization of 2H-MoS_2.

Jung and co-workers reported a similar approach to functionalizing 2H-MoS_2 with mercaptoundecanoic acid (Fig. 1.10).[87] As in previous reports on the reaction between thiols and MoS_2, no thiol S-H (ν(S-H) ~ 2540 cm^{-1}) vibrational modes were observed in the functionalized material, indicating the organic thiol had reacted. FT-IR analysis did show the presence of surface aliphatic and carbonyl groups. XPS analysis also confirmed the presence of organic groups on the 2H-MoS_2 surface, however, did not provide insight into the nature of the thiol/2H-MoS_2 interaction (*i.e.* no comparison of the thiol XPS versus the thiol functionalized 2H-MoS_2 was provided). Lee and coworkers later used the same protocols to prepare alkane-thiol functionalized 2H-MoS_2.[88] The resulting materials were probed electrochemically. Lee postulated that vacancies in the 2H-MoS_2 were 'passivated' by the organic thiols, although limited support for this postulate was provided. The functionalized nanomaterials did indeed display different physical properties compared to pristine 2H-MoS_2, however, the exact nature of the organic thiol/2H-MoS_2 interaction had not been probed sufficiently.

Above all, significant progress has been made in the field of 2D TMD functionalization in the past 2-3 years. The functionalization modes related to the surface chemistry of 2D TMDs can be classified into three categories: covalent interaction with electrophiles (e.g., diazonium salts and organohalides), coordinating interactions with metal cations (e.g., metal acetate salts) and Lewis acids (e.g., Ti^{4+}, B^{3+}), and interactions with organic thiols. Of these, the covalent functionalization chemistry demonstrated by Chhowalla and Backes represents the only well-characterized examples of covalent tethering of organic functionalities to TMDs. However, how the covalent bonds affect the structure and properties of 2D TMDs requires further exploration. Moreover, ce-1T-MoS_2 obtained from chemical exfoliation possesses a negatively charged and multiphasic structure, which greatly complicates the understanding of the underlying mechanism of ce-1T-MoS_2 and electrophiles. Further efforts towards improving the understanding of the structure and surface properties of 1T-MoS_2 and isolation and identification of the reaction by-products can possibly provide more in-depth insight on this point. The second part of this thesis (Chapter 4 and 5) demonstrates an example to use this covalent functionalization chemistry as a bridge to connect dye molecules to 2D MoS_2 and fabricate proof-to-concept dye-sensitized photo-sensing devices. The influence of covalently bound surface addends on the structural and catalytic activity of 2D MoS_2 was investigated in detail, providing some evidence for covalent bonding induced surface property, conductivity, and catalytic activity change.

As described in sections **1.6.1** and **1.6.2** there are now many examples of organic thiols reacting with MoS_2 yielding functionalized MoS_2. This functionalization technique has been described as a bond-forming or covalent functionalization method, *i.e.* a Mo–S bond between an S-atom in the organic functional group and a Mo-atom in the MoS_2 has been formed. This conclusion is drawn from infrared spectroscopy that shows the loss of S–H vibrational modes after the MoS_2 has reacted with the thiols. Unfortunately, these studies have not provided sufficient further experimental support for this 'bonding' description to be attributed. Future efforts in the 'ligand conjugation' area thus need to provide more insight into the interaction between organic thiols and MoS_2. The research gap in this topic will be addressed in the first part of this research (Chapter 2 and 3).

1.7 Applications of 2D TMDs in Hydrogen Evolution Reaction

The energy consumption boom and related environmental issues make the development of renewable and environment friendly energy sources and technology more urgent than ever. H_2 is regarded as one of the most important sustainable and clean energy sources due to its high energy density and pollution-free combustion process.[89-91] Splitting water into hydrogen via electrolysis or photolysis is emerging as one of the most promising solutions to achieve the renewable and green fuel production.[89, 92, 93] The overall water splitting reaction can be expressed as $2H_2O \rightarrow 2H_2 + O_2$. This reaction is an uphill process, thus the input energy of $\Delta G = 237.1$ kJ/mol is required, which corresponds to a thermodynamic voltage requirement of

1.23 V.[89, 94] The water splitting reaction can be divided into two half-reactions: hydrogen evolution reaction (HER) and oxygen evolution reaction (OER). These processes are expressed as follows in acidic electrolyte: $2H^+ + 2e^- \rightarrow H_2$ (HER); $2H_2O \rightarrow O_2 + 4H^+ + 4e^-$ (OER). To improve the efficiency of water splitting, catalysts are required for both HER and OER. Herein, we focus on HER catalysis.

1.7.1 TMDs in electrocatalytic HER

General principle for electrocatalytic HER in heterogeneous system

In an electrochemical water splitting cell, the HER takes place at the cathode and the OER takes place at the anode. An external circuit is required to provide energy to drive the water-splitting process and the catalysts are needed to reduce the overpotential (the difference between applied potential and thermodynamic potential) and improve the efficiency of the particular electrochemical process.[12, 95] The HER is the reductive half-reaction of water splitting, which involves two successive reaction steps. Firstly, one proton reacts with one electron to give one hydrogen atom which adsorbed on the electrode surface as H_{ad} (Volmer step). Then either the combination of two H_{ad} atoms (Tafel step) or the combination of one H_{ad} atom with one proton and one electron (Heyrovsky step) takes place to give H_2. The HER may proceed via the Volmer-Tafel mechanism or the Volmer-Heyrovsky mechanism, both of which involves the adsorption of H atoms on the electrode surface. Therefore, the rate of overall reaction is highly related to the free energy of hydrogen atom adsorption (ΔG_H). The ideal electrocatalyst for HER should have the surface-hydrogen bond neither too weak nor too strong, as indicated by the value of ΔG_H close to zero.[96]

In electrochemical kinetics, the reaction rate of HER directly associated with current density depends on the overpotential. And the relationship between the overpotential and current density is described by the Bulter-Volmer equation, which can be simplified as the Tafel equation when $\eta > 0.05$ V as follows:

$$\eta = \mathrm{a} + \mathrm{b} \log j$$

Where η is the overpotential, the value of η varies between cells and operation conditions. It is usually defined as the potential required to reach a current density of 10 mA/cm^2. The value of the overpotential depends on both the activation energy and the kinetics of each step. A similar term, namely onset potential normally refers to the smallest potential where the HER process starts.[97, 98] The constant b is defined as Tafel slope, denoting the additional voltage required to increase the current density by one order of magnitude, with the unit of mV per decade. Tafel slope, as an inherent property of a catalyst, can reflect the reaction mechanism under model HER catalysis systems and the value depends on both the reaction pathway as well as the adsorption conditions of active sites. Generally, under high surface coverage of adsorbed hydrogen H_{ad}, desorption of H_2 (Heyrovsky or Tafel step) is the rate-limiting step, thereby a small Tafel slope of 40 or 30 mV/dec is obtained; whereas under low surface coverage of H_{ad}, adsorption of H_{ad} is rate-limiting, thereby a larger Tafel slope of ~120 mV/dec is obtained. j is the current density given by the equation: $j = J/(\text{electrode area})$, wherein J is the measured current.[4, 99, 100] Another parameter associated with the intrinsic catalytic activity of electrocatalysts is the exchange current density j_o, which describes the electrochemical reaction rate at equilibrium. The value of exchange current density can be extracted from Tafel plot (η versus $\log/j/$), determining how promptly the electrochemical reaction can occur. The exchange current density alone can’t be used to rank catalytic activity since it relies on both the per-site turnover frequency as well as the number of active sites. In general, an ideal HER catalyst should have low overpotential, high exchange current density and low Tafel slope.[11, 12, 98]

MoS_2-based electrocatalysts

The attempt to employ MoS_2 as an electrocatalyst for HER dates back to 1970s. However, the bulk MoS_2 showed poor catalytic activity due to the limited active sites and unfavorable conductivity. Until 2005, Jens Nørskov's and co-workers discovered that the calculated ΔG_H of MoS_2 edges was comparable to Pt, while the basal plane was catalytically inactive.[35] Since then, massive research efforts have been devoted to exploring the nanostructured TMD based HER catalysts (the majority efforts are focusing on MoS_2) aiming to improve the HER performance[98]. The main strategies towards improving the catalytic activity of MoS_2 based catalysts involve increasing the number of active sites per unit volume, improving the electron transport within the catalytic devices and tuning the intrinsic catalytic activity of MoS_2.

(1) Increasing the number of catalytically active sites.

Considering only the edges of MoS_2 are catalytically active, the controllable growth of nanostructured MoS_2 with various morphologies, such as nanoparticles, nanowires, nanosheets and other modified structures, to increase the number of accessible edge sites per unit volume of catalyst is a straightforward way to tune the catalytic activity. (Table 1.1) In 2012, Jaramillo and co-workers designed a mesoporous 2H-MoS_2 with double-gyroid morphology[99]. The high surface curvature of this catalyst facilitated the exposure of a large fraction of edge sites, leading to excellent HER catalytic activity with the overpotential l of -0.22 V vs. RHE and a Tafel slope of 50 mV/dec. One drawback of this MoS_2 double gyroid was the long electron transfer distance from the active site to the substrate, which caused an increase in resistive losses.

To reduce the resistive losses during vertical electron transport with respect to the MoS_2 basal plane, Cui and co-workers developed a vertically aligned 2H-MoS_2 catalyst via CVD growth.[101] The vertically oriented morphology allowed exposure of only edge sites of MoS_2 nanoflakes to the reaction medium, and fast electron transport from MoS_2 single layer to the conducting substrate, leading to 10 times higher exchange current density (2.2 $\mu A/cm^2$) than previous reported MoS_2 nanoparticle-based electrodes, and a high TOF of 0.013 s^{-1}. This results confirmed that the whole surface of the edge-terminated film was catalytically active. However, the catalytic activity of this catalyst was not satisfactory with the overpotential of 0.44 V vs. RHE and a Tafel slope of 120 mV/dec. The overall performance of this catalytic system could be improved by tuning the substrate morphology or adopting different substrate.

Other than engineering the morphology and orientation, Xie's group demonstrated a defects modulation strategy, in which defect-rich and ultrathin (5.9 nm, 9 layers) 2H-MoS_2 nanosheets were synthesized via a hydrothermal reaction[102]. The rich defects in the basal plane of 2H-MoS_2 partially cracked the nanosheets and enabled the exposure of additional active edge sites, leading to enhanced activity with a small overpotential of 0.12 V vs. RHE and a Tafel slope of 50 mV/dec as well as excellent electrochemical durability.

(2) Improving the electron transport.

It is known that the electrical resistivity across different layers is 2200 times higher than that within the layers. In addition, a recent work by Cao and co-workers has demonstrated the HER catalytic activity of CVD-grown MoS_2 nanosheets decreased a factor of ~4.47 for the addition of every one additional layer,[103] suggesting the interlayer electron transfer is crucial to the overall HER performance. Therefore, using single-layer MoS_2 nanosheets would be more favorable than using multilayered MoS_2. However, thin layered MoS_2 tends to restack during the material processing, which would limit the vertical charge transport and exposure of enough catalytically active sites, thus decreasing the activity.

To circumvent the conductivity and processibility limitations of MoS_2, the most popular strategy is to hybridize MoS_2 nanosheets with other conductive materials such as noble metal NPs[104], carbon-based materials (carbon nanotubes[105], graphene[106], RGO[4], carbon nanofibres[107] et.al) and metal oxides to boost the HER catalytic activity. For example, carbon-based nanomaterials are of great interest in use as electrocatalyst supports due to their stability and high conductivity. For example, hybridization of TMDs with carbon based nanomaterials can be achieved by mechanical mixing or in-situ growth. In 2011, Dai and co-workers developed a 2H-MoS_2 NPs/RGO nanocomposite via a solvothermal method[4]. The ultrafine 2H-MoS_2 NPs with abundant active edges in combination with a highly conductive RGO sheets enabled a superior electrocatalytic activity for HER with the overpotential of ~0.10 V vs. RHE and a Tafel slope of 41 mV/dec. To effectively prevent the aggregation of 2D MoS_2, Liu and co-workers developed a 3D electrode structure by in-situ formation of MoS_2 NPs on mesoporous graphene foams (MoS_2/MGF)[108], Benefiting from the 3D-MGF structure that provided more space to growth MoS_2 and the excellent conductivity, the resulting MoS_2/MGF nanocomposite showed a high catalytic activity with the overpotential of -0.1 V vs. RHE and a small Tafel slope of 42 mV/dec. The nanocarbon materials served as templates for mediating the growth of MoS_2 with the specific structure and enhanced the conductivity of whole MoS_2 nanocomposite.

In real cases, the structural design of HER catalyst should take both the active site exposure and conductivity into consideration in order to achieve a high catalytic activity. To synergistically modulate both the active sites and conductivity for efficient HER performance, Xie and co-workers demonstrated controllable incorporation of oxygen into MoS_2 nanosheets, leading to the formation of an oxygen incorporated MoS_2 ultrathin nanosheets with tunable degrees of disorder.[109] The disordered structure provided abundant unsaturated sulfur atoms as active sites and the incorporated oxygen effectively regulated the electronic structure and thus improved the conductivity. This catalyst demonstrated a superior catalytic activity with a small overpotential of ~0.12 V vs. RHE, low Tafel slop of 55 mV/dec, and a high exchange current density of 12.6 μA/cm^2 as well as excellent stability, representing one of the best single-component MoS_2 electrocatalyst.

(3) Tuning the intrinsic catalytic activity

Apart from regulating the number of active sites and conductivity, tuning the intrinsic catalytic is another way to improve the overall performance of MoS_2- based catalysts. Several strategies have emerged in recent years such as employing metallic 1T-MoS_2 instead of 2H-MoS_2 and activating the edge sites by chemical doping. In 2013, Jing and co-workers[110] demonstrated that the 1T-MoS_2 nanosheets obtained from chemical exfoliation displayed a dramatically improved HER catalytic activity with an onset potential of -0.187 V vs. RHE and a Tafel slope of 43 mV/dec compared to the as-grown 2H-MoS_2 (overpotential of ~-0.2 V vs. RHE and a Tafel slope of 117 mV/dec). The dramatically improved Tafel slope confirmed the facile electrode kinetics and low-loss electrical transport of metallic 1T-MoS_2.

Subsequently, Chhowalla and co-workers[36] investigated the origin of high catalytic activity 1T-MoS_2 by comparison of the HER performance of 1T-MoS_2 nanosheets before and after oxidative passivation of edges. Rather than 2H-MoS_2, which showed significantly reduced HER activity after edge-site passivation, the catalytic activity of 1T-MoS_2 remained unaffected. This retained activity in 1T-MoS_2 indicated that basal plane of 1T-MoS_2 was also catalytically active for HER. Recently, structural investigations of chemically exfoliated MoS_2 nanosheets (prepared by lithium intercalation and exfoliation) have found the existence of a quasi-metallic 1T'-polymorph in addition to the 2H- and 1T- polymorph, which displayed a tiny bandgap compared to semiconducting 2H-polymorph but with a similar properties to metallic 1T-polymorph and near zero ΔG_H value. It was proposed that the favored hydrogen adsorption Gibbs free energy on the basal plane of quasi-metallic 1T'-polymorph together with the excellent electric conductivity accounted for the good catalytic activity of multiphasic MoS_2 nanosheets[111] Taking the advantageous activity of 1T-MoS_2 for HER, Cui and co-workers developed a 3D catalyst by loading the lithium intercalated 1T-MoS_2 nanoparticles on 3D carbon fiber paper (CFP).[112] The obtained nanocomposite demonstrated a high HER catalytic activity with the overpotential of ~0.118 V vs. RHE and a Tafel slope of 62 mV/dec, and the exchange current density of 0.167 mA/cm^2 as well as excellent stability under HER conditions.

Admittedly, the edges of MoS_2 are the active sites for HER. Nevertheless, only the sulfide Mo edges with calculated ΔG_H ~0.08 eV are catalytically active, which accounts for only ~25% of all the edge sites[31, 35]. Therefore, activation of the S-edges would be an effective way to increase the intrinsic activity of MoS_2. In this regard, DFT calculation has shown that doping Co at the S-edge of Mo can effectively decrease the ΔG_H from 0.18 to 0.10,[113] thus it is possible to tune the ΔG_H of S-edge to approach by chemical doping. Along with this direction, chemical doping of Mn, Fe, Co, Ni, Cu and Zn on amorphous MoS_3 films has been demonstrated by Hu and co-workers[114]. Among them, the Co doped MoS_3 displayed a 300% increase of active surface area which led to a higher HER performance with the overpotential of

0.17 V vs. RHE than pristine MoS_3 film.

Table 1.1 Catalytic properties of MoS_2 based HER electrocatalysts[a]

catalyst	**structure**	**Overpotential V**	**Tafel slope mV/dec**	**Exchange current density mA/cm²**
2H-MoS_2	0D NPs[31]	-0.15	55-60	N/A
2H-MoS_2	Double gyroid[99]	-0.22	50	N/A
2H-MoS_2	2D vertically aligned[101]	-0.44	120	2.2×10^{-3}
2H-MoS_2	2D defect-rich[102]	-0.12	50	N/A
2H-MoS_2/RGO	NPs/nanosheet[4]	-0.1	41	N/A
2H-MoS_2/MGF	3D[108]	-0.1	42	N/A
2H-MoS_2	2D oxygen incorporation.[109]	-0.12	55	12.6×10^{-3}
2H-MoS_2	2D from CVD [110]	-0.2	117	N/A
1T- MoS_2	2D[110]	-0.187	43	N/A
1T- MoS_2/CFP	3D[112]	-0.118	62	0.167

[a] In 0.5 M H_2SO_4.

Development of MoS_2 based electrocatalysts has made great progress in the past 10 years, and most of them are focused on semiconducting 2H-MoS_2 due to its well established exfoliation and fabrication method and structural properties. However, the development of metallic 1T-MoS_2 based electrocatalysts remains in the infant stage albeit having a higher catalytic activity compared to 2H-MoS_2. This is possibly due to its specific synthetic route and uncertain stability as well as ambiguous HER mechanism. In this regard, Chapter 5 illustrated a study on the modulation of catalytic activity and conductivity of 1T-MoS_2 nanosheets by controllable functionalization, which would improve the understanding of the origin of catalytic activity of 1T-MoS_2 and facilitate the rational design of highly active 1T-MoS_2 based HER catalysts in the future.

1.7.2 TMDs in photocatalytic HER

General principle for photocatalytic HER in heterogeneous system

Sunlight-driven H_2 generation through photocatalytic water splitting has increasingly gained attention for solar energy conversion and storage as well as clean fuel production since 1970's[115], which has been regarded as one of the promising solutions to address energy shortages and the environmental crisis. The photocatalytic HER devices are typically based on earth-abundant semiconductors to absorb sunlight and generate charge carriers, thereby H_2O can be split into H_2 without an external electricity input. Therefore, the catalytic ability of a semiconductor-based photocatalyst depends on both its bandgap and the absolute band position. The bandgap determines the energy of the absorbed photon and the energy of the produced exciton as well as the solar energy utilization efficiency. The band position determines the redox potential of catalyst, thus the driving force for HER. The ideal semiconductor-based photocatalyst should have a proper bandgap in the range of 1.23 to 3.0 eV in order to efficiently use solar energy to split water. [116] Meanwhile, the conduction band edge of the semiconductor should be more negative than the redox potential of the H^+/H_2 couple, so that photogenerated electrons can participate in proton reduction, leading to the generation of H_2.

MoS_2-based photocatalysts

2D MoS_2 based nanomaterial hold great promise for photocatalytic HER due to their distinctive electronic, optical and catalytic properties. However, the studies on directly applying MoS_2 as a photocatalyst for HER are rarely reported due to the low yield production of single-layered MoS_2 nanosheets[12]. Besides, the insufficient light adsorption, fast charge recombination as well as the instability in aqueous solution would also limit the energy-conversion efficiency of such a single component photocatalyst. Therefore, the majority of the MoS_2 based photocatalytic systems reported are multi-component by coupling a light-absorber with a separate electrocatalyst.

In recent years, 2D MoS_2 nanosheets have been extensively explored as co-catalysts for photocatalytic HER. A number of reports have demonstrated that loading 2D MoS_2 co-catalysts onto the light harvesting semiconductors can significantly enhance the photocatalytic activity of photocatalytic devices.[38-40] The synthetic methods to prepare the semiconductor-MoS_2 photocatalytic devices are mostly based on wet chemistry co-growth, such as impregnation and calcination/sulfidation, hot injection, photo-reduction, hydrothermal synthesis, electrodeposition and ball milling.[117, 118] For example, Zhang and co-workers demonstrated a CdS-MoS_2 composite prepared by one-pot chemical synthesis. Coupling of p-type MoS_2 with n-type CdS enabled the formation of p-n junction at the interface, which can facilitate the effective separation of photogenerated carriers via the internal electrostatic field at the junction interface, and thus lead to higher photocatalytic activity than that of pure CdS as well as excellent stability under long-time visible light irradiation [41].

Taking the advantage of the excellent electrocatalytic activity, MoS_2 has recently been successfully integrated into a photo-electrode for photoelectrochemical H_2 production. One example is the 2H-MoS_2-n^+pSi photocathode,[119] which was fabricated by conformal coating of the MoS_2 thin film on the surface doped Si wafer. The 2H-MoS_2 served as both a protecting layer and a catalyst. The obtained photocathode exhibited an excellent stability after 100 h^{-1}, which was attributed to the anticorrosion protection by 2H-MoS_2. The remarkably reinforced current density as well as the significant anodic shift of the photocurrent onset potential indicated the capability of as-prepared semiconductor-MoS_2 photoelectrode for efficient photoelectrochemical HER. However the dark catalytic activity was not satisfactory due to the low density of active edges. In order to overcome the active site limitation, thiomolybdate nanoclusters $[Mo_3S_{13}]^{2-}$ was deposited on the photocathode, leading to the significantly improved HER onset potential.

So far, a large number of research on the semiconductor-MoS_2 based heterogeneous HER photocatalyst has been published with the particular interest in the preparation of MoS_2-semiconductor composites with various composition and morphology. However, constructing such MoS_2-semiconductor composite often requires intense lab work to tune the size and morphology of each nanocomponent in order to get an ideal interface connection and the most exposure of active sites. Therefore, development of facile fabrication techniques or designing other photocatalytic systems with simple assembly methods and high efficacy would provide more chances for practical application of MoS_2 based photocatalyst.

Dye-sensitized photocatalytic HER

Dye-sensitized photocatalysis (DSP) system has emerged as one of the most promising routes for solar-to-fuel conversion.[120-122] A typical dye-sensitized photocatalytic H_2 production process involves the light capturing by molecular dyes, and electron transfer from photo-excited dyes to the active sites of HER catalysts, where H_2 generation takes place, via the conduction band of the semiconductor. The oxidized dyes are then regenerated by taking electrons from sacrificial donors. (Fig. 1.11) Besides these photocatalysis promoting electron transfer processes, other side reactions such as photo-generated electron-hole recombination, charge recombination between the oxidized dye and CB of the semiconductor as well as the photo-degradation of dye would take place simultaneously with the photo-hydrogen production process, and thus considerably affect the solar-hydrogen conversion efficiency and durability of the whole photocatalytic system. Therefore, adoption of robust dye molecules with high visible light adsorption ability and elongating the charge-carrier lifetime through spatial separation of photo-generated electrons and holes are two prerequisites for designing effective dye-sensitized photocatalytic system for HER.

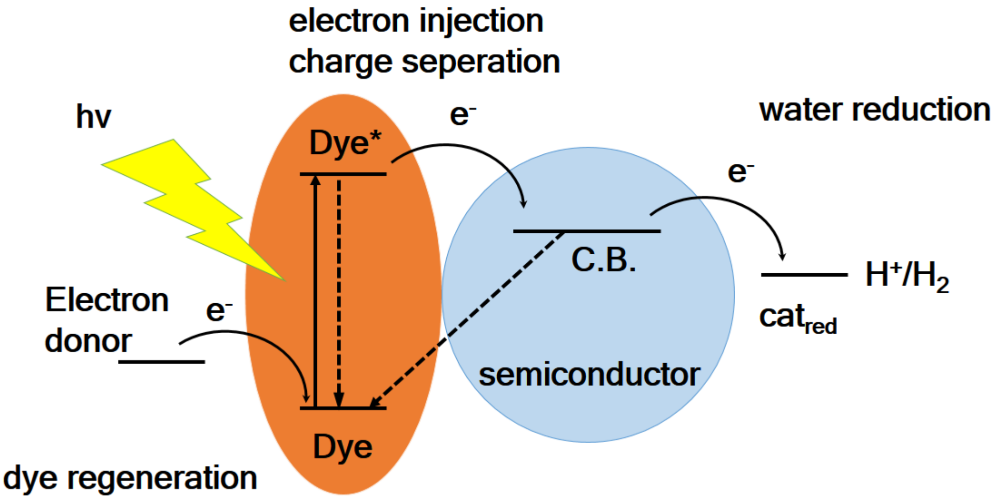

Figure 1.11 Simplified working principle of a dye-sensitized photocatalytic HER system.

Taking inspiration from the dye-sensitized solar cells (DSCs)[123], a wide range of molecular dyes including Ru^{II} complexes, metal porphyrins, and organic dyes (such as Eosin-Y) can be used as visible light sensitive dyes in the dye-sensitized photocatalysis system. Among them, Ru^{II} complexes are some of the most popular dyes in dye-sensitized H_2 production system due to their long-lived excited states, tunable structure, and spectral responsive ability.[124] So far, the Ru^{II} complexes used in dye-sensitized photocatalytic HER system are mainly based on Ru^{II} polypyridyl complexes and their derivatives. (Fig. 1.12)

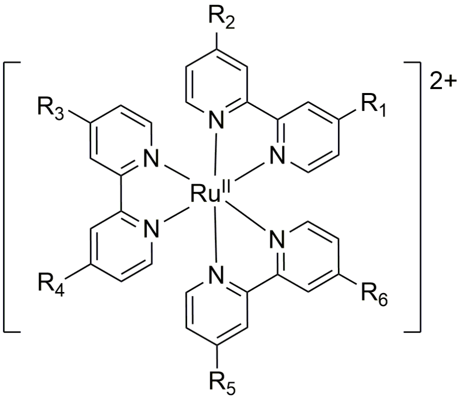

$[Ru^{II}(bpy)_3]^{2+}$: $R_1 \sim R_6 = H$

$[Ru^{II}(dcbpy)_3]^{2+}$: $R_1 \sim R_6 = -COOH$

$Ru^{II}P^{2+}$: $R_1 = R_2 = -H_2PO_3$, $R_3 = R_4 = R_5 = R_6 = H$

Figure 1.12 Molecular structures of typical Ru^{II} complexes used in a dye-sensitized photocatalytic HER system.[120]

Gratzel's group[125] reported the first dye-sensitized water splitting device by using $[Ru^{II}(bpy)_3]^{2+}$ sensitized $Pt/TiO_2/RuO_2$. Considering the slow diffusion of electrons at the heterogeneous surface would affect the photo-generated electron injection and thus charge separation, Sasse and co-workers[126] demonstrated a $[Ru^{II}(dcbpy)_3]^{2+}$ sensitized Pt/TiO_2 electrode. They found that sensitization required the strong adsorption of sensitizer molecules onto the semiconductor surface. Since then, Ru^{II} polypyridyl complexes bearing carboxylate anchoring groups were extensively applied to sensitize various semiconductors such as TiO_2[127], Al_2O_3[128], and reduced graphene oxide (RGO)[129]. However, this carboxylate anchoring groups were found to easily detach from the metal oxide surface in acidic condition (pH 4), which limits its practical applications.[130] Alternatively, Mallouk's group[131] demonstrated a Ru^{II} polypyridyl complex bearing phosphonate anchoring group, which showed stronger bonding to the semiconductor surface. Later research by Choi's group[132] confirmed that Ru^{II} polypyridyl complex sensitized TiO_2 with phosphonate anchoring groups showed higher activity compared to carboxylate anchoring groups, yet electron transfer rate was slower. Therefore, the linkage between dye molecules and semiconductor play an important role in interfacial electron transfer. Thereafter, lots of efforts have been focused on improving the binding affinities of the dye onto the semiconductor surface and electron transfer rate at interfaces.[133, 134]

Recently, Du's group[129] demonstrated a method to covalently bind Ru^{II} polypyridyl complex onto graphene nanosheets, leading to formation of $[Ru^{II}(bpy)_2(py)Cl]/G/Pt$ construct. The obtained $[Ru^{II}(bpy)_2(py)Cl]/G/Pt$ displayed excellent photoactivity and stability for H_2 production.[129] Therefore, coupling dye molecules to semiconductors via covalent bonds is favorable for constructing dye-sensitized photocatalytic systems with high resistance to hydrolysis and high electron injection efficiency. In Chapter 4, the effect of covalent linkages on the photocatalytic activity of dye-sensitized H_2 production was further elucidated using a Ru^{II} complex sensitized MoS_2 system.

Dye-sensitized MoS_2 for photocatalytic HER

MoS_2 based nanomaterials have gained great attention in recent years due to their high electrocatalytic activity and durability.[11, 12] Moreover, the good intralayer conductivity of 2D MoS_2 would enable fast electron transfer to the catalytically active sites. To date, there are only a few examples of the dye-sensitized MoS_2 photocatalyst. In 2009, D. Wang and co-workers[135] reported a $[Ru^{II}(bpy)_3]^{2+}$ sensitized MoS_2 photocatalysis system for visible light driven H_2 production. The as-built system (12.5μmol of MoS_2 NPs and 10 μmol of $[Ru^{II}(bpy)_3]^{2+}$) revealed the optimal H_2 production of 466 μmol with TOF of 75 under 6 hours irradiation by a 300 W Xe lamp. Given to the higher photostability of Ir^{III} cyclometalated complexes compared to Ru^{II} polypyridyl complexes, Z. Zou and co-workers developed a multicomponent photocatalytic hydrogen production system by incorporation of a series of Ir^{III} cyclometalated complexes bearing carboxylate groups with the colloidal

MoS_2 nanoparticles.[136] The combined system (20 μM of MoS_2 NPs and 100 μM of Ir^{III} complexes) displayed the highest quantum conversion efficiency of 12.4% and TON of 1421 at 400 nm in a methanol-water solution containing triethanolamine (TEOA) (pH 7) as a sacrificial donor after 4h irradiation by a 300 W Xe lamp. They attributed the high photocatalytic activity to the presence of carboxylate ancillary groups in Ir^{III} cyclometalated complexes, which facilitated the adsorption of dye onto MoS_2 surface and thereby aided the electron injection.

Apart from using colloidal MoS_2 NPs, the fast-growing technology based on two-dimensional material processing allows facile constructing of TMD nanosheets-based photocatalysts in solution. For example, Lu and co-workers[137] demonstrated an Eosin Y-sensitized few-layered 2H-MoS_2/RGO photocatalyst for efficient light-driven hydrogen evolution, leading to a high apparent quantum efficiency (AQE) of 24.0% at 460 nm in TEOA-H_2O solution (pH 7). It was demonstrated that electrons involved in the reduction of H_2O to H_2 were actually originating from the photo-excited Eosin Y, which were transferred to MoS_2 catalysts via the conductive RGO. Thus, employing conductive MoS_2 nanosheets instead of semiconducting 2H-MoS_2 nanosheets would be more rewarding for the overall photocatalytic system. By taking this concept, Rao and co-workers[34] developed an Eosin Y-sensitized 1T-MoS_2 photocatalysis device, which revealed a high turn-over frequency (TOF) of 6.25 h^{-1} in TEOA aqueous solution under irradiation by 100 W halogen lamp, nearly 3 times higher than the Eosin Y-sensitized 2H-MoS_2/N-doped graphene. The high activity of this dye-sensitized 1T-MoS_2 catalyst was likely attributed to the good conductivity of 1T-MoS_2.

It is noticed that all the reported dye-sensitized MoS_2 photocatalysts were built by simply mixing dye molecules and MoS_2 nanosheets in solution. Lacking of linkage between the dye and MoS_2 catalyst would limit the electronic communications between the two components, thus potentially inhibiting the hydrogen photo-production efficiency. Moreover, the ill-defined mixture will impede the in-depth understanding of the interactions between dye molecules and MoS_2 and thus block the way to rationally design more effective dye-sensitized system for solar fuel production. To bridge this research gap, a novel dye-sensitized MoS_2 photocatalytic system was designed and assembled in Chapter 4. The effect of dye structure on the activity of the overall dye-sensitized system was investigated in Chapter 5.

1.7 Conclusion

In this chapter, the recent progress in preparation, functionalization and applications of 2D TMDs nanosheet (in particular 2D MoS_2) in electrocatalytic and photocatalytic HER has been summarized. Compared to mechanical cleavage, CVD growth, and wet chemistry techniques, preparation of 2D TMDs using solution based exfoliation methods such as liquid exfoliation and chemical exfoliation are more advantageous due to their scalable production ability, facile fabrication procedure and easy hybridization with other materials. Nevertheless, there are lots of challenges associated with the purification, processing and fabrication of exfoliated TMDs into devices. To this end, chemical functionalization of 2D TMDs offers a significant opportunity to further tune their properties, processibility and thus improve their versatilities and broaden their applications. The reports of last 4 years have provided multiple routes to functionalize 2D TMDs, though the following research gaps need to be addressed to further advance this field: can we covalently functionalize 2H-MoS_2 directly using thiol chemistry based technique? How the 2D TMDs interact with organic thiols, is it mediated by defect sites or not? How does the covalent bonding affect the structural, electronic and catalytic properties of 2D

TMDs? Can we fabricate multifunctional devices through surface functionalization of 2D TMDs?

Based on the excellent catalytic activity of 2D MoS_2 toward HER, the 2D MoS_2 based electrocatalysts have been extensively studied, while studies of 2D MoS_2 in the field of photocatalytic HER remains in the infant stage. The majority of established photocatalysis systems are built based on the MoS_2/semiconductor heterostructure fabrication, which is limited in their scalability and generality. One possible way to circumvent this challenge is to exchange semiconductors with molecular dyes, forming a dye-sensitized photocatalysis system. To date, there are only a few examples of dye-sensitized MoS_2 photocatalyst, and almost all of them were built by simply mixing dye molecules and 2D MoS_2, thereby they are inherently mass transfer limited, which potentially inhibits the hydrogen photo-production efficiency. Therefore, a highly efficient dye-sensitized photocatalysis system that is able to overcome the slow diffusion rate of dye molecules to MoS_2 surface is urgently required. Moreover, the catalysis mechanism of dye-sensitized MoS_2 for HER should be explored further.

1.8 Aims and scope of this thesis

Considering the aforementioned research gaps in the functionalization of 2D TMDs and application of 2D MoS_2 for photocatalytic hydrogen production ,the aim of this thesis is to functionalize 2D TMDs toward modified physical and chemical properties as well as catalytic activity, to understand the chemistry of functionalization techniques, and to develop novel dye-sensitized photo-sensing or photocatalytic devices by covalent functionalization of 2D MoS_2 with Ru^{II} complexes-based photosensitizers.

To this end, functionalization strategies developed and evaluated came under two main headings: *Functionalization of 2H-MoS$_2$ with Organic Thiols* and *Covalent Functionalization of ce-1T-MoS$_2$ with Ru^{II} Complexes*.

For *Functionalization of 2H-MoS$_2$. with Organic Thiols*, a general route to functionalize liquid exfoliated 2D TMDs with cysteine (an organic thiol) was developed. The dispersibility and stability of functionalized MoS$_2$ were evaluated. The interactions between organic thiols and 2H-MoS$_2$ were analyzed by spectroscopic characterization and kinetic studies. Ultimately, the underlying mechanism of 2H-MoS$_2$/thiol interactions at macro-level was explored. (Fig. 1.13)

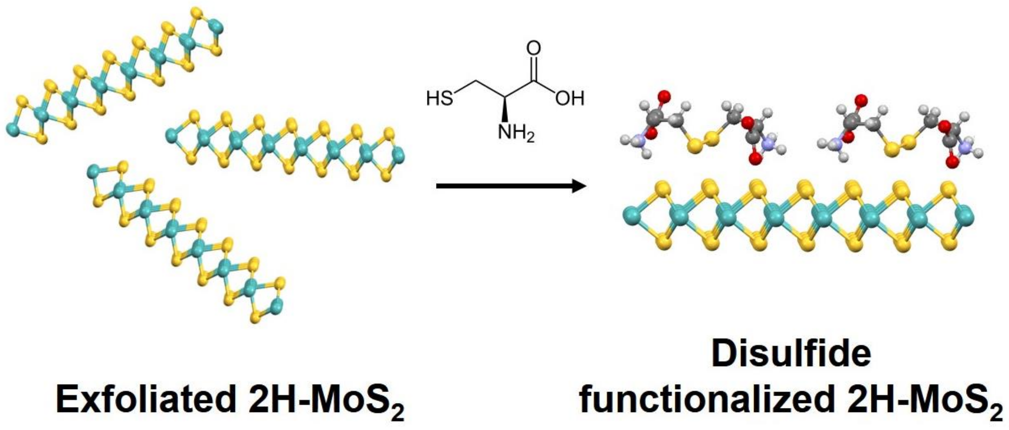

Figure 1.13 Schematic representation of functionalization of liquid-exfoliated 2H-MoS$_2$ with cysteine.

For *Covalent Functionalization of ce-1T-MoS$_2$ with Ru^{II} Complexes,* a stepwise functionalization approach to covalently binding Ru^{II} polypyridyl complexes onto chemically exfoliated MoS$_2$ nanosheets (ce-1T-MoS$_2$) was developed. The effects of covalent functionalization with various functional addends on the catalytic activity of ce-1T-MoS$_2$ were evaluated. The obtained dye-functionalized MoS$_2$ devices were tested in a photoelectrochemical cell as photocathode materials for potential use in a solar-hydrogen generator. In addition, the effect of covalent linkages and the structure of dye molecules on the photoelectrochemical performance was investigated. Finally, the electrochemical and photophysical properties of a series of dye-functionalized MoS_2 devices and associated model complexes were elucidated and the possible working mechanism of as-prepared dye-sensitized MoS_2 photocatalytic system was proposed. (Fig. 1.14)

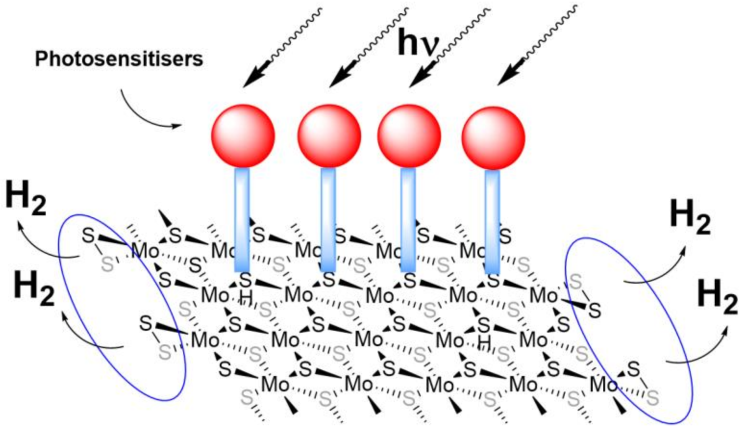

Figure 1.14 Schematic representation of dye-sensitized MoS_2 system for light-driven H_2 production.

References

[1] B. Radisavljevic, A. Radenovic, J. Brivio, V. Giacometti, A. Kis, *Nat. Nanotechnol.* **2011**, *6*, 147-150.

[2] M. Chhowalla, H. S. Shin, G. Eda, L.-J. Li, K. P. Loh, H. Zhang, *Nat. Chem.* **2013**, *5*, 263-275.

[3] B. Seger, A. B. Laursen, P. C. K. Vesborg, T. Pedersen, O. Hansen, S. Dahl, I. Chorkendorff, *Angew. Chem. Int. Ed.* **2012**, *51*, 9128-9131.

[4] Y. Li, H. Wang, L. Xie, Y. Liang, G. Hong, H. Dai, *J. Am. Chem. Soc.* **2011**, *133*, 7296-7299.

[5] J. N. Coleman, M. Lotya, A. O'Neill, S. D. Bergin, P. J. King, U. Khan, K. Young, A. Gaucher, S. De, R. J. Smith, I. V. Shvets, S. K. Arora, G. Stanton, H.-Y. Kim, K. Lee, G. T. Kim, G. S. Duesberg, T. Hallam, J. J. Boland, J. J. Wang, J. F. Donegan, J. C. Grunlan, G. Moriarty, A. Shmeliov, R. J. Nicholls, J. M. Perkins, E. M. Grieveson, K. Theuwissen, D. W. McComb, P. D. Nellist,

V. Nicolosi, *Science* **2011**, *331*, 568-571.

[6] R. J. Smith, P. J. King, M. Lotya, C. Wirtz, U. Khan, S. De, A. O'Neill, G. S. Duesberg, J. C. Grunlan, G. Moriarty, J. Chen, J. Wang, A. I. Minett, V. Nicolosi, J. N. Coleman, *Adv. Mater.* **2011**, *23*, 3944-3948.

[7] Z. Zeng, Z. Yin, X. Huang, H. Li, Q. He, G. Lu, F. Boey, H. Zhang, *Angew. Chem. Int. Ed.* **2011**, *50*, 11093-11097.

[8] K.-K. Liu, W. Zhang, Y.-H. Lee, Y.-C. Lin, M.-T. Chang, C.-Y. Su, C.-S. Chang, H. Li, Y. Shi, H. Zhang, C.-S. Lai, L.-J. Li, *Nano Letters* **2012**, *12*, 1538-1544.

[9] L. Niu, K. Li, H. Zhen, Y.-S. Chui, W. Zhang, F. Yan, Z. Zheng, *Small* **2014**, *10*, 4651-4657.

[10] K. F. Mak, C. Lee, J. Hone, J. Shan, T. F. Heinz, *Phys. Rev. Lett.* **2010**, *105*, 136805.

[11] J. D. Benck, T. R. Hellstern, J. Kibsgaard, P. Chakthranont, T. F. Jaramillo, *ACS Catal.* **2014**, *4*, 3957-3971.

[12] F. Wang, T. A. Shifa, X. Zhan, Y. Huang, K. Liu, Z. Cheng, C. Jiang, J. He, *Nanoscale* **2015**, *7*, 19764-19788.

[13] X. Zhang, Z. Lai, C. Tan, H. Zhang, *Angew. Chem. Int. Ed.* **2016**, *55*, 8816-8838.

[14] D. Voiry, A. Goswami, R. Kappera, C. D. C. E. Silva, D. Kaplan, T. Fujita, M. Chen, T. Asefa, M. Chhowalla, *Nat. Chem.* **2015**, *7*, 45-49.

[15] K. C. Knirsch, N. C. Berner, H. C. Nerl, C. S. Cucinotta, Z. Gholamvand, N. McEvoy, Z. Wang, I. Abramovic, P. Vecera, M. Halik, S. Sanvito, G. S. Duesberg, V. Nicolosi, F. Hauke, A. Hirsch, J. N. Coleman, C. Backes, *ACS Nano* **2015**, *9*, 6018-6030.

[16] C. Backes, N. C. Berner, X. Chen, P. Lafargue, P. La Place, M. Freeley, G. S. Duesberg, J. N. Coleman, A. R. McDonald, *Angew. Chem. Int. Ed.* **2015**, *54*, 2638-2642.

[17] S. S. Chou, B. Kaehr, J. Kim, B. M. Foley, M. De, P. E. Hopkins, J. Huang, C. J. Brinker, V. P. Dravid, *Angew. Chem. Int. Ed.* **2013**, *52*, 4160-4164.

[18] K. S. Novoselov, A. K. Geim, S. V. Morozov, D. Jiang, Y. Zhang, S. V. Dubonos, I. V. Grigorieva, A. A. Firsov, *Science* **2004**, *306*, 666-669.

[19] M. Chhowalla, H. S. Shin, G. Eda, L. J. Li, K. P. Loh, H. Zhang, *Nat. Chem.* **2013**, *5*, 263-275.

[20] M. Osada, T. Sasaki, *Adv. Mater.* **2012**, *24*, 210-228.

[21] D. Golberg, Y. Bando, Y. Huang, T. Terao, M. Mitome, C. Tang, C. Zhi, *ACS Nano* **2010**, *4*, 2979-2993.

[22] K. J. Koski, Y. Cui, *ACS Nano* **2013**, *7*, 3739-3743.

[23] M. Naguib, V. N. Mochalin, M. W. Barsoum, Y. Gogotsi, *Adv. Mater.* **2014**, *26*, 992-1005.

[24] K. K. Kam, B. A. Parkinson, *J. Phys. Chem.* **1982**, *86*, 463-467.

[25] S. Bertolazzi, J. Brivio, A. Kis, *ACS Nano* **2011**, *5*, 9703-9709.

[26] L. F. Mattheiss, *Phys. Rev. B* **1973**, *8*, 3719-3740.

[27] P. D. Fleischauer, J. R. Lince, P. A. Bertrand, R. Bauer, *Langmuir* **1989**, *5*, 1009-1015.

[28] M. Kan, J. Y. Wang, X. W. Li, S. H. Zhang, Y. W. Li, Y. Kawazoe, Q. Sun, P. Jena, *J. Phys. Chem. C* **2014**, *118*, 1515-1522.

[29] E. Benavente, M. A. Santa Ana, F. Mendizábal, G. González, *Coord. Chem. Rev.* **2002**, *224*, 87-109.

[30] G. Eda, H. Yamaguchi, D. Voiry, T. Fujita, M. Chen, M. Chhowalla, *Nano Lett.* **2011**, *11*, 5111-5116.

[31] T. F. Jaramillo, K. P. Jørgensen, J. Bonde, J. H. Nielsen, S. Horch, I. Chorkendorff, *Science* **2007**, *317*, 100-102.

[32] Q. H. Wang, K. Kalantar-Zadeh, A. Kis, J. N. Coleman, M. S. Strano, *Nat. Nanotechnol.* **2012**, *7*, 699-712.

[33] R. Coehoorn, C. Haas, R. A. de Groot, *Phys. Rev. B* **1987**, *35*, 6203-6206.

[34] U. Maitra, U. Gupta, M. De, R. Datta, A. Govindaraj, C. N. R. Rao, *Angew. Chem. Int. Ed.* **2013**, *52*, 13057-13061.

[35] B. Hinnemann, P. G. Moses, J. Bonde, K. P. Jørgensen, J. H. Nielsen, S. Horch, I. Chorkendorff, J. K. Nørskov, *J. Am. Chem. Soc.* **2005**, *127*, 5308-5309.

[36] D. Voiry, M. Salehi, R. Silva, T. Fujita, M. Chen, T. Asefa, V. B. Shenoy, G. Eda, M. Chhowalla, *Nano Lett.* **2013**, *13*, 6222-6227.

[37] H. Wang, Z. Lu, S. Xu, D. Kong, J. J. Cha, G. Zheng, P.-C. Hsu, K. Yan, D. Bradshaw, F. B. Prinz, Y. Cui, *Proc. Natl. Acad. Sci. U. S. A.* **2013**, *110*, 19701-19706.

[38] K. Chang, Z. Mei, T. Wang, Q. Kang, S. Ouyang, J. Ye, *ACS Nano* **2014**, *8*, 7078-7087.

[39] L. Yang, D. Zhong, J. Zhang, Z. Yan, S. Ge, P. Du, J. Jiang, D. Sun, X. Wu, Z. Fan, S. A. Dayeh, B. Xiang, *ACS Nano* **2014**, *8*, 6979-6985.

[40] Y. Hou, A. B. Laursen, J. Zhang, G. Zhang, Y. Zhu, X. Wang, S. Dahl, I. Chorkendorff, *Angew. Chem. Int. Ed.* **2013**, *52*, 3621-3625.

[41] J. Chen, X.-J. Wu, L. Yin, B. Li, X. Hong, Z. Fan, B. Chen, C. Xue, H. Zhang, *Angew. Chem. Int. Ed.* **2015**, *54*, 1210-1214.

[42] W. Zhou, Z. Yin, Y. Du, X. Huang, Z. Zeng, Z. Fan, H. Liu, J. Wang, H. Zhang, *Small* **2013**, *9*, 140-147.

[43] W. S. Yun, S. W. Han, S. C. Hong, I. G. Kim, J. D. Lee, *Phys. Rev. B* **2012**, *85*, 033305.

[44] X. Zong, H. Yan, G. Wu, G. Ma, F. Wen, L. Wang, C. Li, *J. Am. Chem. Soc.* **2008**, *130*, 7176-7177.

[45] X. Zong, G. Wu, H. Yan, G. Ma, J. Shi, F. Wen, L. Wang, C. Li, *J. Phys. Chem. C* **2010**, *114*, 1963-1968.

[46] K. S. Novoselov, D. Jiang, F. Schedin, T. J. Booth, V. V. Khotkevich, S. V.

Morozov, A. K. Geim, *Proc. Natl. Acad. Sci. U. S. A.* **2005**, *102*, 10451-10453.

[47] J. N. Coleman, M. Lotya, A. O'Neill, S. D. Bergin, P. J. King, U. Khan, K. Young, A. Gaucher, S. De, R. J. Smith, I. V. Shvets, S. K. Arora, G. Stanton, H.-Y. Kim, K. Lee, G. T. Kim, G. S. Duesberg, T. Hallam, J. J. Boland, J. J. Wang, J. F. Donegan, J. C. Grunlan, G. Moriarty, A. Shmeliov, R. J. Nicholls, J. M. Perkins, E. M. Grieveson, K. Theuwissen, D. W. McComb, P. D. Nellist, V. Nicolosi, *Science* **2011**, *331*, 568-571.

[48] C. N. R. Rao, H. S. S. Ramakrishna Matte, U. Maitra, *Angew. Chem. Int. Ed.* **2013**, *52*, 13162-13185.

[49] Y.-H. Lee, X.-Q. Zhang, W. Zhang, M.-T. Chang, C.-T. Lin, K.-D. Chang, Y.-C. Yu, J. T.-W. Wang, C.-S. Chang, L.-J. Li, T.-W. Lin, *Adv. Mater.* **2012**, *24*, 2320-2325.

[50] Y. Zhan, Z. Liu, S. Najmaei, P. M. Ajayan, J. Lou, *Small* **2012**, *8*, 966-971.

[51] H. S. S. Ramakrishna Matte, A. Gomathi, A. K. Manna, D. J. Late, R. Datta, S. K. Pati, C. N. R. Rao, *Angew. Chem. Int. Ed.* **2010**, *49*, 4059-4062.

[52] J. Shen, Y. He, J. Wu, C. Gao, K. Keyshar, X. Zhang, Y. Yang, M. Ye, R. Vajtai, J. Lou, P. M. Ajayan, *Nano Lett.* **2015**, *15*, 5449-5454.

[53] X. Zhang, Z. Lai, C. Tan, H. Zhang, *Angew. Chem.* **2016**, *128*, 8960-8984.

[54] J. N. Coleman, M. Lotya, A. O'Neill, S. D. Bergin, P. J. King, U. Khan, K. Young, A. Gaucher, S. De, R. J. Smith, I. V. Shvets, S. K. Arora, G. Stanton, H. Y. Kim, K. Lee, G. T. Kim, G. S. Duesberg, T. Hallam, J. J. Boland, J. J. Wang, J. F. Donegan, J. C. Grunlan, G. Moriarty, A. Shmeliov, R. J. Nicholls, J. M. Perkins, E. M. Grieveson, K. Theuwissen, D. W. McComb, P. D. Nellist, V. Nicolosi, *Science* **2011**, *331*, 568-571.

[55] A. O’Neill, U. Khan, J. N. Coleman, *Chem. Mater.* **2012**, *24*, 2414-2421.

[56] A. Jawaid, D. Nepal, K. Park, M. Jespersen, A. Qualley, P. Mirau, L. F. Drummy, R. A. Vaia, *Chem. Mater.* **2016**, *28*, 337-348.

[57] S. D. Bergin, Z. Sun, D. Rickard, P. V. Streich, J. P. Hamilton, J. N. Coleman, *ACS Nano* **2009**, *3*, 2340-2350.

[58] K.-G. Zhou, N.-N. Mao, H.-X. Wang, Y. Peng, H.-L. Zhang, *Angew. Chem. Int. Ed.* **2011**, *50*, 10839-10842.

[59] U. Halim, C. R. Zheng, Y. Chen, Z. Lin, S. Jiang, R. Cheng, Y. Huang, X. Duan, *Nat. Commun.* **2013**, *4*, 2213.

[60] C. Backes, B. M. Szydłowska, A. Harvey, S. Yuan, V. Vega-Mayoral, B. R. Davies, P.-l. Zhao, D. Hanlon, E. J. G. Santos, M. I. Katsnelson, W. J. Blau, C. Gadermaier, J. N. Coleman, *ACS Nano* **2016**, *10*, 1589-1601.

[61] D. McAteer, Z. Gholamvand, N. McEvoy, A. Harvey, E. O’Malley, G. S. Duesberg, J. N. Coleman, *ACS Nano* **2016**, *10*, 672-683.

[62] L. Guardia, J. I. Paredes, R. Rozada, S. Villar-Rodil, A. Martinez-Alonso, J. M. D. Tascon, *RSC Adv.* **2014**, *4*, 14115-14127.

[63] E. Benavente, *Coord. Chem.* **2002**, 224, 87-109.
[64] J. V. Acrivos, W. Y. Liang, J. A. Wilson, A. D. Yoffe, *J. Phys. C: Solid State Phys.* **1971**, *4*, L18.
[65] R. B. Somoano, V. Hadek, A. Rembaum, *J. Chem. Phys.* **1973**, *58*, 697-701.
[66] P. Joensen, E. D. Crozier, N. Alberding, R. F. Frindt, *J. Phys. C: Solid State Phys.* **1987**, *20*, 4043.
[67] J. Heising, M. G. Kanatzidis, *J. Am. Chem. Soc.* **1999**, *121*, 11720-11732.
[68] L. Nurdiwijayanto, R. Ma, N. Sakai, T. Sasaki, *Inorg. Chem.* **2017**, *56*, 7620-7623.
[69] H. Wang, Z. Lu, S. Xu, D. Kong, J. J. Cha, G. Zheng, P.-C. Hsu, K. Yan, D. Bradshaw, F. B. Prinz, Y. Cui, *Proc. Natl. Acad. Sci.* **2013**, *110*, 19701-19706.
[70] J. Zheng, H. Zhang, S. Dong, Y. Liu, C. Tai Nai, H. Suk Shin, H. Young Jeong, B. Liu, K. Ping Loh, *Nat. Commun.* **2014**, *5*, 2995.
[71] K. C. Knirsch, N. C. Berner, H. C. Nerl, C. S. Cucinotta, Z. Gholamvand, N. McEvoy, Z. Wang, I. Abramovic, P. Vecera, M. Halik, S. Sanvito, G. S. Duesberg, V. Nicolosi, F. Hauke, A. Hirsch, J. N. Coleman, C. Backes, *ACS Nano* **2015**, *9*, 6018-6030.
[72] V. Georgakilas, M. Otyepka, A. B. Bourlinos, V. Chandra, N. Kim, K. C. Kemp, P. Hobza, R. Zboril, K. S. Kim, *Chem. Rev.* **2012**, *112*, 6156-6214.
[73] D. Voiry, A. Goswami, R. Kappera, C. d. C. C. e. Silva, D. Kaplan, T. Fujita, M. Chen, T. Asefa, M. Chhowalla, *Nat. Chem.* **2015**, *7*, 45-49.
[74] X. Chen, A. R. McDonald, *Advanced Materials* **2016**, *28*, 5738-5746.
[75] X. Chen, N. C. Berner, C. Backes, G. S. Duesberg, A. R. McDonald, *Angew. Chem. Int. Ed.* **2016**, 55, 5803.
[76] Z. Cheng, B. He, L. Zhou, *J. Mater. Chem. A* **2015**, *3*, 1042-1048.
[77] S.-D. Jiang, G. Tang, Z.-M. Bai, Y.-Y. Wang, Y. Hu, L. Song, *RSC Adv.* **2014**, *4*, 3253-3262.
[78] T. Liu, S. Shi, C. Liang, S. Shen, L. Cheng, C. Wang, X. Song, S. Goel, T. E. Barnhart, W. Cai, Z. Liu, *ACS Nano* **2015**, *9*, 950-960.
[79] T. Liu, C. Wang, X. Gu, H. Gong, L. Cheng, X. Shi, L. Feng, B. Sun, Z. Liu, *Adv. Mater. (Weinheim, Ger.)* **2014**, *26*, 3433-3440.
[80] A. Tuxen, J. Kibsgaard, H. Gøbel, E. Lægsgaard, H. Topsøe, J. V. Lauritsen, F. Besenbacher, *ACS Nano* **2010**, *4*, 4677-4682.
[81] T. Wang, R. Zhu, J. Zhuo, Z. Zhu, Y. Shao, M. Li, *Anal. Chem. (Washington, DC, U. S.)* **2014**, *86*, 12064-12069.
[82] S. Lei, X. Wang, B. Li, J. Kang, Y. He, A. George, L. Ge, Y. Gong, P. Dong, Z. Jin, G. Brunetto, W. Chen, Z.-T. Lin, R. Baines, D. S. Galvão, J. Lou, E. Barrera, K. Banerjee, R. Vajtai, P. Ajayan, *Nat. Nanotechnol.* **2016**, *11*, 465-471.
[83] R. H. Goncalves, R. Fiel, M. R. S. Soares, W. H. Schreiner, C. M. P. Silva, E. R. Leite, *Chem. Eur. J.* **2015**, Ahead of Print.

[84] M. Makarova, Y. Okawa, M. Aono, *J. Phys. Chem. C* **2012**, *116*, 22411-22416.

[85] Z. Yu, Y. Pan, Y. Shen, Z. Wang, Z.-Y. Ong, T. Xu, R. Xin, L. Pan, B. Wang, L. Sun, J. Wang, G. Zhang, Y. W. Zhang, Y. Shi, X. Wang, *Nat. Commun.* **2014**, *5*.

[86] E. P. Nguyen, B. J. Carey, J. Z. Ou, J. van Embden, E. D. Gaspera, A. F. Chrimes, M. J. S. Spencer, S. Zhuiykov, K. Kalantar-zadeh, T. Daeneke, *Adv. Mater. (Weinheim, Ger.)* **2015**, Ahead of Print.

[87] J.-S. Kim, H.-W. Yoo, H. O. Choi, H.-T. Jung, *Nano Lett.* **2014**, *14*, 5941-5947.

[88] K. Cho, M. Min, T.-Y. Kim, H. Jeong, J. Pak, J.-K. Kim, J. Jang, S. J. Yun, Y. H. Lee, W.-K. Hong, T. Lee, *ACS Nano* **2015**, *9*, 8044-8053.

[89] M. G. Walter, E. L. Warren, J. R. McKone, S. W. Boettcher, Q. Mi, E. A. Santori, N. S. Lewis, *Chem. Rev.* **2010**, *110*, 6446-6473.

[90] T. Abbasi, S. A. Abbasi, *Renew. Sustain. Energy Rev.* **2011**, *15*, 3034-3040.

[91] A. J. Bard, M. A. Fox, *Acc. Chem.Res.* **1995**, *28*, 141-145.

[92] Y. Wang, Q. Wang, X. Zhan, F. Wang, M. Safdar, J. He, *Nanoscale* **2013**, *5*, 8326-8339.

[93] C.-Y. Lee, H. S. Park, J. C. Fontecilla-Camps, E. Reisner, *Angew. Chem. Int. Ed.* **2016**, *55*, 5971-5974.

[94] A. Kudo, Y. Miseki, *Chem. Soc. Rev.* **2009**, *38*, 253-278.

[95] Y. Sun, S. Gao, F. Lei, Y. Xie, *Chemical Society Reviews* **2015**, *44*, 623-636.

[96] J. Greeley, T. F. Jaramillo, J. Bonde, I. Chorkendorff, J. K. Norskov, *Nat. Mater.* **2006**, *5*, 909-913.

[97] A. B. Laursen, S. Kegnaes, S. Dahl, I. Chorkendorff, *Energy Environ. Sci.* **2012**, *5*, 5577-5591.

[98] Y. Yan, B. Xia, Z. Xu, X. Wang, *ACS Catal.* **2014**, *4*, 1693-1705.

[99] J. Kibsgaard, Z. Chen, B. N. Reinecke, T. F. Jaramillo, *Nat. Mater.* **2012**, *11*, 963-969.

[100] Z. Chen, D. Cummins, B. N. Reinecke, E. Clark, M. K. Sunkara, T. F. Jaramillo, *Nano Lett.* **2011**, *11*, 4168-4175.

[101] D. Kong, H. Wang, J. J. Cha, M. Pasta, K. J. Koski, J. Yao, Y. Cui, *Nano Lett.* **2013**, *13*, 1341-1347.

[102] J. Xie, H. Zhang, S. Li, R. Wang, X. Sun, M. Zhou, J. Zhou, X. W. Lou, Y. Xie, *Ad. Mater.* **2013**, *25*, 5807-5813.

[103] Y. Yu, S.-Y. Huang, Y. Li, S. N. Steinmann, W. Yang, L. Cao, *Nano Lett.* **2014**, *14*, 553-558.

[104] J. Kim, S. Byun, A. J. Smith, J. Yu, J. Huang, *J. Phys. Chem. Lett.* **2013**, *4*, 1227-1232.

[105] D. J. Li, U. N. Maiti, J. Lim, D. S. Choi, W. J. Lee, Y. Oh, G. Y. Lee, S. O. Kim, *Nano Lett.* **2014**, *14*, 1228-1233.

[106] S. Mao, Z. Wen, S. Ci, X. Guo, K. Ostrikov, J. Chen, *Small* **2015**, *11*, 414-419.

[107] H. Zhu, M. Du, M. Zhang, M. Zou, T. Yang, S. Wang, J. Yao, B. Guo, *Chem. Commun.* **2014**, *50*, 15435-15438.

[108] L. Liao, J. Zhu, X. Bian, L. Zhu, M. D. Scanlon, H. H. Girault, B. Liu, *Ad. Funct. Mater.* **2013**, *23*, 5326-5333.

[109] J. Xie, J. Zhang, S. Li, F. Grote, X. Zhang, H. Zhang, R. Wang, Y. Lei, B. Pan, Y. Xie, *J. Am. Chem. Soc.* **2013**, *135*, 17881-17888.

[110] M. A. Lukowski, A. S. Daniel, F. Meng, A. Forticaux, L. Li, S. Jin, *J. Am. Chem. Soc.* **2013**, *135*, 10274-10277.

[111] S. S. Chou, N. Sai, P. Lu, E. N. Coker, S. Liu, K. Artyushkova, T. S. Luk, B. Kaehr, C. J. Brinker, *Nat. Commun.* **2015**, *6*, 8311.

[112] H. Wang, Z. Lu, D. Kong, J. Sun, T. M. Hymel, Y. Cui, *ACS Nano* **2014**, *8*, 4940-4947.

[113] J. Bonde, P. G. Moses, T. F. Jaramillo, J. K. Norskov, I. Chorkendorff, *Faraday Discuss.* **2009**, *140*, 219-231.

[114] D. Merki, H. Vrubel, L. Rovelli, S. Fierro, X. Hu, *Chem. Sci.* **2012**, *3*, 2515.

[115] A. Fujishima, K. Honda, *Nature* **1972**, *238*, 37-38.

[116] Y. Qu, X. Duan, *Chem. Soc. Rev.* **2013**, *42*, 2568-2580.

[117] X. Huang, Z. Zeng, H. Zhang, *Chem. Soc. Rev.* **2013**, *42*, 1934-1946.

[118] B. Han, Y. H. Hu, *Energy Sci. Eng.* **2016**, *4*, 285-304.

[119] J. D. Benck, S. C. Lee, K. D. Fong, J. Kibsgaard, R. Sinclair, T. F. Jaramillo, *Ad. Energy Mater.* **2014**, *4*, n/a-n/a.

[120] X. Zhang, T. Peng, S. Song, *J. Mater. Chem. A* **2016**, *4*, 2365-2402.

[121] J. Willkomm, K. L. Orchard, A. Reynal, E. Pastor, J. R. Durrant, E. Reisner, *Chem. Soc. Rev.* **2016**, *45*, 9-23.

[122] A. Reynal, J. Willkomm, N. M. Muresan, F. Lakadamyali, M. Planells, E. Reisner, J. R. Durrant, *Chem. Commun.* **2014**, *50*, 12768-12771.

[123] A. Hagfeldt, G. Boschloo, L. Sun, L. Kloo, H. Pettersson, *Chem. Rev.* **2010**, *110*, 6595-6663.

[124] M. Grätzel, *Acc. Chem. Res.* **2009**, *42*, 1788-1798.

[125] E. Borgarello, J. Kiwi, E. Pelizzetti, M. Visca, M. Gratzel, *Nature* **1981**, *289*, 158-160.

[126] D. N. Furlong, D. Wells, W. H. F. Sasse, *J. Phys. Chem.* **1986**, *90*, 1107-1115.

[127] N. Lakshminarasimhan, E. Bae, W. Choi, *J. Phys. Chem. C* **2007**, *111*, 15244-15250.

[128] A. Reynal, A. Forneli, E. Palomares, *Energy Enviro. Sci.* **2010**, *3*, 805-812.

[129] B. Xiao, X. Wang, H. Huang, M. Zhu, P. Yang, Y. Wang, Y. Du, *J. Phys. Chem. C* **2013**, *117*, 21303-21311.

[130] C. Law, S. C. Pathirana, X. Li, A. Y. Anderson, P. R. F. Barnes, A. Listorti, T. H. Ghaddar, B. C. O′Regan, *Ad. Mater.* **2010**, *22*, 4505-4509.

[131] G. B. Saupe, T. E. Mallouk, W. Kim, R. H. Schmehl, *J. Phys. Chem. B* **1997**, *101*, 2508-2513.

[132] E. Bae, W. Choi, *J. Phys. Chem. B* **2006**, *110*, 14792-14799.
[133] A. Kruth, S. Hansen, T. Beweries, V. Brüser, K.-D. Weltmann, *ChemSusChem* **2013**, *6*, 152-159.
[134] J. Park, J. Yi, T. Tachikawa, T. Majima, W. Choi, *J. Phys. Chem. Lett.* **2010**, *1*, 1351-1355.
[135] X. Zong, Y. Na, F. Wen, G. Ma, J. Yang, D. Wang, Y. Ma, M. Wang, L. Sun, C. Li, *Chem. Commun.* **2009**, 4536-4538.
[136] Y.-J. Yuan, Z.-T. Yu, X.-J. Liu, J.-G. Cai, Z.-J. Guan, Z.-G. Zou, *Sci. Rep.* **2014**, *4*, 4045.
[137] S. Min, G. Lu, *J. Phys. Chem. C* **2012**, *116*, 25415-25424.

PART I

Functionalization of 2H-MoS_2 with Organic Thiols

CHAPTER 2 Functionalization of Two-Dimensional MoS_2: On the Reaction between MoS_2 and Organic Thiols

This Chapter is based on the following manuscript:

X. Chen, N. C. Berner, C. Backes, G. S. Duesberg, A. R. McDonald*, *Angew. Chem. Int. Ed.* **2016**, *55*, 5803.

Author contributions: X. Chen performed the liquid exfoliation, functionalization, and characterization of TMD nanosheets and was responsible for the data analysis. N. C. Berner performed the XPS measurements. C. Backes provided training on Raman Spectroscopy. X. Chen and A. R. McDonald* prepared the manuscript.

2.1. Introduction

In the rich family of two-dimensional (2D) layered nanomaterials, layered transition metal dichalcogenides (TMDs) have sparked increasing interest due to their unique structures, wide range of chemical compositions, and a vast array of unique physical properties.[1-11] TMDs have potential applications in electronic devices, optoelectronics, sensing, energy storage and catalysis. A major focus of experimental research in recent years has concentrated on the development of synthetic routes to produce high-quality TMD nanosheets.[12-17] However, as of yet, routes towards the efficient high-yield synthesis or exfoliation of TMDs are lacking, hindering the production of large quantities of TMD nanosheets. Functionalization of such layered materials could facilitate the production of higher quantities of 2D TMDs, while also allowing for the tuning of their physical properties.

Molybdenum disulfide (MoS_2) is a prototypical TMD and acts as an excellent model system to explore the chemistry of 2D TMDs. 2D MoS_2 is most often isolated as one of two polymorphs:[15] semiconducting 2H-MoS_2 and metallic 1T-MoS_2. The covalent functionalization of 1T-MoS_2 has recently been reported [18, 19] employing an extremely harsh chemical exfoliation (ce) procedure. No well-characterized examples of covalent functionalization of 2H-MoS_2 have been reported to date. Our group recently reported the mild functionalization of 2H-MoS_2 through ligation of surface S-atoms to coordination complexes,[20] the efforts here are now focused on exploring routes towards the covalent functionalization of 2H-MoS_2.

Recent reports have shown the functionalization of both ce-1T- and 2H-MoS_2 by reaction with organic thiols. In a seminal paper, Dravid and co-workers described the reaction between ce-1T-MoS_2 and organic thiols yielding functionalized ce-1T-MoS_2.[21] This was described as 'ligand conjugation' to ce-1T-MoS_2 presumably meaning coordination of the thiol to Mo-atoms at S-vacancies (a dative Mo–S bond formed). Later work has demonstrated further applications of this technique.[22-30] Unfortunately, in all of these reports, there remains little to no insight into the thiol ligand/MoS_2 interaction. At the inception of this work, we too postulated that 2H-MoS_2 could be functionalized using organic thiols by coordination of the thiol group to Mo-atoms at S-atom vacancies (Fig. 2.1). Herein, the one-step surface functionalization of 2H-MoS_2 nanosheets with an organic thiol (cysteine) is demonstrated, resulting in functionalized 2H-MoS_2. The thiol/MoS_2 interaction were explored in detail, revealing that organic thiols may actually be physisorbed on MoS_2 as disulfides, rather than undergoing any bond-forming process with the MoS_2.

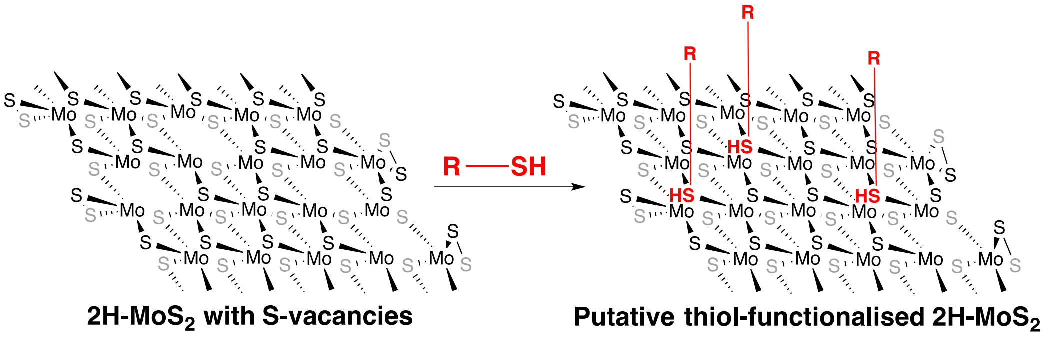

Figure 2.1 Postulated method to functionalize 2D 2H-MoS_2 at sulfur vacancies.

2.2 Results and discussion

2.2.1 Functionalization and characterization

As we reported previously,[20] in the functionalization of 2H-MoS_2 it was necessary to disperse few-layer thick 2H-MoS_2 in 2-propanol (IPA), and not the standard (toxic) dispersion/exfoliating solvents N-Methyl-2-pyrrolidone (NMP) or N-cyclohexyl-2- pyrrolidone (CHP).[3, 12] The IPA dispersions of 2H-MoS_2 displayed mean lateral dimension <L> of ~260 nm and degree of exfoliation <N> of 9-10 layers. The IPA-exfoliated 2H-MoS_2 was thus an ideal 2D TMD for functionalization studies.

2H-MoS_2 normally displays S: Mo ratios of approximately 1.8:1 (± 0.2) as suggested by X-ray photoelectron spectroscopy (XPS).[20, 31] Transmission electron microscopy (TEM) analysis corroborates this, showing that basal-plane S-vacancies are common.[27, 32, 33] We postulated that thiol-containing organic molecules could fill these sulfur vacancies (Fig. 2.1). To test this postulate we reacted liquid exfoliated 2H-MoS_2 with a thiol-containing organic molecule, cysteine. Cysteine was chosen because it is bio-relevant, commercially available, and contains functional groups (carboxylate and amine) that would allow for simple characterization and also further derivatization. 2H-MoS_2 nanosheets (0.5 g/L) dispersed in IPA (20 mL) were reacted with the hydrochloride salt of L-cysteine dissolved in IPA (20 g/L, 10 mL) by combining the dispersion and solution and performing tip ultra-sonication on the mixture for 0.5 h at room temperature (see Experimental section for full experimental details). Following the ultra-sonication, the resulting dispersion was subjected to high-speed centrifugation to precipitate all dispersed materials. The resulting sediment was subsequently exhaustively washed with aqueous solutions, and then re-dispersed in IPA (10 mL) for further characterization.

The cysteine-functionalized re-dispersed 2H-MoS_2 (Cys-2H-MoS_2) displayed a markedly different dispersibility in IPA compared to pristine 2H-MoS_2. The electronic extinction spectrum of Cys-2H-MoS_2 displayed very high degrees of nanosheet aggregation as evidenced by the rather large baseline shift when comparing pristine 2H-MoS_2 to Cys-2H-MoS_2 (Fig. 2.2 (a)).[34] This difference was noticeable to the human eye - Cys-2H-MoS_2 flocculated (formed clumpy materials) readily in IPA, whereas dispersions of pristine 2H-MoS_2 did not. Furthermore, Cys-2H-MoS_2 yielded dispersions that were black in color, whereas pristine 2H-MoS_2 dispersions tended to be yellowish-greenish (Fig. 2.2(b)). These observations are a clear indication that the surface properties in the Cys-2H-MoS_2 had been altered dramatically compared to pristine 2H-MoS_2.

Importantly, functionalization appeared to have caused minimal changes to the relative intensities or energies of excitonic transitions attributed to exfoliated

2H-MoS_2 (Fig. 2.2(a)). The transitions at λ_{max} = 459, 614 and 675 nm are typical of 2H-MoS_2. Cys-2H-MoS_2 displayed a similar set of features (λ_{max} = 496, 629 and 689 nm), displaying a small degree of red-shifting compared to the parent pristine 2H-MoS_2, which we postulate is as a result of the rather large baseline shift caused by flocculation. These observations are very important, because they establish that functionalization yielded a slightly modified 2H-MoS_2 and, critically, did not yield the 1T-polytype (1T-MoS_2 has an extinction spectrum very distinct from 2H-MoS_2).[35] Most other covalent functionalization techniques to date have yielded 1T-MoS_2.

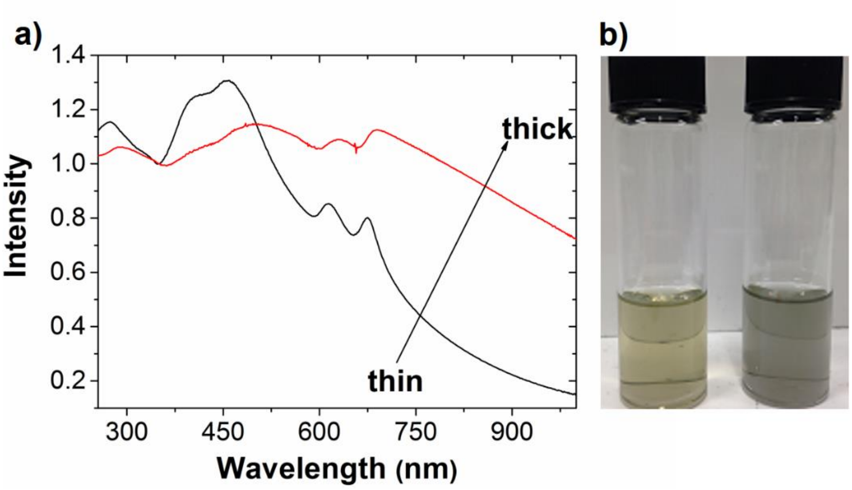

Figure 2.2 a) UV-Vis extinction spectra of 2H-MoS_2 (black trace) and Cys-2H-MoS_2 (red trace) in IPA normalized to the local minimum at ~350 nm. b) Color photograph of diluted dispersions of 2H-MoS_2 (left) and Cys-2H-MoS_2 (right) in IPA.

Comparison of the diffuse reflectance infrared Fourier transform (DRIFT) spectra of 2H-MoS_2 and Cys-2H-MoS_2 demonstrated a sharp feature at 384 cm^{-1} that is typical of 2H-MoS_2 (Fig. 2.3),[36] indicating that the functionalization had not affected the vibrational properties or overall morphology in the Cys-2H-MoS_2. Importantly, the DRIFT spectrum for Cys-2H-MoS_2 showed a number of new features that we attributed to the introduction of a cysteine derivative to the surface of the nanomaterial. A comparison of the DRIFT spectra of cysteine with Cys-2H-MoS_2 showed that the vibrational properties of the cysteine on the 2H-MoS_2 surface have been altered considerably through reaction with 2H-MoS_2. Firstly, in cysteine a feature at 2532 cm^{-1} attributed to the $\nu_{(S-H)}$ was observed.[37] This feature was absent in Cys-2H-MoS_2, and there were no new features in this region of the DRIFT spectrum. This would suggest that the thiol group of cysteine has reacted in the presence of 2H-MoS_2. All previous reports on the reaction between organic thiols and MoS_2 showed a similar loss of the $\nu_{(S-H)}$ by infra-red spectroscopy, leading to the conclusion that the thiol had reacted with the MoS_2.[22-30] Secondly, cysteine displayed broad features at 1745 cm^{-1} and 1377 cm^{-1} corresponding to stretches of its carboxylate group.[37] In Cys-2H-MoS_2 these features had shifted to lower energy (1644 and 1354 cm^{-1} respectively), presumably, again, as a result of a reaction between cysteine and 2H-MoS_2. In all, the DRIFT spectrum of Cys-2H-MoS_2 indicates that cysteine is coupled to the surface of the 2H-MoS_2. However, the clear and dramatic changes to the vibrational properties of the cysteine suggest that the cysteine had been chemically altered.

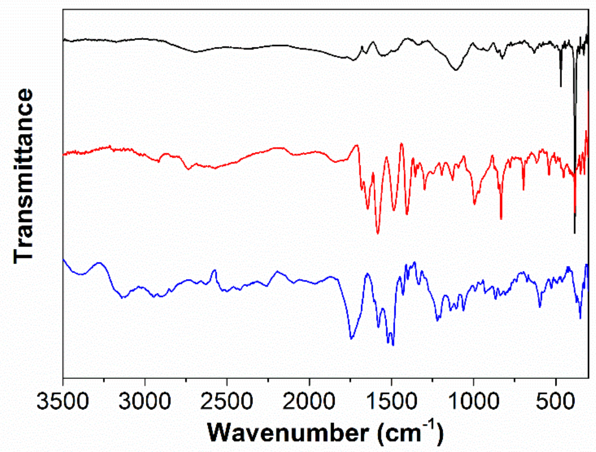

Figure 2.3 DRIFT spectra of pristine 2H-MoS_2 (black trace), cysteine (blue trace) and Cys-2H-MoS_2 (red trace).

Raman spectroscopy also indicated that the reaction between cysteine and 2H-MoS_2 yielded a slightly altered 2H-MoS_2 surface. Minor changes to the relative intensities of resonantly enhanced features in the Raman spectrum (Fig. 2.4 and Appendix Fig. S2.1) of Cys-2H-MoS_2 indicate organic functionalities were interacting with the 2H-MoS_2 surface.[31, 33, 38, 39]

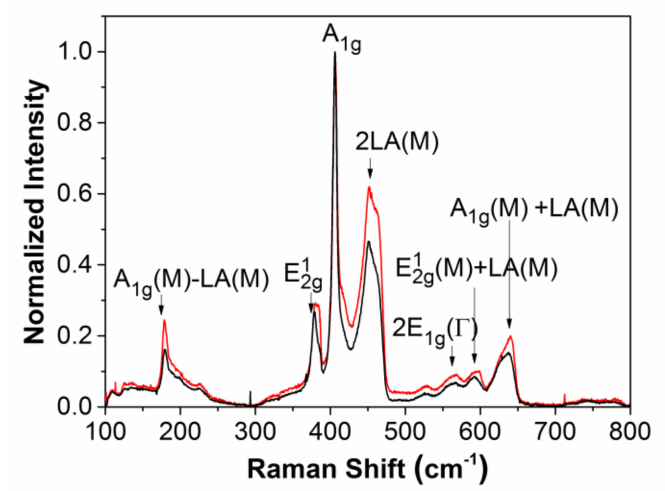

Figure 2.4 Raman spectra of pristine 2H-MoS_2 (black trace) and Cys-2H-MoS_2 (red trace) at room temperature after excitation with 633 nm laser. A mean of 121 spectra is displayed and the Raman modes were assigned according to previous work.[40]

To examine the atomic-level 2H-MoS_2/cysteine interaction in Cys-2H-MoS_2, high-resolution X-ray photoelectron spectroscopy (XPS) analysis was performed. Firstly, we observed that the Cys-2H-MoS_2 nanosheets preserved the semiconducting 2H polymorph after functionalization, and are not the 1T polymorph[1].[18, 21, 41] The XPS spectrum of cysteine (Fig. 2.5 (b)) exhibited a single doublet of S 2p peaks with the S $2p_{3/2}$ binding energy at 163.5 eV. In contrast, peak fitting of the S 2p spectrum of Cys-2H-MoS_2 results in two doublets. The first

---

[1] If it were 1T-MoS_2, features at 228.6 and 231.7 ± 0.15 eV would be expected, supporting our UV-Vis observations.

doublet with S $2p_{3/2}$ binding energy at 161.8 eV made the largest contribution (68%) and was comparable to the S $2p_{3/2}$ peak of the pristine 2H-MoS_2. The other smaller doublet with S $2p_{3/2}$ binding energy at 163.3 eV can be attributed to the surface cysteine entities. A minor shift (0.2 eV) in the binding energy in this doublet relative to pure cysteine was observed, consistent with a chemical change to the cysteine molecule. The higher binding energy component represented 32% of the S-atoms on the sample surface, indicating a degree of functionalization of 32%. We note that thermo-gravimetric analysis (TGA, Fig. 2.6) also suggests ~30% loading of cysteine in Cys-2H-MoS_2.

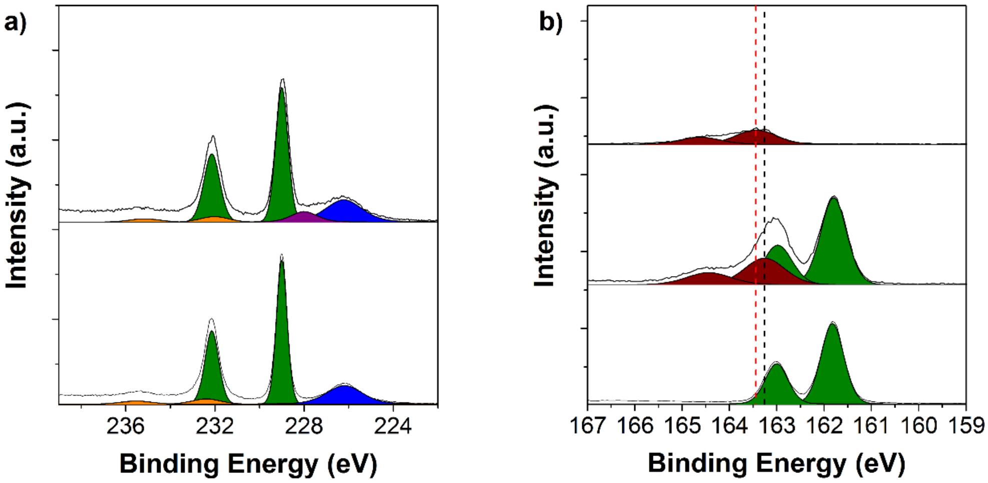

Figure 2.5 Fitted XPS spectra. a) Mo 3d core level spectra of Cys-2H-MoS_2 (top), and pristine 2H-MoS_2 (bottom). Fit components are attributed to 2H-MoS_2 (green), MoO_3 (orange), S 2s (blue) and cysteine-like entities (purple) in both cases. b) S 2p core level spectra of cysteine salt (top), Cys-2H-MoS_2 (middle), and pristine 2H-MoS_2 (bottom). Fit components are attributed to 2H-MoS_2 (green), and cysteine-like entities (red).

Critically, the binding energy of the surface S-atoms in 2H-MoS_2 was not affected by the presence of a functional group on the MoS_2 surface. The S 2p XPS data was best fit with only two S-atom components - a cysteine-like component and a 2H-MoS_2

component. Furthermore, the Mo 3d XPS spectra (Fig.2.5 (a)) displayed no differences between 2H-MoS_2 and Cys-2H-MoS_2, showing that the electronic environment around the Mo-atoms in Cys-2H-MoS_2 had not been altered upon functionalization. Previous reports showed that changes in the S 2p region of the XPS spectra of functionalized ce-1T-MoS_2 were indicative of the presence of functionality C- to MoS_2 S-bonds on the ce-1T-MoS_2 surface.[18, 21] These observations suggest that chemical modification of the 2H-MoS_2 surface in Cys-2H-MoS_2 was unlikely to have occurred, while a chemical modification of cysteine had occurred.

TGA of Cys-2H-MoS_2 revealed a clear stepwise degradation (Fig. 2.6). Pristine 2H-MoS_2 did not display any degradation below 500 °C. In Cys-2H-MoS_2, an approximately 30% weight loss took place between 215-265 °C. The thermal decomposition temperature of cysteine is from 200-230 °C (Fig. 2.6), we inferred that the significant weight loss was caused by the decomposition of cysteine-like molecules bound to the 2H-MoS_2 surface. According to TGA-coupled infra-red (TGA-IR) spectroscopy, the major gaseous product evolved from Cys-2H-MoS_2 was identified as CO_2 (Fig. 2.6, right, 2349 cm^{-1}) which presumably derives from the decomposition of cysteine. The TGA thus indicates that an organic functionality, very similar to cysteine, is tethered to 2H-MoS_2 in Cys-2H-MoS_2.

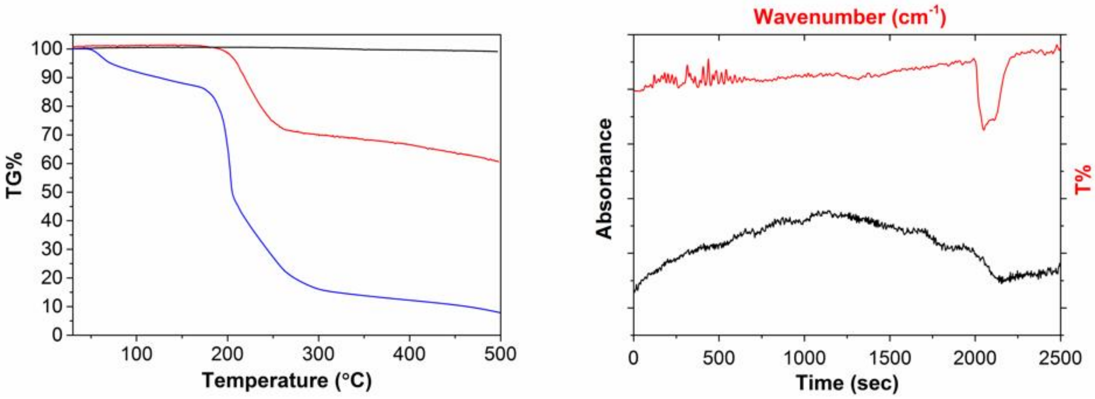

Figure 2.6 Left: TGA of cysteine (blue trace), pristine 2H-MoS_2 (black trace), and

Cys-2H-MoS_2 (red trace). Right: TGA-IR spectra obtained at the maximum evolution rate during the thermal degradation process of Cys-2H-MoS_2. The black trace is the gas evolution profile of Cys-2H-MoS_2 during the heating process. The red trace is the FT-IR spectrum of the gaseous product from Cys-2H-MoS_2 decomposition, at the maximum gas evolution rate of Cys-2H-MoS_2 decomposition.

Having thoroughly characterized Cys-2H-MoS_2 we then probed the effect of the cysteine functionalities on the dispersibility of the 2H-MoS_2. We found that Cys-2H-MoS_2 was readily re-dispersed in water (Fig. 2.7, left). Pristine 2H-MoS_2 did not disperse in water (Fig. 2.7), and few methods to effectively disperse 2H-MoS_2 in water by functionalization exist.[25, 42] Importantly, the aqueous Cys-2H-MoS_2 dispersions were stable for at least one week. Furthermore, we could vary the pH of the aqueous dispersions, with no effect on the dispersibility of the 2H-MoS_2 (Fig. 2.7, right). We previously identified methods to enhance TMD dispersibility in acetone,[20] but the present water dispersion results are very important, potentially eliminating the use of organic solvents altogether.

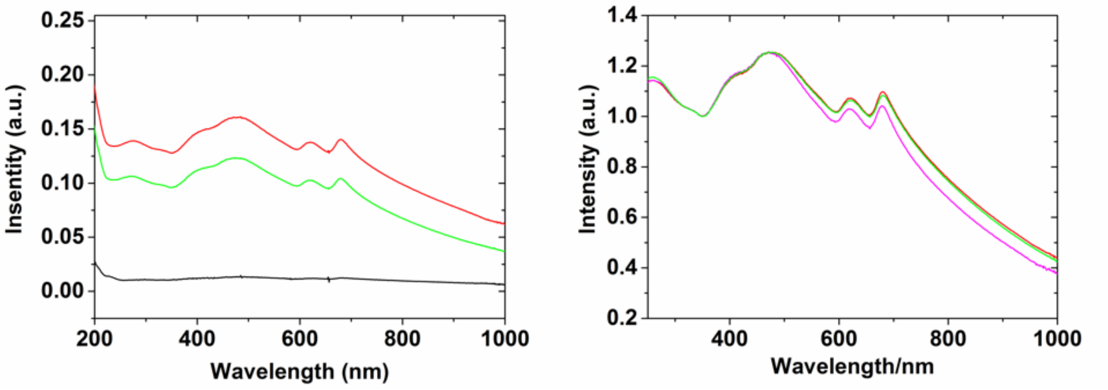

Figure 2.7 Left: Extinction spectra of re-dispersed pristine 2H-MoS_2 (black trace) and Cys-2H-MoS_2 (red trace: immediately after functionalization, and green trace: after one week) in DI water. Right: normalized extinction spectra of redispersed Cys-2H-MoS_2 at different pH values (pH = 6, red; pH = 1, green; pH = 12, magenta).

A number of experiments have been performed to verify further the nature of the interaction between 2H-MoS_2 and cysteine. As earlier stated, XPS indicated that no change to the MoS_2 S- or Mo-atoms in Cys-2H-MoS_2 had occurred, with a very minor change to the surface cysteine. These observations indicate that the functionalization in Cys-2H-MoS_2 was not covalent and also suggested that cysteine S-atoms were not filling S-atom vacancies. However, the surface properties of the 2H-MoS_2 in Cys-2H-MoS_2 had clearly been altered as evidenced by UV-Vis spectroscopy and re-dispersion measurements. XPS, TGA, and Raman analyses confirmed the presence of surface functionalities in Cys-2H-MoS_2, however, these analyses provided no evidence for covalent or dative bonding formation between the 2H-MoS_2 and functionality. Finally, the DRIFT measurements suggested a chemical change to the cysteine molecules on the surface, while the 2H-MoS_2 remained in a pristine state.

2.2.2 Identification the chemical nature of surface functional groups

In order to probe the surface functional groups further, the functional groups were removed from the surface via de-functionalization. De-functionalization was achieved by firstly dispersing the Cys-2H-MoS_2 in IPA and subsequently centrifuging this dispersion and decanting the IPA (repeated numerous times). Secondly, after the multiple washings, the resultant solids were re-dispersed in water, placed in a dialysis bag, and dialyzed for four days. After dialysis, the solvent was removed from the resulting dialysate under vacuum, and the obtained product (de-functionalized organic material) was analyzed by ^{1}H NMR, while the resulting 2H-MoS_2 was subjected to XPS. The ^{1}H NMR spectrum (Appendix, Fig. S2.2) showed the obtained product was not cysteine, but in fact was the oxidized (disulfide) derivative of cysteine, cystine. The identification of the disulfide product accounts for the disappearance of the $\nu_{(S-H)}$ resonance in the DRIFT spectrum of

Cys-2H-MoS_2. XPS analysis of the post-dialysis 2H-MoS_2 showed that the de-functionalized nanomaterial was pristine 2H-MoS_2 (Fig. 2.8, no organic S-features, confirming complete de-functionalization). As postulated, these observations confirm that the reaction between the organic thiol and 2H-MoS_2 caused the thiol to be converted to a new entity, but the 2H-MoS_2 was chemically unchanged.

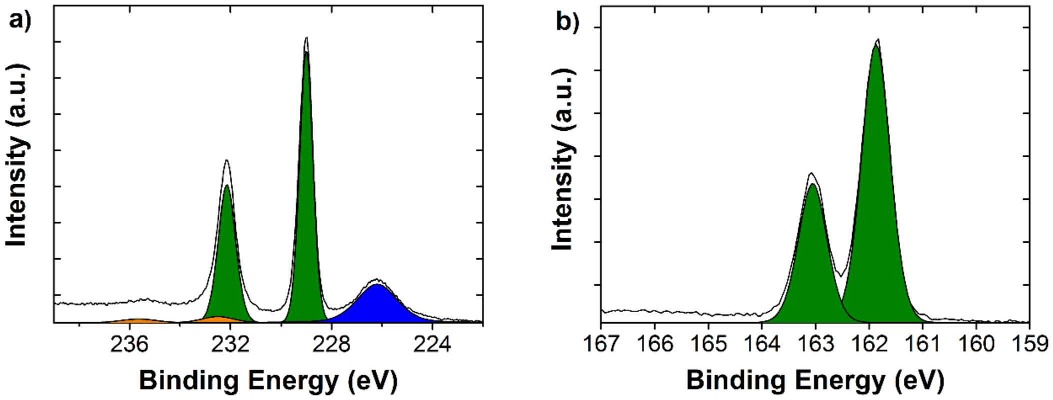

Figure 2.8 Fitted XPS spectra. a) Mo 3d core level spectra of Cys-2H-MoS_2 after exhaustive dialysis. Fit components are attributed to 2H-MoS_2 (green), MoO_3 (orange), and S 2s (blue). b) S 2p core level spectra of Cys-2H-MoS_2 after exhaustive dialysis. Fit components are attributed to 2H-MoS_2 (green).

Further comparison the DRIFT spectrum of Cys-2H-MoS_2 with the DRIFT spectrum of cystine (Fig. 2.9) revealed an almost perfect overlap of resonances (of particular note is the S–S vibrational mode ($\nu_{(S-S)}$ = 540 cm^{-1})[43] demonstrating that in fact cystine (and not cysteine) was docked on the surface in Cys-2H-MoS_2. The lack of a chemical change to the 2H-MoS_2 in Cys-2H-MoS_2 *and* ease at which the cystine was de-functionalized from the surface, would suggest that cystine was simply physisorbed to the 2H-MoS_2 surface.

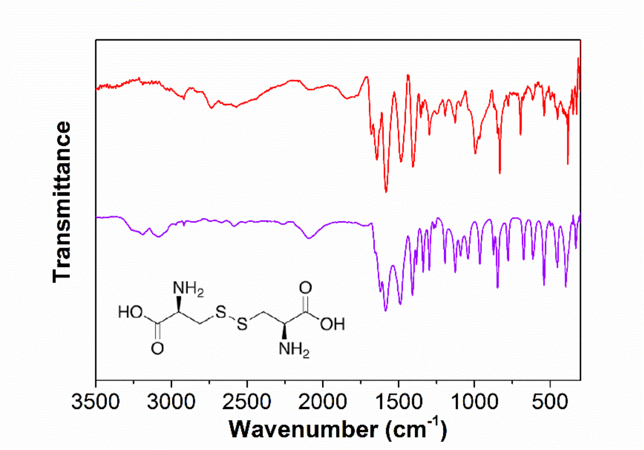

Figure 2.9 DRIFT spectra of Cys-2H-MoS_2 (red trace) and cystine (purple trace).

2.2.3 Control experiments

It was intriguing that the 2H-MoS_2 facilitated oxidation of cysteine to cystine yielding 'functionalization through physisorption of cystine. Earlier work demonstrated the functionalization of ce-1T-MoS_2 through 'ligand conjugation'.[21] The reaction of cysteine with ce-1T-MoS_2 (following the 'ligand conjugation' methods) were also explored (see details in Experimental section) and obtained DRIFT spectra that showed cystine was tethered to the surface of ce-1T-MoS_2 (Fig. 2.10), rather than cysteine. Thus in both 2H- and 1T-polymorphs of MoS_2, their reaction with cysteine yields cystine-functionalized MoS_2.

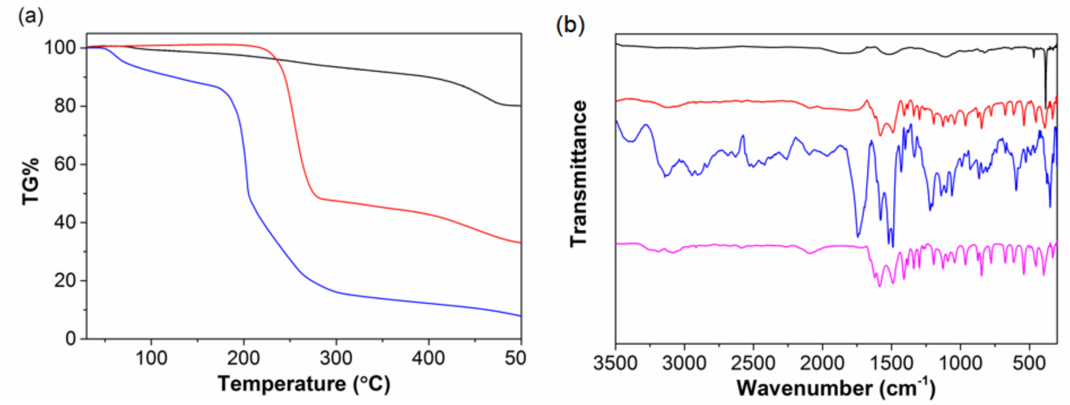

Figure 2.10 (a) TGA profile of ce-1T-MoS_2 (black trace), and Cys-1T-MoS_2 (red

trace), cysteine (blue trace). (b) DRIFT spectra of ce-1T-MoS_2 (black trace), and Cys-1T-MoS_2 (red trace), cysteine (blue trace), and cystine (magenta trace). Spectra are offset for clarity.

In addition, a control experiment was carried out by reacting of cysteine with 2H-MoS_2 under an inert atmosphere (N_2, thus in the absence of air (an oxidant)). Under these inert conditions, the same Cys-2H-MoS_2 were obtained, containing the disulfide product cystine, as evidenced by DRIFT spectroscopy (Fig. 2.11). This demonstrated that dioxygen was not facilitating the oxidation of cysteine to cystine, and that MoS_2 is likely the mediator of this transformation.

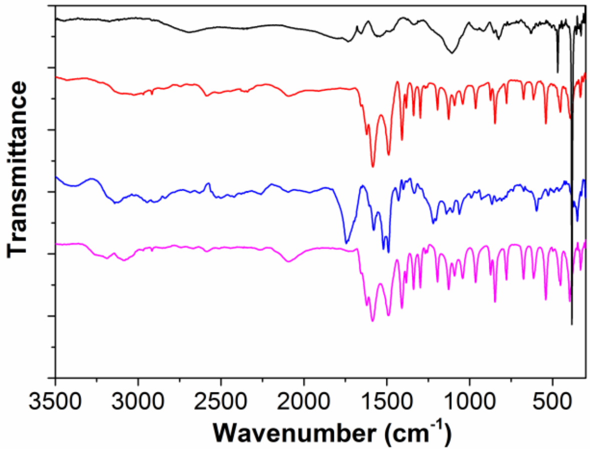

Figure 2.11 DRIFT spectra of pristine 2H-MoS_2 (black trace), and Cys-2H-MoS_2 (red trace) prepared under an inert atmosphere, cysteine (blue trace), and cystine (magenta trace). Spectra are offset for clarity.

In order to explore if oxidation was caused by the functionalization methods, a solution of cysteine was sonicated itself in IPA in the absence of MoS_2 (thus under the functionalization conditions). The ^{1}H-NMR spectrum (Appendix, Fig. S2.3) of the solids resulting from this experiment showed resonances typical of cysteine, and not cystine, verifying that the functionalization methods do not lead to the oxidation of cysteine. Finally, the analogous reaction between cysteine and liquid exfoliated 2H-WS_2 yielded similar results to 2H-MoS_2 (thus Cys-2H-WS_2, with cystine functionalities, Fig. 2.12).

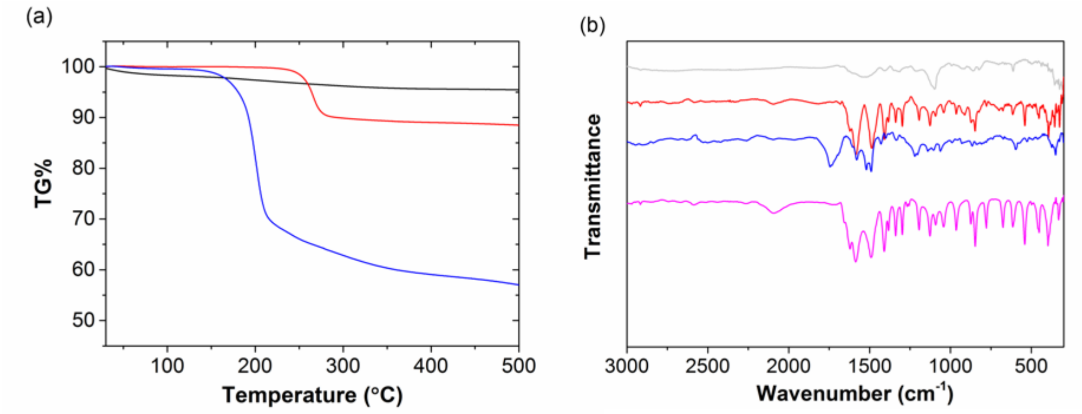

Figure 2.12 (a) TGA of cysteine (blue trace), pristine WS_2 (black trace), and Cys-WS_2 (red trace). (b) DRIFT spectra of pristine 2H-WS_2 (grey trace), Cys-2H-WS_2 (red trace), cysteine (blue trace), and cystine (magenta trace). Spectra are offset for clarity.

The functionalization of liquid exfoliated 2H-MoS_2 with another commercially available thiol (1-octanethiol) were also investigated and identified oxidized disulfide products. The DRIFT spectrum of the 1-octanethiol/2H-MoS_2 product showed a characteristic S–S vibrational peak at $\nu_{(S-S)}$ = 540 cm^{-1} (Fig. 2.13) suggesting the formation of the disulfide $H_{17}C_8$–S–S–C_8H_{17}. Furthermore, the observation of $\nu_{(C-S)}$ = 615 cm^{-1}, as observed previously for dioctyl-disulfide functionalized nanoparticles,[44] provided a very strong indication of disulfide formation when 1-octanethiol reacted with 2H-MoS_2. Furthermore, GC-MS analysis of the 2H- MoS_2/1-octanethiol reaction mixture showed the presence of the disulfide product ($C_{16}H_{34}S_2$, Appendix, Fig. S2.4).

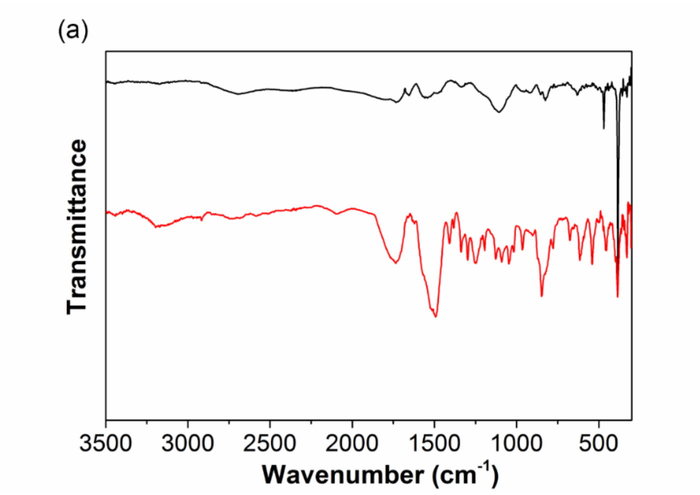

Figure 2.13 DRIFT spectra of pristine 2H-MoS_2 (black trace) and 1-octanethiol functionalized 2H-MoS_2 (red trace). A $\nu_{(S\text{-}C)}$ gauche band was observed as a strong peak at 615 cm^{-1}, indicating that the 1-octanethiol on the surface was a gauche conformation which was in agreement with a dioctyl disulfide structure, suggesting 1-octanethiol was oxidized to disulfide during functionalization.[44]

2.2.4 Postulation of reaction mechanism

It thus appears that TMDs facilitate the oxidation of organic thiols to disulfides (Fig. 2.14). The formed disulfides appear to have physisorbed on the 2D TMD surface presumably through electrostatic interactions. The further investigations on MoS2 mediated thiol oxidation will be demonstrated in Chapter 3.

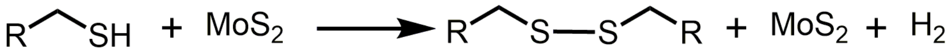

Figure 2.14 MoS_2-mediated conversion of organic thiol to disulfide.

2.3 Conclusion

In conclusion, a general route for the functionalization of 2H-MoS_2 nanosheets with cysteine was demonstrated. Functionalization was achieved by blending a dispersion of liquid exfoliated 2H-MoS_2 with a solution of cysteine. The resulting Cys-2H-MoS_2 was fully characterized by UV-Vis, DRIFT, XPS, TGA, and Raman. We discovered that MoS_2 was facilitating the oxidation of cysteine to cystine during functionalization. Rather than coordinating as a thiol (cysteine) at S-vacancies in the 2H-MoS_2, as originally conceived, cystine was simply physisorbed on the nanosheet. These observations were found to be true for other organic thiols and indeed other TMDs. Based on our findings, we urge caution with methods that employ organic thiols to chemically functionalize TMDs - the thiols may not be forming bonds with the surface. Present explorations in our lab are focused on alternative methods for the covalent functionalization of 2H-MoS_2.

2.4 Experimental section

2.4.1 Materials

2H-MoS_2 powder (6μm particle size), L-cysteine hydrochloride (anhydrous), L-cystine (anhydrous), 1-octanethiol (98.5% purity), isopropanol (IPA, 99.7 % purity) were purchased from Sigma Aldrich. All chemicals were used as received without further purification.

2.4.2 Sample preparation

2H-MoS_2 nanosheets were produced by liquid exfoliation. Firstly, bulk 2H-MoS_2 powder (20 g/L in IPA) was sonicated in 100 mL IPA under ice-cooling for 1 h with a flathead sonic tip (Sonics VX-750, 60% amplitude, 6 s pulse on, 2 s pulse off). The cloudy dispersion (6×15 mL) was then subjected to centrifugation at 5000 rpm for 1 h (2739 *g*, Thermo Scientific Heraeus Megafuge 16 benchtop centrifuge equipped with a Fiberlite fixed angle rotor F15-6×100). The blue supernatant containing impurities in the starting powder was discarded and the grey sediment was collected for subsequent sonication (Sonics VX-750, flathead sonic tip, 60 % amplitude, 6 s pulse on, 2 s pulse off). After 4 h consecutive ultra-sonication under ice-cooling, the resultant dispersion was centrifuged at 1500 rpm (247 *g*) for 1 h to remove un-exfoliated 2H-MoS_2. The grey sediment (un-exfoliated 2H-MoS_2) was discarded and the green supernatant (exfoliated 2H-MoS_2) was decanted and used for further functionalization. The concentration of 2H-MoS_2/IPA was estimated according to the extinction coefficient of the local minimum at λ = 345 nm: ε = 69 mL mg^{-1} cm^{-1}.[45] The typical concentration of 2H-MoS_2/IPA obtained was approximately 0.5 g/L (3.1 mM).

Cys-2H-MoS_2 nanosheets were prepared by blending the exfoliated 2H-MoS_2 dispersion (3.1 mM) and an L-cysteine/IPA solution (0.13 M) followed by ultra-sonication. 200 mg of L-cysteine hydrochloride salt was initially dissolved in 10 mL IPA and treated by mild sonication in a sonic bath (Branson Ultrasonic Cleaner B1510MT, 40 kHz) for 5 min. It was then added to the 20 mL exfoliated 2H-MoS_2 dispersion and subjected to ultra-sonication with a tapered micro tip under ice cooling for 0.5 h (Sonics VX-750, 40 % amplitude, 4 s pulse on, 4 s pulse off). Following the ultra-sonication, the resultant dispersion was subjected to high-speed centrifugation at 11000 rpm (13257 *g*) for 1 h to precipitate all the nanomaterial. After that, the sediment was re-dispersed in IPA/H_2O (1:1 v/v) and centrifuged at 11000 rpm (13257 *g*) for 1 h (2 times) to remove all free, unbound molecules. The supernatant was decanted and the sediment was collected with 10 mL IPA. The concentration of functionalized sample was determined by filtering a 2 mL dispersion of Cys-2H-MoS_2 on the Whatman® Anodisc inorganic filter membrane (pore size 0.02 μm, diameter 47 mm) and weighing it after drying in air overnight. The typical concentration of functionalized sample was about 2.68 g/L. After evaporating the solvent from the 2H-MoS_2/IPA and the Cys-2H-MoS_2/IPA dispersions, using mild heating (50-60 °C), dried powders were collected for DRIFT and TGA measurements.

2.4.3 Control experiments

Functionalization of chemically exfoliated MoS_2 (ce-1T-MoS_2) with Cysteine

Chemically exfoliated MoS_2 was synthesized by lithium intercalation and exfoliation according to a literature procedure.[46] 350 mg bulk MoS_2 powder was dispersed in 3.5 mL of 2.5 M n-BuLi/hexane and stirred for 2 days under nitrogen. The resulting intercalated Li_xMoS_2 was collected by filtration and washed with 60 mL anhydrous hexane to remove excess organic residues. Subsequently, exfoliation was accomplished by sonicating the semi-dry Li_xMoS_2 in deionized water (100 mL) in a sonic bath (Branson Ultrasonic Cleaner B1510MT, 40 kHz) for 1 h. The resulting aqueous dispersion was centrifuged at 700 rpm (54 *g,* Thermo Scientific Heraeus Megafuge 16 benchtop centrifuge equipped with a Fiberlite fixed angle rotor F15-6×100) for 1 h at 20 °C to remove non-exfoliated MoS_2 as sediment. The supernatant was then collected and was treated with further centrifugations at 11000 rpm (13257 *g*) at 20 °C for 1 h until pH ~ 7 was obtained in order to remove very small flakes of MoS_2 and LiOH, affording 1T-MoS_2 nanosheets dispersed in water. The concentration of ce-1T-MoS_2 was determined by drying 10 mL of the ce-1T-MoS_2 dispersion and weighing the dried powder. The typical concentration of ce-1T-MoS_2 was determined as 1 g/L.

The aqueous dispersion of ce-1T-MoS_2 was mixed with the solution of cysteine in IPA in a mole ratio of 1/20. The mixture was sonicated by using a tapered point tip (Sonics VX-750, 40% amplitude, 4s pulse on, 4s pulse off) in an ice bath for 30 min. The resultant dispersion was subjected to centrifugation at 11000 rpm (13257 *g*) at

20 °C for 1 h to spin down all the materials. The supernatant after centrifugation was decanted and the sediment was collected and then dispersed in IPA/H_2O (1:1 v/v) and subjected to further high-speed centrifugation (11000 rpm = 13257 *g*). This washing step was repeated 3 times and the resulting product was collected in 10 mL IPA and the solvent was evaporated at 50-60 °C and the dried material was analyzed using TGA and DRIFT.

Functionalization of 2H-MoS_2 with cysteine under an inert atmosphere

200 mg L-cysteine hydrochloride salt was dissolved in 15 mL of pre-degassed IPA followed by mild sonication in a sonic bath for 10 min. At the same time, 15 mL of 0.5 mg/mL 2H-MoS_2/IPA was degassed in a Schlenk tube under vacuum for 15 min. Then the cysteine/IPA solution was transferred to the Schlenk containing 2H-MoS_2/IPA by syringe under Ar protection. After that, the Schlenk that contained the cysteine and 2H-MoS_2 mixture was mildly sonicated in a bath (Branson Ultrasonic Cleaner B1510MT, 40 kHz) for 1h and then stirred overnight under Ar protection. The resultant dispersion was subjected to high-speed centrifugation at 11000 rpm (13257 *g*) for 1h to precipitate all the materials. After that, the sediment was re-dispersed in IPA/H_2O (1:1 v/v) and centrifuged at 11000 rpm (13257 *g*) for 1 h for 2 times to remove all ‘free’ soluble molecules. The supernatant was decanted and the sediment was collected with 10 mL IPA, the solvent was evaporated and the dried material was obtained for DRIFT characterization.

Sonication of cysteine/IPA in the absence of 2H-MoS_2.

A control experiment was carried out by sonication a cysteine/IPA solution in the absence of 2H-MoS_2 in an ice bath under the same sonication condition as the functionalization of 2H-MoS_2 was performed. 150 mg of cysteine hydrochloride salt was dissolved in 30 mL IPA, which was facilitated by sonication in a bath for 10 min

(Branson Ultrasonic Cleaner B1510MT, 40 kHz). Then this cysteine/IPA solution was treated by ultra-sonication by using a tapered point tip Sonics VX-750, 40 % amplitude, 4 s pulse on, 4 s pulse off) in an ice bath for 30 min. The resultant solution was dried with N_2 flow and the white powder was obtained after evaporation of all the solvent.

Functionalization of 2H-MoS_2 with 1-octanethiol

Following the same procedure to synthesize Cys-2H-MoS_2, we also treated liquid exfoliated 2H-MoS_2 with 1-octanethiol.

Functionalization of liquid exfoliated WS_2 nanosheets with L-cysteine

2H-WS_2 nanosheets were produced by liquid exfoliation. Firstly, bulk WS_2 powder (20 g/L in IPA) was sonicated in 100 mL isopropanol in an ice bath under ice-cooling for 1 h with a flathead sonic tip (Sonics VX-750, 60 % amplitude, 6 s pulse on, 2 s pulse off). Then the cloudy dispersion (6 × 15 mL) was subjected to centrifugation at 4000 rpm for 1 h (1753 g, Thermo Scientific Heraeus Megafuge 16 benchtop centrifuge equipped with a Fiberlite fixed angle rotor F15-6×100). The blue supernatant containing impurities in the starting powder was discarded and the grey sediment was collected for subsequent sonication (Sonics VX-750, flathead sonic tip, 60 % amplitude, 6 s pulse on, 2 s pulse off). After 4 h of ultra-sonication under ice-cooling, the resultant dispersion was centrifuged at 800 rpm (70 g) for 1 h to remove un-exfoliated WS_2. The grey sediment (un-exfoliated WS_2) was discarded and the yellow supernatant (exfoliated WS_2) was decanted and used for further functionalization. The concentration of WS_2/IPA was determined by drying 10 mL of WS_2/IPA dispersion and weighing the dried powder. The typical concentration of WS_2/IPA obtained was 0.3 g/L.

The functionalized WS_2 nanosheets were prepared by blending the exfoliated WS_2 dispersion (1.2 mM) and an L-Cysteine/IPA solution (50.7 mM) followed by ultra-sonication. 80 mg L-Cysteine hydrochloride salt that was initially dissolved in 10 mL IPA and treated by mild sonication in sonic bath (Branson Ultrasonic Cleaner B1510MT, 40 kHz) for 5 min. It was then added to the 20 mL exfoliated WS_2 dispersion and subjected to ultra-sonication with a tapered micro tip under ice cooling for 0.5 h (Sonics VX-750, 40 % amplitude, 4 s pulse on, 4 s pulse off). Following the ultra-sonication, the resultant dispersion was subjected to high-speed centrifugation at 11000 rpm (13257 g) for 1 h to precipitate all the nanomaterials. After that, the sediment was re-dispersed in IPA/H_2O (1:1 v/v) and centrifuged at 11000 rpm (13257 g) for 1 h (twice) to remove all free, unbound molecules. The supernatant was decanted and the sediment was collected with 10 mL IPA. After evaporating the solvent from the WS_2/IPA dispersion and functionalized WS_2/IPA dispersion using mild heating (50-60 °C), the dried powder was collected for TGA and DRIFT measurement.

2.4.4 Characterization and Instrumentation

UV-Vis Spectroscopy was measured on a Hewlett-Packard (Agilent) 8453 diode array spectrophotometer in quartz cuvettes. DRIFT spectra were acquired using a Perkin Elmer Frontier spectrometer equipped with a diffuse reflectance unit. Samples were prepared by grinding the MoS_2 samples with CsI (Sigma Aldrich, 99.9 % purity). The CsI baseline was subtracted from the spectra. All the spectra were baseline corrected after acquisition. Raman Spectroscopy was carried out on Horiba Scientific LabRam HR at 1.96 eV (with a 633 nm excitation laser) in air under ambient conditions. 10% of the laser power was used corresponding to ~ 2 mW. The Raman emission was collected by a 100 Å ~ objective (N.A. = 0.8) and dispersed by 600 lines mm^{-1} grating. The mean of 121 spectra from a 100 μm^2 map is displayed. X-ray Photoelectron Spectroscopy was carried out in ultra-high vacuum conditions (< 45×10-10 mbar) and taken using monochromated Al Kα X-rays from an Omicron XM1000 MkII X-ray source and an Omicron EA125 energy analyzer. An Omicron CN10 electron flood gun was used for charge compensation and the binding energy scale was referenced to the carbon 1s core-level at 284.8 eV. Mo 3d and S 2p core-level regions were recorded at an analyzer pass energy of 15 eV and with slit widths of 6 mm (entry) and 3 mm x 10 mm (exit), resulting in an instrumental resolution of 0.49 eV. After subtraction of a Shirley background, the core-level spectra were fitted with Gaussian-Lorentzian line shapes using the software CasaXPS. Relative atomic percentages were calculated from the ratios of the peak areas after normalization using the relative sensitivity factors (R.S.F.) as provided by the CasaXPS software. Samples were prepared by vacuum filtration onto porous cellulose filter membranes (MF-Millipore membrane, mixed cellulose esters, hydrophilic, 0.025 µm, and 47 mm). Thermogravimetric analysis (TGA) was carried out on a Perkin Elmer Pyris Thermogravimetric Analyser with the following programmed time-dependent temperature profile: hold at 30 °C for 2 min; 30 °C -500 °C with 10 °C /min. The experiments were carried out under N_2 gas flow. TGA-IR was carried out on PerkinElmer TG-IR-CCMS Interface TL 8000. ^{1}H-NMR analyses were performed on Agilent 400 NMR two channel instrument with a 5mm one NMR probe. GC/MS was performed using a GCT Premier GC/MS System.

References

[1] H. Zhang, K. P. Loh, C. H. Sow, H. Gu, X. Su, C. Huang, Z. K. Chen, *Langmuir* **2004**, *20*, 6914-6920.

[2] Radisavljevic B., Radenovic A., Brivio J., Giacometti V., Kis A., *Nat. Nanotechnol.* **2011**, *6*, 147-150.

[3] G. Eda, H. Yamaguchi, D. Voiry, T. Fujita, M. Chen, M. Chhowalla, *Nano Lett.* **2011**, *11*, 5111-5116.

[4] Y. Li, H. Wang, L. Xie, Y. Liang, G. Hong, H. Dai, *J. Am. Chem. Soc.* **2011**,

133, 7296-7299.

[5] K.-K. Liu, W. Zhang, Y.-H. Lee, Y.-C. Lin, M.-T. Chang, C.-Y. Su, C.-S. Chang, H. Li, Y. Shi, H. Zhang, C.-S. Lai, L.-J. Li, *Nano Letters* **2012**, *12*, 1538-1544.

[6] T. Cao, G. Wang, W. Han, H. Ye, C. Zhu, J. Shi, Q. Niu, P. Tan, E. Wang, B. Liu, J. Feng, *Nat. Commun.* **2012**, *3*, 887.

[7] K. F. Mak, K. He, J. Shan, T. F. Heinz, *Nat. Nanotechnol.* **2012**, *7*, 494-498.

[8] H. Zeng, J. Dai, W. Yao, D. Xiao, X. Cui, *Nat. Nanotechnol.* **2012**, *7*, 490-493.

[9] H. J. Conley, B. Wang, J. I. Ziegler, R. F. Haglund, S. T. Pantelides, K. I. Bolotin, *Nano Lett.* **2013**, *13*, 3626-3630.

[10] K. Lee, R. Gatensby, N. McEvoy, T. Hallam, G. S. Duesberg, *Ad. Mater.* **2013**, *25*, 6699-6702.

[11] V. Nicolosi, M. Chhowalla, M. G. Kanatzidis, M. S. Strano, J. N. Coleman, *Science* **2013**, *340*, 1420.

[12] J. N. Coleman, M. Lotya, A. O'Neill, S. D. Bergin, P. J. King, U. Khan, K. Young, A. Gaucher, S. De, R. J. Smith, I. V. Shvets, S. K. Arora, G. Stanton, H.-Y. Kim, K. Lee, G. T. Kim, G. S. Duesberg, T. Hallam, J. J. Boland, J. J. Wang, J. F. Donegan, J. C. Grunlan, G. Moriarty, A. Shmeliov, R. J. Nicholls, J. M. Perkins, E. M. Grieveson, K. Theuwissen, D. W. McComb, P. D. Nellist, V. Nicolosi, *Science* **2011**, *331*, 568-571.

[13] H. Li, Z. Yin, Q. He, H. Li, X. Huang, G. Lu, D. W. H. Fam, A. I. Y. Tok, Q. Zhang, H. Zhang, *Small* **2012**, *8*, 63-67.

[14] Y. Zhan, Z. Liu, S. Najmaei, P. M. Ajayan, J. Lou, *Small* **2012**, *8*, 966-971.

[15] M. Chhowalla, H. S. Shin, G. Eda, L.-J. Li, K. P. Loh, H. Zhang, *Nat. Chem.* **2013**, *5*, 263-275.

[16] M. O'Brien, N. McEvoy, T. Hallam, H.-Y. Kim, N. C. Berner, D. Hanlon, K. Lee, J. N. Coleman, G. S. Duesberg, *Sci. Rep.* **2014**, *4*, 7374.

[17] C. Yim, M. O'Brien, N. McEvoy, S. Riazimehr, H. Schäfer-Eberwein, A. Bablich, R. Pawar, G. Iannaccone, C. Downing, G. Fiori, M. C. Lemme, G. S. Duesberg, *Sci. Rep.* **2014**, *4*, 5458.

[18] K. C. Knirsch, N. C. Berner, H. C. Nerl, C. S. Cucinotta, Z. Gholamvand, N. McEvoy, Z. Wang, I. Abramovic, P. Vecera, M. Halik, S. Sanvito, G. S. Duesberg, V. Nicolosi, F. Hauke, A. Hirsch, J. N. Coleman, C. Backes, *ACS Nano* **2015**, *9*, 6018-6030.

[19] D. Voiry, A. Goswami, R. Kappera, C. d. C. C. e. Silva, D. Kaplan, T. Fujita, M. Chen, T. Asefa, M. Chhowalla, *Nat. Chem.* **2015**, *7*, 45-49.

[20] C. Backes, N. C. Berner, X. Chen, P. Lafargue, P. LaPlace, M. Freeley, G. S. Duesberg, J. N. Coleman, A. R. McDonald, *Angew. Chem. Int. Ed.* **2015**, 54, 2638.

[21] S. S. Chou, M. De, J. Kim, S. Byun, C. Dykstra, J. Yu, J. Huang, V. P. Dravid, *J. Am. Chem. Soc.* **2013**, *135*, 4584–4587.

[22] M. Makarova, Y. Okawa, M. Aono, *J. Phys. Chem. C* **2012**, *116*, 22411-22416.

[23] S.-D. Jiang, G. Tang, Z.-M. Bai, Y.-Y. Wang, Y. Hu, L. Song, *RSC Adv.* **2014**, *4*, 3253-3262.

[24] L. Zhou, B. He, Y. Yang, Y. He, *RSC Adv.* **2014**, 4, 32570.

[25] R. Anbazhagan, H.-J. Wang, H.-C. Tsai, R.-J. Jeng, *RSC Adv.* **2014**, *4*, 42936-42941.

[26] J.-S. Kim, H.-W. Yoo, H. O. Choi, H.-T. Jung, *Nano Lett.* **2014**, *14*, 5941-5947.

[27] Z. Yu, Y. Pan, Y. Shen, Z. Wang, Z.-Y. Ong, T. Xu, R. Xin, L. Pan, B. Wang, L. Sun, J. Wang, G. Zhang, Y. W. Zhang, Y. Shi, X. Wang, *Nat. Commun.* **2014**, *5*.

[28] T. Liu, S. Shi, C. Liang, S. Shen, L. Cheng, C. Wang, X. Song, S. Goel, T. E. Barnhart, W. Cai, Z. Liu, *ACS Nano* **2015**, *9*, 950-960.

[29] E. P. Nguyen, B. J. Carey, J. Z. Ou, J. van Embden, E. D. Gaspera, A. F. Chrimes, M. J. S. Spencer, S. Zhuiykov, K. Kalantar-zadeh, T. Daeneke, *Adv. Mater. (Weinheim, Ger.)* **2015**, Ahead of Print.

[30] K. Cho, M. Min, T.-Y. Kim, H. Jeong, J. Pak, J.-K. Kim, J. Jang, S. J. Yun, Y. H. Lee, W.-K. Hong, T. Lee, *ACS Nano* **2015**, *9*, 8044-8053.

[31] M. Donarelli, F. Bisti, F. Perrozzi, L. Ottaviano, *Chem. Phys. Lett.* **2013**, *588*, 198-202.

[32] H. Qiu, T. Xu, Z. Wang, W. Ren, H. Nan, Z. Ni, Q. Chen, S. Yuan, F. Miao, F. Song, G. Long, Y. Shi, L. Sun, J. Wang, X. Wang, *Nat. Commun.* **2013**, *4*.

[33] H.-P. Komsa, S. Kurasch, O. Lehtinen, U. Kaiser, A. V. Krasheninnikov, *Phys. Rev. B* **2013**, *88*, 035301.

[34] C. Backes, R. J. Smith, N. McEvoy, N. C. Berner, D. McCloskey, H. C. Nerl, A. O'Neill, P. J. King, T. Higgins, D. Hanlon, N. Scheuschner, J. Maultzsch, L. Houben, G. S. Duesberg, J. F. Donegan, V. Nicolosi, J. N. Coleman, *Nat. Commun.* **2014**, *5, 4576*.

[35] A. Splendiani, L. Sun, Y. Zhang, T. Li, J. Kim, C.-Y. Chim, G. Galli, F. Wang, *Nano Lett.* **2010**, *10*, 1271-1275.

[36] G. Berhault, L. Cota Araiza, A. Duarte Moller, A. Mehta, R. Chianelli, *Catal. Lett.* **2002**, *78*, 81-90.

[37] A. Pawlukojć, J. Leciejewicz, A. J. Ramirez-Cuesta, J. Nowicka-Scheibe, *Spectrochimica Acta Part A: Mol. Biomol. Spectrosc.* **2005**, *61*, 2474-2481.

[38] X. Zhang, X.-F. Qiao, W. Shi, J.-B. Wu, D.-S. Jiang, P.-H. Tan, *Chem. Soc. Rev.* **2015**, *44*, 2757-2785.

[39] M. A. Pimenta, E. del Corro, B. R. Carvalho, C. Fantini, L. M. Malard, *Acc. Chem. Res.* **2015**, *48*, 41-47.

[40] K. Gołasa, M. Grzeszczyk, R. Bożek, P. Leszczyński, A. Wysmołek, M. Potemski, A. Babiński, *Solid State Commun.* **2014**, *197*, 53-56.

[41] If it were 1T-MoS2, features at 228.6 and 231.7 ±0.15 eV would be expected,

supporting our UV-vis observations.

[42] W. Zhang, Y. Wang, D. Zhang, S. Yu, W. Zhu, J. Wang, F. Zheng, S. Wang, J. Wang, *Nanoscale* **2015**, *7*, 10210-10217.

[43] E. J. Bastian, R. B. Martin, *J. Phys. Chem.* **1973**, *77*, 1129-1133.

[44] B. S. Zelakiewicz, G. C. Lica, M. L. Deacon, Tong, *J. Am. Chem. Soc.* **2004**, *126*, 10053-10058.

[45] C. Backes, R. J. Smith, N. McEvoy, N. C. Berner, D. McCloskey, H. C. Nerl, A. O'Neill, P. J. King, T. Higgins, D. Hanlon, N. Scheuschner, J. Maultzsch, L. Houben, G. S. Duesberg, J. F. Donegan, V. Nicolosi, J. N. Coleman, *Nat. Commun.* **2014**, *5*.

[46] S. S. Chou, B. Kaehr, J. Kim, B. M. Foley, M. De, P. E. Hopkins, J. Huang, C. J. Brinker, V. P. Dravid, *Angew. Chem. Int. Ed.* **2013**, *52*, 4160-4164.

Chapter 3 Kinetic Studies of 2D MoS_2 Catalyzed 1-Octanethiol Oxidation

This Chapter is based on the manuscript in preparation:

X. Chen, A. R. McDonald*, Kinetic studies of two-dimensional MoS_2 mediated thiol oxidation-towards a comprehensive understanding of the mechanism of MoS_2/thiol interactions. (In preparation).

3.1 Introduction

Thin layered MoS_2 nanosheets have been stimulating increasing interest in a wide array of applications owing to their unique electronic, optoelectronic and catalytic properties.[1-3] The significant progress in the synthesis of MoS_2 nanosheets has enabled the production of thin layered and large-area of MoS_2 nanosheets on the lab scale.[2, 4] Nevertheless, the obtained MoS_2 nanosheets, with randomly distributed sulfur vacancies (SVs), are normally not perfect lattices.[5, 6] These sulfur vacancies (SVs) have been found to be a double-edged sword, they can either serve as active sites for various catalytic reactions [7, 8] or act as trap states affecting the intra-layer charge transport.[9, 10] From the fabrication of electronic devices point of view, defect-free MoS_2 nanosheets are highly desired. To this end, thiol chemistry based techniques have been applied widely in recent years aiming to either repair the

SVs[11] via uptake the S atoms from thiols to SVs sites or to passivate/functionalize the SVs of MoS_2 nanosheets through binding the thiolate ligands to the unsaturated Mo atoms in SVs sites[12]. However, the exact nature of the thiol molecules/MoS_2 interaction remains unclear.

In Chapter 2, we have demonstrated a general route to functionalize 2H-MoS_2 with cysteine (an organic thiol). Critically, MoS_2 was found to be facilitating the oxidation of the thiol, cysteine, to the disulfide, cystine during the functionalization process (Chapter 2). The resulting cystine was physisorbed on MoS_2 nanosheets rather than any bond-forming process having occurred. To further understand the MoS_2 mediated thiol oxidation process, and elucidate the role of surface defects of MoS_2 nanosheets in the thiol oxidation process, herein the experimental and kinetic analyses of 1-octanethiol oxidation in the presence of exfoliated MoS_2 nanosheets with and without O_2 were carried out. Several reaction parameters were considered, including MoS_2 concentration, 1-octanethiol concentration, kinetic isotope effect, light effect and thickness effect. As a result, oxidation of 1-octanethiol to dioctyl disulfide catalyzed by MoS_2 nanosheets mechanism was proposed.

3.2 Results and discussion

In this study, the reaction between 1-octanethiol (one of the typical alkanethiols) and thin-layered MoS_2 nanosheets was demonstrated as an example to investigate the reaction mechanism between the organic thiols and nanostructured MoS_2. The thin-layered MoS_2 nanosheets were prepared by ultrasonication of bulk MoS_2 in 2-propanol (IPA) as illustrated in Chapter 2, yielding the exfoliated 2H-MoS_2 nanosheets with 9-10 layers thick. Then, an excess amount of 1-octanethiol was mixed with exfoliated 2H-MoS_2 powder in d_4-methanol (unless otherwise stated) followed by refluxing the mixture in the presence or absence of O_2. Here, methanol served as a polar protic solvent to facilitate the dispersion of MoS_2 nanosheets. In addition, the deuterated form (d_4-methanol) will allow simply monitoring of the reaction progress by ^{1}H-NMR. In ^{1}H-NMR spectra, 1-octanethiol displayed a characteristic triplet signal at $\delta = 2.49$ ppm corresponding to the protons bonded to α-carbon ($-CH_2-SH$), whereas this triplet shifted to the lower field region in dioctyl disulfide due to the de-shielding effect of S-S bond, giving rise to a new triplet peak at $\delta = 2.68$ ppm. The rate of the reaction was determined by monitoring of the changes in 1-octanethiol concentration as a function of time using ^{1}H-NMR (see Experimental Section).

3.2.1 Oxidation of 1-octanethiol in the presence of O_2 but in the absence of MoS_2.

Oxidation of 1-octanethiol was performed by solely refluxing of 1-octanethiol (200 μL, 1.15 mmol) in d_4-methanol (1 mL) at 100 °C under air for 24 hrs. The ^{1}H-NMR spectrum of the resulting solution showed the identical features to the pure 1-octanethiol and no detectable dioctyl disulfide-related signals, suggesting that oxidation of 1-octanethiol to dioctyl disulfide under air in the absence of added catalysts was negligible. (Fig. 3.1)

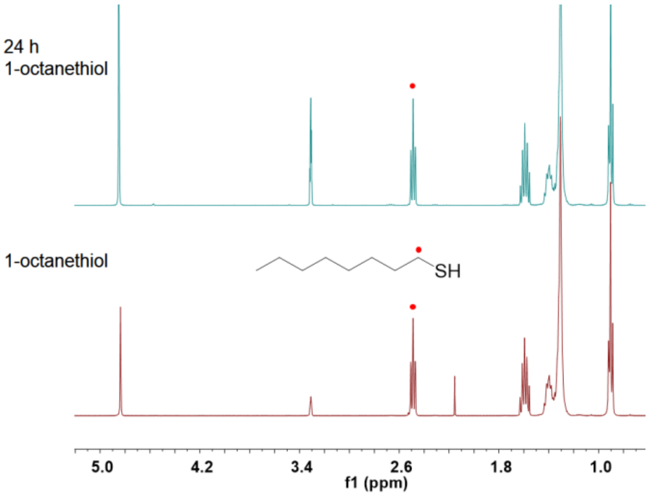

Figure 3.1 ^{1}H-NMR (400 MHz, d_4-CH_3OH) spectra of pure 1-octanethiol, and the

product after refluxing 1-octanethiol itself for 24 h. The peaks at $\delta = 4.87$ and 3.31 ppm were d_4-CH_3OH signals. The peak at $\delta = 2.19$ ppm was the acetone signal. The triplet feature in 1-octanethiol was marked as red dot.

3.2.2 Oxidation of 1-octanethiol in the presence of O_2 and MoS_2.

A control experiment was then performed by adding trace amount (less than 1 mol %) of exfoliated MoS_2 powder to the above resulting solution. This reaction mixture was refluxed at 100 °C under air for 24 h and the reaction progress was monitored by ^{1}H-NMR (Fig. 3.2). The ^{1}H-NMR spectra of reaction mixture displayed two sets of signals corresponding to 1-octanethiol and the dioctyl disulfide. Importantly, a gradual increase of features associated with dioctyl disulfide was observed during the reaction period, suggesting a gradual generation of the dioctyl disulfide. Furthermore, the concentration of 1-octanethiol decreased by ~20%, 27% and 55% with respect to the starting concentration after refluxing 4 h, 6 h, and 24 h, respectively. The increase of dioctyl disulfide accompanied by the decrease of 1-octanethiol indicated that oxidation of 1-octanethiol to dioctyl disulfide took place in the presence of MoS_2 nanosheets. Therefore, it can be deduced that MoS_2, acting as a catalyst, was required for the oxidation of thiol to disulfide in the as-studied system. This result was also consistent with our previous observations during functionalization of liquid exfoliated MoS_2 with cysteine in Chapter 2.

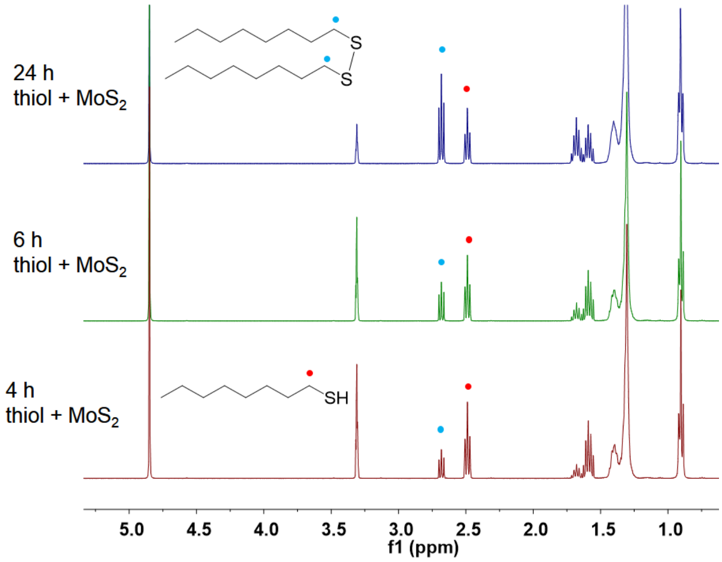

Figure 3.2 ^{1}H-NMR (400 MHz, d_4-CH_3OH) spectra of 1-octanethiol/exfoliated MoS_2 reaction (in the presence of O_2) mixture after 4 h (red), 6 h (green), and 24 h (blue). The triplet feature in 1-octanethiol was marked with a red dot, while the triplet feature in dioctyl disulfide was marked with a blue dot.

3.2.3 Oxidation of 1-octanethiol in the presence of MoS$_2$ but in the absence of O$_2$.

To exclude the influence of O_2, and gain more insight on the role of MoS_2 nanosheets in the 1-octanethiol oxidation process, the reaction of 1-octanethiol with MoS_2 in the absence of O_2 were performed. To do this, 1-octanethiol (200 μL, 961 mM) was mixed with exfoliated MoS_2 (10 mg, 52 mM) in d_4-methanol (1 mL) and the deoxygenated solution was refluxed at 100 °C under Ar atmosphere. The reaction progress was monitored by ^{1}H-NMR (Fig. 3.3). Similar to the reaction in the presence of O_2 (Fig. 3.2), the ^{1}H-NMR spectra of the reaction mixture in the absence of O_2 displayed two sets of signals corresponding to 1-octanethiol and the dioctyl disulfide, indicating that dioctyl disulfide formed even without O_2. This result was consistent with the previous observation during functionalization of liquid exfoliated MoS_2 with cysteine under the inert atmosphere in Chapter 2.

Moreover, the increased dioctyl disulfide features accompanied with the decreased 1-octanethiol features in the absence of O_2 but in the presence of MoS_2 nanosheets was observed, indicating that when MoS_2 nanosheets were present in the mixture, oxidation of 1-octanethiol to dioctyl disulfide can take place without O_2. This observation verified that MoS_2 nanosheets acting as catalysts facilitated the conversion of 1-octanethiol to dioctyl disulfide. It was also noticeable that the concentration of 1-octanethiol decreased by 17% with respect to the starting concentration after refluxing for 24 h, which was much smaller than the 1-octanethiol consumption in the reaction with O_2 (Fig. 3.2, 55%), indicating that oxidation of 1-octanethiol to dioctyl disulfide can be greatly accelerated with the aid of O_2 (a typical oxidant), although O_2 is not a necessity to realize this thiol-to-disulfide conversion.

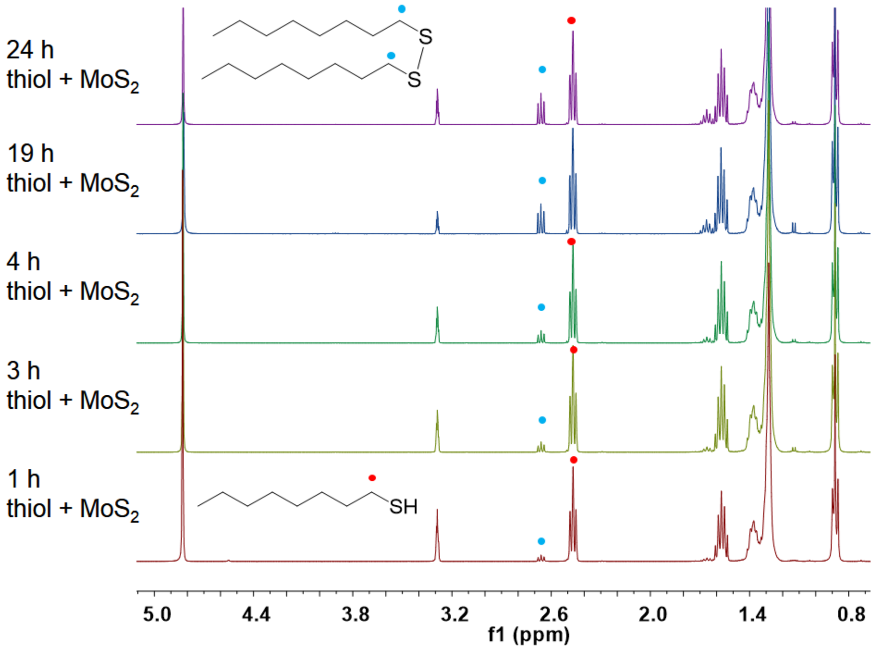

Figure 3.3 ^1H-NMR (400 MHz, d_4-CH_3OH) spectra of 1-octanethiol/exfoliated MoS_2 reaction (in the absence of O_2) mixture after 1h (red), 3 h (yellow), 4 h (green),

19 h (blue) and 24 h (purple). The triplet feature in 1-octanethiol was marked with a red dot, while the triplet feature in dioctyl disulfide was marked with a blue dot.

3.2.4 Kinetic study of 1-octanethiol oxidation in the presence of MoS_2 but in the absence of O_2.

To simplify the reaction mechanism study, the kinetic measurements were performed over a series of reactions of 1-octanethiol with MoS_2 in the absence of O_2. To do this, 1-octanethiol was mixed with exfoliated MoS_2 in d_4-methanol (1 mL) in various molar ratios, and the deoxygenated solutions were refluxed at 100 °C under Ar atmosphere.

Fixed concentration of 1-octanethiol and varied concentrations of MoS_2

Firstly, reactions with a fixed concentration of 1-octanethiol (524 mM) and varied concentrations of exfoliated MoS_2 (28, 57 and 227 mM) were carried out and the concentrations of free 1-octanethiol were measured at different reaction times. The plots of the concentration of free 1-octanethiol ([RSH]) against time (Fig. 3.4, left) displayed a linear relationship, suggesting that the reaction was pseudo zero-order within the reaction time range. In heterogeneous catalysis systems, the local concentration of reagents in the vicinity of catalytically active sites was limited, thereby the reaction rate was limited by the adsorption/ desorption ability of solid-state catalysts other than the random collisions. This result further elucidated that MoS_2 nanosheets, acting as solid state catalysts, were involved in the 1-octanethiol oxidation process. Furthermore, the rates of 1-octanethiol consumption ($-d[\mathrm{RSH}]/dt$) were plotted against initial MoS_2 concentrations to investigate the effect of MoS_2 concentration on the change of reaction rates. As depicted in Fig. 3.4 (right), the larger reaction rate was obtained when the more MoS_2 nanosheets were added in the system. This accelerated 1-octanethiol oxidation with the increased initial concentration of MoS$_2$ was likely attributed to the increased number of active sites in MoS$_2$ nanosheets.

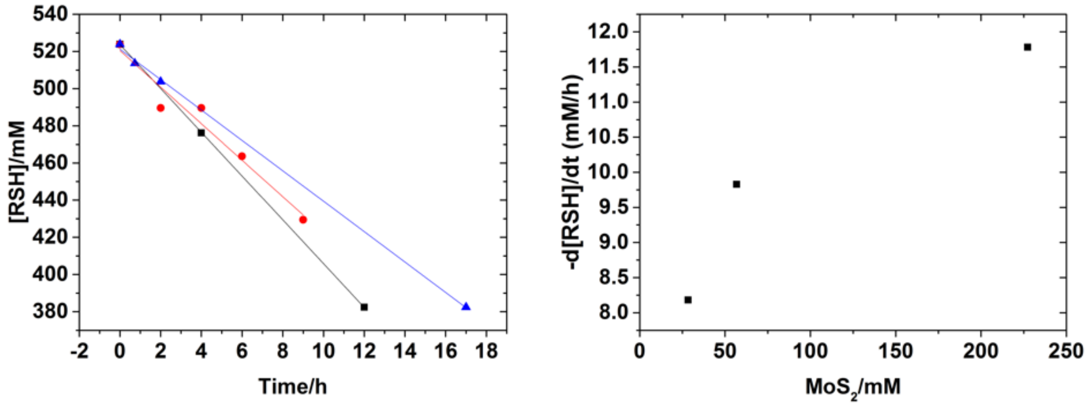

Figure 3.4 Left: plots of concentration of 1-octanethiol ([RSH]) versus reaction time under varied concentrations of exfoliated MoS$_2$: 28 mM (blue), 57 mM (red), and 227 mM (black). Right: plot of observed rates of 1-octanethiol oxidation (-*d*[RSH]/*d*t) versus concentrations of exfoliated MoS$_2$.

Fixed concentration of MoS$_2$ and varied concentrations of 1-octanethiol

Similarly, reactions with a fixed concentration of exfoliated MoS$_2$ (52 mM) and varied concentrations of 1-octanethiol (274, 524, 961 and 1921 mM) were performed to study the dependence of reaction rate on the concentration of 1-octanethiol. The plots of free concentrations of 1-octanethiol [RSH] against time (Appendix, Fig. S3.1) revealed an exponential decay, and a linear relationship was observed when plotting the inverse concentrations of free 1-octanethiol (1/[RSH]) against time (Fig. 3.5, left), suggesting that the oxidation 1-octanethiol appeared to be a second-order reaction with respect to 1-octanethiol. Moreover, the exponential decay of 1-octanethiol concentration with time (Fig. S3.1) implied a gradually decelerated 1-octanethiol consumption with time. This observation indicated that under the fixed concentration of MoS$_2$ catalysts, the rate of 1-octanethiol oxidation was highly dependent on the concentration of free 1-octanethiol in the reaction system. It then can be deduced that MoS_2-mediated 1-octanethiol oxidation was likely to proceed via an intermolecular mechanism, where the free 1-octanethiol molecules not only the adsorbed 1-octanethiol were involved in the 1-octanethiol oxidation to dioctyl disulfide process.

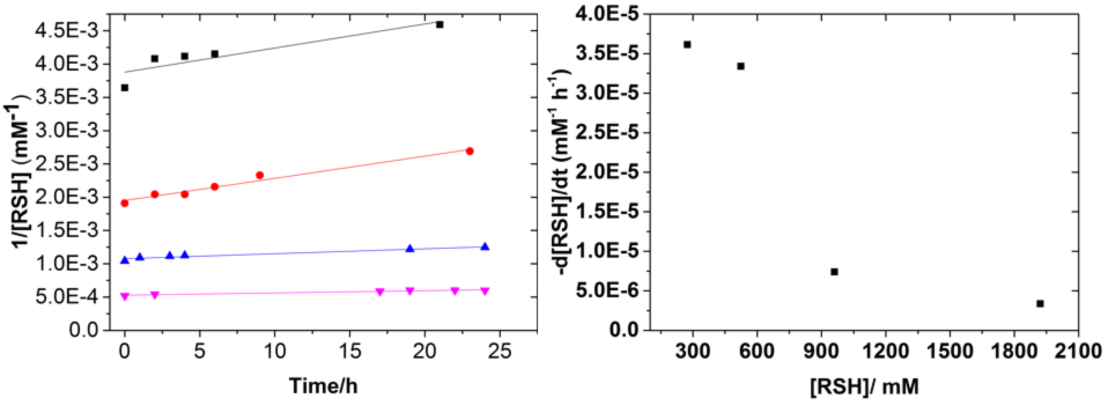

Figure 3.5 Left: plots of inverse concentration of 1-octanethiol [RSH] versus reaction time under varied concentrations of 1-octanethiol: 274 mM (black), 524 mM (red), 961 mM (blue) and 1921 mM (magenta). Right: plot of observed rates of 1-octanethiol oxidation ($-d$[RSH]/dt) versus the initial concentrations of 1-octanethiol ([RSH]).

In addition, the second-order rate constants (k_{obs}) were obtained by linearly fitting the plots of inverse concentrations of free 1-octanethiol (1/[RSH]) against time and calculating the slopes of the resulting linear plots (Fig. 3.5, left). Subsequently the rates of 1-octanethiol consumption ($-d$[RSH]/dt, the absolute value of k_{obs}) were plotted against the initial concentration of 1-octanethiol (Fig. 3.5, right) to study the influence of 1-octanethiol concentration on the reaction rate. Interestingly, the rate of 1-octanethiol consumption dropped dramatically when a large excess (>10 fold) of 1-octanethiol was used at the start. This observation verified again the engagement of MoS_2 nanosheets in the 1-octanethiol oxidation, in which the reaction rate was not proportional to the collision probability of 1-octanethiol molecules. In fact, a possible reason for the reduction of 1-octanethiol consumption rate was the decreased number of accessible active sites in MoS_2 in the presence of an extremely high concentration of 1-octanethiol. In that situation, a majority of active sites were already occupied by 1-octanethiol, whereby continuous absorption of 1-octanethiol for the forward reaction would be delayed until the active sites were freed by desorption of molecules from these sites. Therefore, the rate-limiting step of 1-octanethiol oxidation in the presence of a large excess (>10 fold) of 1-octanethiol was the desorption step of reactive species from the active sites of MoS_2.

Kinetic Isotope Effect

The possibility of a kinetic isotope effect to the MoS_2-mediated 1-octanethiol oxidation was then studied by performing the parallel reactions with exfoliated MoS_2 (52 mM) and 1-octanethiol (961 mM) in methanol or d_4-methanol (1 mL), respectively (Appendix, Fig. S3.2, and Fig.3.6, left). It was found that the oxidation rate in methanol was ~2 times higher than that in d_4-methanol (Fig. 3.6, left), suggesting that proton/H transfer was involved in or prior to the rate-determining step (RDS) of the 1-octanethiol oxidation reaction.

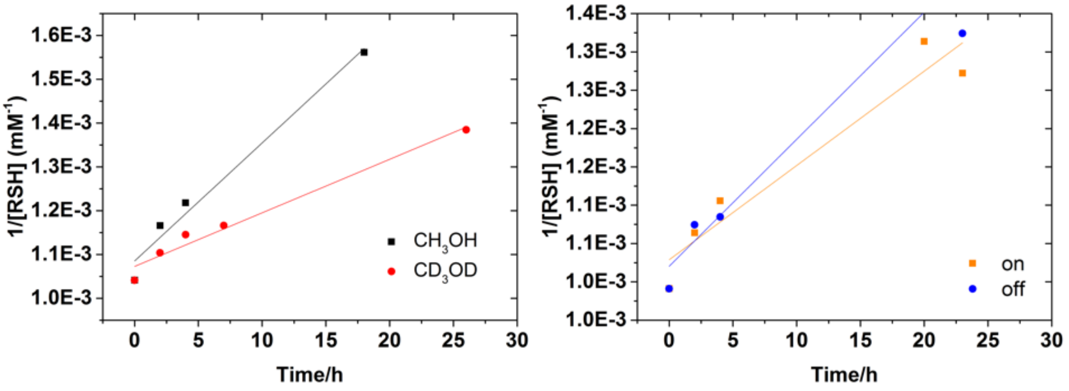

Figure 3.6 Plots of inverse concentration of 1-octanethiol ([RSH]) versus reaction

time for the reaction of exfoliated MoS_2 (52 mM) and 1-octanethiol (961 mM) under various conditions. Left: isotope effect. Right: light effect.

Light effect

Analogous experiments with exfoliated MoS_2 (52 mM) and 1-octanethiol (961 mM) in d_4-methanol (1 mL) were performed in darkness and ambient light, respectively (Fig.3.6, right). The reaction rates observed in both situation were almost same within the experimental error, indicating that ambient light irradiation was not the dominant factor for triggering the 1-octanethiol oxidation.

Thickness effect

Instead of using exfoliated MoS_2 nanosheets (9-10 layers)[13], bulk MoS_2 (52 mM) was reacted with 1-octanethiol (961 mM) in d_4-methanol (1 mL) by refluxing at 100 °C for 24 hrs. The resulting solution was analyzed by ^{1}HNMR. (Fig. 3.7) The concentration of free 1-octanethiol was calculated to be 906.1 mM, suggesting that approximately ~6% of 1-octanethiol was consumed. In comparison, reaction carried out in exfoliated MoS_2 nanosheets led to ~30% consumption[2] under the same reaction condition. The increase in the conversion efficiency using an exfoliated MoS_2 sample was likely attributed to the increased number of active sites in the exfoliated MoS_2 samples. This result indicated that the catalytically active sites of MoS_2 for this thiol oxidation reaction were presumably located at the edges or vacancies sites of nanosheets, which was similar to the catalytic activity of MoS_2 in hydrodesulfurization reaction (HDS)[14] and hydrogen evolution reaction (HER)[7]. Thus the exfoliation of bulk MoS_2 to nanosheets enabled MoS_2 to expose more active sites, leading to a higher conversion efficiency of 1-octanethiol to dioctyl disulfide than their bulk counterparts.

---

[2] The exfoliated MoS_2 nanosheets was the different batch of samples as 3.2.3.

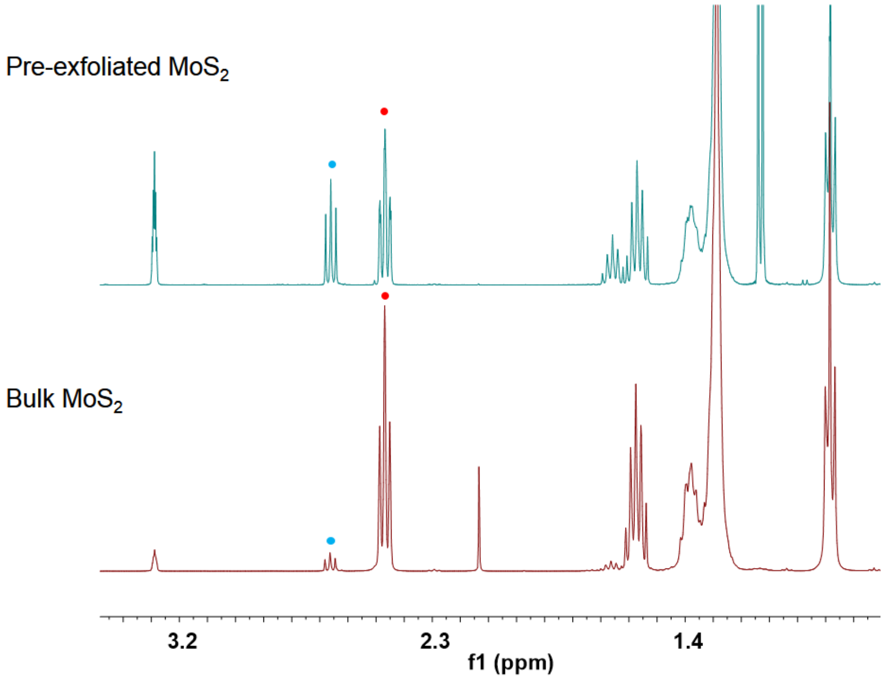

Figure 3.7 ^{1}H-NMR (400 MHz, d_4-CH_3OH) spectra of 1-octanethiol/exfoliated MoS_2 reaction mixture (blue) and 1-octanethiol/bulk MoS_2 reaction mixture (red) after 24 h.

3.2.5 Postulation of reaction mechanisms for MoS_2 catalyzed 1-octanethiol oxidation

Two possible reaction mechanisms that can induce the conversion of 1-octanethiol to dioctyl disulfide via SVs in MoS_2 nanosheets were postulated as Fig. 3.8. Each mechanism began with the physical adsorption of 1-octanethiol (RSH) on the sulfur vacancy site (SV), followed by S-H bond cleavage and proton transfer to a Mo atom in the vicinity of SV, leaving the thiolate group (RS^-) attached on another Mo center. The subsequent electron transfer led to the formation of a thiyl radical (RS•) and a Mo-H bond. (Black arrows in Fig. 3.8) Thereafter, the thiyl radical (RS•) can be expelled from Mo site immediately after it formed and coupled with another expulsed thiyl radical (RS•) to form disulfide product in solution. The dissociation of H_2 gas may take place by breaking the Mo-H bonds, resulting in the unchanged MoS_2. (Mechanism 1, blue arrows in Fig. 3.8)

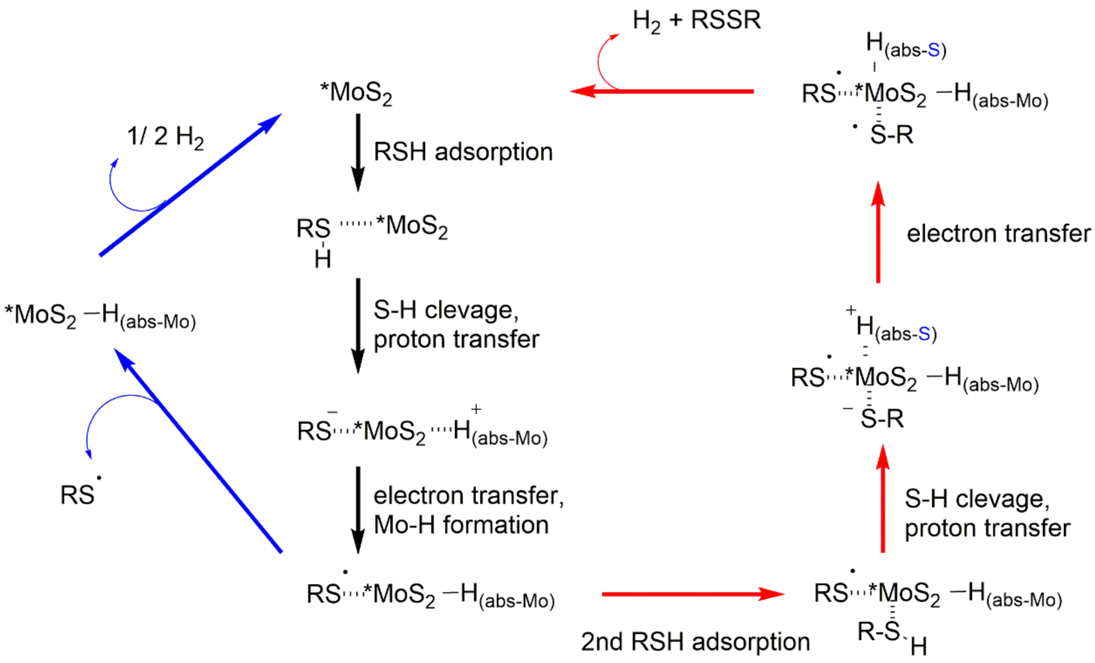

Figure 3.8 Proposed reaction mechanisms for MoS_2 nanosheets catalyzed 1-octanethiol oxidation. The disulfide formed either through thiyl radical-radical coupling outside (blue) or within (red) the cavity of catalytically active sites.

In an alternative mechanism (Mechanism 2, red arrows in Fig. 3.8), the thiyl radical (RS•) remained attached to the Mo atom in the SV site after it formed, while another 1-octanethiol molecule approached the SV, forming the second thiyl radical (RS•). Eventually, the disulfide product-dioctyl disulfide formed by the combination of two thiyl radicals (RS•) along with the generation of H_2 in the catalyst cavity. Since there are only three unsaturated Mo atoms in the SV cavity (Appendix, Fig. S3.3), which have been occupied by two thiolate groups and one H, the proton from the second thiol molecules was most likely attached to the surface S atoms in the vicinity of SV like the HER Volmer step[15].

Based on the aforementioned analysis, both mechanisms involved the S-H bond cleavage. This was consistent with the reported experimental observations in functionalization of MoS_2 using organic thiols,[12, 16] in which the S-H vibrational mode (ν= 2500 cm^{-1}) had disappeared in IR spectra of functionalized samples. Moreover, the proton transfer took place before desorption of reactive species from SV sites, and generation of dioctyl disulfide occurred in both mechanisms. This coincided well with the observed kinetic isotope effect (Fig. 3.6, left) in MoS_2 mediated 1-octanethiol oxidation reaction.

Secondly, both mechanisms involved the formation of Mo-H bond and this bond can be further broken down, resulting in the formation of H_2. Comparing the DRIFT spectra of 1-octanethiol/2H-MoS_2 reaction product with pristine 2H-MoS_2 (Fig. 3.9, blue trace) demonstrated a peak at ~1735 cm^{-1}, which was in the same range as the literature reported Mo-H bond stretching vibration mode (~1780 cm^{-1}),[17, 18] suggesting that Mo-H bonds presumably formed after the 1-octanethiol/2H-MoS_2 reaction. A similar feature was also observed in the DRIFT spectra of cysteine functionalized 2H-MoS_2 (~1770 cm^{-1}, Fig. 3.9, red trace), 2-aminoethanethiol/2H-MoS_2 reaction product (~1709 cm^{-1}, Fig. 3.9, green trace) and 3-mercaptopropionic acid functionalized 2H-MoS_2 (~1798 cm^{-1}, Fig. 3.9, orange trace). These observations indicated that functionalization of 2H-MoS_2 with organic thiols led to the formation of Mo-H bonds at the SVs. This experimental result also supported by the recently reported thiol/MoS_2 interaction theoretical model[18], in which the dissociated hydrogen from S-H group migrated to the Mo atom in the SV site, forming the molybdenum hydride (Mo-H) bond.

In addition, the presence of the Mo-H vibrational feature in thiol functionalized MoS_2 samples suggested the further dissociation of Mo-H bonds to generate H_2 was less prone to occur under the demonstrated reaction conditions (bath-sonication followed by magnetic stirring at room temperature). Further experiments to probe the H_2 formation is necessary for unambiguously elucidating the reaction mechanism.

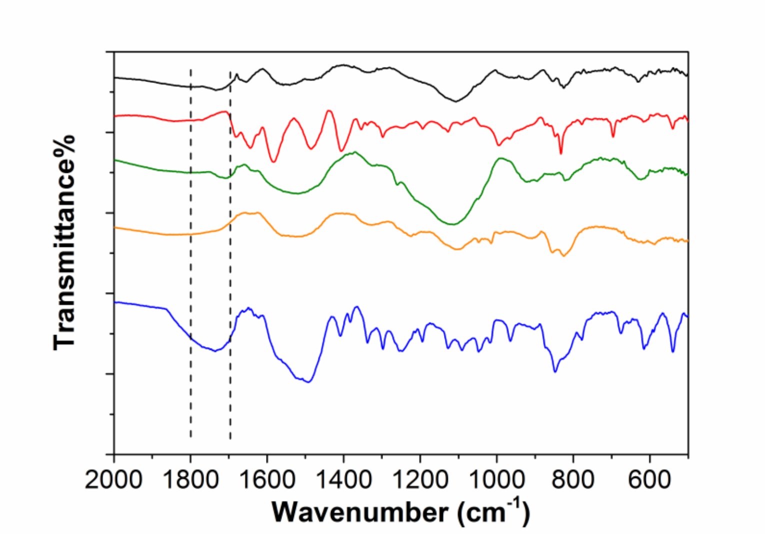

Figure 3.9 DRIFT spectra of pristine 2H-MoS_2 (black) and functionalized MoS2 samples with Cysteine (red), 2-aminoethanethiol (green), 3-mercaptopropionic acid (orange) and 1-octanethiol (blue). The Mo-H bond vibrational mode presumably located in the range of 1800- 1700 cm^{-1} was marked as dashed lines.[17]

Having identified the bond-breaking and bond-formation processes in the two mechanisms, it was found that both mechanisms involved the S-H bond cleavage and Mo-H bond formation. In this regard, both mechanisms matched well with the experimental observations. To distinguish two mechanisms, correlation of results from kinetic studies with reaction mechanisms was performed. Previous kinetic studies in Fig. S3.1 (the amount of 1-octanethiol was in large excess compared to MoS_2 and the number of active sites) have revealed that MoS_2-mediated 1-octanethiol oxidation was likely to proceed via an intermolecular pathway, wherein both adsorbed 1-octanethiol and free 1-octanethiol were involved in the oxidation of 1-octanethiol to disulfide. Mechanism 1 featured the formation of thiyl radical (RS•) and expulsion from SV cavity once it formed. Therefore, the rate of disulfide generation was dependent on the rate of two thiyl radicals (RS•) formation. When the number of active sites was limited compared to the number of thiol molecules, generation of the second thiyl radical required desorption of the first thiyl radical from active site accompanied by adsorption of second thiol molecule at SV site, thereby the free thiols in the reaction mixture was involved in the rate-limiting step. This was in a good agreement with the experimental kinetic study. On the contrary, when the number of thiol molecules was limited, the number of SVs were enough to adsorption all the thiol molecules at the same time, the rate of disulfide generation was therefore solely dependent on the adsorbed thiols. This situation was not covered in this research.

In comparison, mechanism 2 featured the disulfide formation via thiyl radical-radical coupling within the cavity of catalytically active sites. Thus, the rate of disulfide generation was reliant on the rate of formation of two thiyl radicals (RS•) at the SV site. Therefore, both the rate of thiyl radical (RS•) formation as well as the rate of adsorption of the second thiol in the SV site were key to the disulfide generation no matter if the number of thiol molecules was limited or not. However, accommodating two thiol molecules simultaneously at one SV site was challenging, especially for the large organic thiols like 1-octanethiol, due to the repulsion force between two molecules and steric hindrance, which would limit the formation of disulfide at the catalyst cavity via mechanism 2. Therefore, 1-octanethiol oxidation most likely proceeded via mechanism 1.

Other possible mechanisms?

Apart from the aforementioned reaction mechanisms, the SVs repairing mechanism[18] was also considered. In this mechanism, following the thiol (RSH) physical adsorption on the SV site, S-H bond scission led to the formation of a thiolate intermediate (RS^-) which was bound to the unsaturated Mo in the SV site, leaving the H adsorbed on the nearest surface S atom. Then, homolytic cleavage of C-S bond led to the formation of the free radical R• in the vicinity of the surface, which can then be hydrogenated to form an alkane (Fig. 3.10), or undertake other re-arrangement or dehydrogenation to give other surface intermediates.[19-21] As a result, the local SVs were literally repaired by taking the S atoms from the thiol molecules and organic thiols were converted to alkanes/hydrocarbons. However, the ^{1}H-NMR analysis of 1-octanethiol and MoS_2 nanosheets reaction mixture revealed the dioctyl disulfide was the only product. In addition, GC-MS analysis (Appendix, Fig. S3.4) confirmed the reaction mixture consisted of only 1-octanethiol and dioctyl disulfide with the retention time of 11.2 and 34.2 min, respectively. And there were no other detectable 1-octanethiol derivatives. Therefore, 1-octanethiol consumption in the presence of exfoliated MoS_2 nanosheets via a SVs repairing pathway was less likely to occur in the demonstrated experimental conditions (T = 100 °C, -173 K). This was found to be true because previous investigations by other groups have demonstrated that hydrogenated or re-arranged products after homolytic cleavage of S-C bonds were detected when the sample was annealing at higher temperature (> 600K)[20] [19].

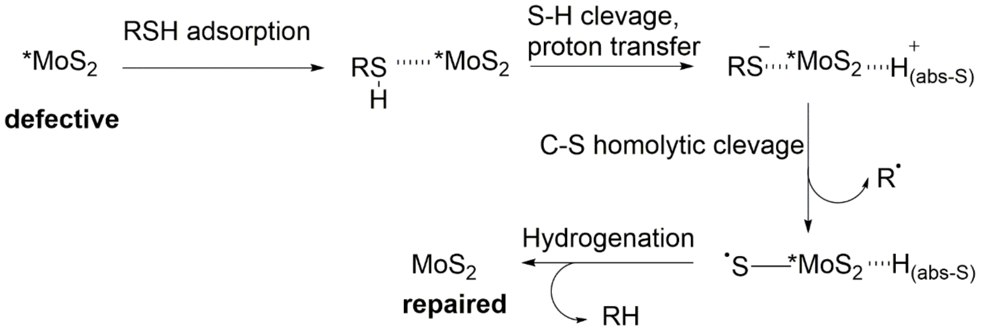

Figure 3.10 Proposed mechanism for MoS_2 catalyzed 1-octanethiol consumption

via a SVs repairing pathway. *MoS_2 represents the defective MoS_2 nanosheets with numbers of sulfur vacancies. MoS_2 represents the locally repaired MoS_2.

3.3 Conclusion

In summary, the kinetics of MoS_2 nanosheets-catalyzed 1-octanethiol oxidation in the absence of O_2 was systematically studied. The results unraveled that 1-octanethiol did not undergo significant oxidation in the presence of oxygen and absence of a catalyst. However, in the presence of MoS_2 nanosheets, 1-octanethiol can be readily oxidized even without O_2. The thickness of MoS_2 nanosheets plays a significant role in the catalytic activity for 1-octanethiol oxidation. By correlation of two possible reaction mechanisms with our kinetic study results, dioctyl disulfide was postulated to be formed via thiyl radical-radical coupling outside the cavity of catalytically active sites. To further confirm the postulation and understand the mechanism, identification of reaction intermediates and by-products such as H_2 would be critical in the following studies. Although this study concentrated on a specific organic thiol-MoS_2 interaction, this study provided insights into the mechanistic details of MoS_2-thiol interactions. Further investigation to elucidate both electronic and steric impacts in the thiol-MoS_2 heterogeneous interface reaction should be considered in the follow-up study, which could lead to a better understanding of the thiol chemistry directed functionalization strategy and development of an accurate surface modification model for practical applications.

3.4 Experimental section

3.4.1 Materials

MoS_2 powder (6 μm), 1-octanethiol (≥97%), d_4-methanol and other chemicals and reagents were purchased from Sigma-Aldrich and were used as supplied without further purification.

3.4.2 Instrumentation

^{1}H magnetic resonance (NMR) analyses were performed on an Agilent MR400 instrument two channel instrument (400 MHz) with a 5 mm one NMR probe. Gas chromatography/mass spectrometry (GC/MS) was performed using a GCT Premier Micromass time of flight mass spectrometer.

3.4.3 Methods

Preparation of thin-layered MoS_2 nanosheets

Thin-layered MoS_2 nanosheets were produced by liquid exfoliation as illustrated in Chapter 2. The resulting 2H-MoS_2/2-Propanol (IPA) dispersion (0.3-0.4 g L^{-1}) was vacuum-filtered using porous cellulose filter membranes (0.025 µm). And the dried powder was collected after leaving in the ambient condition for 24 h.

Thiol oxidation in the presence of O_2 but in the absence of MoS_2.

1-Octanethiol (200 µL, 1.15 mmol) was added to d_4-methanol (1.0 mL) and the solution was refluxed at 100 °C for 24 hrs.

Reaction of exfoliated 2H-MoS_2 nanosheets with 1-octanethiol in the absence of O_2

The reaction was performed under an inert (Ar) atmosphere using standard Schlenk techniques. Briefly, the exfoliated 2H-MoS_2 powder was ground thoroughly and dissolved in d_4-methanol. To this mixture, an excess amount of 1-octanethiol was added and followed by subsequent bath-sonication of reaction mixture for 5 min.

Then the reaction mixture was subjected to Freeze-pump-thaw cycling three times and then refluxed at 100 °C for 24 h under Ar atmosphere. For ^{1}H-NMR measurement, ~30 μL of reaction mixture was diluted with 0.3 mL of d_4-methanol and subjected to NMR measurement immediately.

Reaction of exfoliated 2H-MoS_2 nanosheets with various organic thiols in the presence of O_2 (Fig. 3.9)

Reactions of exfoliated 2H-MoS_2 nanosheets with various organic thiols (cysteine, 2-aminoethanethiol, 3-mercaptopropionic acid and 1-octanethiol) were prepared by blending the exfoliated 2H-MoS_2 dispersion (3.1 mM) and an organic thiol/IPA solution (0.13 M) followed by ultra-sonication. Organic thiols were initially dissolved in 10 mL IPA and treated by mild sonication in a sonic bath (Branson Ultrasonic Cleaner B1510MT, 40 kHz) for 5 min. This was then added to the 20 mL exfoliated 2H-MoS_2 dispersion and subjected to ultra-sonication with a tapered micro tip under ice cooling for 0.5 h (Sonics VX-750, 40 % amplitude, 4 s pulse on, 4 s pulse off). Following the ultra-sonication, the resultant dispersion was subjected to high-speed centrifugation at 11000 rpm (13257 *g*) for 1 h to precipitate all the nanomaterial. After that, the sediment was re-dispersed in IPA/H_2O (1:1 v/v) and centrifuged at 11000 rpm (13257 *g*) for 1 h (2 times) to remove all free, unbound molecules. The supernatant was decanted and the sediment was collected with 10 mL IPA. The concentration of functionalized sample was determined by filtering a 2 mL dispersion of Cys-2H-MoS_2 on the Whatman® Anodisc inorganic filter membrane (pore size 0.02 μm, diameter 47 mm) and weighing it after drying in air overnight. The dried powders were collected for DRIFT.

Monitoring the consumption of 1-octanethiol as a function of time using ^{1}H magnetic resonance (NMR)

The concentration of free 1-octanethiol (RSH) in the reaction solution was determined by the ratio of dioctyl disulfide (RSSR) to 1-octanethiol, which displayed two distinct triplets in the ^{1}H-NMR spectrum region of 2.40-2.75 ppm for α-H. The α-H referred to the hydrogen bonded to α- carbon ($-CH_2-SH$). The triplet at $\delta = 2.49$ ppm corresponded to the α-H signal in 1-octanethiol, whereas the triplet at $\delta = 2.68$ ppm corresponded to the α-H signal in dioctyl disulfide. The shifted α-H signal in the disulfide product can be attributed to the de-shielding effect by the S-S bond. Therefore, the ratio of dioctyl disulfide to 1-octanethiol was proportional to the integrated peak ratio of α-H (RSSR) to α-H (RSH):

$$\frac{[\mathrm{RSSR}]}{[\mathrm{RSH}]} = \frac{1}{2}\,\frac{\alpha\mathrm{H}\ (\mathrm{RSSR})}{\alpha\mathrm{H}\ (\mathrm{RSH})} = \frac{1}{2}\mathrm{N}$$

Where N represents the integrated peak ratio of α-H (RSSR) to α-H (RSH).

Assuming the concentration of free 1-octanethiol [RSH] was C,

$$\frac{\mathrm{C}}{\mathrm{C}_0} = \frac{\alpha\mathrm{H}\ (\mathrm{RSH})}{\alpha\mathrm{H}\ (\mathrm{RSH}) + \alpha\mathrm{H}\ (\mathrm{RSSR})} = \frac{1}{1+\mathrm{N}}$$

So, the free 1-octanethiol in reaction mixture

$C = C_o/(1+N)$

References

[1] Q. H. Wang, K. Kalantar-Zadeh, A. Kis, J. N. Coleman, M. S. Strano, *Nat. Nanotechnol.* **2012**, *7*, 699-712.

[2] M. Chhowalla, H. S. Shin, G. Eda, L. J. Li, K. P. Loh, H. Zhang, *Nat. Chem.* **2013**, *5*, 263-275.

[3] Y. Chen, C. Tan, H. Zhang, L. Wang, *Chem. Soc. Rev.* **2015**, *44*, 2681-2701.

[4] X. Zhang, Z. Lai, C. Tan, H. Zhang, *Angew. Chem. Int. Ed.* **2016**, *55*, 8816-8838.

[5] C. Backes, N. C. Berner, X. Chen, P. Lafargue, P. LaPlace, M. Freeley, G. S. Duesberg, J. N. Coleman, A. R. McDonald, *Angew. Chem. Int. Ed.* **2015**, *54*, 2638-2642.

[6] M. Donarelli, F. Bisti, F. Perrozzi, L. Ottaviano, *Chem. Phys. Lett.* **2013**, *588*, 198-202.

[7] T. F. Jaramillo, K. P. Jørgensen, J. Bonde, J. H. Nielsen, S. Horch, I. Chorkendorff, *Science* **2007**, *317*, 100-102.

[8] J. D. Benck, T. R. Hellstern, J. Kibsgaard, P. Chakthranont, T. F. Jaramillo, *ACS Catal.* **2014**, *4*, 3957-3971.

[9] H. Qiu, T. Xu, Z. Wang, W. Ren, H. Nan, Z. Ni, Q. Chen, S. Yuan, F. Miao, F. Song, G. Long, Y. Shi, L. Sun, J. Wang, X. Wang, *Nat. Commun.* **2013**, *4*, 2642.

[10] Z. Yu, Y. Pan, Y. Shen, Z. Wang, Z.-Y. Ong, T. Xu, R. Xin, L. Pan, B. Wang, L. Sun, J. Wang, G. Zhang, Y. W. Zhang, Y. Shi, X. Wang, *Nat. Commun.* **2014**, *5*, 5290.

[11] M. Makarova, Y. Okawa, M. Aono, *]J. Phys. Chem. C* **2012**, *116*, 22411-22416.

[12] X. Chen, A. R. McDonald, *Ad. Mater.* **2016**, *28*, 5738-5746.

[13] X. Chen, N. C. Berner, C. Backes, G. S. Duesberg, A. R. McDonald, *Angew. Chem. Int. Ed.* **2016**, *55*, 5803-5808.

[14] J. Brenner, C. L. Marshall, L. Ellis, N. Tomczyk, J. Heising, M. Kanatzidis, *Chem. Mater.* **1998**, *10*, 1244-1257.

[15] J. Greeley, T. F. Jaramillo, J. Bonde, I. Chorkendorff, J. K. Norskov, *Nat. Mater.* **2006**, *5*, 909-913.

[16] S. S. Chou, M. De, J. Kim, S. Byun, C. Dykstra, J. Yu, J. Huang, V. P. Dravid, *J. Am. Chem. Soc.* **2013**, *135*, 4584-4587.

[17] C. M. Sayers, *J. Phys. C: Solid State Phys.* **1981**, *14*, 4969.

[18] Q. Li, Y. Zhao, C. Ling, S. Yuan, Q. Chen, J. Wang, *Angew. Chem. Int. Ed.* **2017**, *56*, 10501-10505.

[19] C. G. Wiegenstein, K. H. Schulz, *J. Phys. Chem. B* **1999**, *103*, 6913-6918.

[20] S. L. Peterson, K. H. Schulz, *Langmuir* **1996**, *12*, 941-945.

[21] K. E. Dungey, M. D. Curtis, *J. Am. Chem. Soc.* **1997**, *119*, 842-843.

PART II

Covalent Functionalization of ce-1T-MoS$_2$ with Ru^{II} Complexes

CHAPTER 4 Ru^{II} Photosensitizer Functionalized Two-Dimensional MoS_2 for Light-Driven Hydrogen Evolution

This Chapter is based on the following manuscript:

X. Chen, D. MacAteer, C. McGuinness, I. Godwin, J. N. Coleman, A. R. McDonald*, *Chem. Eur. J.* **2017**, 23, 1.

4.1 Introduction

Solar-driven water splitting is emerging as one of the most promising solutions to achieve the renewable hydrogen fuel production.[1-3] This can be accomplished by a photoelectrochemical system (PEC),[4, 5]which integrates the functions of light harvesting and hydrogen generation into one system, enabling solar energy conversion and storage as well as clean fuel production.[1] The typical PEC system consists of two components: light absorber and an electrocatalyst that catalyzes the hydrogen evolution reaction (HER). Platinum (Pt) is the most well-known catalyst for HER owing to its negligible overpotential and excellent kinetics.[6] However, Pt's scarcity and high cost make it commercially unfeasible. Therefore, it is necessary to develop non-noble metal catalysts for economical hydrogen generation from water.

In pursuit of highly reactive, earth-abundant and robust proton reduction catalysts, exfoliated transition metal dichalcogenides (TMDs), in particular two-dimensional (2D) MoS_2, have gained considerable attention in recent years due to their excellent catalytic activity and durability [7, 8] MoS_2 mainly exists in two phases (2H and 1T). In the 2H-phase, the coordination of Mo is trigonal prismatic, while in the 1T-phase, the Mo atom has an octahedral coordination environment. The monolayer 2H-MoS_2 is a semiconductor with a 1.9 eV band gap, whereas 1T-phase displays a metallic nature.[9] Both theoretical and experimental investigations revealed that the edges of MoS_2 were catalytically active while the basal plane remained inert.[10] Later studies demonstrated that phase transformation from 2H- to 1T-MoS_2 via lithium intercalation can enhance the HER activity, which could be attributed to an active basal plane. [11, 12]

Electrochemical HER by MoS_2 has been studied in detail [7, 8, 13], however, photoelectrochemical HER by MoS_2 remains in its infancy. The use of monolayer 2H-MoS_2 as a photocathode (MoS_2 acts as both light absorber and electrocatalyst) for the H_2 generation has displayed poor performance due to the low yield production of mono-layer MoS_2 nanosheets, insufficient light adsorption, and fast charge recombination.[14, 15] One strategy to circumvent this is to combine photo-absorbers with MoS_2. While there have been a large number of studies on the semiconductor-MoS_2 based heterogeneous systems [16-20], examples of molecular dye-sensitized MoS_2 photocatalytic devices remain rare due to the inert nature of MoS_2 basal plane, which brings about the challenge to covalently couple molecular photosensitizers to MoS_2 surface. This is apparent from the fact that, so far all the previously reported molecular dyes ($[Ru(bpy)_3]^{2+}$,[21] cyclometalated Ir^{III} complexes,[22] and Eosin Y[23]) sensitized MoS_2 devices were simply formed by mixing/physisorption, thus limiting the electronic communications between dye and the catalyst, and thus inhibiting the light-dirven HER efficiency. It is also noted that most molecular dye-sensitized MoS_2 photocatalytic devices are based on semiconducting 2H-MoS_2. Very recently, Rao and co-workers[24] developed an Eosin Y-sensitized 1T-MoS_2 photocatalysis device, that demonstrates a TOF that is 3 times higher than the Eosin Y-sensitized 2H-MoS_2/N-doped graphene. The high activity of this dye-sensitized 1T-MoS_2 catalyst was likely attributed to the good conductivity of 1T-MoS_2. With this in mind, a covalently tethered dye-sensitized 1T-MoS_2 system would hold great promise for solar-driven HER.

Ru^{II} polypyridyl complexes are a typical type of photosensitizers, which have been extensively studied in dye-sensitized solar cells and other photosynthesis systems due to their long-lived excited states, unique light harvesting and redox properties,[25] therefore are ideal photosensitizers for such a system. However, directly binding Ru^{II} polypyridyl complex to 1T-MoS_2 is challenging, because the 1T-MoS_2 nanosheets produced from lithium intercalation and exfoliation are negatively charged, which tend to aggregate promptly when mixed with Ru^{II} polypyridyl complexes due to the strong electrostatic interaction. This aggregated hybrid would prevent the vertical charge transport and limit the protons' access to the catalytically active sites, leading to negative impacts on the activity of the overall device for HER. Therefore, development of a more precise and controllable surface attachment strategy to covalently immobilize Ru^{II} polypyridyl complex onto 1T-MoS_2 nanosheets is highly desired.

Chhowalla and co-workers[9] have demonstrated a method to covalently functionalize 1T-MoS_2 nanosheets by reacting chemically exfoliated MoS_2 with organohalides, which offers a way to connect organic architecture to 2D 1T-MoS_2. Inspired by this work, herein we demonstrate an approach to covalently binding the molecular photosensitizer $[Ru^{II}(bpy)_3]^{2+}$ (bpy = 2,2'-bipyridine) onto 1T-MoS_2 nanosheets and demonstrate light-driven HER from 1T-MoS_2.

4.2 Results and discussion

4.2.1 Ligands and model complex synthesis

Monobromomethyl substituted bipyridine ligand was synthesized from monomethyl bipyridine starting materials according to the prior literature[26]. The 5-methy-2,2'-bipyridine (2) was prepared starting from 2-acetylpyridine, which was treated with iodine in pyridine to give the pyridinium salt (1) in 50% yield. Then this salt was reacted with 2-methylprop-2-enal followed by treatment with ammonium acetate to afford the corresponding 5-methyl-2,2'-bipyridine (2). The bromination reaction was performed by refluxing the 5-methyl-2,2'-bipyridine (2) and NBS in anhydrous CCl_4 with a trace of AIBN as a radical initiator, leading to the formation of 5-bromomethyl-2,2'- bipyridine (3) in 90% yield (Fig. 4.1).

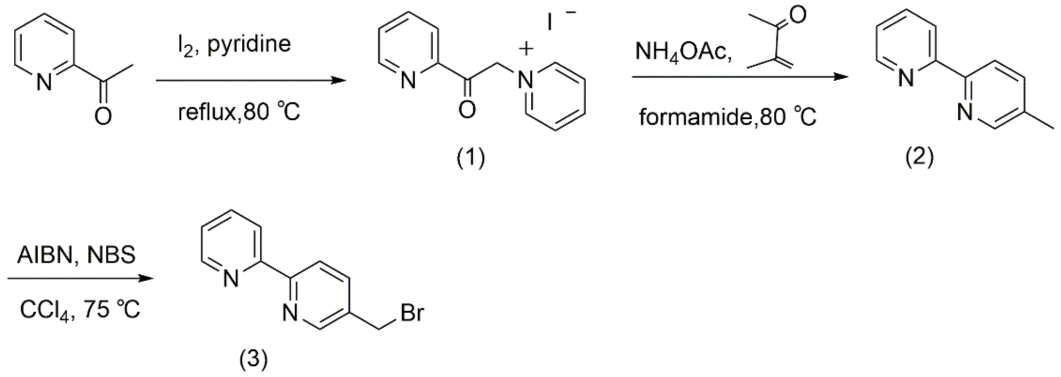

Figure 4.1 Synthetic route to 5-bromomethyl-2,2'-bipyridine.

Considering the toxicity of CCl_4, an alternative route towards synthesizing the 5-bromomethyl-2,2'-bipyridine (3) was also employed as shown in Fig. 4.2. Likewise, 5-methyl-2,2'-bipyridine (2) was used as a starting material, which was first oxidized to corresponding carboxylic acid (5) as a white crystal by reacting with $KMnO_4$, and then converted to the ester (6) with acyl chloride as an intermediate. After that, reduction of ester (6) by $NaBH_4$ gave the alcohol (7) in 76% yield after flash column chromatography. Finally, the hydroxyl group of alcohol (7) was substituted by bromide through reacting with PBr_3, leading to the formation of 5-bromomethyl-2,2'-bipyridine (3) with 43% yield after purification.

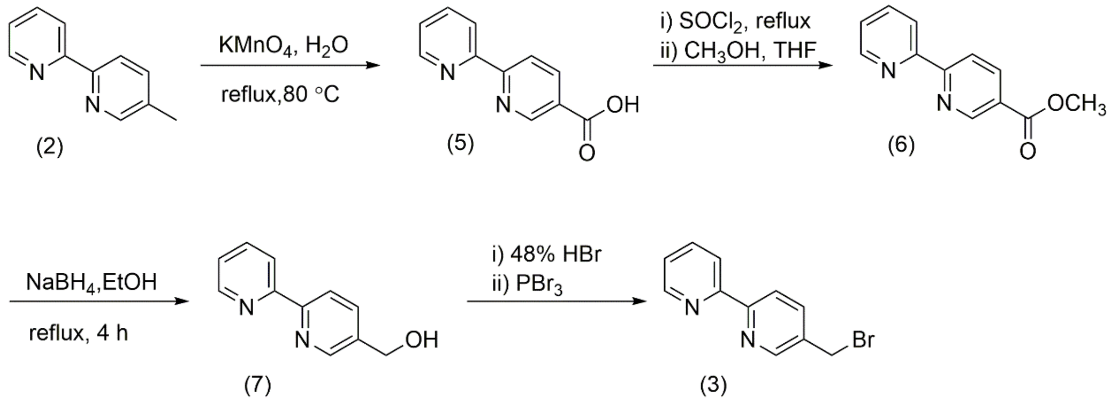

Figure 4.2 Alternative synthetic route to 5-bromomethyl-2,2'-bipyridine.

For characterization purposes, $[Ru^{II}(bpy)_3](PF_6)_2$ model complex was also synthesized by mixing $[Ru^{II}(bpy)_2Cl_2]$ precursors (prepared according to the procedure in literature[27]) with 5-methyl-2,2'-bipyridine (2) in a mixed solvent (ethanol/H_2O, v/v = 1/1) and refluxing at 110 °C under Ar for 4 h. The resulting mixture was subjected to centrifugation to remove all the unreacted $[Ru^{II}(bpy)_2Cl_2]$ followed by gradual addition of saturated NH_4PF_6 aqueous solution into the clear filtrate. The obtained precipitate was purified by flash column chromatography on aluminum oxide, affording a red solid product in 75% yield. Then recrystallization of red product from acetonitrile/ether yielded the red crystals of $[Ru^{II}(bpy)_3](PF_6)_2$.

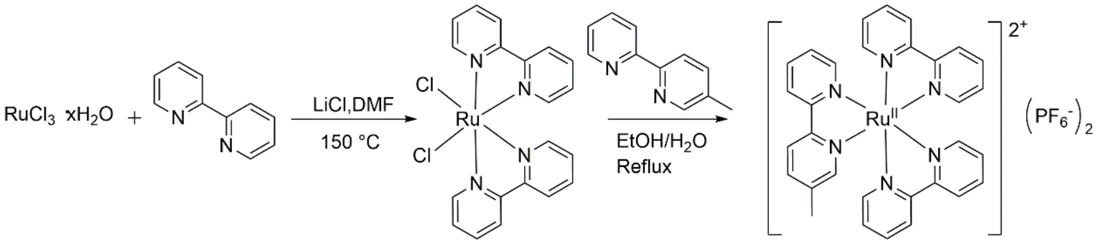

Figure 4.3 Synthetic route to $[Ru^{II}(bpy)_3](PF_6)_2$ model complex.

4.2.2 Preparation and characterization of ce-1T-MoS$_2$ nanosheets.

Thin layered ce-1T-MoS$_2$ nanosheets were prepared according to a literature procedure,[9] by soaking bulk 2H-MoS$_2$ powder in n-butyllithium solution (n-BuLi, 1.6 M in hexane) at room temperature for 3 days and then exfoliating the intercalated compound ($Li_x[MoS_2]^{x-}$) in H_2O. The ce-1T-MoS$_2$ sample was characterized by electronic absorption, X-ray photoelectron (XPS) and Raman spectroscopies (Appendix, Fig. S4.1-4.3), confirming that the exfoliated MoS$_2$ was predominantly 1T-polymorph. The zeta potential (ζ) of the ce-1T-MoS$_2$ was determined to be -46 mV.

4.2.3 Functionalization

A step-wise functionalization of ce-1T-MoS$_2$ with $[Ru^{II}(bpy)_3]^{2+}$ was performed (Figure 4.4, for details see experimental section). 5-Bromomethyl-2,2'-bipyridine was reacted with ce-1T-MoS$_2$ in a manner analogous to the previously reported covalent functionalization of ce-1T-MoS$_2$ by organoiodides.[9] 5-Bromomethyl-2,2'-bipyridine (10 equiv. per ce-1T-MoS$_2$), pre-dissolved in propan-2-ol (IPA) solution (10 mL, 24.9-31.1 mg/mL), and trace amounts of NaI (2 mg) were added to an aqueous dispersion of ce-1T-MoS$_2$ (20 mL, 5-6.25 mM). The mixture was sonicated in the dark for 1 h and then stirred at room temperature under the dark condition for 48 h. The resulting dispersion was subjected to high-speed centrifugation to precipitate all the dispersed materials. The resulting product (defined as bpy-MoS_2) was washed and re-dispersed in IPA (10 mL) for further characterization. Bpy-MoS_2 (10 mg) and $[Ru^{II}(bpy)_2Cl_2]$ (5 mg, 0.01 mmol) were combined in a water/ethanol mixture (30 mL, 1:1, v/v) and the reaction mixture was heated to reflux at 120 °C for 12 h. In the course of the reaction, the color of the reaction mixture changed from black to red, indicating the successful formation of a $[Ru^{II}(bpy)_3]^{2+}$-like species. The resulting functionalized ce-1T-MoS_2 (defined as $[Ru^{II}(bpy)_3]$-MoS_2) was then separated from the reaction mixture through high-speed centrifugation, and subsequently thoroughly washed and re-dispersed in deionized water (5 mL) for further characterization.

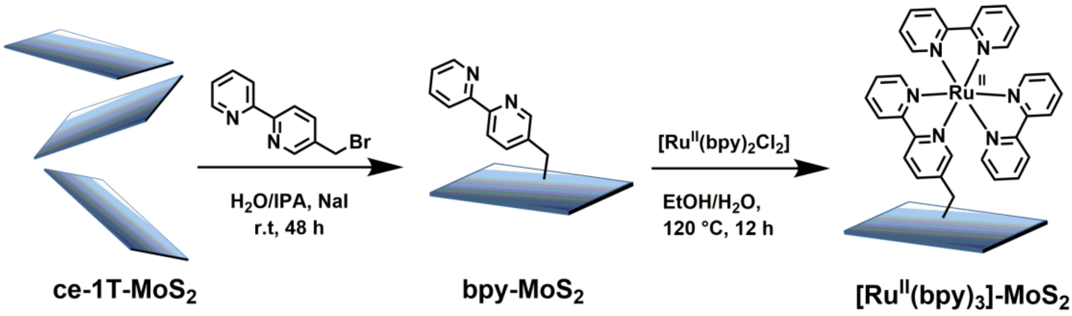

Figure 4.4 Schematic representation of step-wise functionalization of ce-1T-MoS_2 with $[Ru^{II}(bpy)_3]^{2+}$.

4.2.4 Material characterization

$[Ru^{II}(bpy)_3]$-MoS_2 displayed a markedly different electronic extinction spectrum compared to non-functionalized ce-1T-MoS_2 (Fig. 4.5). The spectrum showed two features in the visible region: one sharp feature at $\lambda_{max} = 304$ nm and a broad shoulder centered at $\lambda_{max} = 450$ nm. In contrast, the ce-1T-MoS_2 precursor displayed two characteristic features at $\lambda_{max} = 258$ and 309 nm and no shoulder in the visible region.[28] The emergence of new features in $[Ru^{II}(bpy)_3]$-MoS_2 can be attributed to the introduced $[Ru^{II}(bpy)_3]^{2+}$ functionalities. Importantly, comparison of the electronic absorption spectra of $[Ru^{II}(bpy)_3]$-MoS_2 and $[Ru^{II}(bpy)_3](PF_6)_2$ (Figure 4.5) revealed that those new features in $[Ru^{II}(bpy)_3]$-MoS_2 were well matched to the ligand Π-Π* (λ_{max} = 288 nm) and metal-to-ligand charge transfer band (λ_{max} = 451 nm) of $[Ru^{II}(bpy)_3](PF_6)_2$. Moreover, an absorbance band at λ_{max} = 550 nm, typical of the $[Ru^{II}(bpy)_2Cl_2]$ precursor, was not detected (Appendix, Fig. S4.4). This shows that there was no unreacted $[Ru^{II}(bpy)_2Cl_2]$ present.

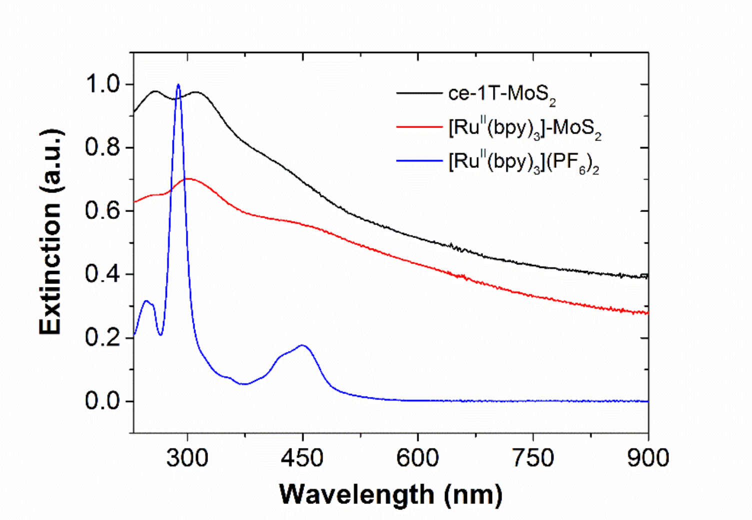

Figure 4.5 Electronic extinction spectra of ce-1T-MoS_2 (black) and $[Ru^{II}(bpy)_3]$-MoS_2 (red) and absorbance spectrum of$[Ru^{II}(bpy)_3](PF_6)_2$ (blue).

Comparison of the diffuse reflectance infrared Fourier transform (DRIFT) spectra of ce-1T-MoS_2, bpy-MoS_2, $[Ru^{II}(bpy)_3]$-MoS_2, and $[Ru^{II}(bpy)_3](PF_6)_2$ provided further proof of the tethering of $[Ru^{II}(bpy)_3]^{2+}$ to the ce-1T-MoS_2 (Figure 4.6). The DRIFT spectrum of bpy-MoS_2 displayed features in the range of 1302 to 1630 cm^{-1} associated with $\nu_{(C=C)}$ and $\nu_{(C=N)}$ modes in the bipyridine ligand. These features were shifted to higher frequencies in $[Ru^{II}(bpy)_3]$-MoS_2, suggesting the bipyridine ligand had interacted with Ru^{II} ion. Critically, $[Ru^{II}(bpy)_3]$-MoS_2 exhibited nearly identical vibrational features to that of $[Ru^{II}(bpy)_3](PF_6)_2$, verifying the incorporation of $[Ru^{II}(bpy)_3]^{2+}$ onto ce-1T-MoS_2.

In addition, a resonance at ν = 695 cm^{-1} was detected in bpy-MoS_2. This was associated with $\nu_{(C-S)}$ vibrational mode, as observed previously for covalently functionalized ce-1T-MoS_2,[9, 29] confirming the formation of covalent C-S bonds upon functionalization. This peak was still discernable in $[Ru^{II}(bpy)_3]$-MoS_2, implying that the covalent linkages remained intact after complexation to Ru^{II} center. Comparison of the DRIFT spectra of $[Ru^{II}(bpy)_3]$-MoS_2 and $[Ru(bpy)_2Cl_2]$ precursor (Appendix, Fig. S4.5) demonstrated marked changes of characteristic vibration modes of the bipyridine ring in the spectra range ~1600- 1400 cm^{-1}, and the absence of fingerprint $\nu_{(Ru-Cl)}$ stretching mode[30] at 327 cm^{-1} in $[Ru^{II}(bpy)_3]$-MoS_2, indicating that the bond strength of $\nu_{(C=C)}$ and $\nu_{(C=N)}$ in bipyridine rings had been considerably altered by replacing σ-donating chloride ligands with π-accepting bipyridine moieties and no $[Ru^{II}(bpy)_2Cl_2]$ precursor was present in the purified $[Ru^{II}(bpy)_3]$-MoS_2 sample. These observations confirm that $[Ru^{II}(bpy)_3]^{2+}$ was covalently assembled on the surface of ce-1T-MoS_2.

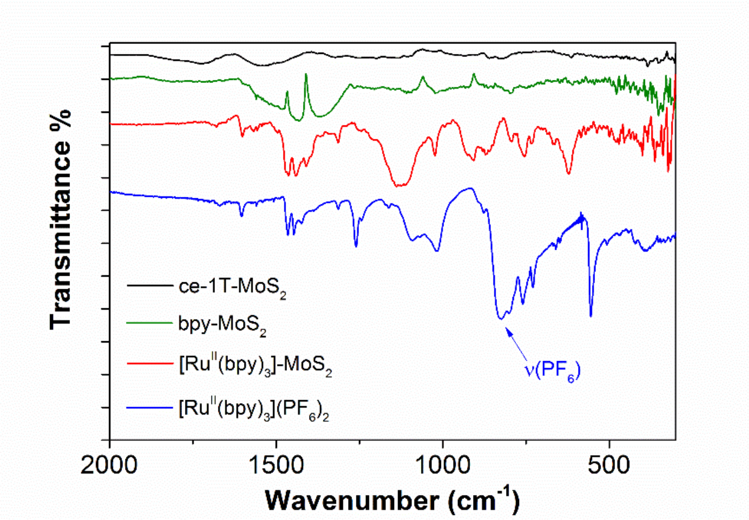

Figure 4.6 DRIFT spectra of ce-1T-MoS_2, bpy-MoS_2, $[Ru^{II}(bpy)_3]$-MoS_2 and $[Ru^{II}(bpy)_3](PF_6)_2$. The intense resonance at 823 cm^{-1} in $[Ru^{II}(bpy)_3](PF_6)_2$ was attributed to PF_6^- counter ions.

Atomic-level inspection of both bpy-MoS_2 and [Ru^{II}(bpy)$_3$]-MoS_2 by high-resolution XPS further confirmed the chemical composition and elemental properties of the functionalized nanosheets. Compared to precursor ce-1T-MoS_2, the XPS survey spectrum of bpy-MoS_2 (Appendix, Fig. S4.6) showed additional C (285 eV) and N (399.5 eV) elements associated with the attached bipyridine moieties, whereas no Br or I signal was detected, suggesting that coupling of 5-bromomethyl-2,2'-bipyridine to ce-1T-MoS_2 was achieved via displacement of Br. Furthermore, the survey spectrum of [Ru^{II}(bpy)$_3$]-MoS_2 displayed additional C, N, and Ru elements deriving from the attached [Ru^{II}(bpy)$_3$]$^{2+}$ (Appendix, Fig. S4.7).

To gain a deeper insight into the chemical identity of the functionalities in bpy-MoS_2 and [Ru^{II}(bpy)$_3$]-MoS_2, high-resolution N 1s /Mo 3p XPS spectra were recorded (Fig. 4.7). The N 1s core level spectrum of bpy-MoS_2 was fitted with one predominant component centered at 398.7 eV, corresponding to the N-atoms of bpy.[31] The N 1s spectrum of [Ru^{II}(bpy)$_3$]-MoS_2 displayed two distinct and intense N features at 398.3 eV and 399.8 eV, implying the presence of two types of nitrogen species. The 399.8 eV component was assigned to N-atoms that are coordinated to a Ru^{II} center; while the lower binding energy N component was assigned to uncoordinated N-atoms, as are present in bpy-MoS_2.[31] The emergence of the 399.8 eV in the post-complexation product validates our synthetic efforts of constructing the [Ru^{II}(bpy)$_3$]$^{2+}$ entity on the ce-1T-MoS_2 surface.[3]

---

[3] However, the presence of non-coordinated pyridyl-N species suggested that not all the surface tethered bipyridine moieties were bonded to Ru^{II} center forming complex, thus the [Ru^{II}(bpy)$_3$]-MoS_2 actually contained both non-coordinated bipyridine moieties and [Ru^{II}(bpy)$_3$]$^{2+}$-complexes.

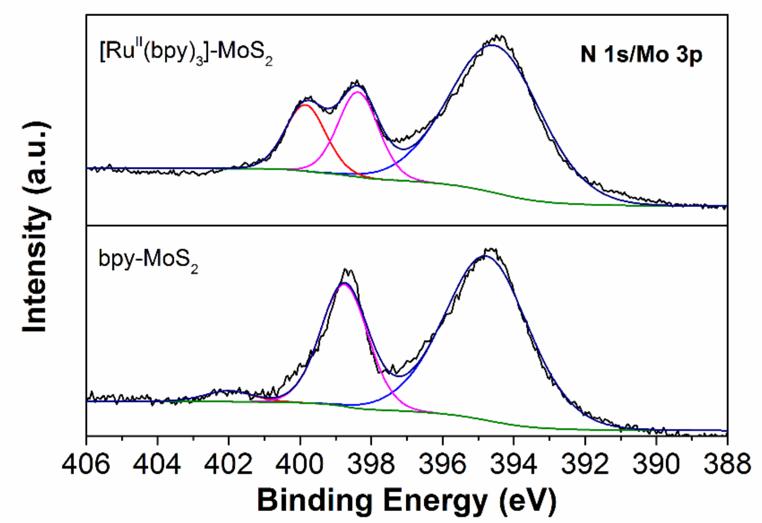

Figure 4.7 Fitted N 1s/Mo 3p spectra of bpy-MoS$_2$ and [Ru^{II}(bpy)$_3$]-MoS$_2$. Color code: blue, Mo 3p$_{3/2}$; pink, N-atoms in bipyridine; red, coordinated N-atoms; and black, fitted envelope. The low intensity feature at 402.0 eV was assigned to quaternized N-atoms[32], presumably derived from the protonated-N species during functionalization.

The degree of ligand functionalization in bpy-MoS$_2$ was estimated by calculating the ratio of the amount of N-atoms to Mo-atoms. Likewise, the loading of [Ru^{II}(bpy)$_3$]$^{2+}$ photosensitizer in [Ru^{II}(bpy)$_3$]-MoS$_2$ was estimated by calculating the ratio of the amount of coordinated N-atoms to Mo-atoms according to the fitted N 1s/Mo 3p spectra (Fig. 4.7). Thus, the ratio of bipyridine groups per MoS$_2$ was approximately 60% per MoS$_2$ in bpy-MoS$_2$ and the ratio of [Ru^{II}(bpy)$_3$]$^{2+}$ per MoS$_2$ was approximately 10% in [Ru^{II}(bpy)$_3$]-MoS$_2$.

The high-resolution S 2p core level spectra (Fig. 4.8) of ce-1T-MoS$_2$ displayed a well-defined double-peak feature associated with S 2p$_{3/2}$ and S 2p$_{1/2}$ signals of MoS$_2$ (2H- and 1T-polymorphy) and a small shoulder at ~163.7 eV associated with edge-S species (the area under green lines).[29] This high binding energy feature became more pronounced in bpy-MoS$_2$, indicating an increased content of electron-poor S species, which presumably derived from functionalized S-atoms (covalent C–S bond).[29, 33] Similar observations were reported for covalent functionalization of ce-1T-MoS$_2$ with organoiodide and diazonium salts.[9] Importantly, this feature was preserved in [Ru^{II}(bpy)$_3$]-MoS$_2$, indicating that the covalent linkers remain intact after complexation treatment.

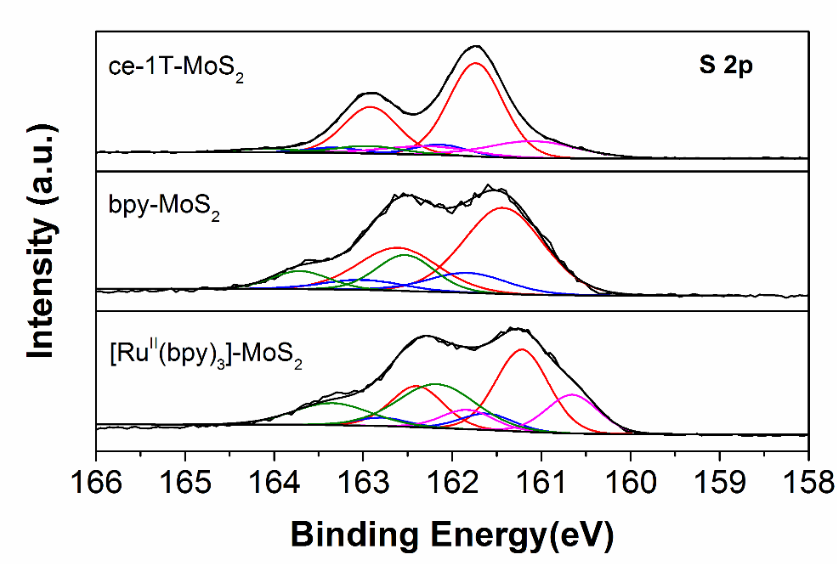

Figure 4.8 Fitted S 2p core level spectra of ce-1T-MoS$_2$, bpy-MoS$_2$ and [Ru^{II}(bpy)$_3$]-MoS$_2$. The S species of 1T-MoS$_2$, 2H-MoS$_2$, electron-rich S and edge (+functionalized) S were marked as red, blue, pink and green, respectively. Fitted envelope was marked as a black trace. The S component at lowest binding energy (the area under pink lines) were assigned as the electron-rich species, which presumably derived from the charge residues after chemical exfoliation. [29]

Unlike S 2p core level spectra, the fitted Mo 3d core level spectra (Fig. 4.9) of bpy-MoS$_2$ and [Ru^{II}(bpy)$_3$]-MoS$_2$ displayed similar features to ce-1T-MoS$_2$ with little change upon functionalization. Furthermore, de-convoluted Mo 3d core level spectra revealed that the proportion of 1T-phase remained predominant in both functionalized samples. This is important, because for efficient HER reactivity we require the MoS$_2$ to maintain the 1T phase.

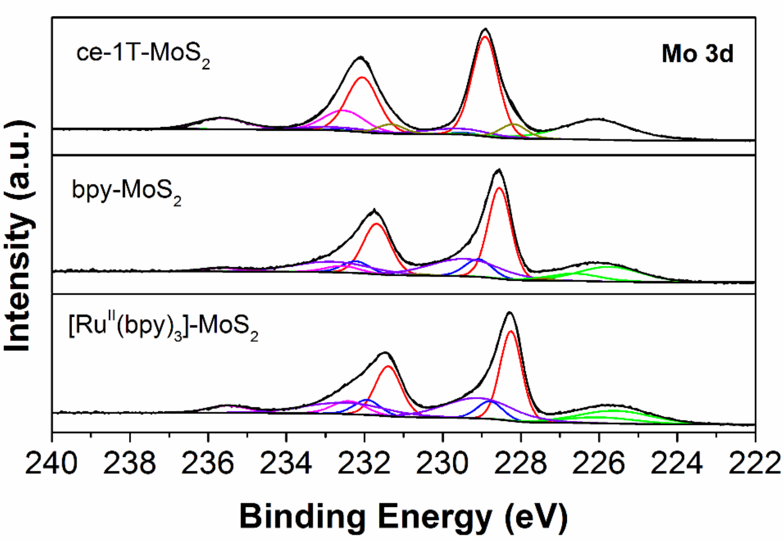

Figure 4.9 Fitted Mo 3d core level spectra of ce-1T-MoS$_2$, bpy-MoS$_2$ and [Ru^{II}(bpy)$_3$]-MoS$_2$. Color code: green, S 2s; red, 1T-MoS$_2$; blue, 2H-MoS$_2$; pink, MoO$_2$; purple, MoO$_3$; and black, fitted envelope.

To further probe the functionalities at bulk level, thermogravimetric analysis (TGA) was performed over carefully dried ce-1T-MoS$_2$, bpy-MoS$_2$, and [Ru^{II}(bpy)$_3$]-MoS$_2$ samples. (Fig. 4.10) Bpy-MoS$_2$ displayed a total mass loss of approximately ~37 wt% before 600 °C, proceeding in two major steps, consistent with the literature observations for other functionalized ce-1T-MoS$_2$ samples.[9] In contrast, the ce-1T-MoS$_2$ only displayed 3% mass loss over the same temperature range. In the same temperature range, [Ru^{II}(bpy)$_3$]-MoS$_2$ displayed ~23 wt% mass loss. The differences in weight loss between bpy-MoS$_2$ and [Ru^{II}(bpy)$_3$]-MoS$_2$ can be ascribed to a higher degree of physisorbed organic material bpy-MoS$_2$ that is likely washed away under the extreme conditions during the preparation of [Ru^{II}(bpy)$_3$]-MoS$_2$. Given that XPS analysis demonstrated that there were some non-coordinated bipyridine entities in $[Ru^{II}(bpy)_3]$-MoS_2 , it is not possible to calculate the degree of complex functionalization by TGA. A rough estimation (5-25 at%) coincides with the value obtained from XPS analysis.

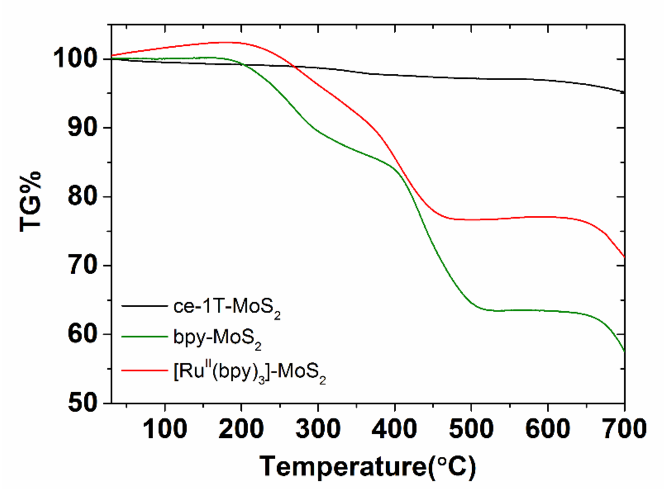

Figure 4.10 TGA profiles of ce-1T-MoS_2, bpy-MoS_2 and $[Ru^{II}(bpy)_3]$-MoS_2.

The X-ray powder diffraction (XRD) pattern (Fig. 4.11) of ce-1T-MoS_2 showed a diffraction peak at 2θ = 14 °, corresponding to the (002) plane of restacked MoS_2. In addition to the (002) signature of restacked ce-1T-MoS_2, two new diffraction peaks at the 2θ value of 5.6 ° and 10.6 ° were also detected, corresponding to the inter-layer expansion of 9.5 Å and 2.3 Å due to the attachment of bipyridine entities on the surface of ce-1T-MoS_2. Importantly, the observed expansions were consistent with the length of horizontally and vertically aligned bipyridine ligands, demonstrating that surface bonded bipyridine entities displayed various orientations in relative to the ce-1T-MoS_2 basal plane, which was possibly attributed to the flexible methylene linkers.

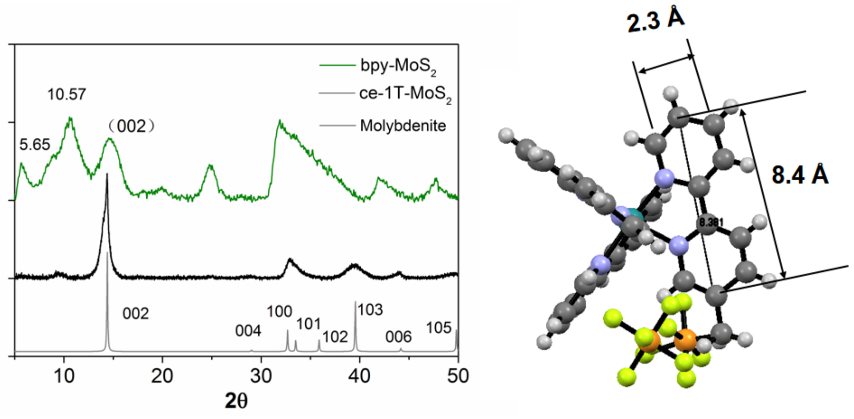

Figure 4.11 Left: powder X-ray diffraction patterns of molybdenite, ce-1T-MoS_2, and bpy- MoS_2. Right: crystal structure of [$Ru^{II}(bpy)_3$]-MoS_2 for ligand size estimation.

The morphology analysis of ce-1T-MoS_2 and [$Ru^{II}(bpy)_3$]-MoS_2 was performed using scanning electron microscopy (SEM). The SEM images displayed both materials as nanoflakes with irregular shapes and diverse lateral sizes of hundred nanometers (Fig. 4.12). Compared to ce-1T-MoS_2, which exhibited the nanoflower-like morphology with well-defined edges, indicating the high crystallinity of the sample, [$Ru^{II}(bpy)_3$]-MoS_2 exhibited aggregations, which could be attributed to surface property change upon functionalization. The energy dispersive X-ray spectroscopy (EDX) mapping (Fig. 4.13) of [$Ru^{II}(bpy)_3$]-MoS_2 demonstrated the uniformly distributed Mo and S elements as well as Ru and N, further verifying the chemical composition of the [$Ru^{II}(bpy)_3$]-MoS_2 functionalized product.

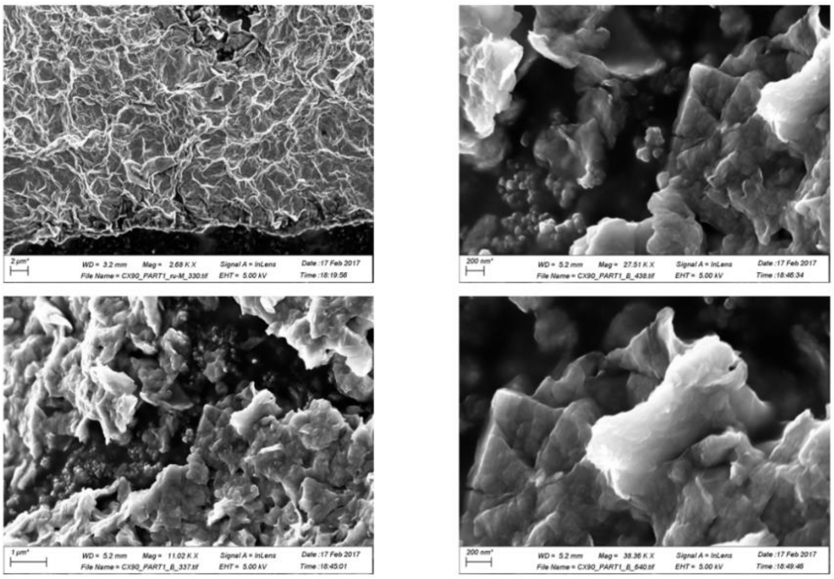

Figure 4.12 SEM images of ce-1T-MoS_2 (top) and [$Ru^{II}(bpy)_3$]-MoS_2 (bottom).

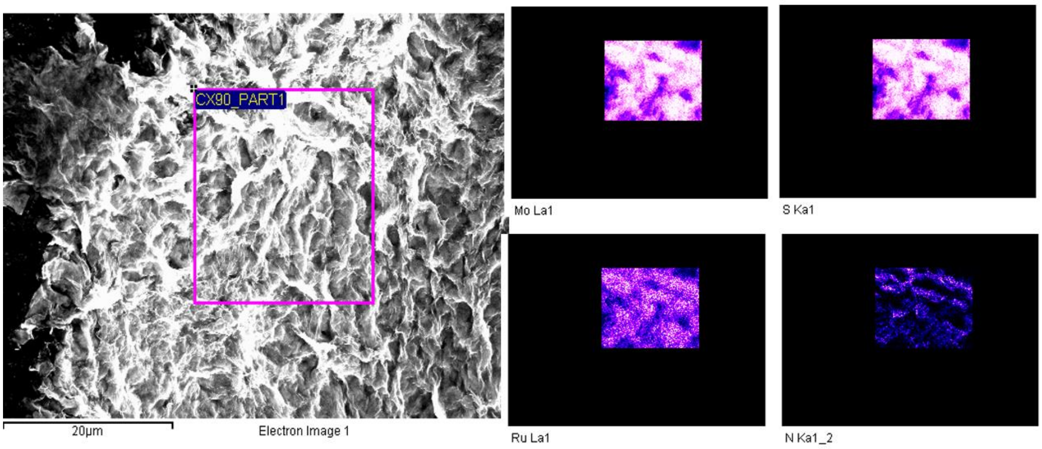

Fig. 4.13 SEM image and EDX elements distribution maps of selected area of [$Ru^{II}(bpy)_3$]-MoS_2.

The zeta potential of the ce-1T-MoS_2 aqueous solution was determined to be -46 mV; whereas the zeta potential of bpy-MoS_2 and [$Ru^{II}(bpy)_3$]-MoS_2 was -11 mV and 5 mV, respectively (Appendix, Fig. S4.8). The significantly shifted zeta potential of the functionalized samples indicated the dramatic surface changes through functionalization.

The Raman Spectra (λ_{exc} = 633 nm, Fig. 4.14) of ce-1T-MoS$_2$, bpy-MoS$_2$ and [Ru^{II}(bpy)$_3$]-MoS$_2$ demonstrated signals typical of MoS$_2$: two intense peaks at ~380 cm^{-1} and ~410 cm^{-1} corresponding to in-plane E$^1_{2g}$ and out-of-plane A$_{1g}$ modes, a resonantly enhanced peak at ~450 cm^{-1} in related to 2LA(M) mode, as well as a series of characteristic peaks related to 1T-MoS$_2$ in the range of 150-300 cm^{-1}.[34, 35] Importantly, the 2LA(M) and A$_{1g}$ modes, which are both highly sensitive to the surface chemical environment change, had demonstrated considerable intensity change in the functionalized samples compared to ce-1T-MoS$_2$, indicating functionalization had occurred.

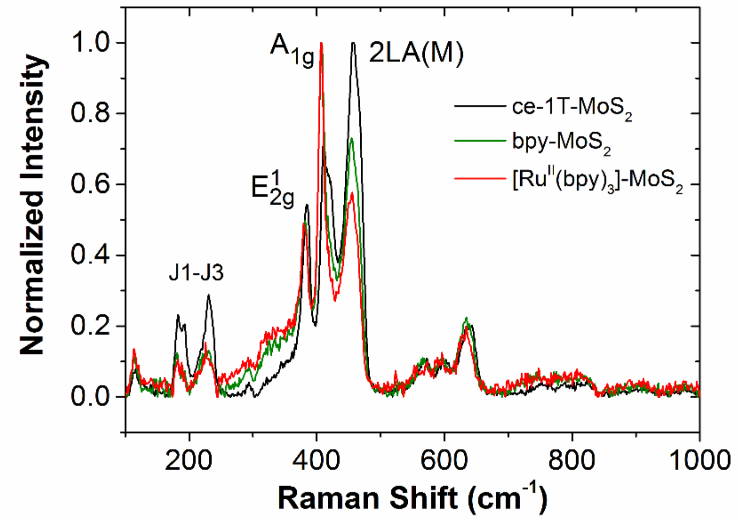

Fig. 4.14 Resonance Raman spectra of ce-1T-MoS$_2$, bpy-MoS$_2$ and [Ru^{II}(bpy)$_3$]-MoS$_2$. Excited at λ = 633 nm.

4.2.5 Photoelectrochemical study

The photoelectrochemical (PEC) performance of the [Ru^{II}(bpy)$_3$]-MoS$_2$ was evaluated in a three-electrode electrochemical cell with 10 mM ascorbic acid electrolyte (Fig. 4.15). The working electrode was illuminated with a 150 W Xe lamp. The photocurrent onset potential (defined here as the potential required to reach -0.2 mA/cm^2) of [$Ru^{II}(bpy)_3$]-MoS_2 photocathode was -0.35 V versus the reversible hydrogen electrode (RHE). For comparison, the same [$Ru^{II}(bpy)_3$]-MoS_2 electrode was also tested with no illumination, exhibiting the maximum current of -0.170 mA/cm^2 at -0.35 V vs. RHE. The marked current density increase upon light illumination indicated that photocurrent was generated by [$Ru^{II}(bpy)_3$]-MoS_2.

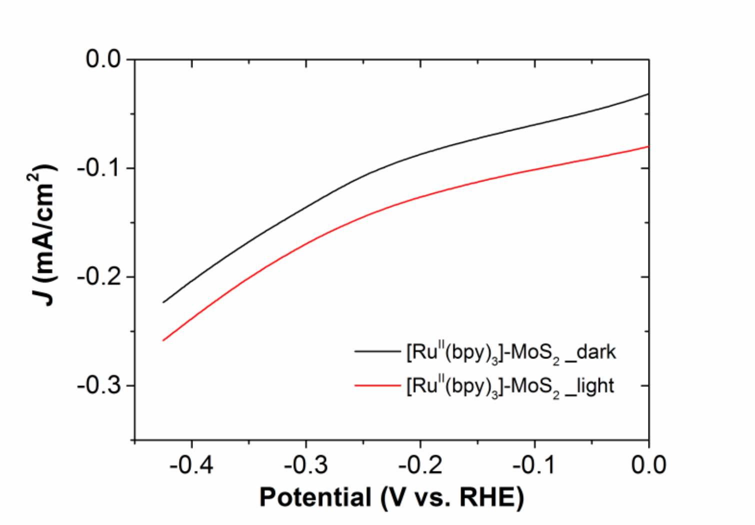

Figure 4.15 Linear sweep voltammograms (LSVs) of the [$Ru^{II}(bpy)_3$]-MoS_2 under darkness and light illumination in 10 mM ascorbic acid aqueous solution (pH= 3).

To verify the role of surface-tethered [$Ru^{II}(bpy)_3$]$^{2+}$ in the photocurrent generation, a control experiment was performed by monitoring the current responses of ce-1T-MoS_2 and [$Ru^{II}(bpy)_3$]-MoS_2 cathodes at an applied bias potential of -0.33 V vs. RHE (the minimum potential required to drive HER using ce-1T-MoS_2 electrode) with chopped light illumination in 60 s intervals (Fig. 4.16). Both ce-1T-MoS_2 and [$Ru^{II}(bpy)_3$]-MoS_2 displayed steady and recyclable photo-enhanced current responses. The photosensitivity of the ce-1T-MoS_2 cathode can be ascribed to the existence of the semiconducting 2H-phase in the ce-1T-MoS_2 sample.[24, 36]

Nevertheless, a much higher current density enhancement was achieved with a value of ΔJ = 33 µA/cm^2 for [Ru^{II}(bpy)$_3$]-MoS_2, compared to ce-1T-MoS_2 (10 µA/cm^2), suggesting a higher photocurrent generation by [Ru^{II}(bpy)$_3$]-MoS_2. In addition, a more prompt photocurrent increase was observed when irradiating [Ru^{II}(bpy)$_3$]-MoS_2 electrode, reflecting a faster photocurrent generation rate.

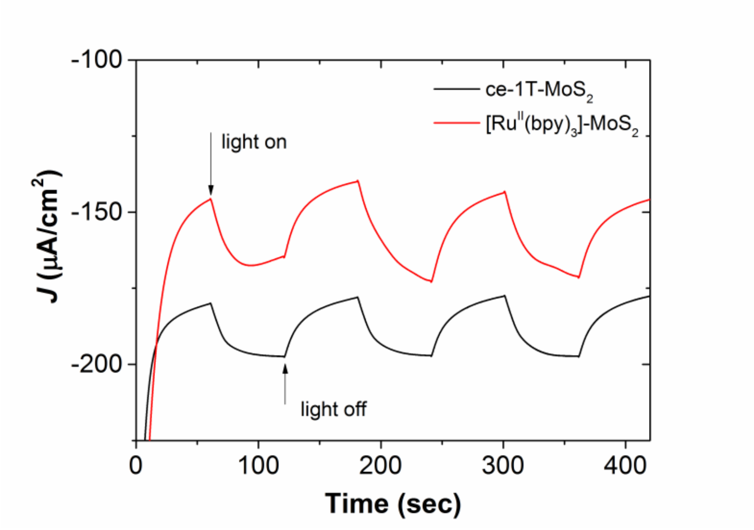

Figure 4.16 Chronoamperometry measurement at E = -0.33 V vs. RHE with ce-1T-MoS_2 and [Ru^{II}(bpy)$_3$]-MoS_2 electrodes in 10 mM ascorbic acid aqueous solution (pH= 3) under chopped light irradiation.

Noticeably, the [Ru^{II}(bpy)$_3$]-MoS_2 cathode exhibited a slightly lower HER activity with a higher photocurrent onset potential (-0.35 V vs. RHE) than non-functionalized ce-1T-MoS_2 (-0.32 V vs. RHE) (Fig. 4.17). Considering that the photocurrent onset potential depends on the photovoltage produced by illumination of light absorbers and overpotential required for driving the HER process, two control experiments were performed to gain more insight on the PEC performance of [Ru^{II}(bpy)$_3$]-MoS_2 for HER. Firstly, the dark catalytic activities of the ce-1T-MoS_2 and [Ru^{II}(bpy)$_3$]-MoS_2 were measured (Fig. 4.17). The [Ru^{II}(bpy)$_3$]-MoS_2 displayed a dark onset potential of -0.40 V vs. RHE, whereas the ce-1T-MoS_2 showed a dark onset potential of -0.34 V vs. RHE when J = -0.2 mA/cm². The lower activity of $[Ru^{II}(bpy)_3]$-MoS_2 is not surprising concerning to the lower density of HER active sites and decreased intralayer conductivity by surface functionalization treatment.[36, 37] Further investigation of the effect of ligand or complex functionalization on the catalytic activity of ce-1T-MoS_2 will be highlighted in Chapter 5. The photovoltage produced in ce-1T-MoS_2 and $[Ru^{II}(bpy)_3]$-MoS_2 was estimated by the difference between dark onset potential and photocurrent onset potential when J = -0.2 mA/cm². For $[Ru^{II}(bpy)_3]$-MoS_2, the photovoltage was calculated to be 50 mV, while ce-1T-MoS_2 only produced a photovoltage of 20 mV. The significantly increased photovoltage generation by $[Ru^{II}(bpy)_3]$-MoS_2 electrode was most likely attributed to the attached $[Ru^{II}(bpy)_3]^{2+}$ photosensitizer.

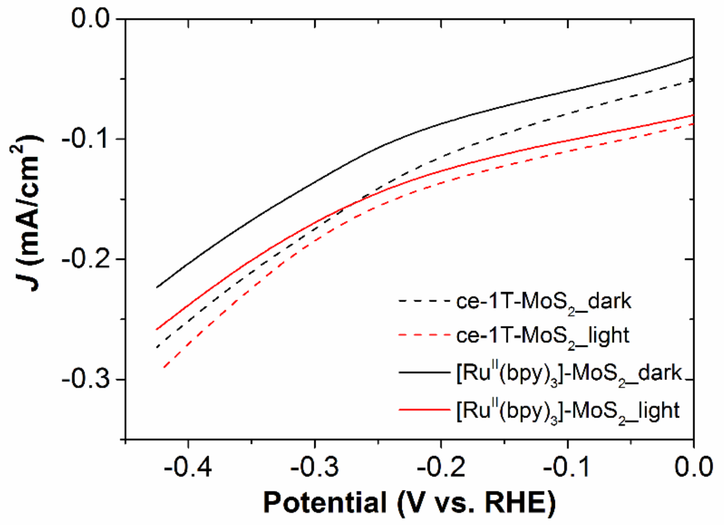

Figure 4.17 Linear sweep voltammograms (LSVs) of the ce-1T-MoS_2 (dashed line) and $[Ru^{II}(bpy)_3]$-MoS_2 (solid line) in darkness (black) and light illumination (red) in 10 mM ascorbic acid aqueous solution (pH= 3).

To evaluate the role of covalent linkage in $[Ru^{II}(bpy)_3]$-MoS_2, an additional control experiment was carried out by simply adding 2 mole equivalents of $[Ru^{II}(bpy)_3](PF_6)_2$ to ce-1T-MoS_2 and performing a Chronoamperometry measurement (CA) at E = -0.33 V vs. RHE. The photocurrent response of the non-tethered mixture against $[Ru^{II}(bpy)_3]$-MoS_2 (Fig. 4.18**)** revealed that $[Ru^{II}(bpy)_3]$-MoS_2 demonstrated a reinforced photocurrent generation as well as a prompt light on/off switching response compared to the non-tethered mixture. It was mostly likely attributed to the presence of covalent linkages in $[Ru^{II}(bpy)_3]$-MoS_2, which inhibited the photogenerated electron-hole recombination and facilitated the efficient interfacial charge transfer, enabling the improved photocurrent generation.

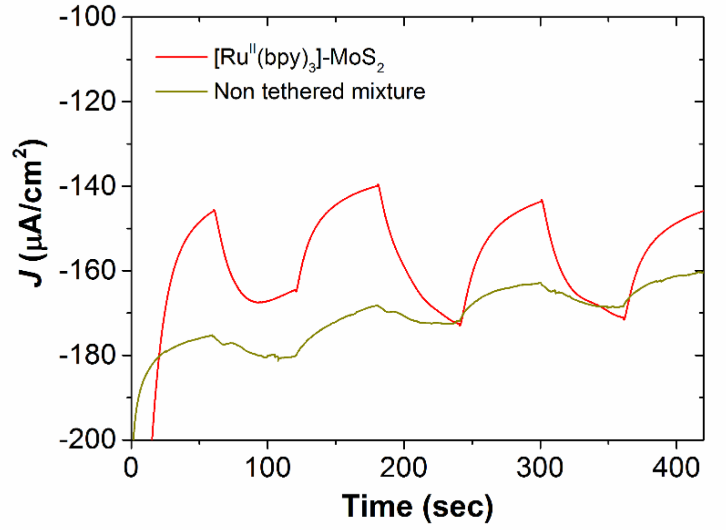

Figure 4.18 Chronoamperometry measurement at E = -0.33 V vs. RHE with $[Ru^{II}(bpy)_3]$-MoS_2 electrode (red) in in 10 mM ascorbic acid aqueous solution and ce-1T-MoS_2 electrode (yellow) in 10 mM ascorbic acid aqueous solution containing $[Ru^{II}(bpy)_3](PF_6)_2$ model complex .

4.3 Conclusion

In conclusion, covalent functionalization of chemically exfoliated MoS_2 nanosheets with $[Ru^{II}(bpy)_3]^{2+}$ dye was accomplished. This was achieved by preparing bpy-functionalized MoS_2 and reacting it with $[Ru^{II}(bpy)_2Cl_2]$. The functionalized materials were characterized by electronic absorption, DRIFT, XPS, Raman spectroscopy, TGA and SEM. Three-electrode PEC measurement of $[Ru^{II}(bpy)_3]$-MoS_2 in ascorbic acid (pH 3) demonstrated a significant improvement of photocurrent generation compared to non-functionalized MoS_2. Efforts to further tune the photo-hydrogen production performance of such 1T-MoS_2 based photocathodes through the covalent incorporation of other photosensitizing molecules and to elucidate the effect of surface functionalization on electrocatalytic activity of 1T-MoS_2 will be demonstrated in Chapter 5.

4.4 Experimental section

4.4.1 Materials

MoS_2 powder was purchased from Sigma Aldrich with particle size of 6 µm and used without purifying. Hexane (Sigma Aldrich) was distilled over a sodium under argon atmosphere before use. N-butyllithium (2.5 M and 1.6 M) in hexane, and other chemicals were purchased from Sigma Aldrich and used as received.

4.4.2 Characterization and Instrumentation

^{1}H-NMR analyses were performed on Agilent 400 NMR two channel instrument with a 5 mm one NMR probe. Electrospray ionization (ESI) mass spectra were acquired using a Micromass time of flight spectrometer (TOF), interfaced to a Waters 2690 HPLC. Thinlayer chromatography (TLC) was performed with Analytical Chromatography alumina sheets coated with silica gel (0.25 mm). Spots were visualized under UV light. Flash column chromatography was conducted with Fluka Silica Gel 60 Å (230–400 mesh). Emission spectra were measured using Horiba Jobin-Yvon FluoroMax-4P spectrometer. UV-Vis Spectroscopy was measured on a Hewlett-Packard (Agilent) 8453 diode array spectrophotometer in quartz cuvettes. DRIFT spectra were acquired using a Perkin Elmer Frontier spectrometer equipped with a diffuse reflectance unit. Samples were prepared by grinding the material samples with CsI (Sigma Aldrich, 99.9 % purity). The CsI baseline was subtracted from the spectra. All the spectra were baseline corrected after acquisition. Raman Spectroscopy was carried out on Horiba Scientific LabRam HR at 1.96 eV (with a 633 nm excitation laser) in air under ambient conditions. 10% of the laser power was used corresponding to ~ 2 mW. The Raman emission was collected by a 100 Å ~ objective (N.A. = 0.8) and dispersed by 600 lines mm^{-1} grating. The mean of 121 spectra from a 100 μm^2 map is displayed. X-ray Photoelectron Spectroscopy was carried out in ultra-high vacuum conditions (<45×10^{-10} mbar) and taken using monochromated Al Kα X-rays from an Omicron XM1000 MkII X-ray source and an Omicron EA125 energy analyzer. An Omicron CN10 electron flood gun was used for charge compensation and the binding energy scale was referenced to the carbon 1s core-level at 284.8 eV. Mo 3d and S 2p core-level regions were recorded at an analyzer pass energy of 15 eV and with slit widths of 6 mm (entry) and 3 mm x 10 mm (exit), resulting in an instrumental resolution of 0.49 eV. After subtraction of a Shirley background, the core-level spectra were fitted with Gaussian-Lorentzian line shapes using the software CasaXPS. Relative atomic percentages were calculated from the ratios of the peak areas after normalization using the relative sensitivity factors (R.S.F.) as provided by the CasaXPS software. Samples were prepared by vacuum filtration onto porous cellulose filter membranes (MF-Millipore membrane, mixed cellulose esters, hydrophilic, 0.025 μm, and 47 mm). Thermogravimetric analysis (TGA) was carried out on a Perkin Elmer Pyris Thermogravimetric Analyser with the following programmed time-dependent temperature profile: hold at 30 °C for 2 min; 30 °C -700 °C with 10 °C /min. The experiments were carried out under N$_2$ gas flow. SEM images were obtained using a ZEISS Ultra Plus (Carl Zeiss Group), 5 kV accelerating voltage, 30 μm aperture, and a working distance of approximately 3-5 mm. The samples were loaded onto the SEM stub using sticky carbon tape.

4.4.3 Synthesis of ligands and model complexes

5-Methyl-2,2’-bipyridine was synthesized according to the prior literature[26] as an orange oil in 90% yield.

5-Bromomethyl-2,2’-bipyridine was synthesized according to the prior literature[26] with a little modification as a yellow solid in 96% yield.
5-methyl-2,2’-bipyridine (2.2 g, 13.0 mmol), *N*-bromo- succinimide (NBS, 2.3 g, 13.0 mmol), and 2,2’-azobis(2-methylpropio- nitrile) (AIBN, 528.2 mg, 3.2 mmol) were dissolved in dry CCl_4 (200 mL). The reaction mixture was refluxed at 80 °C under an Ar atmosphere for 2 h and then stirred at 45 °C for 48 h. The resulting mixture was filtered and the remnant solid was washed with $CHCl_3$ (50 mL). The combined filtrate was collected and reduced in volume to about 50 mL. The filtrate was subsequently neutralized by addition of the saturated aqueous solution of $NaHCO_3$ (50 mL). The organic layer was extracted and washed with 50 mL of brine and dried over $MgSO_4$. The solvent was evaporated and the residue was dried under vacuum for 6 h, yielding 5-bromomethyl-2,2’-bipyridine as a yellow solid (3.2 g, 96%). ^1H NMR (400 MHz, $CDCl_3$) δ 4.51 (s, 2H), 7.25-7.33 (m, 1H), 7.74-7.86 (m, 2H), 8.37 (d, *J* =8.0 Hz, 2H), 8.64-8.66 (m, 2H).

Bis(2,2’-bipyridine)-ruthenium-5-methyl-2,2’-bipyridinehexafluorophos-phate) ($[Ru^{II}(bpy)_3](PF_6)_2$)

$[Ru^{II}(bpy)_2Cl_2]$ was synthesized according to the prior literature[27] as black crystals in 50.6%. $[Ru^{II}(bpy)_2Cl_2]$ (100 mg, 0.21 mmol) and 5-methyl-2,2’-bipyridine (35 mg, 0.21 mmol) were added to an ethanol/water mixed solvent (10 mL, v/v 1:1). The reaction mixture was deaerated for 10 min and then refluxed at 110 °C under Ar atmosphere for 4 h, resulting in a red solution. After cooling to room temperature, the resultant mixture was subjected to centrifugation (3000 rpm, 10 min) to remove un-reacted [$Ru^{II}(bpy)_2Cl_2$] as the sediment. To the clear supernatant solution, a saturated aqueous solution of ammonium hexafluorophosphate (NH_4PF_6) was added, yielding the crude product as an orange-red precipitate. After flash column chromatography on aluminum oxide (50-200 μm，60 Å) (dichloromethane: acetonitrile = 50 : 1, v/v), the pure product was isolated as a red powder (113 mg, 0.155 mmol, 75%). Recrystallization from acetonitrile/diethyl ether yielded red crystals suitable for X-ray diffraction study. ^1H NMR (400 MHz, DMSO) δ 8.88 – 8.70 (m, 6H), 8.15 (q, J = 7.4 Hz, 5H), 8.02 (d, J = 8.2 Hz, 1H), 7.78 – 7.64 (m, 5H), 7.60 – 7.42 (m, 6H), 2.21 (s, 3H). ESI-MS: m/z 745.1231 ([M - PF_6^-]$^+$), $C_{32}H_{30}N_6F_6PRu$, Cal. 745.1217.

Crystal data and structure refinement for [$Ru^{II}(bpy)_3$](PF_6)$_2$.

Empirical formula: $C_{31}H_{26}F_{12}N_6P_2Ru$

Formula weight: 873.59

Temperature: 100.0 K

Wavelength: 1.54178 Å

Crystal system: Triclinic

Space group: $P\bar{1}$

Unit cell dimensions: a = 11.5180(4) Å, α= 104.759(3)°.

b = 13.2859(6) Å, β= 96.471(3)°.

c = 13.5374(6) Å, γ= 100.076(3)°.

Volume: 1945.24(14) Å3

Z: 2

Density (calculated): 1.491 Mg/m3

Absorption coefficient : 4.840 mm-1

F(000): 872

Crystal size: 0.18 x 0.09 x 0.04 mm3

Theta range for data collection: 3.423 to 68.524°.

Index ranges: $-13 \leq h \leq 12$, $-15 \leq k \leq 16$, $-16 \leq l \leq 16$

Reflections collected: 25308

Independent reflections: 7104 [R(int) = 0.0664]

Completeness to theta: 67.679° 99.5 %

Absorption correction Semi-empirical from equivalents

Max. and min. transmission: 0.7531 and 0.5072

Refinement method Full-matrix least-squares on F2

Data / restraints / parameters: 7104 / 14 / 466

Goodness-of-fit on F2: 1.063

Final R indices: $[I>2\sigma(I)]$ R1 = 0.0821, wR2 = 0.2204

R indices (all data): R1 = 0.0927, wR2 = 0.2291

Largest diff. peak and hole: 0.894 and -0.825 e.Å-3

4.4.4 Stepwise synthesis of $[Ru^{II}(bpy)_3]$-MoS_2

Chemically exfoliated MoS_2 (ce-1T-MoS_2) was synthesized by lithium intercalation and exfoliation according to a literature procedure.[38] The typical concentration of ce-1T-MoS_2 was determined as 1 mg/mL (50-70 mL in total). Alternatively, The concentration can also be estimated according to the extinction coefficient of the local minimum at λ = 500 nm: ε = 27.4 mL mg^{-1} cm^{-1}[9].

Preparation of bpy-MoS_2: 5-bromomethyl-2,2'-bipyridine in IPA (10 mL, 25-30 mg/mL) was mixed with an aqueous dispersion of ce-1T-MoS_2 (20 mL, 0.8-1.0 mg/mL) followed by addition of a catalytic amount of NaI (2 mg, 0.013 mmol). The reaction mixture was bath-sonicated (Branson Ultrasonic bath, 750 W) under darkness for 1 h and then kept at room temperature with magnetic stirring for 48 hrs. The resultant dispersion was subjected to high-speed centrifugation at 11000 rpm (13257 *g*) for 1 h to spin down all the functionalized materials and remove the other non-functionalized small flakes and excess organic (dissolved) species. After that, the sediment was washed with ethanol, IPA, and de-ionized water (twice for each solvent). The final sediment was collected in 10 mL of IPA and characterized as such.

Preparation of [$Ru^{II}(bpy)_3$]-MoS_2: Carefully dried bpy-MoS_2 (10 mg) and [$Ru^{II}(bpy)_2Cl_2$] (5 mg, 0.01 mmol) were added to a ethanol/water mixture (30 mL, 1:1 v/v). The reaction mixture was bath-sonicated for 10 min and de-aerated for 15 min by N_2 purging and then refluxed at 120 °C for 12 h under Argon protection. The resulting red-brown suspension was cooled to room temperature and subjected to centrifugation at 11000 rpm for 1 h to spin down all the functionalized materials. The sediment was then subjected to thorough washing with ethanol and water until the supernatant became colorless. The final sediment was collected in 10 mL of de-ionized water for UV-Vis and Zeta potential (ζ) measurements. For XPS, the dispersions of bpy-MoS_2 and [$Ru^{II}(bpy)_3$]-MoS_2 were vacuum-filtered using porous cellulose filter membranes (0.025 μm). The dried powder of bpy-MoS_2 and [$Ru^{II}(bpy)_3$]-MoS_2 were collected after leaving in a vacuum oven at 50 °C for 4 h, and used for DRIFT and TGA. For Raman, SEM, and EDX measurements, aqueous dispersions were drop-cast on Si/SiO_2 wafers or glass slides.

4.4.5 Photoelectrochemical (PEC) measurement

The photoelectrochemical measurement was carried out using a standard three-electrode cell with a platinum (Pt) wire as the counter electrode, a saturated KCl

Ag/AgCl reference electrode and an indium-tin oxide (ITO) glass with samples as the working electrode in one compartment. The working electrode was prepared by drop-casting the material in aqueous dispersion onto ITO glass and dried at room temperature overnight. The mass per area for all the samples was 0.25 mg/cm². 10 mM ascorbic acid aqueous solution (pH 3) was used as the electrolyte and sacrificial donor and a 150W Xe lamp as a light source. The assembled cell was de-aerated with the nitrogen flow for 15 min prior to each measurement. Three-electrode linear sweep voltammetry (LSV) and Chronoamperometry (CA) were performed using a computer-controlled electrochemical workstation (CHI). One or two LSVs were used to activate the electrodes and test for proper electrical connection. Then the current-voltage performance was measured using a LSV from +0.17 V to -0.43 V vs. RHE at a scan rate of 5 mV/s, and the polarization curves were plotted without iR correction. We defined the photocurrent or dark onset potential as the potential observed at a current density of 0.2 mA/cm². Before the CA measurement, samples were conditioned at a given voltage for 20 s. All the CA measurements were held at a constant potential of -0.33 V vs RHE with chopped light illumination in 60 s intervals for 500 s.

References

[1] M. G. Walter, E. L. Warren, J. R. McKone, S. W. Boettcher, Q. Mi, E. A. Santori, N. S. Lewis, *Chem. Rev.* **2010**, *110*, 6446-6473.

[2] Y. Wang, Q. Wang, X. Zhan, F. Wang, M. Safdar, J. He, *Nanoscale* **2013**, *5*, 8326-8339.

[3] C.-Y. Lee, H. S. Park, J. C. Fontecilla-Camps, E. Reisner, *Angew. Chem. Int. Ed.* **2016**, *55*, 5971-5974.

[4] B. A. Pinaud, J. D. Benck, L. C. Seitz, A. J. Forman, Z. Chen, T. G. Deutsch, B. D. James, K. N. Baum, G. N. Baum, S. Ardo, H. Wang, E. Miller, T. F. Jaramillo, *Energy Environ. Sci.* **2013**, *6*, 1983-2002.

[5] C. Xiang, A. Z. Weber, S. Ardo, A. Berger, Y. Chen, R. Coridan, K. T. Fountaine, S. Haussener, S. Hu, R. Liu, N. S. Lewis, M. A. Modestino, M. M. Shaner, M. R. Singh, J. C. Stevens, K. Sun, K. Walczak, *Angew. Chem. Int.*

Ed. **2016**, *55*, 12974-12988.
[6] A. Kudo, Y. Miseki, *Chem. Soc. Rev.* **2009**, *38*, 253-278.
[7] J. D. Benck, T. R. Hellstern, J. Kibsgaard, P. Chakthranont, T. F. Jaramillo, *ACS Catal.* **2014**, *4*, 3957-3971.
[8] F. Wang, T. A. Shifa, X. Zhan, Y. Huang, K. Liu, Z. Cheng, C. Jiang, J. He, *Nanoscale* **2015**, *7*, 19764-19788.
[9] D. Voiry, A. Goswami, R. Kappera, e. SilvaCecilia de Carvalho Castro, D. Kaplan, T. Fujita, M. Chen, T. Asefa, M. Chhowalla, *Nat. Chem.* **2015**, *7*, 45-49.
[10] T. F. Jaramillo, K. P. Jørgensen, J. Bonde, J. H. Nielsen, S. Horch, I. Chorkendorff, *Science* **2007**, *317*, 100-102.
[11] D. Voiry, M. Salehi, R. Silva, T. Fujita, M. Chen, T. Asefa, V. B. Shenoy, G. Eda, M. Chhowalla, *Nano Lett.* **2013**, *13*, 6222-6227.
[12] H. Wang, Z. Lu, S. Xu, D. Kong, J. J. Cha, G. Zheng, P.-C. Hsu, K. Yan, D. Bradshaw, F. B. Prinz, Y. Cui, *Proc. Natl. Acad. Sci. U. S. A.* **2013**, *110*, 19701-19706.
[13] Y. Yan, B. Xia, Z. Xu, X. Wang, *ACS Catal.* **2014**, *4*, 1693-1705.
[14] L. F. Schneemeyer, M. S. Wrighton, *J. Am. Chem. Soc.* **1979**, *101*, 6496-6500.
[15] H. Shi, R. Yan, S. Bertolazzi, J. Brivio, B. Gao, A. Kis, D. Jena, H. G. Xing, L. Huang, *ACS Nano* **2013**, *7*, 1072-1080.
[16] K. Chang, Z. Mei, T. Wang, Q. Kang, S. Ouyang, J. Ye, *ACS Nano* **2014**, *8*, 7078-7087.
[17] L. Yang, D. Zhong, J. Zhang, Z. Yan, S. Ge, P. Du, J. Jiang, D. Sun, X. Wu, Z. Fan, S. A. Dayeh, B. Xiang, *ACS Nano* **2014**, *8*, 6979-6985.
[18] Y. Hou, A. B. Laursen, J. Zhang, G. Zhang, Y. Zhu, X. Wang, S. Dahl, I. Chorkendorff, *Angew. Chem. Int. Ed.* **2013**, *52*, 3621-3625.
[19] J. Chen, X.-J. Wu, L. Yin, B. Li, X. Hong, Z. Fan, B. Chen, C. Xue, H. Zhang, *Angew. Chem. Inter. Ed.* **2015**, *54*, 1210-1214.
[20] W. Zhou, Z. Yin, Y. Du, X. Huang, Z. Zeng, Z. Fan, H. Liu, J. Wang, H. Zhang, *Small* **2013**, *9*, 140-147.
[21] X. Zong, Y. Na, F. Wen, G. Ma, J. Yang, D. Wang, Y. Ma, M. Wang, L. Sun, C. Li, *Chem. Commun.* **2009**, 4536-4538.
[22] Y.-J. Yuan, Z.-T. Yu, X.-J. Liu, J.-G. Cai, Z.-J. Guan, Z.-G. Zou, *Nat. Commun.* **2014**, *4*, 4045.
[23] S. Min, G. Lu, *J. Phys. Chem. C* **2012**, *116*, 25415-25424.
[24] U. Maitra, U. Gupta, M. De, R. Datta, A. Govindaraj, C. N. R. Rao, *Angew. Chem. Int. Ed.* **2013**, *52*, 13057-13061.
[25] M. Grätzel, *Acc. Chem. Res.* **2009**, *42*, 1788-1798.
[26] R. Ballardini, V. Balzani, M. Clemente-León, A. Credi, M. T. Gandolfi, E. Ishow, J. Perkins, J. F. Stoddart, H.-R. Tseng, S. Wenger, *J. Am. Chem. Soc.*

2002, *124*, 12786-12795.

[27] B. P. Sullivan, D. J. Salmon, T. J. Meyer, *Inorg. Chem.* **1978**, *17*, 3334-3341.

[28] G. Eda, H. Yamaguchi, D. Voiry, T. Fujita, M. Chen, M. Chhowalla, *Nano Lett.* **2011**, *11*, 5111-5116.

[29] K. C. Knirsch, N. C. Berner, H. C. Nerl, C. S. Cucinotta, Z. Gholamvand, N. McEvoy, Z. Wang, I. Abramovic, P. Vecera, M. Halik, S. Sanvito, G. S. Duesberg, V. Nicolosi, F. Hauke, A. Hirsch, J. N. Coleman, C. Backes, *ACS Nano* **2015**, *9*, 6018-6030.

[30] M. S. Quinby, R. D. Feltham, *Inorganic Chemistry* **1972**, *11*, 2468-2476.

[31] A. M. Beiler, D. Khusnutdinova, S. I. Jacob, G. F. Moore, *Ind. Eng. Chem. Res.* **2016**, *55*, 5306-5314.

[32] D. Marton, K. J. Boyd, A. H. Al-Bayati, S. S. Todorov, J. W. Rabalais, *Phys. Rev. Lett.* **1994**, *73*, 118-121.

[33] C. Backes, R. J. Smith, N. McEvoy, N. C. Berner, D. McCloskey, H. C. Nerl, A. O'Neill, P. J. King, T. Higgins, D. Hanlon, N. Scheuschner, J. Maultzsch, L. Houben, G. S. Duesberg, J. F. Donegan, V. Nicolosi, J. N. Coleman, *Nat. Commun.* **2014**, *5*, 4576.

[34] X. Zhang, X.-F. Qiao, W. Shi, J.-B. Wu, D.-S. Jiang, P.-H. Tan, *Chem. Soc. Rev.* **2015**, *44*, 2757-2785.

[35] S. Jiménez Sandoval, D. Yang, R. F. Frindt, J. C. Irwin, *Phys. Rev. B* **1991**, *44*, 3955-3962.

[36] R. Peng, L. Liang, Z. D. Hood, A. Boulesbaa, A. Puretzky, A. V. Ievlev, J. Come, O. S. Ovchinnikova, H. Wang, C. Ma, M. Chi, B. G. Sumpter, Z. Wu, *ACS Catal.* **2016**, *6*, 6723-6729.

[37] D. A. Henckel, O. Lenz, B. M. Cossairt, *ACS Catal.* **2017**, *7*, 2815-2820.

[38] S. S. Chou, B. Kaehr, J. Kim, B. M. Foley, M. De, P. E. Hopkins, J. Huang, C. J. Brinker, V. P. Dravid, *Angew. Chem. Int. Ed.* **2013**, *52*, 4160-4164.

CHAPTER 5 Tuning Photoelectrochemical Performance of Ru^{II} Complex Sensitized MoS_2 by Manipulation of the Structure of Photosensitizers

5.1 Introduction

In Chapter 4, a stepwise functionalization strategy was illustrated to covalently bind $[Ru^{II}(bpy)_3]^{2+}$ to chemically exfoliated MoS_2 nanosheets (ce-1T-MoS_2), yielding a nanohybrid construct ($[Ru^{II}(bpy)_3]$-MoS_2). Photoelectrochemical (PEC) testing revealed a reinforced photovoltage generation and prompt photocurrent response compared to non-functionalized ce-1T-MoS_2. Given such possibilities and ease of constructing a $[Ru^{II}(bpy)_3]$-MoS_2 coupling, we have sought to examine whether this step-wise strategy can be utilized in a modular fashion on the ce-1T-MoS_2 surface.

To this end, herein we report the preparation of two new Ru^{II} complex functionalized MoS_2 devices $[Ru^{II}(bpy)_2(phen)]$-MoS_2 and $[Ru^{II}(bpy)_2(py)Cl]$-MoS_2 from their precursors phen-MoS_2 and py-MoS_2. The photoelectrochemical (PEC) measurement of $[Ru^{II}(bpy)_2(phen)]$-MoS_2 deposited photocathode in ascorbic acid displayed a remarkable improvement of photovoltage generation compared to the non-functionalized ce-1T-MoS_2 electrode and previously reported $[Ru^{II}(bpy)_3]$-MoS_2. Several factors that limit the photocatalytic activity of Ru^{II} complex sensitized MoS_2

were discussed and two possible electron transfer pathways in this Ru^{II} photosensitizer functionalized MoS_2 system were proposed.

5.2 Results and discussion

5.2.1 Ligands and model complexes synthesis

The synthesis of 5-iodoacetamido-1,10-phenanthroline and 5-chloroacet-amido-1,10-phenanthroline were accomplished according to the established protocols. The 5-iodoacetamido-1,10-phenanthroline (phen-I)[1] was synthesized by stirring of 5-amino-1,10-phenanthroline and freshly prepared iodoacetic acid anhydride in acetonitrile at room temperature in darkness overnight, yielding a pale brown solid after purification. And the 5-chloroacetamido-1,10-phenanthroline (phen-Cl)[2] was synthesized by reacting of 5-amino-1,10-phenanthroline with 1.2 mole equivalents of chloroacetyl chloride in THF containing 1.0 mole equivalents of triethylamine at room temperature under Argon for 12 h, yielding a beige solid after purification.[4]

For characterization purposes, Bis(2,2'-bipyridine)-(5-chloroacetamido-1,10-phenanthroline)ruthenium bis(hexafluorophosphate) (defined as $[Ru^{II}(bpy)_2\text{-}(phen)](PF_6)_2$ in the following context) was synthesized according to the prior literature[3] by refluxing of $[Ru^{II}(bpy)_2Cl_2]$ and 2-fold molar excess of 5-chloro-acetamido- 1,10-phenanthroline in methanol (25 mL) for 3 h. The resulting reaction mixture was subjected to centrifugation to remove all the unreacted $[Ru^{II}(bpy)_2Cl_2]$ followed by gradual addition of saturated NH_4PF_6 aqueous solution into the clear filtrate. The obtained precipitate was purified by alumina column chromatography, yielding an orange solid in 43% yield. Bis(2,2'-bipyridine)- bis(4-methylpyridine)ruthenium bis(hexafluorophosphate) (defined as $[Ru^{II}(bpy)_2(py)_2]$-

---

[4] Thanks to Amy Lynes from Prof. Thorfinnur Gunnlaugsson's group for providing these two ligands.

$(PF_6)_2$ in this thesis) was synthesized according to the previous literature[4] by refluxing of $[Ru^{II}(bpy)_2Cl_2]$ and 10-fold molar excess of 4-methylpyridine in water (50 mL) for 3h. The resulting reaction mixture was filtered off and the filtrate was precipitated by addition of saturated NH_4PF_6 aqueous solution, yielding an orange solid in 45% yield. The obtained solid was washed with water and then subjected to recrystallization from acetonitrile/ether as an orange-red crystal. (Fig. 5.1)

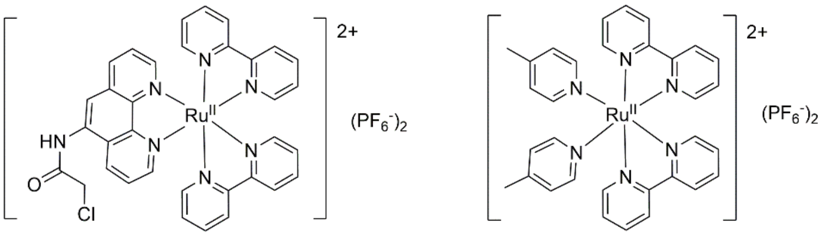

$[Ru^{II}(bpy)_2(phen)](PF_6)_2$ **$[Ru^{II}(bpy)_2(py)_2](PF_6)_2$**

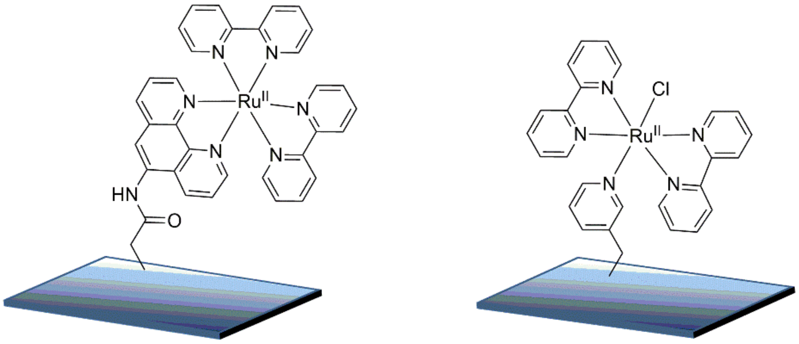

$[Ru^{II}(bpy)_2(phen)]$-MoS_2 **$[Ru^{II}(bpy)_2(py)Cl]$-MoS_2**

Figure 5.1 Structures of the Ru^{II} polypyridyl model complexes and idealized representations of the Ru^{II} polypyridyl complex functionalized MoS_2 analogues.

5.2.2 Functionalization

The step-wise functionalization of ce-1T-MoS_2 with $[Ru^{II}(bpy)_2(phen)]^{2+}$ and $[Ru^{II}(bpy)_2(py)Cl]^{+}$ were performed in a manner analogous to the covalent functionalization of ce-1T-MoS_2 with $[Ru^{II}(bpy)_3]^{2+}$ described in Chapter 4. Specifically, the ligand functionalized MoS_2 sample phen-MoS_2 (or py-MoS_2) was initially prepared by reacting of ce-1T-MoS$_2$ with 10-fold molar excess of 5-iodoacetamido-1,10-phenanthroline (phen-I) (or 3-iodomethylpyridine (py-I)). As the iodide in phen-I or py-I is a good leaving group, thus no catalyst was required in both cases. Subsequently, the obtained phen-MoS$_2$ (or py-MoS$_2$) was mixed with [Ru^{II}(bpy)$_2$Cl$_2$] in a water/ethanol mixture (30 mL, 1:1, v/v) and the reaction mixture was refluxed at 120 °C for 12 h under Ar protection. The resulting reaction mixture was subjected to high-speed centrifugation and the sediment was collected as the complex functionalized product [Ru^{II}(bpy)$_2$(phen)]-MoS$_2$ (or [Ru^{II}(bpy)$_2$-(py)Cl]-MoS$_2$). (Fig. 5.1)

5.2.3 Material characterization

As reported previously, the unmodified ce-1T-MoS$_2$ did not show any absorption band in the visible light region (λ > 400 nm). Both [Ru^{II}(bpy)$_2$(phen)]-MoS$_2$ and [Ru^{II}(bpy)$_2$(py)Cl]-MoS$_2$ displayed a new absorption band centered at around 450 nm, which can be attributed to the characteristic metal-to-ligand charge transfer transition (MLCT) of attached Ru^{II} complex, confirming the successful formation of Ru^{II} complex on MoS$_2$ through our synthetic method.

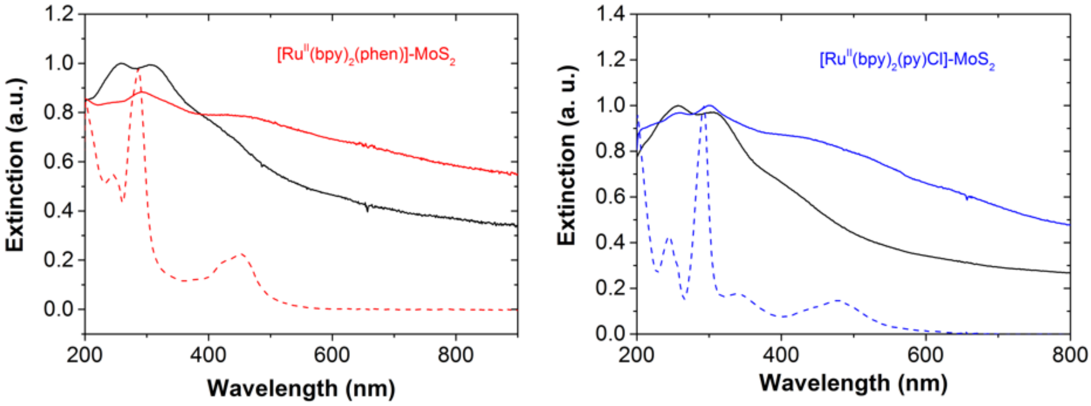

Figure 5.2 The extinction spectra of ce-1T-MoS$_2$ (black, solid line), [Ru^{II}(bpy)$_2$-(phen)]-MoS$_2$ (red, solid line) and [Ru^{II}(bpy)$_2$(py)Cl]-MoS$_2$ (blue, solid line) in H$_2$O.

The absorbance spectra of $[Ru^{II}(bpy)_2(phen)](PF_6)_2$ (red, dashed line) and $[Ru^{II}(bpy)_2(py)_2]$ $(PF_6)_2$ (blue, dashed line) in ethanol.

Characterization of ligand modified MoS_2 nanosheets (phen-MoS_2 and py-MoS_2) and associated post-complexation products ($[Ru^{II}(bpy)_2(phen)]$-MoS_2 and $[Ru^{II}(bpy)_2(py)Cl]$-MoS_2) using DRIFT provided further evidence of covalent functionalization of MoS_2 nanosheets with the desired ligands and complexes (Fig. 5.3, left). The DRIFT spectra of phen-MoS_2 displayed a series of new features between 1660 to 1400 cm^{-1} corresponding to $\nu_{(C=C)}$ and $\nu_{(C=N)}$ modes in 1,10-phenanthroline and two intense peaks at around 1684 cm^{-1} and 1535 cm^{-1} associated with the C=O stretching vibration and in plane N-H bending of the ancillary amide group; while comparison of DRIFT spectra of $[Ru^{II}(bpy)_2(phen)]$-MoS_2 with $[Ru^{II}(bpy)_2(phen)](PF_6)_2$ revealed a perfect overlap, confirming the chemical identity of the attached $[Ru^{II}(bpy)_2(phen)]^{2+}$ complex in $[Ru^{II}(bpy)_2(phen)]$-MoS_2. Most importantly, the presence of the amide group emphasized that the $[Ru^{II}(bpy)_2(phen)]^{2+}$ complex was attached to MoS_2 via an amide linkage in $[Ru^{II}(bpy)_2(phen)]$-MoS_2.

For $[Ru^{II}(bpy)_2(py)Cl]$-MoS_2 (Fig. 5.3, right), in addition to the characteristic features in the spectra range ~1600-1260 cm^{-1} associated with the stretching vibration of C=C, C=N and C-N bonds of the bipyridyl ring and the fingerprint C=C bond vibration mode of the pyridine ring at around 1499 cm^{-1}, another feature with mild intensity was observed at 324 cm^{-1}, which can be assigned as the $\nu_{(Ru\text{-}Cl)}$ stretching[5] mode, suggesting the presence of a Ru-Cl bond in the post-complexation product. This observation was within our expectations considering the mono-dentate nature of the pyridine moiety and the octahedral geometry of Ru^{II} complex, which makes coordinating two surface tethered pyridine ligands to Ru^{II} center at the same time more difficult. Overall, the collective information regarding the chemical bonds and the change in environment verified the successful coordination of the surface- tethered ligand to the Ru^{II} center by displacement of one (in case of $[Ru^{II}(bpy)_2(py)Cl]$-MoS_2) or two (in case of $[Ru^{II}(bpy)_2(phen)]$-MoS_2) axial chloride ligands and supported the proposed binding modes in the complex functionalized samples.

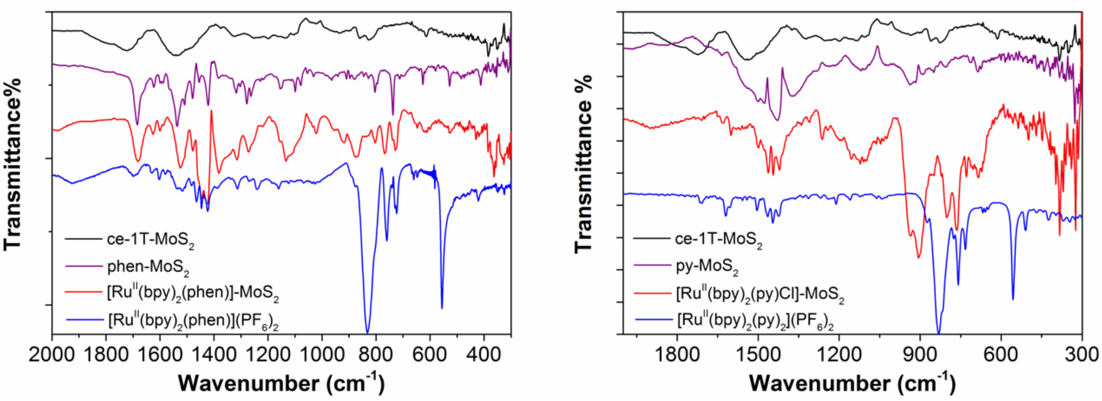

Figure 5.3 Left: DRIFT spectra of ce-1T-MoS_2, phen-MoS_2, $[Ru^{II}(bpy)_2(phen)]$-MoS_2 and $[Ru^{II}(bpy)_2(phen)](PF_6)_2$. Right: DRIFT spectra of ce-1T-MoS_2, py-MoS_2, $[Ru^{II}(bpy)_2(py)Cl]$-MoS_2 and $[Ru^{II}(bpy)_2(py)_2](PF_6)_2$. The spectra are normalized for comparison. The feature at 385 cm^{-1} in all spectra corresponded to the typical feature of Mo-S bond vibration in MoS_2. And the intense feature at 832 cm^{-1} in model complexes attributed to the PF_6^-.

To gain more insight into the chemical composition and the loading of functionalities in functionalized materials, X-ray photoelectron spectroscopy (XPS) was conducted. The successful functionalization of MoS_2 with ligands was confirmed by observing signals from N 1s and C 1s in XPS at ~395 eV and ~286 eV, respectively. And complex functionalized samples displayed an additional Ru 3p signal at~ 462 eV and incredibly increased C content, suggesting the formation of Ru^{II} complex in

$[Ru^{II}(bpy)_2(phen)]$-MoS_2 and $[Ru^{II}(bpy)_2(py)Cl]$-MoS_2 through functionalization (Fig. S5.1-5.4). The degree of functionalization estimated by calculating the ratio of atomic percentage of Ru $3p_{3/2}$ at 462.50 eV to Mo was found to be 5.4 at% and 10.2 at% per MoS_2 for $[Ru^{II}(bpy)_2(phen)]$-MoS_2 and $[Ru^{II}(bpy)_2(py)Cl]$-MoS_2, respectively.

From N 1s core level spectra (Fig. 5.4), there was no detectable N species in the non-functionalized MoS_2 sample. The N 1s spectra of phen-ceMoS_2 can be de-convoluted into two predominant peaks at 398.7 eV and 399.8 eV. The peak at 399.8 eV was attributed to nitrogen species from the ancillary amide chain of ligands.[6] And the largest contribution at 398.7 eV corresponded to N-atoms from 1, 10-phenanthroline.[6] For $[Ru^{II}(bpy)_2(phen)]$-MoS_2 sample, the best fitting of N 1s spectra gave rise to two components at ~399.4 eV and ~400.72 eV, corresponding to the N-atoms in 1,10-phenanthroline and N-atoms in amide [6], respectively. It was noted that the proportion of the nitrogen component at high BE was increased considerably in $[Ru^{II}(bpy)_2(phen)]$-MoS_2, which can be attributed to appearance of a new type of nitrogen that had a higher BE than N-atoms in 1,10-phenanthroline, but very closed to the BE of N-atoms in amide. This new type of nitrogen was likely derived from the coordinated N species in $[Ru^{II}(bpy)_2(phen)]^{2+}$ complex. The coordination of N-atoms of 1,10-phenanthroline to the Ru^{II} center reduced the electron density in N outer shells and then a stronger attraction was applied to the inner shells (N 1s), resulting in the XPS peaks with a higher binding energy than non-coordinated N atoms.

The degree of ligand functionalization in phen-MoS_2, estimated by calculating the ratio of the amount of N-atoms to Mo-atoms, was found to be ~ 57 at% per MoS_2; whereas the degree of complex functionalization in $[Ru^{II}(bpy)_2(phen)]$-MoS_2, estimated by calculating the ratio of the amount of N-coordinated atoms to Mo-atoms, was found to be 17 at% per MoS_2.[5]

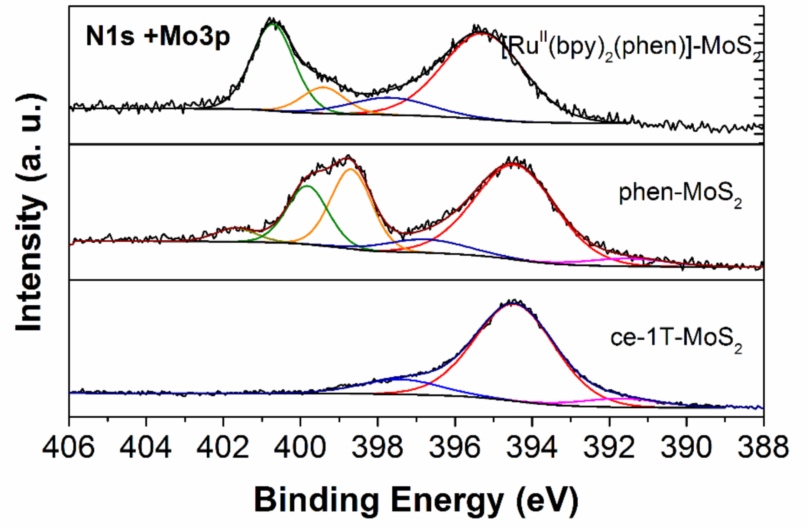

Figure 5.4 Fitted N 1s/Mo 3p core level spectra of ce-1T-MoS_2, phen-MoS_2 and [$Ru^{II}(bpy)_2(phen)$]-MoS_2. Color code: red, 1T-Mo $3p_{3/2}$; blue, 2H-Mo $3p_{3/2}$; orange, N-atoms in 1,10-phenanthroline; green, N-atoms in amide ancillary group and N-coordinated atoms; black, fitted envelope. The low intensity feature at 401.7 eV was assigned to quaternized N-atoms[7], presumably derived from the pronated N.

To study the change of S valence states upon functionalization, the S 2p core level spectra of ce-1T-MoS_2, phen-MoS_2 and [$Ru^{II}(bpy)_2(phen)$]-MoS_2 were recorded (Fig. 5.5). The pristine ce-1T-MoS_2 displayed a well-defined double-peak feature associated with S $2p_{3/2}$ and S $2p_{1/2}$ from 2H-MoS_2 and 1T-MoS_2. After functionalization with 1, 10-phenanthroline ligands, a new feature at high binding energy appeared, which was attributed to the functionalized sulfur component (S-C bonds). Previous studies on covalent functionalization of ce-1T-MoS_2 using

---

[5] The presence of non-coordinated N-atoms in [$Ru^{II}(bpy)_2(phen)$]-MoS_2 suggested that not all the surface-tethered ligands were coordinated to Ru^{II}, therefore the functionalities in [$Ru^{II}(bpy)_2(phen)$]-MoS_2 included both uncoordinated ligands and [$Ru^{II}(bpy)_2(phen)$]$^{2+}$ complex.

organoiodides also demonstrated the a similar trend, leading to the conclusion that covalent functionalization was achieved by covalently bind functionalities on the surface S atoms of MoS_2[8, 9] Most importantly, this feature remained existing in $[Ru^{II}(bpy)_2(phen)]$-MoS_2, indicating that covalent linkers remained intact even after complexation treatment. Similar analysis of the N 1s and S 2p region of py-MoS_2 and $[Ru^{II}(bpy)_2(py)Cl]$-MoS_2 (Fig. S5.5) revealed the successful formation of $[Ru^{II}(bpy)_2(py)Cl]^+$ on the surface of MoS_2 and the presence of C-S linkages in functionalized samples.

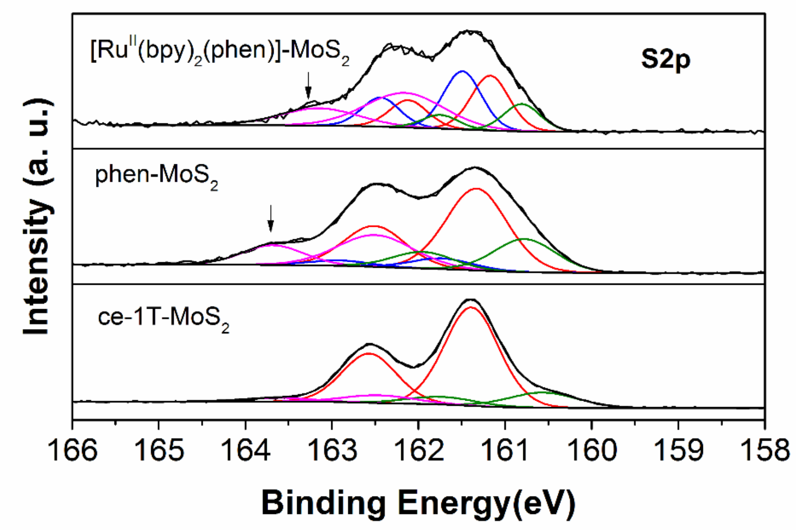

Figure 5.5 Fitted S 2p core level spectra of ce-1T-MoS_2, phen-MoS_2 and $[Ru^{II}(bpy)_2(phen)]$-MoS_2. The S species of 1T-MoS_2, 2H-MoS_2, electron rich S and edge (+functionalized) S are marked as red, blue, magenta and green, respectively. Fitted envelope is marked as a black trace. The S component at lowest binding energy (the area under pink lines) were assigned as the electron-rich species, which presumably derived from the charge residues after chemical exfoliation. [8]

The effect of the Ru^{II} complex functionalization on the zeta potentials of the ce-1T-MoS_2 was depicted in Fig. 5.6. The zeta potential of the ce-1T-MoS_2 aqueous solution was determined to be -43 mV; whereas the zeta potential of

$[Ru^{II}(bpy)_2(phen)]$-MoS_2 and $[Ru^{II}(bpy)_2(py)Cl]$-MoS_2 was determined to be 15 mV and 5 mV, respectively. The significant positive shift of zeta potential in complex functionalized samples indicated the dramatic surface property and surface charge change upon adding functional entities.

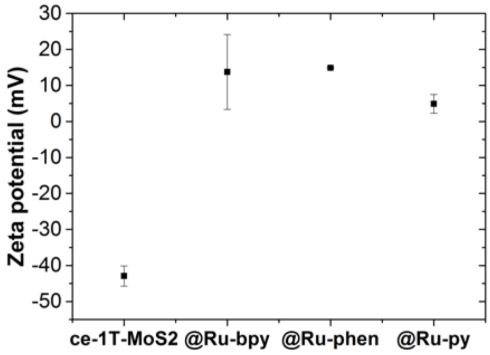

samples	Ru^{II} Complex per MoS_2 (mole)
$[Ru^{II}(bpy)_3]$-MoS_2	11 at%
$[Ru^{II}(bpy)_2(phen)]$ -MoS_2	17 at%
$[Ru^{II}(bpy)_2(py)Cl]$-MoS_2	10 at%

Figure 5.6 Effect of the Ru^{II} complex functionalization on the zeta potentials of the ce-1T-MoS_2. The error bars represent the s.d. of three replicate measurements. Inset table: the functionalization degree of the Ru^{II} complex functionalized MoS_2 samples.

Thermogravimetric analysis (TGA) revealed (Fig. 5.7, left) that the degree of functionalization was 25 wt% and 32 wt% for phen-MoS_2 and py-MoS_2, respectively, further confirming the successful ligand functionalization. In addition, comparison of the Raman spectra ((λ_{exc} = 633 nm, Fig. 5.7, right) of phen-MoS_2 and py-MoS_2 with as-prepared ce-1T-MoS_2 revealed a significantly attenuated resonant peak (2LA(M) mode) at ~450 cm^{-1} in functionalized samples compared to pristine ce-1T-MoS_2. This indicated a dramatic change in the resonant Raman process after functionalization, which was likely due to the strong interaction of surface functionalities and MoS_2.

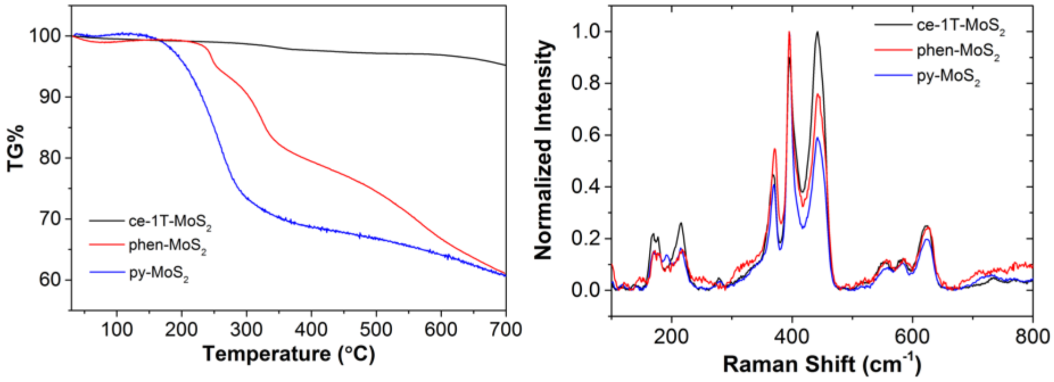

Figure 5.7 TGA and Raman spectra of ce-1T-MoS_2, phen-MoS_2 and py-MoS_2.

The SEM images (Fig. 5.8) of restacked ce-1T-MoS_2 displayed lots of wavy features, indicative of a large extent of exposed edges due to the back-folding of nanosheets and reduced thickness of nanosheets. The charging effect observed at edges was due to the metallic 1T-phase which was present in significant amounts.[10] After ligand functionalization, the surface charges were effectively annihilated by the high extent of ligand coverage, resulting in well-resolved shapes of nanoflakes with the size of around 500 nm. In addition, the severe aggregation can be observed in both phen-MoS_2 and py-MoS_2 samples, which can be attributed to the dramatically altered surface property upon functionalization.

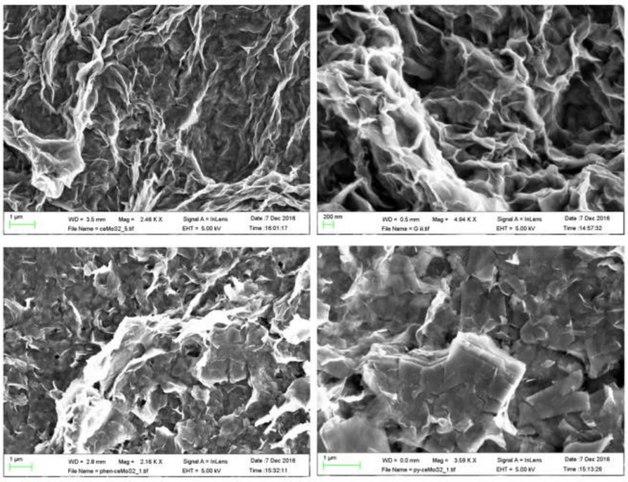

Figure 5.8 SEM images of ce-1T-MoS_2 (top), phen-MoS_2 (bottom, left) and

py-MoS_2 (bottom, right).

5.2.4 Photoelectrochemical study in ascorbic acid

The photoelectrochemical (PEC) performance of the $[Ru^{II}(bpy)_2(phen)]$-MoS_2 was evaluated in a three-electrode electrochemical cell with 10 mM ascorbic acid electrolyte (Fig. 5.9). The working electrode was illuminated with a 150 W Xe lamp. The photocurrent onset potential (defined here as the potential required to reach -0.2 mA/cm^2) of $[Ru^{II}(bpy)_2(phen)]$-MoS_2 photocathode was -0.56 V vs. the reversible hydrogen electrode (RHE). The same $[Ru^{II}(bpy)_2(phen)]$-MoS_2 electrode was also tested with no illumination, exhibiting the dark onset potential of -0.62 V vs. RHE, about 59 mV higher than the illuminated electrode, indicating that 60 mV of photovoltage was generated by $[Ru^{II}(bpy)_2(phen)]$-MoS_2 electrode under light illumination. For comparison, the photocurrent onset potential and dark onset potential of ce-1T-MoS_2 were found to be -0.32 V and -0.34 V vs. RHE, respectively. Thus the photovoltage produced by ce-1T-MoS_2 electrode was calculated to be 20 mV. Compared to ce-1T-MoS_2 electrode, the significant increased photovoltage generation of $[Ru^{II}(bpy)_2(phen)]$-MoS_2 electrode was most likely attributed to the anchored $[Ru^{II}(bpy)_2(phen)]^{2+}$ photosensitizer, whereby the photogenerated charges aided the protons reduction, reducing the potential required from the external circuit.

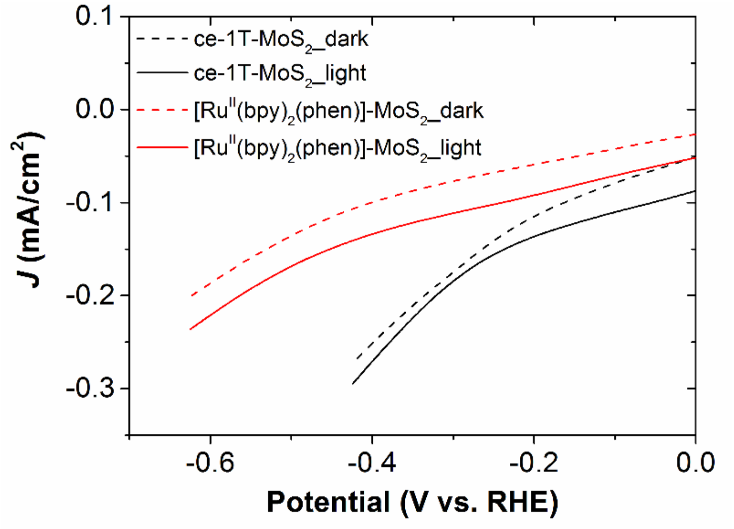

Figure 5.9. Linear sweep voltammograms (LSVs) of the ce-1T-MoS$_2$ (dark) and [Ru^{II}(bpy)$_2$(phen)]-MoS$_2$ (red) in darkness (dashed) and light (solid) illumination in 10 mM ascorbic acid aqueous solution (pH = 3).

The photoelectrochemical properties of [Ru^{II}(bpy)$_2$(phen)]-MoS$_2$ electrode was further examined by monitoring the current responses of the [Ru^{II}(bpy)$_2$(phen)]-MoS$_2$ cathode at an applied bias potential of -0.33 V vs. RHE (the minimum potential required to drive HER using ce-1T-MoS$_2$ electrode) with chopped light illumination in 60 s intervals (Fig. 5.10). Compared with the weak photocurrent response of ce-1T-MoS$_2$ electrode (10 μA/ cm^2), [Ru^{II}(bpy)$_2$(phen)]-MoS$_2$ displayed a much higher cathodic current density enhancement with Δ*J* of 22 μA/cm^2, implying a higher photocurrent generation by [Ru^{II}(bpy)$_2$(phen)]-MoS$_2$ electrode. This observation signified the role of surface-tethered [Ru^{II}(bpy)$_2$(phen)]$^{2+}$ complexes in the photo-current conversion.

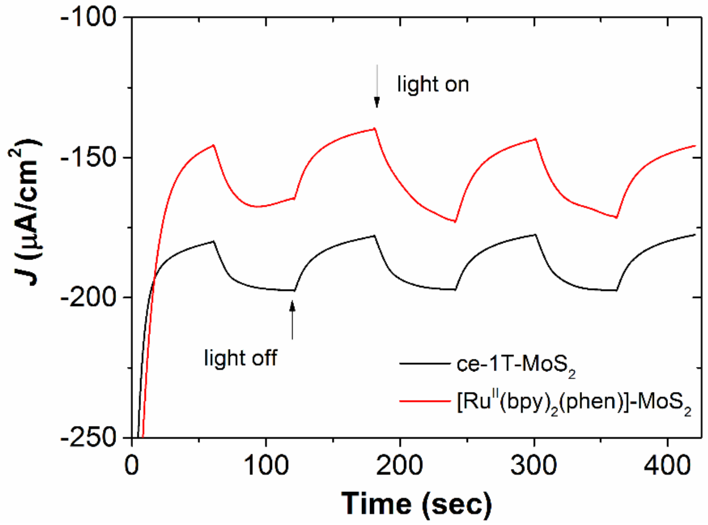

Figure 5.10 Chronoamperometry (CA) measurement at E = -0.33 V vs. RHE with ce-1T-MoS_2 and [Ru^{II}(bpy)$_2$(phen)]-MoS_2 electrodes in 10 mM ascorbic acid aqueous solution (pH = 3).

Interestingly, comparing the photoelectrochemical HER performance of [Ru^{II}(bpy)$_2$(phen)]-MoS_2 with previously demonstrated [Ru^{II}(bpy)$_3$]-MoS_2 (Table 5.1) revealed that the photovoltage generated by [Ru^{II}(bpy)$_2$(phen)]-MoS_2 was about 1.3 times greater than that by [Ru^{II}(bpy)$_3$]-MoS_2, yet the photocurrent produced by [Ru^{II}(bpy)$_2$(phen)]-MoS_2 was only 67% of that by [Ru^{II}(bpy)$_3$]-MoS_2. These results implied that charge transport resistance in the [Ru^{II}(bpy)$_2$(phen)]-MoS_2 electrode was much higher than in the [Ru^{II}(bpy)$_3$]-MoS_2 electrode. Previous investigations on the application of covalently functionalized ce-1T-MoS_2 in Field Effect Transistors by Chhowalla's group[9] have demonstrated that covalent bonding of functional groups would decrease the concentration of free electrons, leading to a less conductive MoS_2 film. Considering this result, it can be deduced that the higher resistance of [Ru^{II}(bpy)$_2$(phen)]-MoS_2 device was presumably related to the higher content of surface covalent bonding due to functionalization. However, the degree of covalent functionalization (the degree of ligand functionalization) was estimated to be 57 at% per MoS_2 in [$Ru^{II}(bpy)_2(phen)$]-MoS_2 according to XPS analysis, which was quite similar to that in [$Ru^{II}(bpy)_3$]-MoS_2 60 at% per MoS_2, thus there must be other factors that significantly affected the resistance of dye-sensitized MoS_2 devices. In addition, the dark onset potential of [$Ru^{II}(bpy)_2(phen)$]-MoS_2 was ~220 mV higher compared to that of [$Ru^{II}(bpy)_3$]-MoS_2, demonstrating a much lower electrocatalytic activity for HER. This low electrocatalytic activity of [$Ru^{II}(bpy)_2(phen)$]-MoS_2 appeared to dominate the photoelectrochemical performance, resulting in a larger photocurrent onset potential, regardless of a higher photovoltage generation in comparison to [$Ru^{II}(bpy)_3$]-MoS_2.

Table 5.1 Photoelectrochemical properties of the ce-1T-MoS_2 electrode and dye-sensitized MoS_2 electrodes in 10 mM ascorbic acid aqueous solution (pH= 3).

Electrodes	**Dye per MoS_2**	**[a]Photocurrent onset potential V vs. RHE**	**[a]Photovoltage mV vs. RHE**	**[a]Dark onset potential V vs. RHE**	**[b]Δ*J* μA/ cm^2**
[$Ru^{II}(bpy)_3$]-MoS_2	11%	-0.35	50	-0.40	33
[$Ru^{II}(bpy)_2$ (Phen)]-MoS_2	17%	-0.56	60	-0.62	22
ce-1T-MoS_2	0	-0.32	20	-0.34	10

[a] When J = -0.2 mA/cm^2; [b]E = -0.33 V vs. RHE. All the photoelectrochemical properties of a specific material deposited electrode were obtained based on at least three independent electrodes, each performed in triplicate and the best results are presented.

5.2.5 Electrocatalytic measurements in 0.5 M H_2SO_4

To further probe the effect of covalent functionalization of ce-1T-MoS_2 on the electrocatalytic activity for HER and gain more insight on the HER mechanism of this Ru^{II} complex functionalized MoS_2 system, the electrocatalytic properties (Fig. 5.11, Table S5.1) of ce-1T-MoS_2, phen-MoS_2, [Ru^{II}(bpy)$_2$(phen)]-MoS_2, py-MoS_2 and [Ru^{II}(bpy)$_2$(py)Cl]-MoS_2 were evaluated in a standard acidic electrolyte (0.5 M H_2SO_4). According to the linear sweep voltammograms (LSV), the overpotential (defined here as the potential required to reach -10 mA/cm^2) of ce-1T-MoS_2 was found to be -0.26 V vs. RHE, whereas the overpotential of functionalized samples were observed at -0.50, -0.36 and -0.33 V vs. RHE for [Ru^{II}(bpy)$_2$(phen)]-MoS_2, py-MoS_2 and [Ru^{II}(bpy)$_2$(py)Cl]-MoS_2, respectively. The dramatically increased overpotential of functionalized samples in comparison to ce-1T-MoS_2 indicated the lower electrocatalytic activities of functionalized samples compared to non-functionalized ce-1T-MoS_2.

Interestingly, the overpotential of [Ru^{II}(bpy)$_2$(py)Cl]-MoS_2 was 33 mV lower than its precursor (py-MoS_2), demonstrating a higher electrocatalytic activity of [Ru^{II}(bpy)$_2$(py)Cl]-MoS_2 compared to py-MoS_2, although the extent of surface functional groups (degree of covalent functionalization) were the same. A similar trend was also observed when comparing the electrocatalytic activity of [Ru^{II}(bpy)$_2$(phen)]-MoS_2 with phen-MoS_2. This observation suggested that coordinating the surface-tethered ligands to Ru^{II} centers was in favor of improving the catalytic activity of functionalized MoS_2 devices.

Further comparison of [Ru^{II}(bpy)$_2$(py)Cl]-MoS_2 and [Ru^{II}(bpy)$_2$(phen)]-MoS_2 revealed a better catalytic activity of [Ru^{II}(bpy)$_2$(py)Cl]-MoS_2 compared to [Ru^{II}(bpy)$_2$(phen)]-MoS_2. Since the degree of covalent functionalization in [Ru^{II}(bpy)$_2$(py)Cl]-MoS_2 was higher than in [Ru^{II}(bpy)$_2$(phen)]-MoS_2 based on TGA (Fig. 5.7), thus the active surface area of [Ru^{II}(bpy)$_2$(py)Cl]-MoS_2 was theoretically smaller than [Ru^{II}(bpy)$_2$(phen)]-MoS_2, which was contrary to the observed catalytic activity. Therefore, other than the area of active surface or the number of active sites, there should be other factors that dominantly affected the electrocatalytic activity of functionalized MoS$_2$.

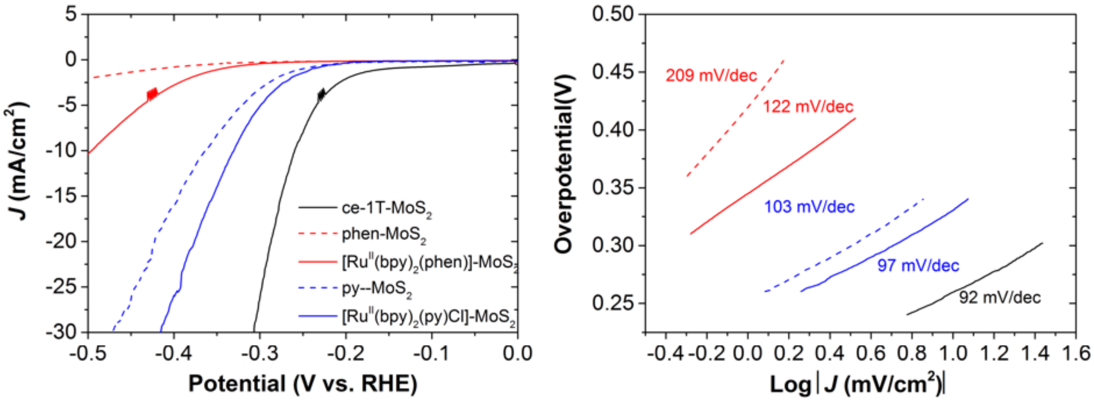

Figure 5.11 Left: Linear sweep voltammograms (LSVs) of the ce-1T-MoS$_2$, phen-MoS$_2$, [Ru^{II}(bpy)$_2$(phen)]-MoS$_2$, py-MoS$_2$ and [Ru^{II}(bpy)$_2$(py)Cl]-MoS$_2$ in 0.5 M H$_2$SO4 (pH= 0). Right: Corresponding Tafel slopes.

To better understand the key factors that limit the catalytic activity and gain more insights on the HER mechanism of Ru^{II} complex functionalized MoS$_2$ system, Tafel slopes (Fig. 5.11) of ce-1T-MoS$_2$, phen-MoS$_2$, [Ru^{II}(bpy)$_2$(phen)]-MoS$_2$, py-MoS$_2$ and [Ru^{II}(bpy)$_2$(py)Cl]-MoS$_2$ were determined by fitting the linear portion of /η/-log/*J*/ curves, where /*η*/ represented the absolute value of overpotential and /*J*/ represented the absolute value of current density.[11] All investigated catalysts displayed Tafel slopes in the range 92-209 mV/decade, indicating the hydrogen adsorption process (Volmer step) was the rate-limiting step[12]. In particular, ce-1T-MoS$_2$ demonstrated the lowest Tafel slope of 92 mV/decade, demonstrating the most favorable HER kinetics compared to covalently functionalized samples, which was in agreement with the trend in linear sweep voltammograms (Fig. 5.11, left).

Furthermore, the Tafel slope of $[Ru^{II}(bpy)_2(phen)]$-MoS_2 was 87 mV/decade smaller than phen-MoS_2, suggesting that coordinating the surface tethered ligands to Ru^{II} centers enabled a favorable hydrogen adsorption process and electron transfer kinetics. Both were key to the better catalytic activity of $[Ru^{II}(bpy)_2(phen)]$-MoS_2 in comparison to phen-MoS_2. Similarly, $[Ru^{II}(bpy)_2(py)Cl]$-MoS_2 demonstrated a smaller Tafel slope than py-MoS_2. Comparing the electrode composition between Ru^{II} complex functionalized MoS_2 and ligand functionalized MoS_2 revealed two differences: the number of free amine groups and the existence of Ru^{II} complexes. The favorable hydrogen adsorption process in Ru^{II} complex functionalized MoS_2 was likely attributed to the decreased number of free amine groups after complexation, which prevented the protons from capturing by free amines for self-protonation, whereby increasing the proton access to the catalytically active sites for H_2 evolution. On the other hand, the formation of $[Ru^{II}(bpy)_2(phen)]^{2+}$on the surface of MoS_2 was presumably account for the improved film conductivity by modifying the Fermi level of functionalized MoS_2.[13]

Further comparison of $[Ru^{II}(bpy)_2(py)Cl]$-MoS_2 and $[Ru^{II}(bpy)_2(phen)]$-MoS_2 revealed a much smaller Tafel slope of $[Ru^{II}(bpy)_2(py)Cl]$-MoS_2 compared to $[Ru^{II}(bpy)_2(phen)]$-MoS_2, which was constant with the trend observed in linear sweep voltammograms (Fig. 5.11, left), indicating the better catalytic activity of $[Ru^{II}(bpy)_2(py)Cl]$-MoS_2 in comparison to $[Ru^{II}(bpy)_2(phen)]$-MoS_2 was likely ascribed to the more favorable HER kinetics (Hydrogen adsorption and charge transportation).

5.2.6 Proposed mechanism for photoelectrochemical H_2 evolution

To gain more insight on the possible electron transfer pathways in the Ru^{II} polypyridyl complexes sensitized MoS_2 devices for light-driven H_2 evolution, and to decode the effect of phototsensitizers' structures on PEC performance, the photophysical and electrical properties of three Ru^{II} model complexes ([Ru^{II}(bpy)$_3$](PF$_6$)$_2$, [Ru^{II}(bpy)$_2$(phen)](PF$_6$)$_2$ and [Ru^{II}(bpy)$_2$(py)$_2$](PF$_6$)$_2$) were determined. According to the absorption spectra (Fig. 5.12, left), all three Ru^{II} model complexes displayed signature metal-to-ligand charge transfer (MLCT) bands in the range of 449-472 nm with molar extinction coefficients ($\varepsilon/10^3$ M^{-1}cm^{-1}) in the same order of magnitude. This result verified that [Ru^{II}(bpy)$_3$](PF$_6$)$_2$, [Ru^{II}(bpy)$_2$(phen)]-(PF$_6$)$_2$ and [Ru^{II}(bpy)$_2$(py)$_2$](PF$_6$)$_2$ all hold the good capability to absorb visible light.

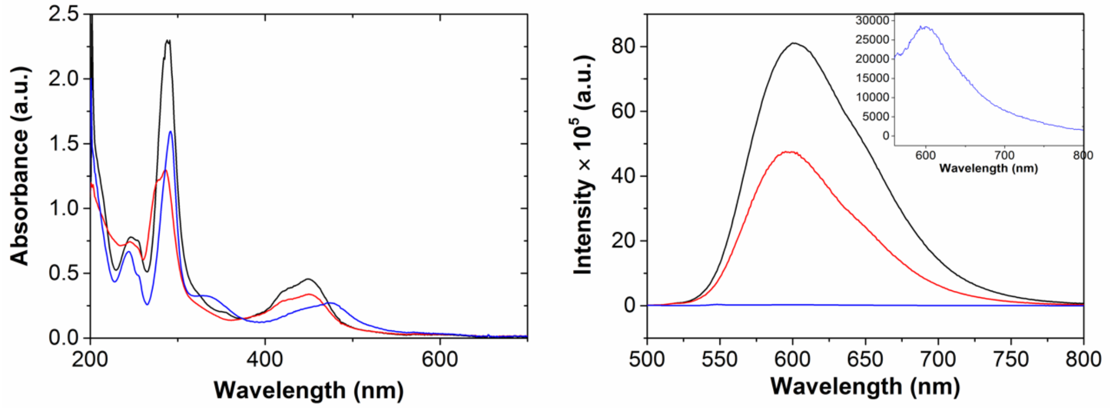

Figure 5.12 Absorption spectra (left) and emission spectra (right) of [Ru^{II}(bpy)$_3$](PF$_6$)$_2$ (black), [Ru^{II}(bpy)$_2$(phen)](PF$_6$)$_2$ (red) and [Ru^{II}(bpy)$_2$(py)$_2$]-(PF$_6$)$_2$ (blue) (0.02 mg/mL) in ethanol at room temperature. Inset: zoom in region of the emission spectrum of [Ru^{II}(bpy)$_2$(py)$_2$](PF$_6$)$_2$.

Upon excitation at the adsorption maximum, all three model complexes exhibited room temperature emission in ethanol (Fig. 5.12, right). However, the emission intensity of [Ru^{II}(bpy)$_2$(py)$_2$](PF$_6$)$_2$ was much lower than the other two, which was presumably due to deactivation of excited state ^{3}MLCT via population of low-lying metal charge transfer band (^{3}MC) in [Ru^{II}(bpy)$_2$(py)$_2$](PF$_6$)$_2$.[14] Considering this self-quenching process and the photo-instability, [Ru^{II}(bpy)$_2$(py)$_2$](PF$_6$)$_2$ was not an ideal candidate for using as a photosensitizer. Therefore, in Chapter 4 and Chapter 5, the photoelectrochemical (PEC) study primarily focused on [Ru^{II}(bpy)$_3$]-MoS$_2$ and [Ru^{II}(bpy)$_2$(phen)]-MoS$_2$.

Table 5.2 Photophysical properties of Ru^{II} model complexes

Photosensitizers	**λmax/nm^a (ε/10^3 M^{-1}cm^{-1})**	**λem/nm^a**
[Ru^{II}(bpy)$_3$](PF$_6$)$_2$	449(19903)	600
[Ru^{II}(bpy)$_2$(phen)](PF$_6$)$_2$	450(16501)	596
[Ru^{II}(bpy)$_2$(py)$_2$](PF$_6$)$_2$	472(12136)	602

^{a} Measured in ethanol under air at room temperature. The molar extinction coefficients ε were obtained from ethanol solutions.

The electrochemical behaviors of [Ru^{II}(bpy)$_3$](PF$_6$)$_2$ and [Ru^{II}(bpy)$_2$(phen)](PF$_6$)$_2$ (1.0 mM) were measured using cyclic voltammetry (Fig. S5.6) in a degassed acetonitrile solution (Bu$_4$NPF$_6$, 0.1 mM). The cyclic voltammograms of both model complexes revealed a one-electron oxidation event corresponding to Ru$^{II/III}$ redox couple and multiple reduction events associated with the reduction of ligands. DeArmond and co-workers have pointed out that in Ru^{II} polypyridyl complexes the π* orbital involved in the first reduction process is the same as that involved in the MLCT absorption and emission processes.[15, 16] Based on the ground state redox potentials, the excited state redox potentials of Ru^{II} polypyridyl complexes can be estimated by the following correlations:[17]

$E(PS^*/PS^-) = E_{1/2red} + E_{0\text{-}0}$;

$E(PS^*/PS^+) = E_{1/2ox} - E_{0\text{-}0}$.

Where PS* referred to the excited state of Ru^{II} complex, PS$^-$ referred to the one-electron reduction product of Ru^{II} complex and PS$^+$ referred to the one-electron oxidation product of Ru^{II} complex. Therefore, the excited oxidation potentials

$E(PS^*/PS^+)$ were calculated to be -1.06 and -1.04 V vs. SHE for $[Ru^{II}(bpy)_3](PF_6)_2$ and $[Ru^{II}(bpy)_2(phen)](PF_6)_2$, respectively. Such close excited oxidation potentials indicated that the thermodynamic driving force for electron transfer from $[Ru^{II}(bpy)_2(phen)]^{2+}$complex to the CB of semiconducting 2H-MoS_2 was similar to that of $[Ru^{II}(bpy)_3]^{2+}$ complex, assuming that the thickness of MoS_2 nanosheets and thus the CB position of MoS_2 were identical in two devices. Nevertheless, in Ru^{II} complex functionalized MoS_2, the predominant phase was metallic 1T-phase. Therefore, electron transfer at the interface of Ru^{II} complexes and MoS_2 basal planes were thermodynamically favorable as long as the suitable linkages were employed. (Table 5.3)

On the other hand, the excited reduction potentials $E(PS^*/PS^-)$ were calculated to be 0.98 V for $[Ru^{II}(bpy)_3](PF_6)_2$ and 1.47 V for $[Ru^{II}(bpy)_2(phen)](PF_6)_2$. Both were more positive than the oxidation potential of ascorbic acid (H_2A, E = -0.223 V vs. SHE[18]), therefore electron transfer from the ascorbic acid to the Ru^{II} complex via a reductive quenching pathway was also thermodynamically feasible.

Table 5.3 Electrochemical data of Ru^{II} model complexes

dye	**$^aE_{0\text{-}0}$ eV**	**$E_{1/2ox}$ V**	**$E_{1/2red}$ V**	**$^bE(PS^*/PS^-)$ V**	**$^cE(PS^+/PS^*)$ V**
$[Ru^{II}(bpy)_3](PF_6)_2$	2.34	1.29	-1.37	0.98	-1.06
$[Ru^{II}(bpy)_2(Phen)](PF_6)_2$	2.33	1.29	-0.86	1.47	-1.04

$^aE_{0\text{-}0}$ values were estimated from the intersections of normalized absorption and emission spectra in ethanol, λint: $E_{0\text{-}0} = 1240/\lambda int$. ^{b}Excited state reduction potential vs. SHE.

Based on above discussion, H_2 evolution over this Ru^{II} complex sensitized MoS_2 device can take place via two possible pathways (Fig. 5.13). In the reductive quenching pathway, the Ru^{II} complexes acted as photosensitizers (PS) absorbed light and underwent photoexcitation, then the photo-excited state (PS*) was reductively quenched by ascorbic acid, giving rise to highly reactive PS^-, followed by the electron transfer from PS^- to the active sites of MoS_2 catalyst, where the protons were reduced to form H_2. In the oxidative quenching pathway, the photo-excited state (PS*) was oxidatively quenched via ejecting electrons from PS* to MoS_2, followed by reduction of oxidized PS^+ with ascorbic acid. In the reductive pathway, generation of PS^- required diffusion of ascorbic acid to the electrode surface, and thus H_2 production was mass-transfer limited, whereas the oxidative pathway involved solely the electron transfer at the interface, whereby a faster electron transfer kinetics would be expected if the dye molecules were strongly connected to MoS_2. To further elucidate the mechanism in this Ru^{II} complex sensitized MoS_2, systematic analysis of electron transfer dynamics at the interface of dye and MoS_2 needs to be explored in the future.

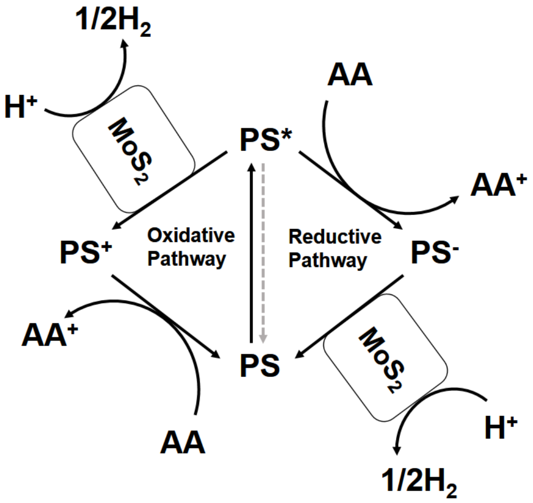

Figure 5.13 Schematic representation of two possible electron transfer pathways in the Ru^{II} complex sensitized MoS_2 device for H_2 production.

5.3 Conclusion

Cumulatively, two new Ru^{II} polypyridyl complex functionalized MoS_2 devices ($[Ru^{II}(bpy)_2(phen)]$-MoS_2 and $[Ru^{II}(bpy)_2(py)Cl]$-MoS_2) were successfully assembled and fully characterized. The photoelectrochemical performance of this Ru^{II} complex sensitized MoS_2 system was found to be highly dependent on both the surface extent of photosensitizers and the catalytic activity of functionalized MoS_2, and the latter was strongly influenced by the number and the kind of functional groups. Compared to previously reported $[Ru^{II}(bpy)_3]$-MoS_2, the $[Ru^{II}(bpy)_2(phen)]$-MoS_2 showed a 14 mV improvement of photovoltage generation, which was likely attributed to the higher surface coverage of $[Ru^{II}(bpy)_2(phen)]^{2+}$ complex in $[Ru^{II}(bpy)_2(phen)]$-MoS_2. However, the photocurrent onset potential of $[Ru^{II}(bpy)_2(phen)]$-MoS_2 photocathode upshifted when comparing with $[Ru^{II}(bpy)_3]$-MoS_2 due to the much lower catalytic activity of the $[Ru^{II}(bpy)_2(phen)]$-MoS_2 construct. Given this adverse effect of high loading of photosensitizers to the photovoltage generation and catalytic activity, it may be possible to overcome this trade-off with further investigation on the surface engineering strategies. In addition, the visible light absorptivity (adsorption region and molar extinction coefficient) of Ru^{II} complexes and the kind of anchoring groups are envisioned to be critical to the light utilization efficiency and rate of interfacial electron transfer of such Ru^{II} complex sensitized MoS_2.

5.4 Experimental section

5.4.1 Materials

MoS_2 powder was purchased from Sigma Aldrich with particle size of 6 μm and used without purifying. Hexane (Sigma Aldrich) was distilled over a sodium under argon atmosphere before use. *N*-Butyllithium (2.5 M and 1.6 M) in hexane, and other chemicals purchased from Sigma Aldrich and used as received. All solvents were purchased from commercial sources and used as received.

5.4.2 Synthesis of ligands and model complexes

5-Iodoacetamido-1,10-phenanthroline and 5-chloroacetamido-1,10-phenanthroline were synthesized according to the prior literatures[2, 3] by Amy Lynes.

Bis(2,2'-bipyridine)-(5-chloroacetamido-1,10-phenanthroline) ruthenium bis(hexafluorophosphate) ($[Ru^{II}(bpy)_2(phen)](PF_6)_2$)

$[Ru^{II}(bpy)_2(phen)](PF_6)_2$[3] was synthesized according to the prior literature as orange solid in 43% yield. ^1H NMR (400 MHz, CH_3CN) δ 9.19 (s, 1H), 8.67 (d, *J* = 7.6 Hz, 1H), 8.57 (d, *J* = 7.3 Hz, 1H), 8.50 (dd, *J* = 16.9, 9.0 Hz, 5H), 8.14 – 7.95 (m, 6H), 7.83 (t, *J* = 5.0 Hz, 2H), 7.77 (dd, *J* = 8.6, 5.2 Hz, 1H), 7.70 (dd, *J* = 8.3, 5.2 Hz, 1H), 7.54 (d, *J* = 5.7 Hz, 2H), 7.48 – 7.40 (m, 2H), 7.27 – 7.18 (m, 2H), 4.43 (s, 2H). ESI-MS: m/z 830.0594 ($[M - PF_6^-]^+$), $C_{34}H_{26}N_7OF_6PClRu$, Cal. 830.0573.

Bis(2,2'-bipyridine)-bis(4-methylpyridine)ruthenium bis(hexafluoro-phosphate) ($[Ru^{II}(bpy)_2(py)_2](PF_6)_2$)

$[Ru^{II}(bpy)_2(py)_2](PF_6)_2$ was synthesized according to the literature[4] as an organge crystals in 45% yield. ^1H NMR (400 MHz, acetone) δ 9.30 (d, *J* = 5.6 Hz, 1H), 8.67 (d, *J* = 8.1 Hz, 1H), 8.59 (d, *J* = 8.2 Hz, 1H), 8.47 (d, *J* = 6.0 Hz, 2H), 8.29 (d, *J* = 8.1 Hz, 1H), 8.27 – 8.22 (m, 1H), 8.07 (t, *J* = 7.9 Hz, 1H), 7.96 – 7.90 (m, 1H), 7.55 – 7.48 (m, 1H), 7.27 (d, *J* = 6.2 Hz, 2H), 2.82 (s, 6H). ESI-MS: m/z 745.1231 ($[M - PF_6^-]^+$), $C_{32}H_{30}N_6F_6PRu$, Cal. 745.1217.

5.4.3 Functionalization

Standard procedure to prepare [$Ru^{II}(bpy)_2(L)Cl_x$]-MoS_2 (L = 3-methylpyridine (py), x = 1; L = 5-acetamido-1,10–phenanthroline (Phen), x = 0)

Step-wise preparation of [$Ru^{II}(bpy)_2(L)Cl_x$]-MoS_2 followed the reaction sequence illustrated in Fig. 4.1 in Chapter 4. Firstly, Ligand functionalized MoS_2 (L-MoS_2, L= phen or py) was synthesized by blending the ce-1T-MoS_2 aqueous dispersion and oraganohalide ligand/IPA solution[9] (e.g., 10 equivalent. 3-iodomethylpyridine hydroiodide or 10 eqv. 5-iodoacetamido-1,10-phenanthroline when L = py or phen). To 20 mL of ce-1T-MoS_2 aqueous dispersion, 10 mL of pre-dissolved oraganohalide ligand/IPA solution was added. Then the mixture was bath-sonicated (Branson Ultrasonic bath, 750W) in darkness for 1 h and then kept at room temperature with magnetic stirring for 24 hrs. The resultant dispersion was subjected to high-speed centrifugation at 11k rpm (13257 *g*) for 1 h to spin down all the functionalized materials and remove the other non-functionalized small flakes. After that, the sediment was washed with ethanol, IPA and de-ionized water (twice for each solvent). The final sediment was collected in 10 mL IPA and subjected to UV-Vis measurement. For XPS, the dispersions were vacuum-filtered using porous cellulose filter membranes (0.025 μm). The dried powder of L-MoS_2 can also be collected after leaving in the vacuum oven at 60 °C for 2 hrs, which was used for DRIFT, TGA and following synthesis step.

[$Ru^{II}(bpy)_2(L)Cl_x$]-MoS_2 was synthesized by reacting ligand functionalized material (L-MoS_2) with [$Ru^{II}(bpy)_2Cl_2$] precursor. To 30 mL of mixed solvent (ethanol: H_2O = 1:1, v/v), L-MoS_2 (10 mg) and [$Ru^{II}(bpy)_2Cl_2$] (5 mg) were added. The mixture was sonicated for 10 min and de-aerated for 15 min by Argon flow and then refluxed at 120 °C for 12 h under Argon protection. The resulting reddish suspension was centrifuged at 11 k rpm for 1h to spin down all the materials. The sediment was then subjected to thorough washing with ethanol and water, respectively until the supernatant became colorless. The final sediment was collected in 10 mL DI-water for UV-Vis and Zeta potential (ζ) and PL measurement. For XPS, the dispersions were vacuum-filtered using porous cellulose filter membranes (0.025 μm). The dried powder of $[Ru^{II}(bpy)_2(L)Cl_x]$-MoS_2 can also be collected after leaving in the vacuum oven at 60 °C overnight, which was used for DRIFT.For Raman and SEM, aqueous dispersions were drop-casted on Si/SiO_2 wafers or glass slides.

5.4.4 Characterization

In addition to the characterization techniques listed in Chapter 4, electrochemical measurements were performed under a nitrogen atmosphere, and the electrolyte used was 0.1 M n-tetrabutylammonium hexafluorophosphate (Bu_4NPF_6) in acetonitrile with a CH electrochemical analyser with a standard three-electrode system consisting of $Ag/AgNO_3$ as the reference electrode, a platinum sheet as counter electrode, a glassy carbon disk as the working electrode. The measurements were calibrated using ferrocene as standard. The redox potential of ferrocene internal reference is taken as 0.391 V vs. SHE.

5.4.5 Photoelectrochemical measurement

The photoelectrochemical measurement was carried out using a standard three-electrode cell with a platinum wire as the counter electrode, a saturated KCl Ag/AgCl reference electrode and an indium-tin oxide (ITO) glass with samples as the working electrode in one compartment. The working electrode was prepared by drop-casting material aqueous dispersion onto ITO glass and dried at room temperature overnight. The mass per area for all the samples is 0.25 mg/cm^2. The

10 mM ascorbic acid aqueous solution (pH 3) was used as the electrolyte and sacrificial donor and the 150 W Xe lamp was used as a light source. The assembled cell was de-aerated with nitrogen for 15 min prior to each measurement. Three-electrode linear sweep voltammetry and Chronoamperometry were performed using a computer-controlled electrochemical workstation (CHI). One or two LSVs were used to activate the electrodes and test for proper electrical connection. Then the current-voltage performance was measured using a LSV from +0.17 V to -0.43 V vs. RHE at a scan rate of 5 mV/s. The polarization curves were plotted without iR correction. Before the Chronoamperometry measurement, samples were conditioned at a given voltage for 20s. All the CA measurements were held at a constant potential of -0.33 V vs. RHE with chopped light illumination at 60 s intervals for 500 s. All the photoelectrochemical properties of a specific material deposited electrode were obtained based on at least three independent electrodes, each performed in triplicate and the best results are presented.

5.4.6 Electrochemical measurement

Electrochemical measurements were performed in a three-electrode electrochemical cell in 0.5 M H_2SO_4, with a platinum wire as the counter electrode, a saturated KCl Ag/AgCl reference electrode and a glassy carbon plate with samples as the working electrode. The working electrode was prepared by drop-casting aqueous dispersion of material onto glassy carbon plate and dried at room temperature overnight. The mass per area for all the samples is 0.25 mg/cm^2. Catalytic activity was measured by performing linear sweep voltammetry (LSV) with a CH Instruments 600E electrochemical analyzer at a scan rate of 5 mV s^{-1} in a window from 0 V to −0.5 V (vs. RHE). All the data was collected without the electrolyte resistance by iR compensation. All the electrochemical properties of a specific material deposited electrode were obtained based on at least three independent electrodes, each performed in triplicate and the best results are presented.

References

[1] R. J. Radford, P. C. Nguyen, F. A. Tezcan, *Inorg. Chem.* **2010**, *49*, 7106-7115.

[2] A. M. Nonat, A. J. Harte, K. Senechal-David, J. P. Leonard, T. Gunnlaugsson, *Dalt. Trans.* **2009**, 4703-4711.

[3] F. N. Castellano, J. D. Dattelbaum, J. R. Lakowicz, *Anal. Biochem.* **1998**, *255*, 165-170.

[4] Aldrik H. Velders, C. Massera, F. Ugozzoli, M. Biagini-Cingi, Anna M. Manotti-Lanfredi, Jaap G. Haasnoot, J. Reedijk, *Eur. J. Inorg. Chem.* **2002**, *2002*, 193-198.

[5] M. S. Quinby, R. D. Feltham, *Inorg. Chem.* **1972**, *11*, 2468-2476.

[6] J. L. Hueso, J. P. Espinós, A. Caballero, J. Cotrino, A. R. González-Elipe, *Carbon* **2007**, *45*, 89-96.

[7] D. Marton, K. J. Boyd, A. H. Al-Bayati, S. S. Todorov, J. W. Rabalais, *Phys. Rev. Lett.* **1994**, *73*, 118-121.

[8] K. C. Knirsch, N. C. Berner, H. C. Nerl, C. S. Cucinotta, Z. Gholamvand, N. McEvoy, Z. Wang, I. Abramovic, P. Vecera, M. Halik, S. Sanvito, G. S. Duesberg, V. Nicolosi, F. Hauke, A. Hirsch, J. N. Coleman, C. Backes, *ACS Nano* **2015**, *9*, 6018-6030.

[9] D. Voiry, A. Goswami, R. Kappera, e. SilvaCecilia de Carvalho Castro, D. Kaplan, T. Fujita, M. Chen, T. Asefa, M. Chhowalla, *Nat. Chem.* **2015**, *7*, 45-49.

[10] C. K. Chua, A. H. Loo, M. Pumera, *Chem. – A Eur. J.* **2016**, *22*, 14336-14341.

[11] J. D. Benck, T. R. Hellstern, J. Kibsgaard, P. Chakthranont, T. F. Jaramillo, *ACS Catal.* **2014**, *4*, 3957-3971.

[12] B. E. Conway, B. V. Tilak, *Electrochimica Acta* **2002**, *47*, 3571-3594.

[13] S. Lei, X. Wang, B. Li, J. Kang, Y. He, A. George, L. Ge, Y. Gong, P. Dong, Z. Jin, G. Brunetto, W. Chen, Z.-T. Lin, R. Baines, D. S. Galvão, J. Lou, E. Barrera, K. Banerjee, R. Vajtai, P. Ajayan, *Nat. Nanotechnol.* **2016**, *11*, 465-471.

[14] J. V. Caspar, T. J. Meyer, *J. Am. Chem. Soc.* **1983**, *105*, 5583-5590.

[15] D. E. Morris, Y. Ohsawa, D. P. Segers, M. K. DeArmond, K. W. Hanck, *Inorg. Chem.* **1984**, *23*, 3010-3017.

[16] A. A. Vlcek, E. S. Dodsworth, W. J. Pietro, A. B. P. Lever, *Inorg. Chem.* **1995**, *34*, 1906-1913.

[17] C. R. Bock, J. A. Connor, A. R. Gutierrez, T. J. Meyer, D. G. Whitten, B. P.

Sullivan, J. K. Nagle, *J. Am. Chem. Soc.* **1979**, *101*, 4815-4824.

[18] H. Borsook, G. Keighley, *Proc. Natl. Acad. Sci. U. S. A.* **1933**, *19*, 875-878.

CHAPTER 6 Conclusion and Future Work

Since the discovery of the extraordinary properties of graphene,[1-5] other two-dimensional (2D) nanomaterials, and in particular the layered transition metal dichalcogenides (TMDs), have garnered great interest.[6-11] This is due to their exciting physical and chemical properties. TMDs have been deemed suitable (and in some cases game-changing) for potential applications in a variety of areas (catalysis, electronics, photonics, energy storage, and sensing). Further tailoring of their colloidal and surface properties, fully harnessing their reactivity, thereby expanding the number of potential applications of 2D TMDs based nanomaterials can be realized through chemical functionalization.[12] The primary objective of this thesis was to explore chemical functionalization of exfoliated TMD nanosheets with various functional addends and understand their tailor-made properties and activities.

6.1 Key findings and contributions

Part I

In the past five years, a great number of synthetic efforts have been devoted toward the chemical functionalization of 2D TMDs (the majority of them have focused on MoS_2).[13-15] Among those, the thiol chemistry based functionalization strategy has emerged as one of the most widely applied techniques to develop the functional MoS_2 nanohybrid.[16] It was proposed that thiol group (-SH) can bind to the unsaturated Mo atoms in SVs.[13] However, the exact nature of MoS_2/thiol interaction remained unclear. Note that the bonding property of MoS_2/thiol interface can largely affect the electronic structure, thereby determining the performance of nanohybrid in a specific application. Therefore, a full understanding of the thiol chemistry based functionalization technique and the nature of MoS_2/thiol interaction is imperative. Towards this end, the first part of this thesis (Chapter 2 and Chapter 3) was focused on the functionalization of liquid exfoliated 2H-MoS_2 nanosheets using organic thiols and the exploration of the nature of the MoS_2/thiol interactions from spectroscopic and kinetic aspects.

In Chapter 2, the functionalization of 2H-MoS_2 nanosheets with cysteine (a typical organic thiol) was initially achieved by blending a dispersion of liquid exfoliated 2H-MoS_2 nanosheets with a solution of cysteine. The resulting functionalized 2H-MoS_2 nanosheets were found to be highly water dispersible and stable against pH change or aging, whereas the pristine 2H-MoS_2 nanosheets didn’t disperse in water, indicating an effective dispersibility modulation upon functionalization. In an effort to verify the nature of the interaction between 2H-MoS_2 and cysteine, both pristine and functionalized 2H-MoS_2 nanosheets were characterized by UV-Vis, DRIFT, XPS, TGA and Raman spectroscopy. Interestingly, MoS_2 was found to be facilitating the oxidation of the thiol cysteine to the disulfide cystine during functionalization. The resulting cystine was physisorbed on MoS_2 rather than coordinated as a thiol (cysteine) filling S-vacancies in the 2H-MoS_2 surface, as originally conceived. In a similar fashion, the functionalization of liquid 2H-MoS_2 with other commercially available organic thiols such as 1-octanethiol and 3-mercaptopropionic acid and functionalization of liquid 2H-WS_2 with cysteine were also achieved. And the disulfide products were identified in all the cases. This work presented a detailed exploration of the thiol/MoS_2 interaction from experimental and spectroscopic aspects. It was the first attempt to reveal that reaction of exfoliated TMDs with organic thiols can lead to the oxidative dimerization of thiols (RSH) to according disulfides (RSSR) derivatives.

One step further, the kinetic behaviors of MoS_2/thiol interaction were investigated in Chapter 3, aiming to provide some insight into the MoS_2 mediated thiol oxidation. The reaction between 1-octanethiol (one of the typical alkanethiols) and thin-layered MoS_2 nanosheets was demonstrated as an example to investigate the mechanism of the organic thiols-nanostructured MoS_2 interactions. The consumption of 1-octanethiol and generation of dioctyl disulfide was quantitatively monitored by ^1H- NMR spectroscopy. The results emphasized that 1-octanethiol was hardly auto-oxidized by oxygen in the absence of a catalyst. In the presence of 2H-MoS_2 nanosheets, 1-octanethiol can be readily oxidized to dioctyl disulfide even without O_2, corroborating the catalytic activity of MoS_2 nanosheets in the 1-octanethiol oxidation reaction. Furthermore, kinetic studies revealed that the rate of 1-octanethiol oxidation increased with increasing the concentration of 2H-MoS_2 nanosheets, yet plunged abruptly when a large excess of 1-octanethiol (>10 fold) was employed, indicating that the number of active sites in MoS_2 played a key role in determining the rate of 1-octanethiol oxidation. This was further confirmed by comparison the 1-octanthiol consumption rate of reactions using bulk MoS_2 nanosheets and exfoliated MoS_2 nanosheets. By correlation of two possible reaction mechanisms with the kinetic study results, dioctyl disulfide was postulated to be formed via thiyl radical-radical coupling outside the cavity of catalytically active sites.

Further studies seek to characterize the reaction intermediates and by-products such as H_2, as well as to elucidate how the inductive and steric factors of different organic thiols affect the reaction kinetics. Should the impacts of these factors be figured out, the MoS_2 catalyzed oxidative dimerization mechanism is expected to be resolved in the future. The knowledge generated from the above studies would be of great benefit to thiol chemistry directed controllable construction of MoS_2 nanohybrid with desired structural features and more precise and predictable tuning of the functions of MoS_2 nanohybrid for specific applications.

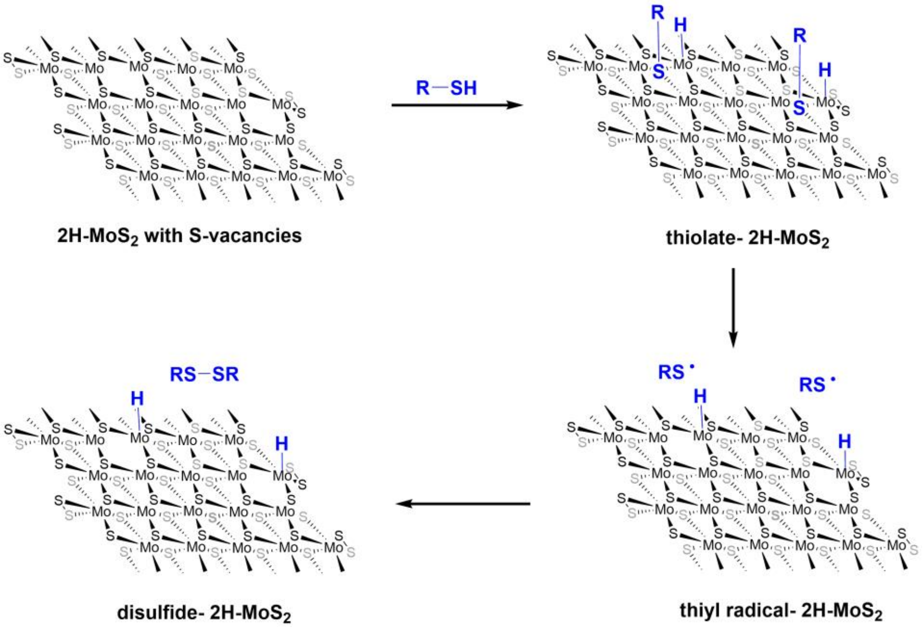

Figure 6.1 MoS_2 catalysed conversion of organic thiol to disulfide.

Part II

The second part of the thesis was devoted to bridging the research gap in the field of dye-sensitized MoS_2 photocatalytic systems for the light-driven hydrogen evolution reaction (HER). In the current literature, the studies on molecular dyes sensitized MoS_2 photocatalytic devices remain rare. The only examples were based on physisorption of dye molecules to MoS_2 films,[17-20] which potentially inhibited the photo-hydrogen production efficiency due to the limited electronic communications between the dye and catalysts. To address this issue, a stepwise functionalization approach was developed in Chapter 4 to covalently bind $[Ru^{II}(bpy)_3]^{2+}$-based photosensitizers onto chemically exfoliated 1T-MoS_2 nanosheets (ce-1T-MoS_2). This was achieved by reacting bipyridine functionalized ce-1T-MoS_2 nanosheets (bpy-MoS_2) with $[Ru^{II}(bpy)_2Cl_2]$ precursors. The resulting construct ($[Ru^{II}(bpy)_3]$-MoS_2) was characterized by electronic absorption (UV-Vis), DRIFT, XPS, Raman spectroscopy, TGA, and SEM. The covalent bonding between $[Ru^{II}(bpy)_3]^{2+}$ and MoS_2 nanosheets was confirmed by DRIFT and XPS. The photoelectrochemical (PEC) measurement of $[Ru^{II}(bpy)_3]$-MoS_2 electrode in ascorbic acid (pH 3) displayed a significant improvement of photocurrent generation compared to the non-functionalized MoS_2, signifying the potential of the $[Ru^{II}(bpy)_3]$-MoS_2 covalent assembly in photo-hydrogen production.

In accordance with this strategy, another two Ru^{II} complex functionalized MoS_2 ($[Ru^{II}(bpy)_2(phen)]$-MoS_2 and $[Ru^{II}(bpy)_2(py)Cl]$-MoS_2) were then synthesized (in Chapter 5), aiming to further tune the PEC performance of such Ru^{II} complex sensitized MoS_2 system and identify the key factors that limit the photocatalytic activity of these Ru^{II} complex sensitized MoS_2 devices. Like the $[Ru^{II}(bpy)_3]$-MoS_2 electrode, the PEC measurement of $[Ru^{II}(bpy)_2(phen)]$-MoS_2 photocathode in ascorbic acid displayed a remarkable improvement of photovoltage generation compared to the non-functionalized ce-1T-MoS_2 electrode. The superior photovoltage generation demonstrates the generalizable advantage of this Ru^{II} complex-MoS_2 covalent assembly in photoelectrochemical hydrogen production. Interestingly, compared to previously reported $[Ru^{II}(bpy)_3]$-MoS_2, the $[Ru^{II}(bpy)_2(phen)]$-MoS_2 showed a moderate improvement of photovoltage generation which was most likely attributed to the slightly higher surface extent of

Ru^{II} photosensitizers in $[Ru^{II}(bpy)_2(phen)]$-MoS_2. This result underlined the controllability of the photovoltage generation in this dye-sensitized MoS_2 system by manipulation of the surface content of dye molecules. Nevertheless, the PEC performance of the whole dye-sensitized MoS_2 device were found to rely on both the surface extent of photosensitizers and the catalytic activity of functionalized MoS_2. For instance, the photocurrent onset potential of $[Ru^{II}(bpy)_2(phen)]$-MoS_2 showed a significant (215 mV) cathodic shift compared to $[Ru^{II}(bpy)_3]$-MoS_2, albeit a much higher photovoltage production by the $[Ru^{II}(bpy)_2(phen)]$-MoS_2 construct. This was attributed to the lower catalytic activity of $[Ru^{II}(bpy)_2(phen)]$-MoS_2 (a more negative dark onset potential) compared to $[Ru^{II}(bpy)_3]$-MoS_2. It was worth noting that many factors such as the number of free amines, the number of Ru^{II} complexes and the inductive effect of functional groups could individually or synergistically affect the catalytic activity of functionalized MoS_2 via modifying the film conductivity, surface charge or even shifting the Fermi-level[21]. Therefore, further efforts towards improving the PEC performance of this Ru^{II} complex sensitized MoS_2 should focus on the development of new surface engineering strategies to increase the local concentration of dye molecules on the surface of MoS_2 without sacrificing the catalytic activity.

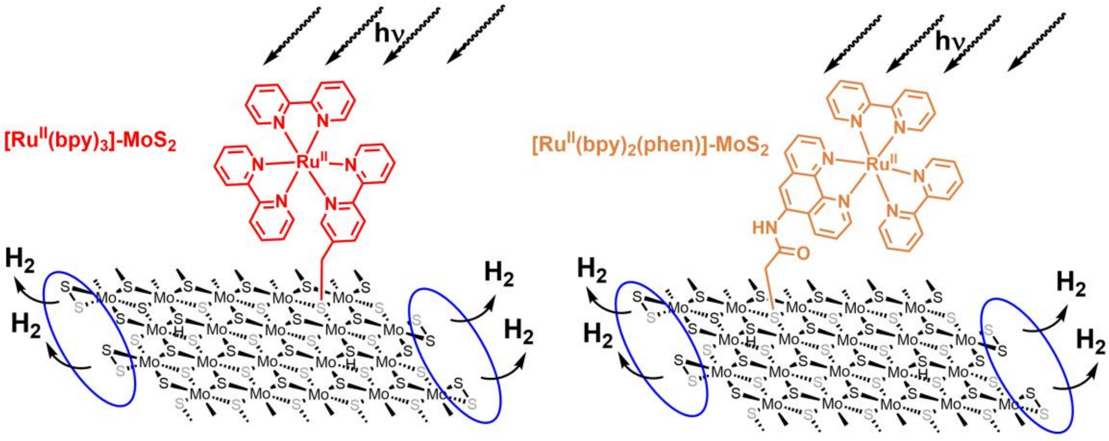

Figure 6.2 Schematic representation of Ru^{II} complex sensitized MoS_2 devices for light-driven H_2 production.

Above all, the fabrication strategy demonstrated in Chapter 4 and 5 offers lots of benefits for scalable construction of robust, low-cost and highly tunable Ru^{II} complex-sensitized photocatalytic HER devices in solution. It was the first attempt to covalently link Ru^{II} photosensitizer on the surface of the metallic 1T-MoS_2 surface for photo-hydrogen production. Dye-sensitized hydrogen production devices are likely to improve the photo-fuel conversion efficiency in profound ways, just as the dye- sensitized solar cells did for the photo-electricity conversion.

6.2 Future works

While the research presented in this thesis has demonstrated some novel outcomes in the field of functionalization of TMD nanosheets, especially on the thiol-chemistry based functionalization techniques and building up dye-sensitized TMD devices via covalent functionalization, there are still many opportunities worth exploring and extending further.

MoS_2/thiol interactions

In terms of the functionalization of TMDs using the thiol chemistry based technique, future research in the following aspects should be conducted in order to obtain a comprehensive understanding of the TMDs/thiol interactions and the mechanism of MoS_2 catalyzed thiol oxidation. Experimentally determining the adsorption isotherms and identifying the surface species (such as thiyl radical-MoS_2 species) and byproducts such as H_2 on the basis of knowledge drawing from the organometallic compounds reaction would provide more information on the reaction mechanism of individual steps during TMDs/thiol interactions. Moreover, for the thiols having different structures (inductive effects), exploring the kinetic behaviors of MoS_2 catalyzed thiol oxidation under various reaction time scales, pH conditions and temperatures would allow for the more in-depth understanding of the rate-limiting step of disulfide formation and the mechanism of thiol oxidation. Finally, with the aid of DFT calculation results and more experimental evidence, the fundamental mechanism of thiol oxidation catalyzed by thin-layered MoS_2 nanosheets is expected to become clear in the near future with the contribution of this work. In the long run, it would be of great interest to develop nanostructured MoS_2 based biosensors for monitoring the level of thiol related antioxidants in biological systems, which will grant significant opportunities for auxiliary diagnosis of health status and various diseases.

Additionally, functionalization of 2D TMDs with organic thiols are normally performed in the air, thus exploring the thiol oxidation mechanism in the presence of both MoS_2 nanosheets and dioxygen (O_2) holds great importance for comprehending the thiol chemistry-based TMDs surface modification technique. The preliminary experiment results in Chapter 3 have pointed out that the presence of dioxygen (O_2) can greatly accelerate the oxidation of thiol to disulfide. One can assume involvement of dioxygen in the reaction may lead to a different thiol oxidation mechanism. The follow-on work should concentrate on addressing the following questions: How is dioxygen involved in the thiol oxidation? Are the thiols oxidized directly by dioxygen or reactive oxygen species (and other oxidative intermediates) that are generated during the reaction? Does the structure of MoS_2 change after interaction with thiol and dioxygen? Are any other byproducts formed? What's the kinetic behavior of thiol oxidation in the presence of dioxygen? Can this nanostructured MoS_2 (with or without dioxygen) oxidize other organic substrates such as triphenylphosphine (PPh_3), thioanisole, and benzyl alcohol?

Covalent functionalization of 2H-MoS$_2$

Given the great potential of monolayer 2H-MoS$_2$ in electronic and optoelectronic applications, development of other alternative approaches to covalently functionalize 2H-MoS$_2$ nanosheets towards modified electronic and optical properties is another promising direction. A recent study by Pulickel and co-workers has revealed that the atoms on the surface of 2D materials usually terminate with lone pair electrons thereby Lewis acids can be attached to achieve functionalization.[21] Inspired by this, one possible way to achieve covalent functionalization is to react 2H-MoS$_2$ nanosheets with organic electrophiles such as acyl halide, tosylate and mesylate. Moreover, the soft nature of surface sulfur atoms in 2H-MoS$_2$ makes it possible to bind with other soft acid cations (e.g., Au^+, Ag^+) according to the Pearson acid-base concept (HSAB theory) to form coordination complexes on the 2D platform.

Dye-sensitized MoS$_2$ photocatalytic devices

In the established dye-sensitized MoS$_2$ photocatalytic devices, the high surface coverage of dye molecules is essential to ensure sufficient light adsorption. However, the higher surface coverage of dyes comes at the expense of lower catalytic activity due to the high coverage of catalytically active surface area (basal plane of 1T-MoS$_2$) and increased film resistance. Future research into mitigating this loss of catalytic activity should include development of other covalent functionalization routes without sacrificing the basal plane active sites in 1T-MoS$_2$, addition of conductive materials such as carbon nanotubes to improve the conductivity of composites and functionalization of MoS$_2$ with polymer chain, which allows grafting of multiple dye molecules onto one polymer brush. Importantly, systematic analysis of electron-transfer dynamics at the interface of dye and MoS$_2$ by carrying out Transient absorption spectroscopy and Time-correlated–single photon counting

(TC-SPC) would provide supplementary information regarding the charge separation and competing for recombination pathways in such dye-sensitized system. In this way, more in-depth understanding of the photo-hydrogen production mechanism will be gained for more rational design of efficient dye-sensitized MoS_2 devices in the future. Secondly, the durability of this photocatalytic system in long-time running should be evaluated for practical applications. Thirdly, different sacrificial donors should be tested to seek for the best performance condition, albeit a system free of sacrificial agents is the priority in the future direction. Last but not least, the H_2 production must be coupled to O_2 generation in order to achieve full water splitting.

From methodology point of view, this step-wise functionalization strategy can be utilized in a modular fashion on ce-1T-MoS_2 surface to hybrid with various metal complexes, Chromophores, MOFs and even other nanomaterials such as noble metal nanoparticles and functionalized graphene, extending the scope of coordination chemistry of 2D MoS_2 surface and enabling the multi-angle tuning of the property of TMDs like MoS_2 for various applications.

References

[1] K. S. Novoselov, A. K. Geim, S. V. Morozov, D. Jiang, Y. Zhang, S. V. Dubonos, I. V. Grigorieva, A. A. Firsov, *Science* **2004**, *306*, 666-669.

[2] A. K. Geim, K. S. Novoselov, *Nat Mater* **2007**, *6*, 183-191.

[3] M. J. Allen, V. C. Tung, R. B. Kaner, *Chemical Reviews* **2010**, *110*, 132-145.

[4] V. Georgakilas, M. Otyepka, A. B. Bourlinos, V. Chandra, N. Kim, K. C. Kemp, P. Hobza, R. Zboril, K. S. Kim, *Chemical Reviews* **2012**, *112*, 6156-6214.

[5] J. N. Coleman, *Accounts of Chemical Research* **2013**, *46*, 14-22.

[6] S. Z. Butler, S. M. Hollen, L. Cao, Y. Cui, J. A. Gupta, H. R. Gutierrez, T. F. Heinz, S. S. Hong, J. Huang, A. F. Ismach, E. Johnston-Halperin, M. Kuno, V. V. Plashnitsa, R. D. Robinson, R. S. Ruoff, S. Salahuddin, J. Shan, L. Shi, M. G. Spencer, M. Terrones, W. Windl, J. E. Goldberger, *ACS Nano* **2013**, *7*, 2898-2926.

[7] C. N. R. Rao, H. S. S. Ramakrishna Matte, U. Maitra, *Angewandte Chemie International Edition* **2013**, *52*, 13162-13185.

[8] V. Nicolosi, M. Chhowalla, M. G. Kanatzidis, M. S. Strano, J. N. Coleman, *Science* **2013**, *340*, 1420-1438.

[9] M. Xu, T. Liang, M. Shi, H. Chen, *Chemical Reviews* **2013**, *113*, 3766–3798.

[10] P. Miro, M. Audiffred, T. Heine, *Chemical Society Reviews* **2014**, *43*, 6537-6554.

[11] R. Lv, J. A. Robinson, R. E. Schaak, D. Sun, Y. Sun, T. E. Mallouk, M. Terrones, *Accounts of Chemical Research* **2015**, *48*, 56-64.

[12] H. Wang, H. Yuan, S. Sae Hong, Y. Li, Y. Cui, *Chemical Society Reviews* **2015**, *44*, 2664-2680.

[13] S. S. Chou, M. De, J. Kim, S. Byun, C. Dykstra, J. Yu, J. Huang, V. P. Dravid, *J Am Chem Soc* **2013**, *135*, 4584-4587.

[14] C. Backes, N. C. Berner, X. Chen, P. Lafargue, P. LaPlace, M. Freeley, G. S. Duesberg, J. N. Coleman, A. R. McDonald, *Angew Chem Int Ed Engl* **2015**, *54*, 2638-2642.

[15] X. Chen, A. R. McDonald, *Advanced Materials* **2016**, *28*, 5738-5746.

[16] S. Presolski, M. Pumera, *Materials Today* **2016**, *19*, 140-145.

[17] X. Zong, Y. Na, F. Wen, G. Ma, J. Yang, D. Wang, Y. Ma, M. Wang, L. Sun, C. Li, *Chemical Communications* **2009**, 4536-4538.

[18] Y.-J. Yuan, Z.-T. Yu, X.-J. Liu, J.-G. Cai, Z.-J. Guan, Z.-G. Zou, **2014**, *4*, 4045.

[19] S. Min, G. Lu, *The Journal of Physical Chemistry C* **2012**, *116*, 25415-25424.

[20] U. Maitra, U. Gupta, M. De, R. Datta, A. Govindaraj, C. N. R. Rao, *Angewandte Chemie International Edition* **2013**, *52*, 13057-13061.

[21] S. Lei, X. Wang, B. Li, J. Kang, Y. He, A. George, L. Ge, Y. Gong, P. Dong, Z. Jin, G. Brunetto, W. Chen, Z.-T. Lin, R. Baines, D. S. Galvão, J. Lou, E. Barrera, K. Banerjee, R. Vajtai, P. Ajayan, *Nat Nano* **2016**, *11*, 465-471.

APPENDIX

CHAPTER 2

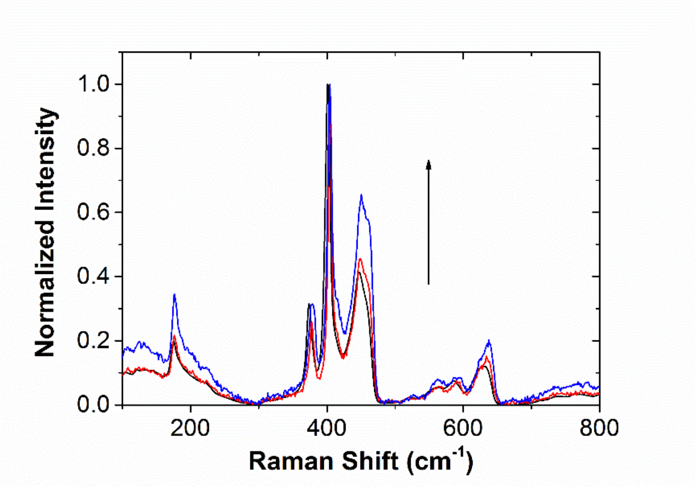

Figure S2.1 Normalized Raman spectra of Cys-2H-MoS_2 measured at different laser intensity and thus temperatures: black trace (10% filter), red trace (25% filter) and blue trace (50% filter).

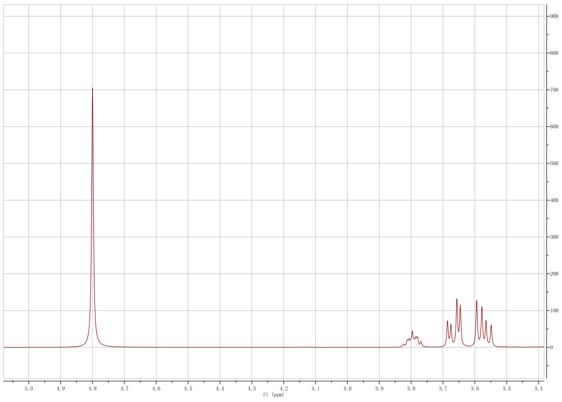

Figure S2.2 ^{1}H-NMR spectrum of dialysate. The spectrum matches very well that previously published for cystine.[1]

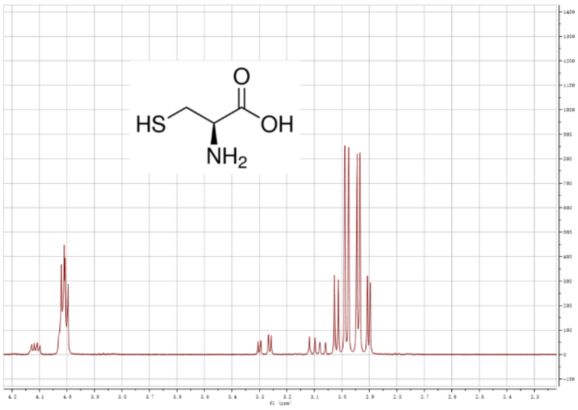

Figure S2.3 ¹H-NMR spectrum of products from sonication of cysteine itself.

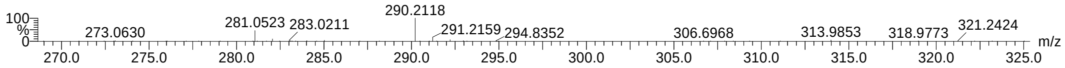

```
Minimum:                                  -1.5
Maximum:                10.0      10.0     50.0

Mass       Calc. Mass   mDa       PPM      DBE      i-FIT      Formula

290.2118   290.2102     1.6       5.5      0.0      1.4        C16  H34  S2
```

Figure S2.4 GC-MS spectrum of supernatant solution from the functionalization reaction, wherein the dominant species with m/z = 290.2118 was associated with dioctyl disulfide (calculated mass is 290.2102).

CHAPTER 3

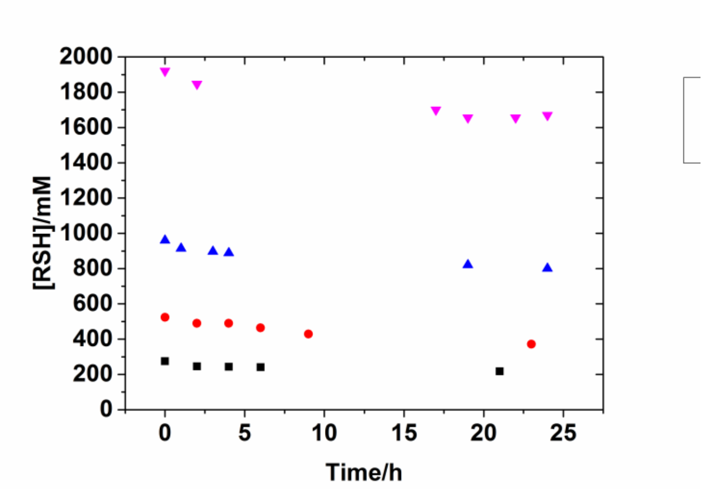

Figure S3.1 Plots of inverse concentration of free 1-octanethiol [RSH] vs. reaction time under varied initial concentrations of 1-octanethiol: 274 mM (black), 524 mM (red), 961 mM (blue) and 1921 (magenta).

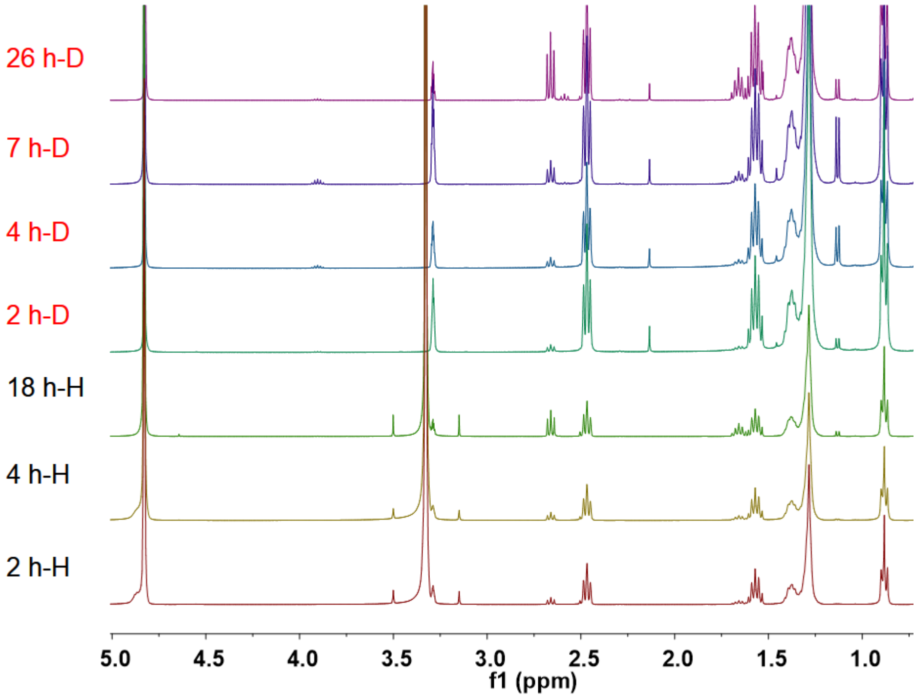

Figure S3.2 ^{1}H-NMR (400 MHz, d_4-CH_3OH) spectra of 1-octanethiol/exfoliated MoS_2 reaction mixture in CH3OH and in d_4-CH_3OH.

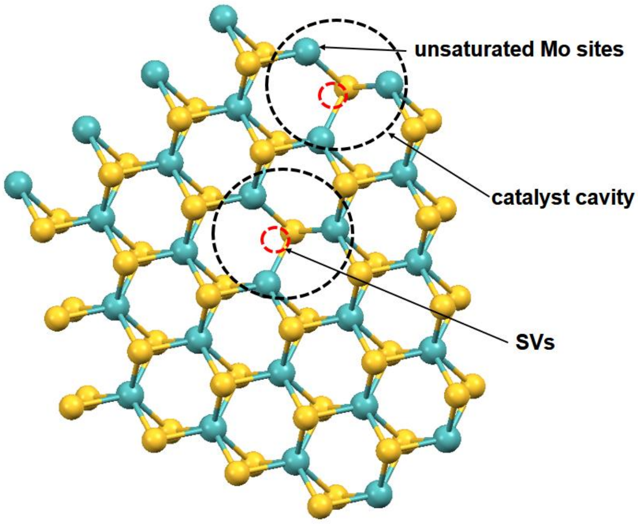

Figure S3.3 Schematic representation of SVs (red circle) and catalyst cavity (black circle).

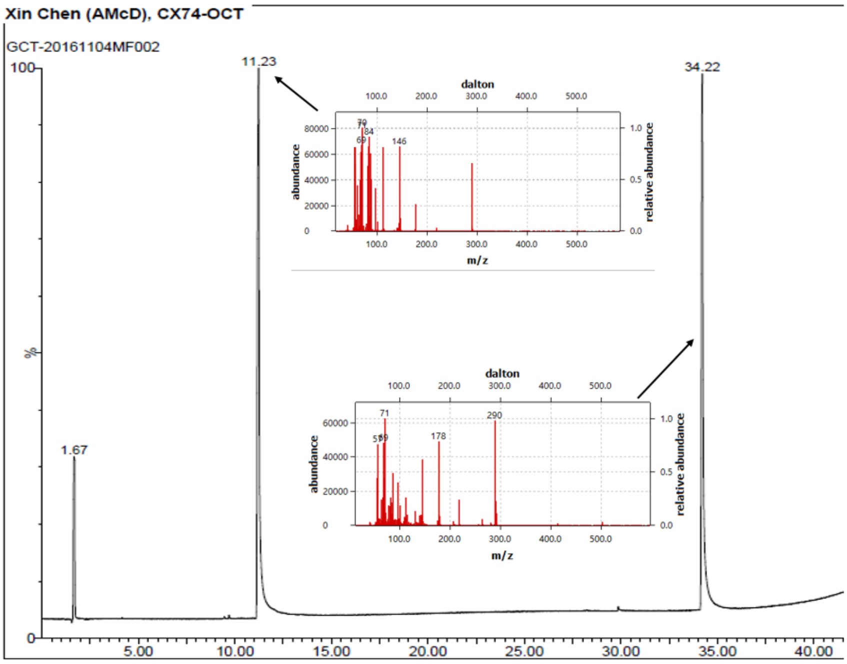

Figure S3.4 GC-MS results of 1-octanethiol/exfoliated MoS_2 reaction mixture.

CHAPTER 4

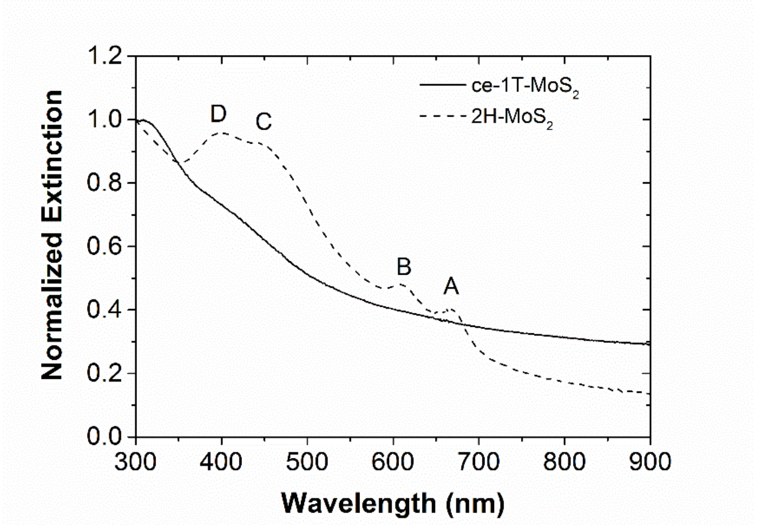

Figure S4.1 Extinction spectra of ce-1T-MoS_2 and 2H- MoS_2.

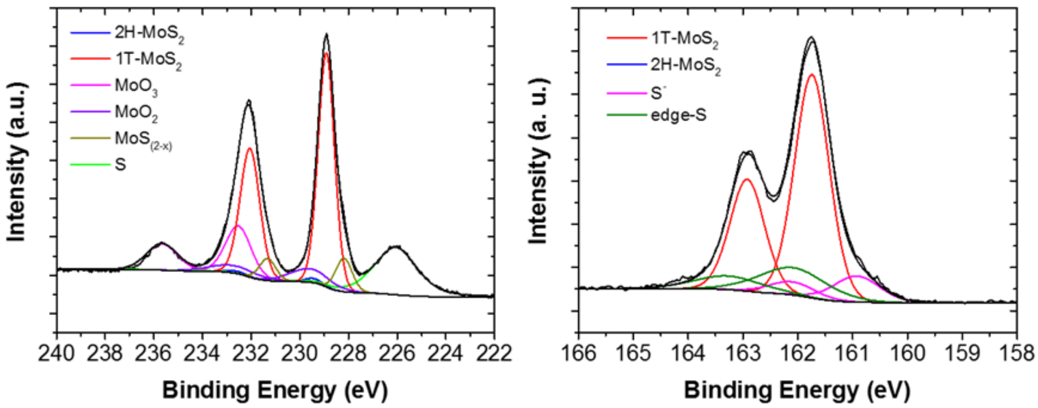

Figure S4.2 Fitted Mo 3d (left) and S 2p (right) core level spectra of ce-1T-MoS_2

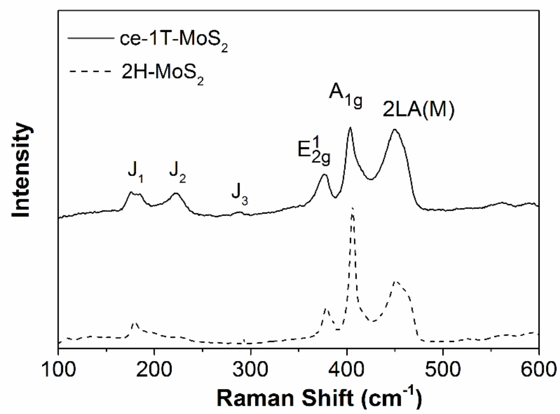

Figure S4.3 Raman spectra of ce-1T-MoS_2 and 2H-MoS_2. Excited at λ= 633 nm.

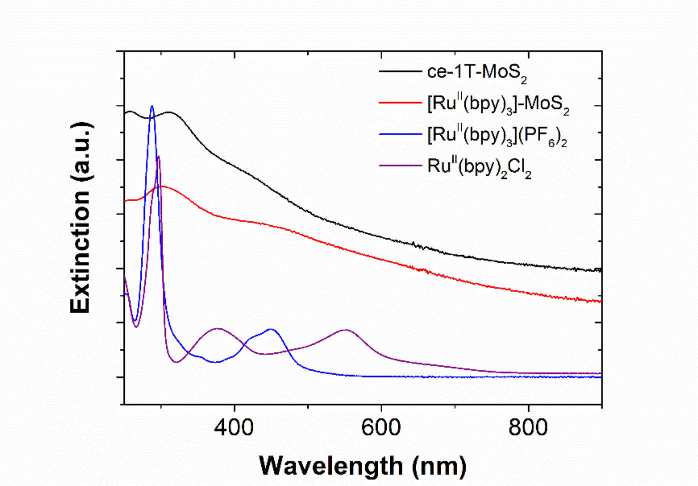

Figure S4.4 Extinction spectra of ce-1T-MoS_2, $[Ru^{II}(bpy)_3]$-MoS_2, $[Ru^{II}(bpy)_3]$-$(PF_6)_2$ and $[Ru^{II}(bpy)_2Cl_2]$.

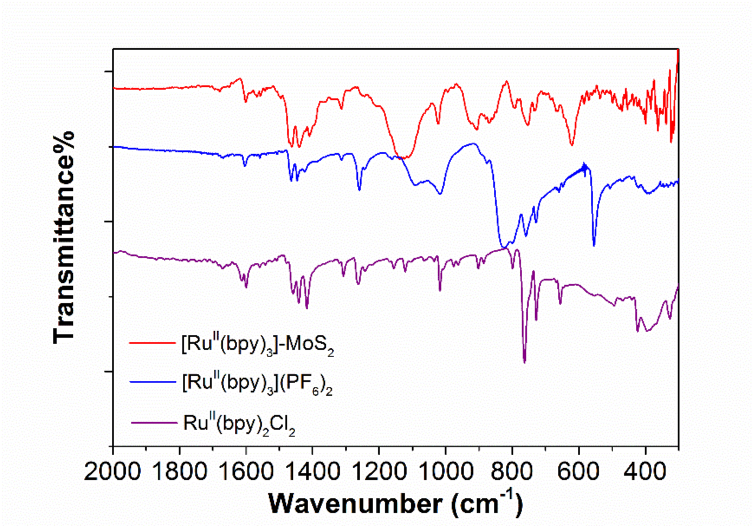

Figure S4.5 DRIFT spectra of [Ru^{II}(bpy)$_3$]-MoS$_2$, [Ru^{II}(bpy)$_3$](PF$_6$)$_2$ and [Ru(bpy)$_2$Cl$_2$].

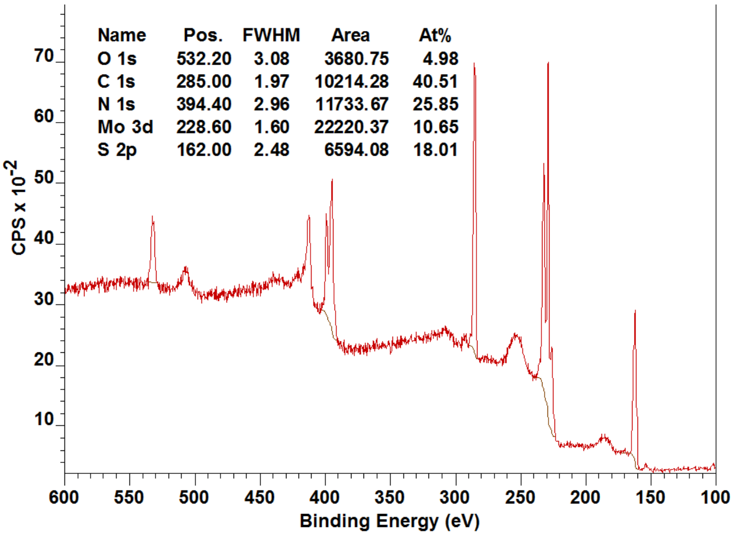

Name	Pos.	FWHM	Area	At%
O 1s	532.20	3.08	3680.75	4.98
C 1s	285.00	1.97	10214.28	40.51
N 1s	394.40	2.96	11733.67	25.85
Mo 3d	228.60	1.60	22220.37	10.65
S 2p	162.00	2.48	6594.08	18.01

Figure S4.6 XPS survey spectrum of bpy-MoS$_2$. The oxygen component (532 eV) was detected due to the presence of MoO$_x$ species.

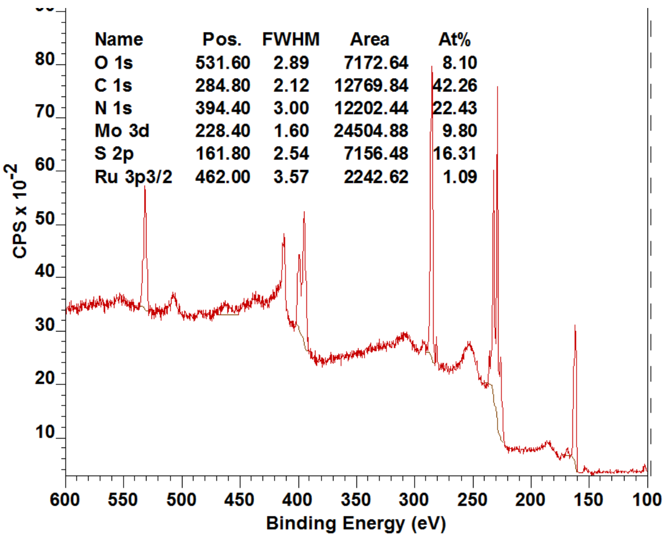

Name	Pos.	FWHM	Area	At%
O 1s	531.60	2.89	7172.64	8.10
C 1s	284.80	2.12	12769.84	42.26
N 1s	394.40	3.00	12202.44	22.43
Mo 3d	228.40	1.60	24504.88	9.80
S 2p	161.80	2.54	7156.48	16.31
Ru 3p3/2	462.00	3.57	2242.62	1.09

Figure S4.7 XPS survey spectrum of [Ru^{II}(bpy)$_3$]-MoS$_2$. The oxygen component (532 eV) was detected due to the presence of MoO$_x$ species.

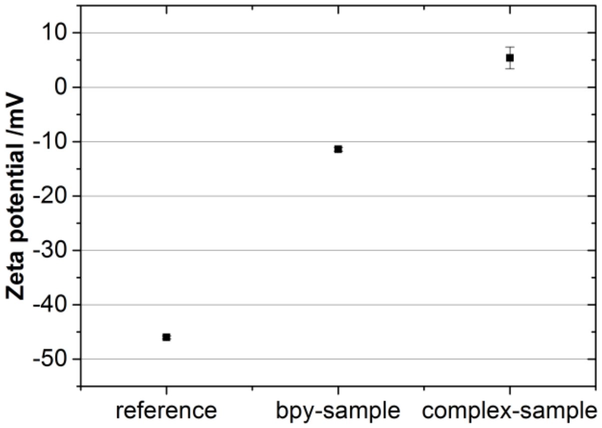

Figure S4.8 Zeta potential of ce-1T-MoS$_2$, bpy-MoS$_2$, Ru^{II}(bpy)$_3$]-MoS$_2$

CHAPTER 5

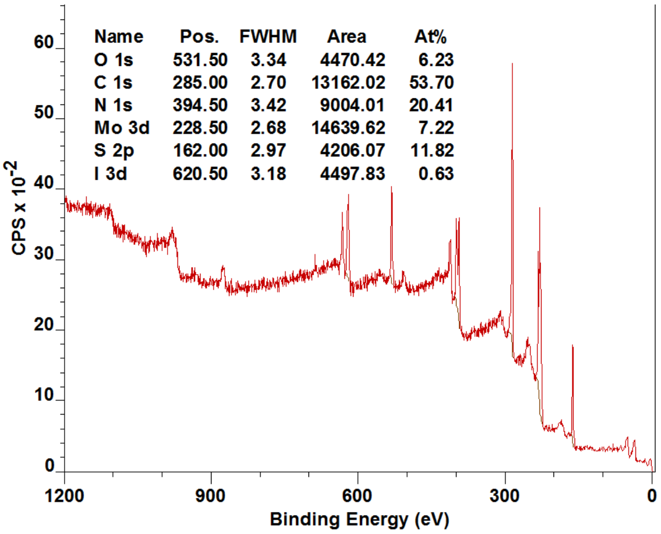

Name	Pos.	FWHM	Area	At%
O 1s	531.50	3.34	4470.42	6.23
C 1s	285.00	2.70	13162.02	53.70
N 1s	394.50	3.42	9004.01	20.41
Mo 3d	228.50	2.68	14639.62	7.22
S 2p	162.00	2.97	4206.07	11.82
I 3d	620.50	3.18	4497.83	0.63

Figure S5.1 XPS survey spectrum of phen-MoS$_2$.

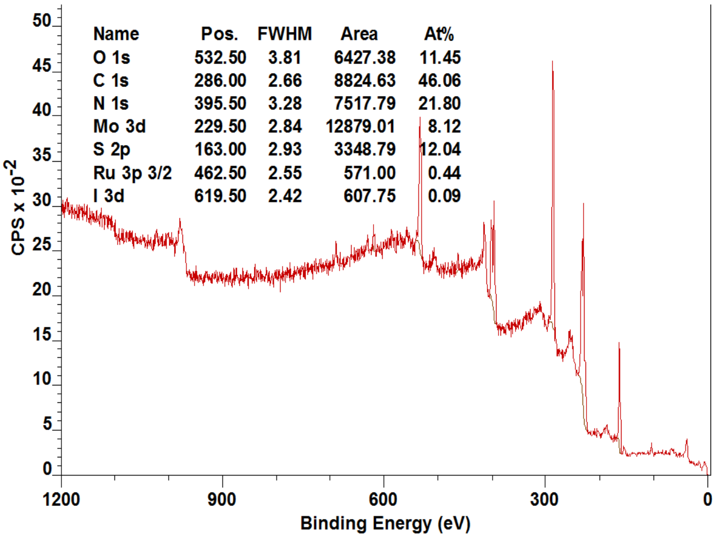

Name	Pos.	FWHM	Area	At%
O 1s	532.50	3.81	6427.38	11.45
C 1s	286.00	2.66	8824.63	46.06
N 1s	395.50	3.28	7517.79	21.80
Mo 3d	229.50	2.84	12879.01	8.12
S 2p	163.00	2.93	3348.79	12.04
Ru 3p 3/2	462.50	2.55	571.00	0.44
I 3d	619.50	2.42	607.75	0.09

Figure S5.2 XPS survey spectrum of [Ru^{II}(bpy)$_2$(phen)]-MoS$_2$.

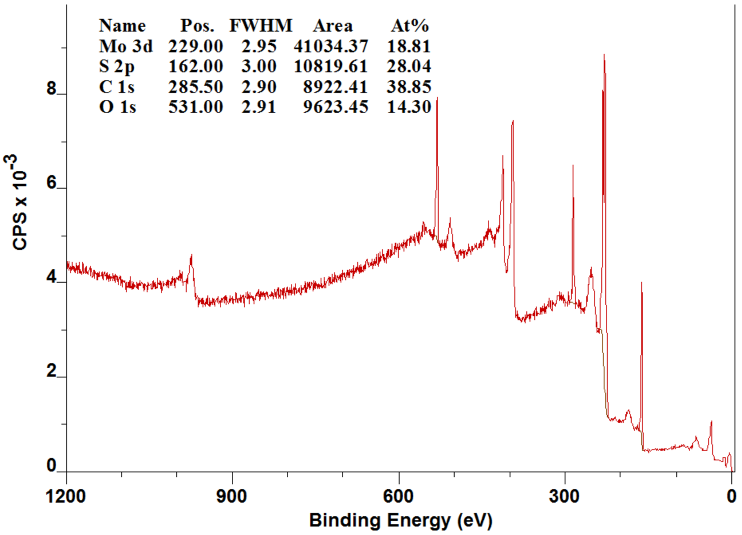

Name	Pos.	FWHM	Area	At%
Mo 3d	229.00	2.95	41034.37	18.81
S 2p	162.00	3.00	10819.61	28.04
C 1s	285.50	2.90	8922.41	38.85
O 1s	531.00	2.91	9623.45	14.30

Figure S5.3 XPS survey spectrum of py-MoS_2.

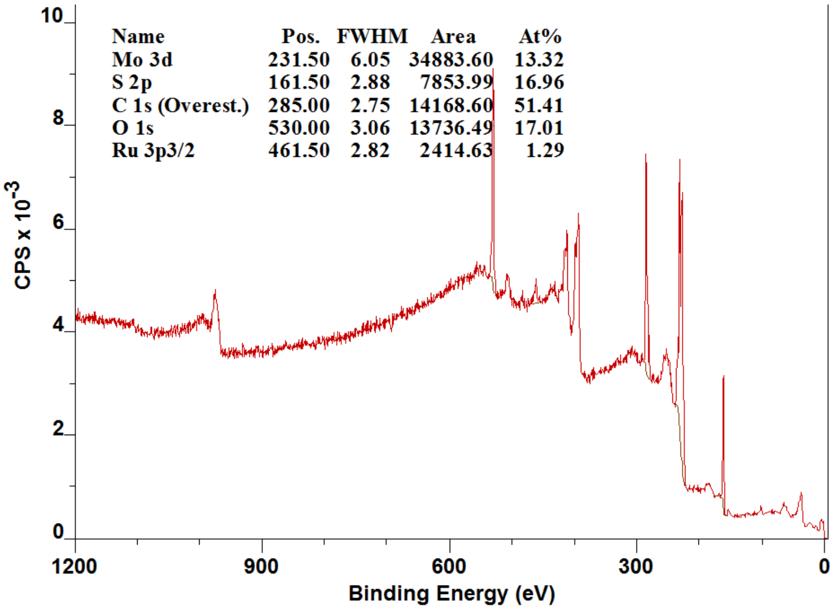

Name	Pos.	FWHM	Area	At%
Mo 3d	231.50	6.05	34883.60	13.32
S 2p	161.50	2.88	7853.99	16.96
C 1s (Overest.)	285.00	2.75	14168.60	51.41
O 1s	530.00	3.06	13736.49	17.01
Ru 3p3/2	461.50	2.82	2414.63	1.29

Figure S5.4 XPS survey spectrum of [$Ru^{II}(bpy)_2(py)Cl$]-MoS_2.

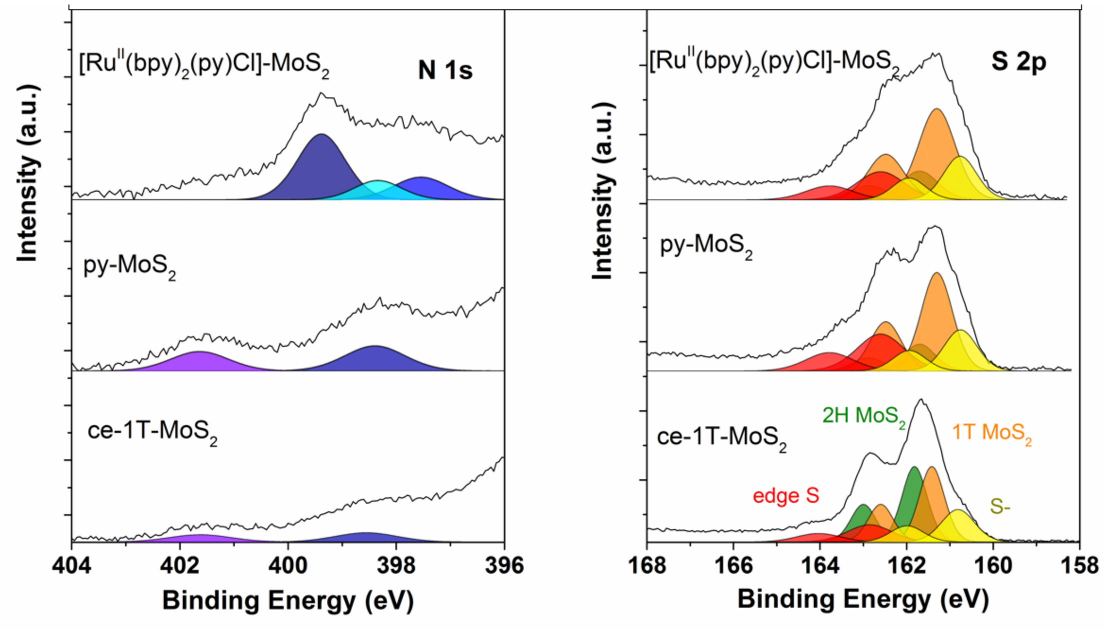

Figure S5.5 Left: fitted N 1s core level spectra of ce-1T-MoS$_2$, py-MoS$_2$ and [Ru^{II}(bpy)$_2$(py)Cl]-MoS$_2$. Right: fitted S 2p core level spectra of ce-1T-MoS$_2$, py-MoS$_2$ and [Ru^{II}(bpy)$_2$(py)Cl]-MoS$_2$.

Table S5.1 Electrocatalytic properties[a] of MoS$_2$-based electrocatalysts

	TS (mV/dec)	**J_o (μA/cm^2)**	**η (V) j= -10mA/cm^2**	**J(mA/cm^2) η = -0.3 V**
ce-1T-MoS$_2$	92	14.9	-0.26	-26.5
phen-MoS$_2$	209	9.7	-	-0.3
[Ru^{II}(bpy)$_2$(phen)]-MoS$_2$	122	1.5	-0.50	-0.4
py-MoS$_2$	103	3.8	-0.36	-3.2
[Ru^{II}(bpy)$_2$(py)Cl]-MoS$_2$	97	4.1	-0.33	-5.1

[a] All the electrochemical properties of a specific material deposited electrode were obtained based on at least three independent electrodes, each performed in

triplicate and the best results are presented.

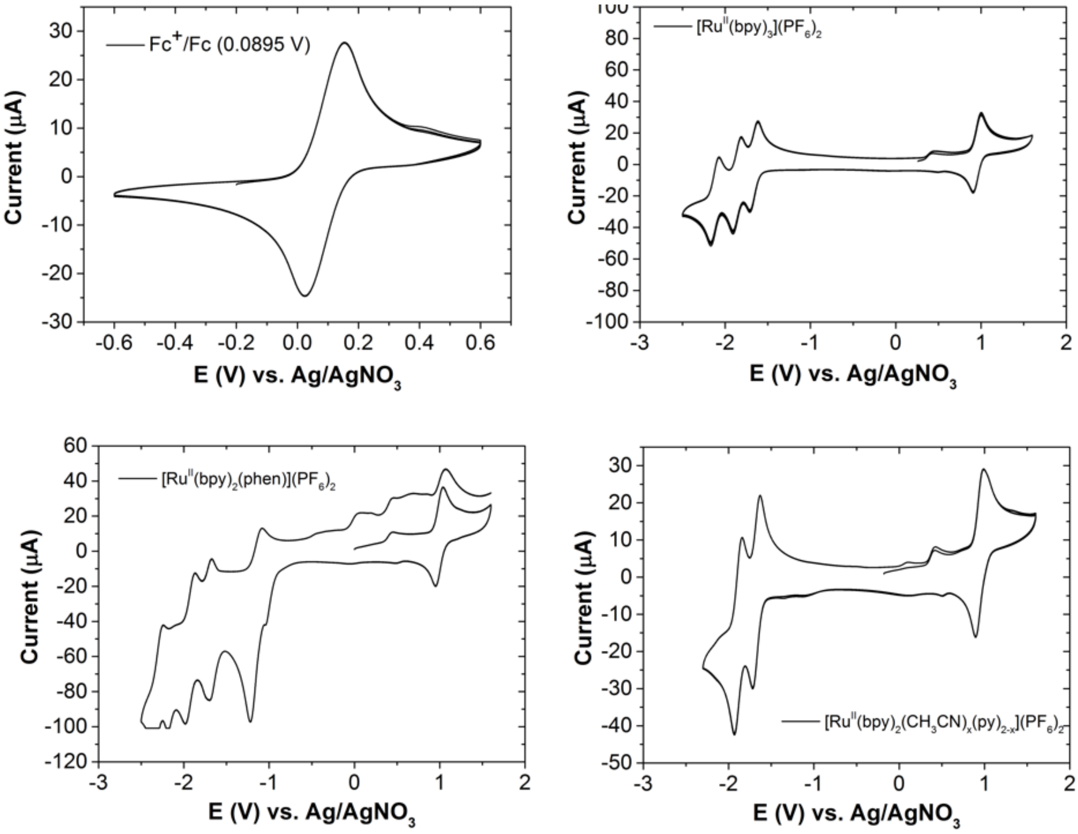

Figure S5.6 The Cyclic voltammograms of ferrocene (1.0 mM) and model complexes (1.0 mM) in Bu$_4$NPF$_6$ (0.1 mM) with Ag/AgNO$_3$ (0.01 M) as reference electrode.

References

[1] A. R. Katritzky, N. G. Akhmedov, O. V. Denisko, *Magn. Reson. Chem.* **2003**, *41*, 37-41.